UNIVERSITY OF LEEDS

Understanding the Structural and Dynamic Foundations of β-Lactam Resistance in PBP2a of methicillin-resistant Staphylococcus aureus

William Alexander-Meddick-Dyson

Submitted in fulfilment of the requirements for the degree of

Doctor of Philosophy

The University of Leeds

School of Molecular and Cellular Biology

Faculty of Biological Sciences

October 2025

Dedication

To my mother and father, who taught me the value of patience, persistence and dedication. Who's own trials are testimony to what good can be done if above all else, values, integrity, and a kind heart are your guide.

To my Beautiful wife, to whom I owe everything. Who drives me every day to be the best possible example of a man. Who inspires me daily with her unwavering kindness and fierce dedication to a life of honesty, integrity and the prioritisation of the lives of others. Who continues to remind me that a life dedicated to selflessness and servitude is a life of peace. I will never feel more blessed than being able to spend my days alongside the greatest role model I will ever know.

Acknowledgements

To Dr Justin Clarke, Dr Luiza Galarion and Professor Alexander O'Neill for their expertise and guidance in troubleshooting and executing all microbiology related experiments. Especially Dr Clarke, who's creativity and breadth of knowledge served as a role model for the standard of academic that I should hope to one day embody.

To Dr Bob Schriffin, for his expertise and guidance in the *de novo* design of mini-proteins and bringing fresh enthusiasm and perspectives to a most challenging project

To Dr Arnout Kalverda for his wealth of knowledge and expertise in guiding complicated experimental series to troubleshoot and overcome the challenges of PBP2a assignment.

To the other members of the NMR faculty for their encouragement, support and insightful discussions.

To Dr Jennifer Tomlinson for her persistence, patience, support and invaluable mentorship throughout what will remain my greatest challenge and achievement. For pushing the boundaries of my academic rigour, and for continually encouraging and embodying standards that uphold the integrity that enables research to have value and contribution. Through Covid-19, my father's cancer diagnosis, and numerous other challenges, Jenny has been patient, professional and proactive in ensuring my research be completed to the highest possible standard. I will carry through these standards in my future work and owe Jenny a great deal of gratitude for preparing me for my future endeavours.

Abstract

Antibiotic resistance is a worldwide calamity, set to become the greatest single cause of human mortality by 2050[1]. β-lactams account for approximately 60% of the total antibiotics used in the clinic[2] however, their overuse has seen their efficacy diminished by rapidly rising resistance rates[3]. Methicillin-resistant *Staphylococcus aureus* (MRSA) remains a major global health threat[2], owing to its expression of penicillin binding protein 2a (PBP2a) – an enzyme that sustains cell wall synthesis despite the presence of β-lactam antibiotics[4]. PBP2a achieves this via an evolved allosteric domain (AD) regulates a 60 Å distal transpeptidase (TP) containing the active site, wherein AD activation increases the volume of the TP domain which has insufficient occupancy in the apo state[4-7]. Critically, PBP2a's canonical substrate peptidoglycan (PG) but not β-lactams activate the AD, thus enabling the selective of inhibitory agents whilst sustaining the crosslinking of PG necessary for cell survival[4-7]. Only two β-lactams retain inhibitory efficacy against PBP2a – the fifth generation cephalosporins ceftaroline (CFT)[8-10] and ceftobiprole (CFB)[11,12]. However, while substantial data evidence has linked CFT's inhibitory capacity to AD activation (as in PG), less is known about the mechanistic details of CFB, where it remains unclear if allostery plays a role and to what extent. The structural and dynamic mechanisms by which PBP2a resists inhibition, and how these may be overcome, remain incompletely understood. This thesis integrates structural biology and NMR spectroscopy to investigate binding of antibiotics to PBP2a and how PBP2a's conformational dynamics govern antibiotic resistance and inhibition. It also investigates whether rationally *de novo* designed mini-proteins can resensitise PBP2a to β-lactam antibiotics as a potential route to antibiotic adjuvant development. A selective methyl-labelling strategy was used to enable residue-level characterisation of PBP2a – previously intractable to conventional NMR assignment strategies due to its size and intrinsic flexibility. NMR relaxation dispersion analyses suggest that the apo enzyme samples a broad dynamic landscape, with coupled motions between its allosteric and transpeptidase domains that regulate active-site accessibility. Binding studies showed that ceftobiprole inhibits PBP2a via a direct, non-allosteric mechanism, engaging the transpeptidase domain and dampening global motions while preserving local flexibility at catalytic loops. This contrasts with ceftaroline, which requires allosteric activation, consistent with the observation that ceftaroline-resistant MRSA isolates carry mutations in both domains[13-18], whereas ceftobiprole resistance arises almost exclusively from substitutions in the catalytic region[16,18-20]. Building on these mechanistic insights, *de novo*

designed mini-protein binders were created using deep-learning-based protein design tools[21-23]. One binder was experimentally validated by chemical shift perturbations to engage PBP2a across both domains and – critically – restore susceptibility of MRSA to oxacillin at 8 μg/mL, showing that such binders are a potential source of antibiotic adjuvant to circumvent this resistance mechanism. Together, these findings show that the structurally related ceftaroline and ceftobiprole inhibit PBP2a by different mechanisms and demonstrate that resistance can be functionally reversed by rationally designed protein ligands, opening new avenues for re-sensitising MRSA to existing β-lactam antibiotics and redefining strategies for targeting antibiotic-resistant pathogens.

Contents

List of Figures

List of Tables

Abbreviations

AD – Allosteric domain

CFB – Ceftobiprole

CFT – Ceftaroline

CPMG – Carr-Purcell-Meiboom-Gill relaxation-dispersion

CSP – Chemical shift perturbation

D_2O – Deuterium oxide

HADDOCK – High Ambiguity Driven protein–protein DOCKing

HMQC – Heteronuclear multiple-quantum coherence

HNCA / HNCO / HN(CO)CA / HNCACB – Triple-resonance NMR experiments correlating amide (^{1}H-^{15}N) signals with carbonyl or alpha/beta carbons

HSQC – Heteronuclear single-quantum coherence

ILVA – Isoleucine, leucine, valine, alanine methyl-labelling scheme

Lobe 1 / Lobe 2 – Structural sub-regions of the allosteric domain in PBP2a

MD – Molecular dynamics (simulation)

MIC – Minimum inhibitory concentration

MRSA – Methicillin-resistant *Staphylococcus aureus*

NMR – Nuclear magnetic resonance spectroscopy

NOE / NOESY – Nuclear Overhauser effect / NOE spectroscopy

NTE – N-terminal extension region of PBP2a

NUS – Non uniform sampling (accelerated NMR acquisition strategy)

PBP – Penicillin binding protein

PBP2a – Penicillin binding protein 2a

PG – Peptidoglycan

SOFAST – Band-selective, optimised flip-angle short-transient

Chapter 1 Introduction

1.1 Antibiotic Resistance

The World Health Organization has declared antimicrobial resistance (AMR) one of the top 10 global public health threats facing humanity, currently causing an estimated 1.27 million deaths directly per year[3]. Resistance is rising rapidly, where by 2050, antibiotic resistance-associated mortalities are expected to exceed those from the most burdensome of diseases, including cancer[1]. Inaction will not only devastate the health of many afflicted by antibiotic resistant infections but also the global economy, with costs in the order multiple trillions of US dollars[1,24]. Last resort prescribing of low therapeutic index, broad spectrum agents (e.g. colistin, polymyxin) because of poor judgement and/or the limitations of available point of care diagnostics remains, arguably, the greatest driver of resistance. Indeed, as much as half of all antibiotics are prescribed at inappropriate doses or are not needed at all[3]. However, agriculture, horticulture, routine laboratory genetic manipulation practices, and even anti-fouling plants used in oil industry all contribute significant evolutionary pressure responsible for the spread of antibiotic resistance[25-27]. The emergence of the post-antibiotic era is a present-day reality[3], where the acquisition of resistance to antimicrobials by microbes is unchallengingly outrunning our ability to replenish our available arsenal of therapeutics. In the absence of antibiotics, not only would treatment of many severe bacterial infections result in failure, routine procedures such as caesarean sections, invasive surgery, joint replacements and even chemotherapy would not be possible[3].

Antibiotics eradicate the consequences of microbial infections by shutting down or subverting a variety of processes essential to both Gram-negative and Gram-positive bacteria . Resistance to antibacterial agents can be chromosomal (intrinsic) or acquired (extrinsic) via horizontal gene transfer (HGT). Key mechanisms underpinning drug resistance include (Figure 1) (i) chemical modification or hydrolysis of the antibiotic (drug inactivation), (ii) reduced drug penetration or increased drug efflux (decreased intracellular concentration) and (iii) target restoration, substitution or alteration (target modification)[28]. Resistance to antibiotics is rising and indeed, some microbes are immune to several classes of antibiotics, such as methicillin- resistant Staphylococcus aureus (MRSA)[4] which is resistant to nearly all penicillins, carbapenems and cephalosporins[7] or extensively drug-resistant Mycobacterium tuberculosis (XDR-TB)[29], with resistance to nearly all antimicrobial compounds[30].

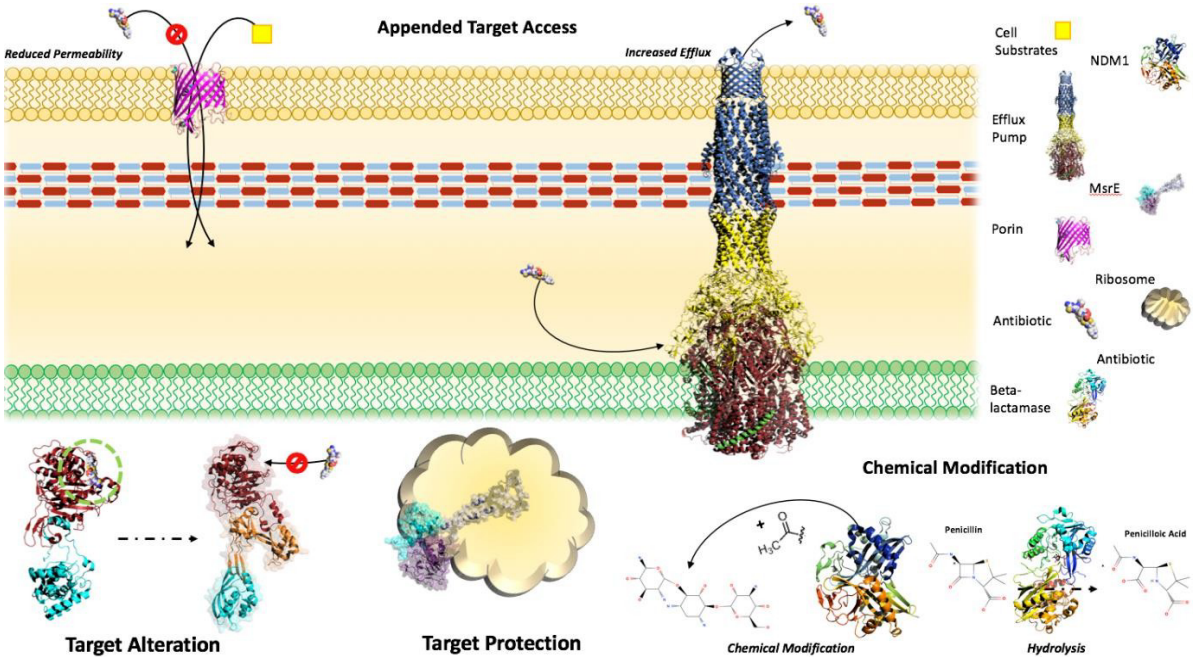

Figure 1: Major classes of antibiotic resistance mechanisms.

Bacteria employ diverse molecular strategies to resist the action of antibiotics. Appended Target Access highlights two mechanisms: reduced permeability, where modifications to selective membrane proteins (e.g., porins, shown in magenta) decrease the influx of antibiotics into the cell, and increased efflux, where dedicated efflux transporter proteins, such as the AcrABZ-TolC complex (depicted in blue, red, and yellow), actively pump antibiotics out of the bacterial cytoplasm. Chemical Modification demonstrates drug inactivation through two primary routes: inactivating hydrolysis, exemplified by β-lactamases like AmpC (coloured in orange, blue and green), which cleave and inactivate β-lactam antibiotics (e.g., penicillin), and chemical modification, such as the action of aminoglycoside-modifying enzymes (e.g NDM-1, coloured by B-factor) which add chemical groups to antibiotics, preventing them from binding to their targets. Target Protection illustrates mechanisms where bacterial proteins (e.g., MsrE, shown in teal and purple) bind to and shield the antibiotic's target (e.g., the ribosome, shown in light yellow) from its effects. Finally, Target Alteration depicts a scenario where the bacterial target itself is modified or replaced. This includes the acquisition of a new, resistant protein (e.g., PBP2a, shown in various shades of brown and green) that can perform the essential cellular function while being insensitive to the antibiotic that normally targets its susceptible counterpart.

Each of these resistance strategies poses a significant clinical challenge. Drug inactivation is a primary mechanism of resistance to some of the most critical antibiotic classes. The classic example is the production of β-lactamase enzymes, which hydrolyse the amide bond in the four-membered β-lactam ring, rendering the antibiotics ineffective[31]. The evolution and dissemination of extended-spectrum β-lactamases (ESBLs)[32] and carbapenemases[33] (e.g. NDM-1, KPC) have severely compromised the efficacy of penicillins, cephalosporins, and even last-resort carbapenems, particularly in Gram-negative pathogens like *Escherichia coli* and *Klebsiella pneumoniae*[34]. Similarly, enzymatic modification by aminoglycoside-modifying enzymes (AMEs) is a widespread cause of resistance to agents such as gentamicin and amikacin[35]. Decreasing the intracellular concentration of an antibiotic is another highly effective strategy. This is frequently achieved by overexpressing multidrug resistance

(MDR) efflux pumps – membrane proteins that actively expel a wide range of antibiotics from the bacterial cell[36]. Pumps such as the AcrAB-TolC system in *E. coli* (Figure 1) or the Mex family in *Pseudomonas aeruginosa* contribute to both intrinsic and high-level acquired resistance, often making a single organism non-susceptible to multiple drug classes simultaneously[37,38]. In Gram-negative bacteria, this mechanism is often coupled with reduced drug entry caused by the modification or loss of outer membrane porin channels, further limiting antibiotic access to intracellular targets[38]. Target modification prevents the antibiotic from binding to its molecular target. This can occur through point mutations, as seen in the quinolone-resistance determining regions of DNA gyrase (*gyrA*) and topoisomerase IV (*parC*), which confer resistance to fluoroquinolones[39]. Another route is enzymatic alteration of the target, such as the methylation of 23S rRNA, which prevents the binding of macrolides, lincosamides, and streptogramins[34].

Given the lack of new drugs in the development pipeline, it is important to understand the underlying molecular mechanisms driving resistance to best direct future therapeutic approaches. While some are well understood, molecular detail is lacking in others. Among the most clinically significant examples of resistance via target alteration is the acquisition of a new penicillin-binding protein, PBP2a (encoded by the *mecA* gene)[4]; the defining resistance determinant of methicillin-resistant *Staphylococcus aureus* (MRSA)[4]. The acquisition of PBP2a confers resistance to nearly all β-lactam antibiotics, which have long been the primary treatment for staphylococcal infections. The global prevalence and associated morbidity and mortality of MRSA make understanding the function of PBP2a a paramount objective in the fight against AMR[40]. It is this critical and clinically intractable resistance mechanism wherein lies the focus of this research.

1.2 Bacterial Cell Wall Biosynthesis

Most bacteria are encased by a rigid cell wall that is indispensable to survival due to its resistance to lysis via intracellular turgor[41], with architectural distinctions that have profound functional consequences between the walls of Gram-positive and Gram-negative bacteria (Figure 2):

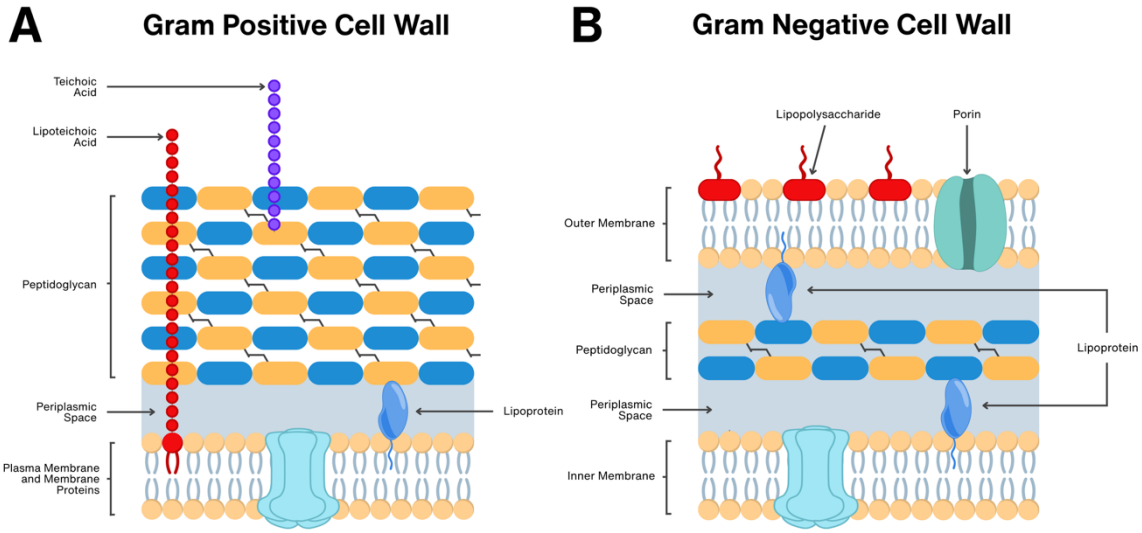

Figure 2: Structural comparison of Gram-positive and Gram-negative bacterial cell walls.

(A) The Gram-positive cell walls contain a thick, multi-layered peptidoglycan (alternating blue and orange blocks) layer that constitutes the major component of the cell wall. Embedded within and extending beyond the peptidoglycan are teichoic acid (purple chain) and lipoteichoic acid (red chain), which are covalently linked to the plasma membrane. The relatively small periplasmic space in Gram-positive bacteria contains few proteins relative to Gram-negative bacteria. Various lipoproteins are associated with the plasma membrane with numerous functions to maintain cell wall integrity, transport and antibiotic resistance. The plasma membrane sits as the innermost layer, comprising a lipid bilayer with embedded membrane proteins (e.g., transport proteins, shown in light blue). (B) The Gram-negative cell wall depicts a more complex, multi-layered structure. The inner membrane is a lipid bilayer with embedded membrane proteins (light blue). The periplasmic space outside the inner membrane is significantly larger than in Gram-positive cell walls and contains a diverse array of proteins, including those involved in nutrient acquisition and antibiotic resistance. A much thinner layer of peptidoglycan (blue and orange blocks) sits inside the periplasmic space. External to the peptidoglycan is the outer membrane, an asymmetrical lipid bilayer, with its inner leaflet composed of phospholipids and its outer leaflet predominantly made up of lipopolysaccharide (LPS) (red structures with wavy chains). Spanning the outer membrane are porins (teal green barrel-shaped proteins), which regulate the passive diffusion of small hydrophilic molecules, including some antibiotics.

From a structural perspective, the Gram-positive wall (Figure 2A) can be conceptualised as a thick, porous exoskeleton. Its principal component, a multi-layered peptidoglycan meshwork, can exceed thicknesses of 100 nm[41], and is primarily responsible for withstanding high internal osmotic pressure and maintaining cell shape. Crosslinking between peptidoglycan strands adds further structural rigidity. This mesh is decorated and reinforced by anionic glycopolymers – the teichoic and lipoteichoic acids – which create a net negative charge on the cell surface. This charge is critical for sequestering divalent cations such as Mg^{2+} and Ca^{2+}, thereby maintaining the structural integrity of the envelope

and mediating interactions with host surfaces[41]. In contrast, the Gram-negative envelope (Figure 2B) represents a more complex, multi-laminar system[42]. The defining feature is the outer membrane, an asymmetric lipid bilayer that serves as a highly selective permeability barrier. Its outer leaflet is composed almost exclusively of lipopolysaccharide (LPS), a large glycolipid whose hydrophilic, repetitive O-antigen chains create a hydrated layer that prevents the passage of hydrophobic molecules, including many detergents and antibiotics. LPS also contributes to pathogenicity and acts as an endotoxin. The passage of essential nutrients and small hydrophilic molecules across this barrier is tightly regulated by transmembrane proteins known as porins, which typically adopt a β-barrel architecture to form size- and charge-selective channels. Situated between the inner and outer membranes is the periplasm, a distinct subcellular compartment containing a thin layer (only a few nm) of peptidoglycan and a concentrated, gel-like matrix of proteins involved in nutrient transport, protein folding, and, critically, the enzymatic degradation of antibiotics (e.g. β-lactamases)[42]. These fundamental structural differences dictate how bacteria interact with their environment, presenting both distinct challenges and targets for the design of antimicrobial therapeutics.

Peptidoglycan (PG) is a major structural component central to both Gram-negative and Gram-positive bacterial cell walls[43], forming a contiguous, mesh-like barrier around the cytoplasmic membrane, reinforcing the cell wall's mechanical strength and protecting it from osmotic lysis. Structurally, peptidoglycan is a heteropolymer composed of long glycan strands of alternating uridine diphosphate N-acetylglucosamine (UDP-GlcNAc) and uridine diphosphate N-acetylmuramic acid (UDP-MurNAc) residues[43]. Considerable variation in PG glycan strand length exists between bacterial strains, wherein the average length for Gram-positive species can vary from as little as 6 units in length to an excess of 250 units, in contrast to Gram-negative species with a narrower average of between 20-40 units[44]. Notably, the dominant PG strand length for *S. aureus* is ~6-10 disaccharides, with a mean of ~18 units, contrasting greatly with that of *Bacilli* with a much broader distribution of extended glycan structures ranging from 50-250 units in length[44,45]. This diversity in PG glycan strand length is apparently important for cell wall flexibility, wherein extended chain lengths resulting from inactivation of *S. aureus* glucosaminidase SagB – a peptidoglycan hydrolase important in glycan strand length regulation with preference for longer strands – were shown to cause increased cell wall stiffness and decreased elasticity due to long, unprocessed strands[46-48]. Additionally, glycan strands from *H. pylori* are particularly short,

with an average chain length of <10 disaccharide units, shortening even further during transition from spiral to coccoid morphologies during stationary growth phases[49,50]. Taken collectively, the short glycan chain length of *S. aureus* is likely a key structural and functional feature.

Covalently attached to the lactyl moiety of each MurNAc residue is a short peptide stem, typically terminating in a D-Ala-D-Ala motif. The final, rigid architecture of the cell wall is achieved when these peptide stems on adjacent glycan strands are cross-linked[43]. The essentiality of this structure, coupled with its absence in eukaryotic cells, makes the peptidoglycan biosynthesis pathway a prime target for many effective antimicrobials, namely, the penicillin binding protein (PBP) inhibiting β-lactam class of antibiotics[43,51]. The intricate process of PG biosynthesis is a highly conserved pathway that can be divided into three distinct stages, as summarised in Figure 3:

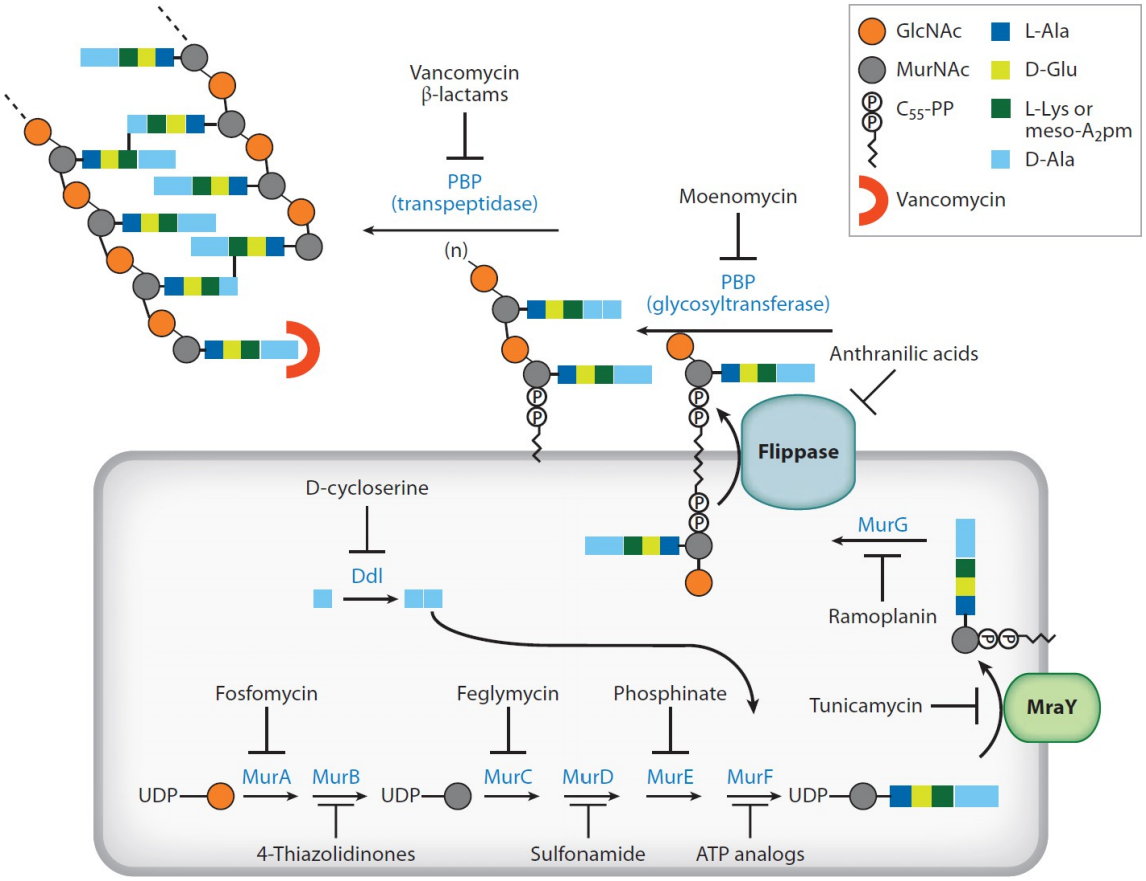

Figure 3: Overview of the bacterial peptidoglycan biosynthesis pathway.

The pathway proceeds from the cytoplasmic synthesis of a UDP-linked precursor to the final periplasmic assembly of the cell wall. The integral membrane proteins MraY and a flippase are shown facilitating the critical step of forming and transporting the Lipid II monomer across the plasma membrane. Enzyme names are highlighted in blue, while their respective inhibitors are shown in black. **Abbreviations:** C_{55}-PP, undecaprenyl diphosphate; D-Ala , D-alanine; Ddl, D-alanyl-D-alanine ligase; D-Glu, D-glutamic acid;

GlcNAc, N-acetylglucosamine; L-Ala, L-alanine; L-Lys, L-lysine; meso-A_2pm, meso-diaminopimelic acid; MurA-G, cytoplasmic biosynthesis enzymes; MurNAc, N-acetylmuramic acid; PBP, penicillin-binding protein. Figure taken from Lovering et al.[43].

PG synthesis is initiated in the cytoplasm by the conversion of fructose-6-phosphate to the key precursors UDP-GlcNAc and subsequently UDP-MurNAc-pentapeptide, a process catalysed by the sequential activity of the Glm and Mur enzyme family members (MurA-F), respectively[52-54]. This soluble precursor is then tethered to the cytoplasmic membrane. The membrane-associated stage begins when the integral membrane enzyme MraY catalyses the transfer of the phospho-MurNAc-pentapeptide moiety from UDP to C_{55}-P, an undecaprenyl phosphate carrier (often referred to as bactoprenol), generating the first lipid-linked intermediate, Lipid I. This is followed by the addition of a GlcNAc residue from UDP-GlcNAc by the peripheral membrane glycosyltransferase MurG, yielding the fundamental building block of peptidoglycan, Lipid II[52,53]. This complete disaccharide-pentapeptide monomer is then translocated across the cell membrane to the outer, periplasmic face by a dedicated Lipid II flippase (e.g. MurJ or FtsW)[55]. Once in the periplasm, Lipid II serves as the substrate for the final stage of PG biosynthesis, which is orchestrated by the penicillin-binding protein (PBP) family of enzymes. The bifunctional Class A PBPs catalyse two distinct reactions. First, their glycosyltransferase (GT) domain polymerises the glycan strands by adding the disaccharide unit of Lipid II to the non-reducing end of a growing glycan chain[56]. Concurrently, the transpeptidase (TP) domain catalyses the formation of peptide cross-links between the stem peptides of adjacent glycan strands. The TP domain first recognises a nascent D-Ala-D-Ala terminating donor stem and forms an acyl-enzyme intermediate following the release of the terminal D-Ala. This acyl group is then transferred to the amino group of an accepter stem on a neighbouring glycan chain, thereby generating the interstrand cross-link that provides the PG sacculus its tensile strength[43,57]. In *S. aureus*, this acceptor is provided not by a direct side-chain nucleophile, but by the amino terminus of a pentaglycine interpeptide bridge attached to the L-lysine residue at position 3 of the neighbouring stem peptide[58,59].

Despite the conservation of the overall logic of PG biosynthesis, considerable variation exists in the chemical composition of the stem peptide and the architecture of the interpeptide cross-bridge across bacterial species[60]. In particular, residues at positions 2, 3 and 5, together with the presence or absence of an interpeptide bridge, highlight important species-specific differences in PG chemistry and in the precise substrate presented to PBP TP domains (

Table 1).

Position	Common variation across bacteria	Representative examples	Relevance to *S. aureus*
1	Usually L-Ala; occasional Gly or L-Ser	Most bacteria (L-Ala); *Mycobacterium leprae* (Gly)*; Butyribacterium rettgeri* (L-Ser)	*S. aureus* retains canonical L-Ala
2	D-isoglutamate commonly modified to D-isoglutamine via amidation in many Gram-positive species	Most Gram-negative species = D-isoglutamate; many Gram-positive species and mycobacteria = D-isoglutamine	*S. aureus* peptidoglycan amidated at position 2, yielding D-isoglutamine
3	Typically a diamino acid; most often meso-A2pm or L-Lys	Gram-negative species and bacilli = meso-A2pm; many Gram-positive species = L-Lys	*S. aureus* contains L-Lys; attachment point for interpeptide bridge
Cross-bridge	May be absent, direct, or extended via interpeptide bridges of different composition	Direct cross-links in many Gram-negative species; varied bridges in Gram-positive species	*S. aureus* distinguished by pentaglycine bridge added to ε-amino group of L-Lys (position 3)
4	Usually D-Ala	Broadly conserved across bacteria	Conserved
5	Usually D-Ala with some variation to D-Ser or D-Lac in some organisms or resistant strains	Most bacteria = D-Ala; *Enterococcus gallinarum* = D-Ser; vancomycin-resistant enterococci = D-Lac	*S. aureus* typically retains terminal D-Ala (prior to transpeptidation)

Table 1: Comparative variation in peptidoglycan stem-peptide composition and cross-bridge architecture across bacterial species

Variation in PG stem composition occurs at defined positions that influence cross-linking chemistry and cell wall architecture. Of particular importance are modifications at position 2 such as amidation of D-isoglutamate, variation at the terminal position which remains central to PBP-mediated acyl transfer, and residue identity at position 3, which determines the nature of the acceptor site for transpeptidation.

The PG precursor of *Staphylococcus aureus* undergoes several distinctive species-specific modifications at the level of its stem peptide and membrane-bound Lipid II intermediate. The stem peptide generated by the Mur ligases is based on L-Ala-D-isoglutamate-L-Lys-D-Ala-D-Ala however, the α-carboxyl group of the D-isoglutamate residue at position 2 is subsequently amidated by the GatD/MurT to generate D-isoglutamine[61,62]. In parallel, the ε-amino group of the L-lysine residue at position 3 is elaborated into the characteristic pentaglycine interpeptide bridge via the sequential action of FemX/FmhB, FemA and FemB responsible for glycyl-tRNA transfer to form Gly1, Gly2-3 and Gly4-5 respectively (Figure 4)[59,63]. This pentaglycine bridge serves as the acceptor in the transpeptidation rection catalysed by PBPs, making these modifications essential to *S. aureus* cell wall assembly, while position-2 amidation ensures efficient cell wall polymerisation contributing to robust methicillin resistance and envelope integrity.

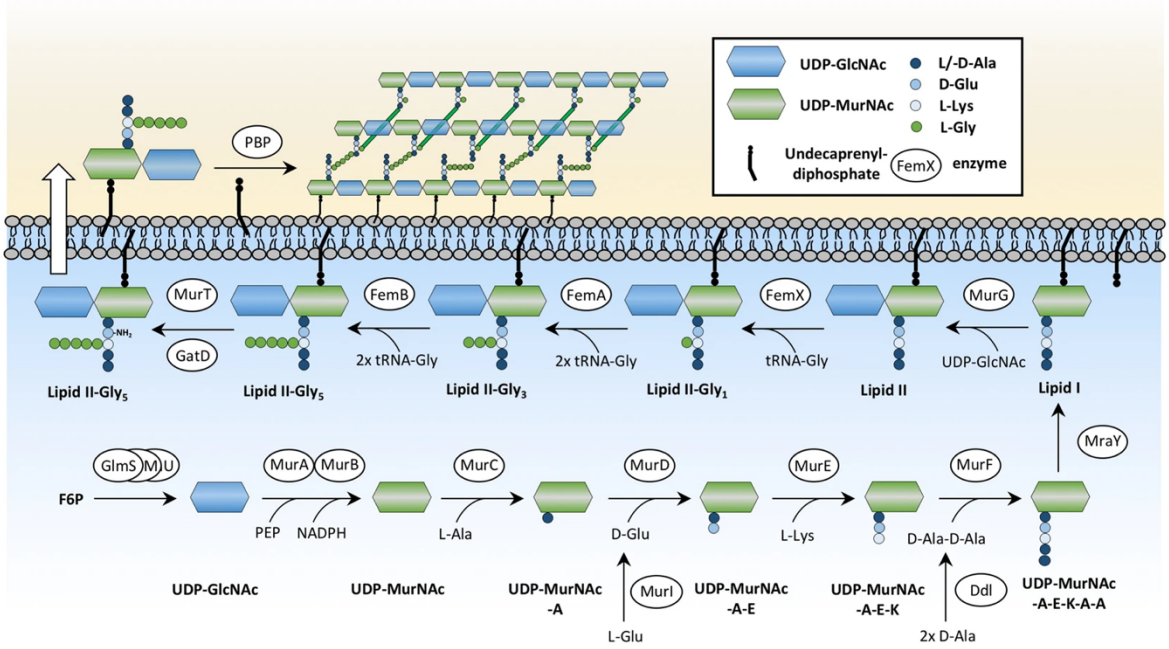

Figure 4: Schematic overview of peptidoglycan precursor synthesis in *S. aureus*.

UDP-GlcNAc is converted to UDP-MurNAc by MurA/MurB, after which MurC-F sequentially assemble the stem pentapeptide precursor. MraY and MurG then generate lipid I and lipid II at the membrane. In *S. aureus*, the precursor is further modified by GatD/MurT-mediated amidation and by sequential pentaglycine bridge addition via FemX/FmhB, FemA and FemB, before translocation and incorporation into the growing cell wall by penicillin-binding proteins. Adapted from Jarick *et al.*[64]

The enzymes responsible for these final, essential steps of cell wall construction – the PBPs – are the primary targets of the β-lactam antibiotics, one of the most successful classes of antibacterial drugs ever developed[65]. However, the selective pressure imposed by decades of antibiotic use has driven the evolution of sophisticated resistance mechanisms. Among the most clinically formidable of these is the strategy employed by methicillin-resistant *Staphylococcus aureus* (MRSA), which involves the acquisition of a novel, low-affinity PBP

(Figure 1 – target alteration) that is refractory to inhibition by almost all β-lactam agents; PBP2a[4]. The following section will focus on the structure, function, and clinical significance of the PBPs.

1.3 PBPs and cell wall biosynthesis

Penicillin binding proteins (PBPs) are a diverse family of membrane-associated enzymes that catalyse the final stages of peptidoglycan assembly on the outer face of the cytoplasmic membrane[43,56]. Their name derives from their ability to be irreversibly acylated by the strained four-membered ring of penicillin, forming a stable covalent bond. Structurally, PBPs are typically anchored in the plasma membrane by an N-terminal transmembrane helix, with their catalytic domains extending into the periplasmic space. These catalytic regions exhibit distinct architectures depending on the PBP class. PBPs are traditionally classified as either high molecular mass (HMM) or low molecular mass (LMM) PBPs[66]. HMM PBPs, the primary synthases, are often bifunctional, possessing both a glycosyltransferase (GT) domain for glycan chain polymerisation and a transpeptidase (TP) domain for peptide cross-linking. In contrast, LMM PBPs are monofunctional, containing only a transpeptidase-like domain. Bacteria typically possess multiple PBPs, each with specialised roles in maintaining cell viability and morphology[66]. They are broadly categorised by function (Figure 5):

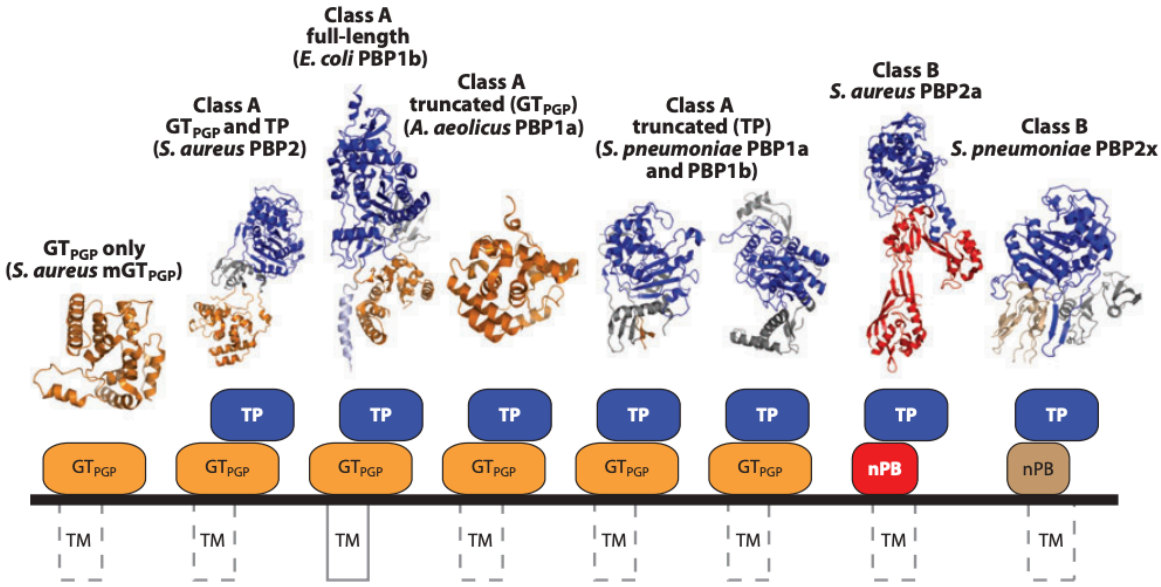

Figure 5: *Structural* summary of high-molecular mass penicillin-binding proteins (PBPs).

Cartoon representations of exemplar high-molecular mass (HMM) penicillin-binding proteins (and a monofunctional glycosyltransferase) are shown from left to right: *Staphylococcus aureus* mGT_{PGP} (PDB code 3HZS[67]), *S. aureus* PBP2 (2OLU[56]), *Escherichia coli* PBP1b (3FWM[68]), *Aquifex aeolicus* PBP1a (2OQO[69]), *Streptococcus pneumoniae* PBP1a (2C6W[70]), *S. pneumoniae* PBP1b (2BG1[71]), *S. aureus* PBP2a (1VQQ[4]), and *S. pneumoniae* PBP2x (1QME[72]). A domain-based schematic is provided beneath each structure, coloured in

accordance with the cartoon representations. Bifunctional Class A HMM PBPs contain both transpeptidase (TP) and glycosyltransferase (GT) domains, while the monofunctional transpeptidases (Class B HMM PBPs) contain only TP domains, often with an N-terminal extension of poorly characterised function (nPB). The cell boundary is indicated with a thick line with the transmembrane region (TM) shown as a hashed line box. Figure taken from Lovering et al[43].

Type A HMM PBPs are bifunctional, containing both GT and TP domains, catalysing both peptidoglycan strand polymerisation and transpeptidation reactions respectively (Figure 6), playing a crucial role in overall cell wall expansion. Class B enzymes, while also essential synthases, are monofunctional transpeptidases which cooperate with dedicated glycosyltransferases (such as RodA) to form multi-protein complexes like the "elongasome" and the "divisome" with critical functions in cell elongation and septum formation during cell division respectively[66,73]. Finally, LMM PBPs (also “class C” PBPs) are single-domain proteins with diverse roles, primarily functioning as carboxypeptidases and endopeptidases, responsible for the maturation, remodelling, and recycling of peptidoglycan by trimming peptide stems or cleaving existing cross-links, as well as cell division[54,74]. This activity is vital for processes such as daughter cell separation after division.

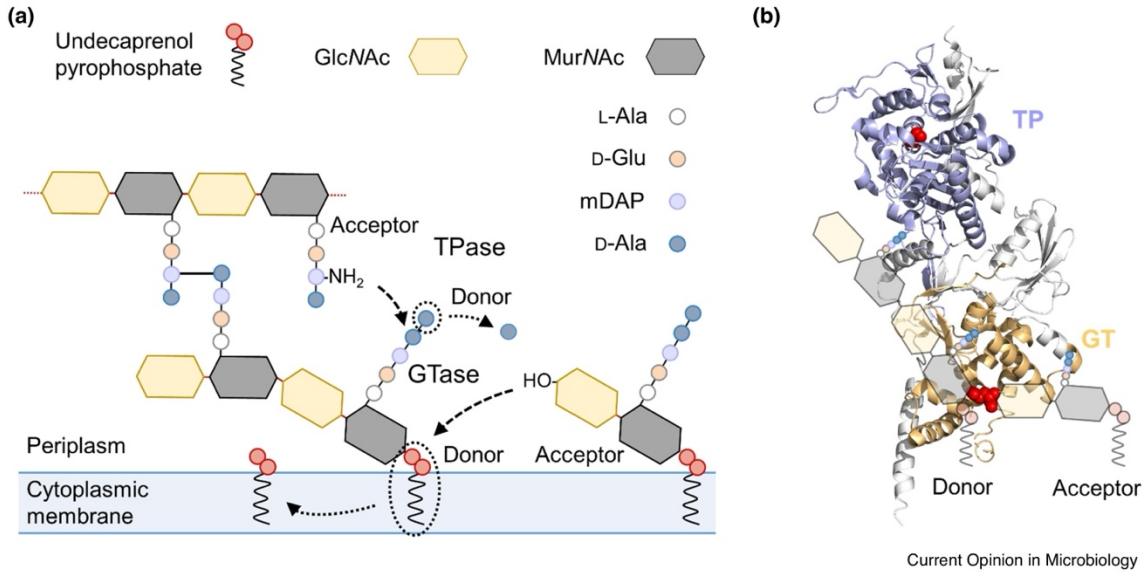

Figure 6: Peptidoglycan synthesis catalysed by a bifunctional PBP.

A) Diagram of the two key reactions: glycosyltransfer (GTase), for glycan chain extension, and transpeptidation (TPase), for peptide cross-linking. (B) The crystal structure of *E. coli* PBP1B (PDB: 3VMA)[68] highlighting the GT domain (orange) and TP domain (purple). Key catalytic residues for each domain (E233 and S510, respectively) are shown as red spheres. The GT domain is shown with its conceptual donor and acceptor binding sites, while the TP domain is shown with its active site serine that engages the donor peptide. Figure taken from Pazos and Vollmer[75].

While some functional redundancy exists among these enzymes, the complete inhibition of the HMM PBP synthase activity is invariably lethal, confirming their essentiality for bacterial survival[43,56]. The vital role of PBPs in maintaining the integrity of the

peptidoglycan sacculus directly explains the bactericidal effect of β-lactam antibiotics[76]. When these enzymes are inhibited, the cell's ability to synthesise and repair the cell wall is compromised. In a growing bacterium, this disruption leads to the formation of a structurally deficient exoskeleton that is unable to withstand the high internal turgor pressure of the intracellular environment. The consequence is a catastrophic loss of morphological integrity, membrane protrusion, and ultimately, cell lysis and death[42,57]. This fatal outcome accounts for the evolution of sophisticated resistance mechanisms to β-lactams through selective pressure imposed by decades of antibiotic use[76]. The TP domain of PBPs catalyses the final and essential step in bacterial cell wall biosynthesis – the crosslinking of adjacent PG strands to provide mechanical strength and shape to the cell wall[53]. During normal catalysis, the TP domain recognises and binds to two distinct regions of the PG precursor: a donor stem peptide containing the terminal D-Ala-D-Ala dipeptide and an acceptor peptide on a neighbouring glycan chain[43]. The active-site serine residue (e.g. Ser403 in *S. aureus* PBP2a) initiates catalysis by performing a nucleophilic attack on the carbonyl carbon of the terminal D-Ala-D-Ala bond within the donor peptide[43]. This attack forms a transient acyl-enzyme intermediate, in which the enzyme becomes covalently linked to the donor peptide while releasing the terminal D-Ala residue. The acyl group is subsequently transferred to the amino group of the acceptor peptide, thereby forming a new 4 to 3 position peptide crosslink between adjacent peptidoglycan strands[43,53]. Through this two-step acylation-deacylation mechanism, PBPs maintain the integrity of the bacterial cell wall and enable controlled expansion during growth and division.

Accordingly, the TP domain of PBPs is the primary target of β-lactam antibiotics. The molecular basis for this inhibition was initially proposed by Tipper and Strominger, who hypothesised that β-lactams act as exceptional structural mimics of the acyl-D-Ala-D-Ala termini of peptidoglycan stem pentapeptides[65]. The strained amide bond within the four-membered β-lactam ring is a potent electronic and conformational analogue of the scissile peptide bond in the natural PBP substrate. This mimicry allows the antibiotic to enter the PBP active site, where the catalytic serine residue, instead of attacking a peptide bond, performs a nucleophilic attack on the carbonyl carbon of the β-lactam ring[65] (Figure 7).

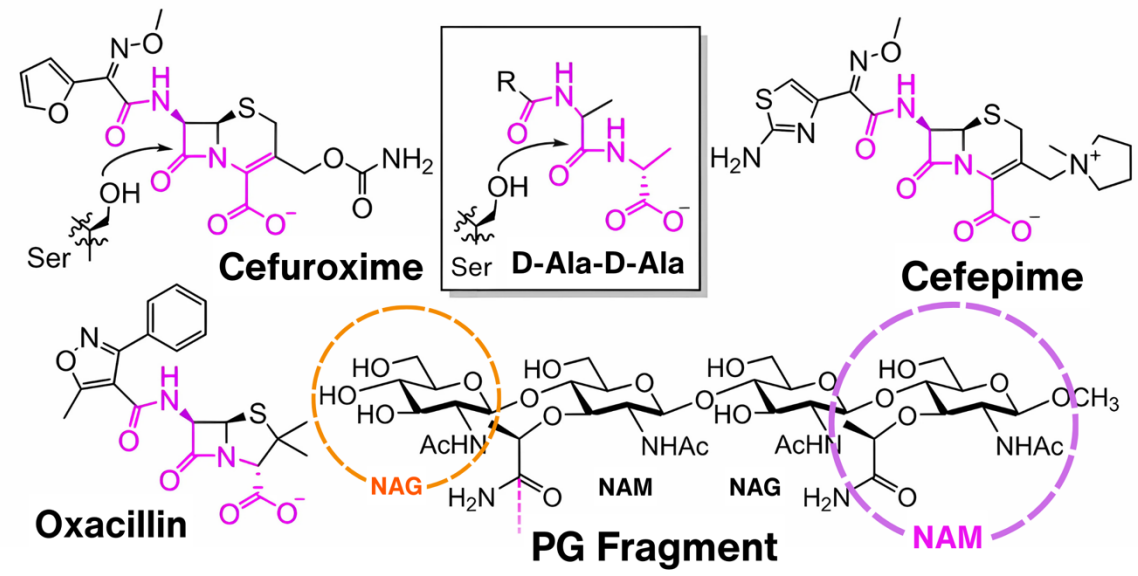

Figure 7: β-lactam antibiotics are exceptional structural mimics of the peptidoglycan acyl-donor substrate.

Representative β-lactams – oxacillin, cefuroxime and cefepime – are shown with the β-lactam amide and acyl-donor side chains highlighted (magenta) to emphasise their resemblance to the D-Ala–D-Ala terminus of the stem pentapeptide (inset). The lower schematic depicts a peptidoglycan fragment with alternating N-acetylglucosamine (NAG, orange) and N-acetylmuramic acid (NAM, purple) saccharides. Curved arrows indicate the nucleophilic attack of the catalytic serine on the scissile carbonyl in the β-lactam ring and, analogously, on the carbonyl of the native D-Ala–D-Ala donor, forming a transient acyl-enzyme that blocks transpeptidation.

This reaction proceeds via an initial noncovalent Michaelis complex (see 2.2.5.3), followed by a rapid acylation step (governed by the rate constant k_2) that opens the ring and forms a stable covalent acyl-PBP intermediate[51]. While the natural enzyme-substrate intermediate is rapidly hydrolysed (deacylated), the penicilloyl-enzyme intermediate formed by the antibiotic is extremely stable, with a deacylation rate constant k_3 that is orders of magnitude lower. This kinetic trap, defined by a high k_2 and a near-zero k_3, results in the essentially irreversible inactivation of the PBP, removing it from the pool of active cell wall synthases[51]. This elegant and potent mechanism of inhibition positioned β-lactam agents as the antibiotic class of choice for treating bacterial infections, particularly those caused by Gram-positive pathogens like *Staphylococcus aureus*, which contribute significantly to human morbidity and mortality[2]. For decades, the management of *S. aureus* infections has relied on this class of therapeutics, which still represents approximately 60% of all antimicrobials in clinical use[77]. The efficacy of β-lactams against *S. aureus* depends entirely on their ability to inhibit the organism's four native, high-molecular-mass PBPs (PBP1-4), each with distinct and vital roles[38]. PBP1 is a bifunctional Class A PBP with both glycosyltransferase and transpeptidase activity, primarily involved in cell division; PBP2 is an essential monofunctional Class B transpeptidase required for cell shape determination and cell wall synthesis; PBP3 is another

monofunctional transpeptidase involved in septum formation; and PBP4 is a non-essential carboxypeptidase that modulates the degree of peptidoglycan crosslinking[38,5]. The covalent inactivation of the essential synthases, particularly PBP1 and PBP2 by β-lactam agents fatally compromises the integrity of the cell wall, leading to osmolysis and cell death[78]. This reliance of the bacterium on its susceptible native PBPs created the immense selective pressure that ultimately drove the evolution and dissemination of methicillin resistance.

1.4 PBP2a and MRSA

In *staphylococcus aureus* strains susceptible to antibiotics (collectively referred to as methicillin-susceptible *S. aureus* (MSSA), only high molecular mass penicillin binding proteins 1 (PBP1) and 2 (PBP2) stands are essential for growth, marking them as primary and essential targets for β-lactam antibiotics[79,80]. Initially thought to be the sole protagonist of transglycosylation in *S. aureus*, abolishment PBP2's TG domain failed to halt the elongation of nascent peptidoglycan (PG) chains[80], where recent work has detailed that the cooperation of RodA and FtsW with PBP3 and PBP1 facilitates lateral and septal PG incorporation respectively following the muting of PBP2[81,82]. No crystal, cryo-electron microscopy or NMR structures have been solved for PBP2 in the presence of β-lactam inhibitors. In MRSA, following β-lactam inhibition of its TP domain, PBP2 likely functions cooperatively with PBP2a, supporting PBP2a transpeptidase activity with its transglycosylase functions[83]. Additionally, PBP2 also appears to play an important role in vancomycin resistance[84,85] and other aspects of cell division, cell wall synthesis and maintenance in both *S. aureus* and other bacteria via its coordination with other critical cell cycle proteins such as FtsL, DivlC and FtsW[55,86]. The absolute requirement of PBP2 for cell viability marks its effective inhibition the foundation of anti-staphylococcal therapy with β-lactams.

Methicillin-resistant *S. aureus* (MRSA), a pathogen with near pan-resistance to all β-lactam agents facilitated by the acquisition of mobile genetic element SCC*mec*[87], remains a key concern in nosocomial infections and mortality. SCC*mec* harbours the *mecA* gene which encodes PBP2a, a monofunctional PBP whose transpeptidase activities remain unaffected in the presence of lethal concentrations of β-lactams[88]. Thus, antibiotic lethality by exposure to β-lactam agents is overcome by MRSA via the substitution of transpeptidase activities of conventional PBPs (1 to 3) by PBP2a[4]. However, this substitution does not render PBP2 without function, wherein its transglycosylation domain – which PBP2a lacks and is not inhibited by β-lactams – works cooperatively with PBP2a's transpeptidase activity for

complete cell wall biosynthesis. PBP2a is comprised of a transpeptidase (TP), allosteric (AD) and N-terminal domain, the latter of which is believed to have little involvement in catalysis (Figure 8).

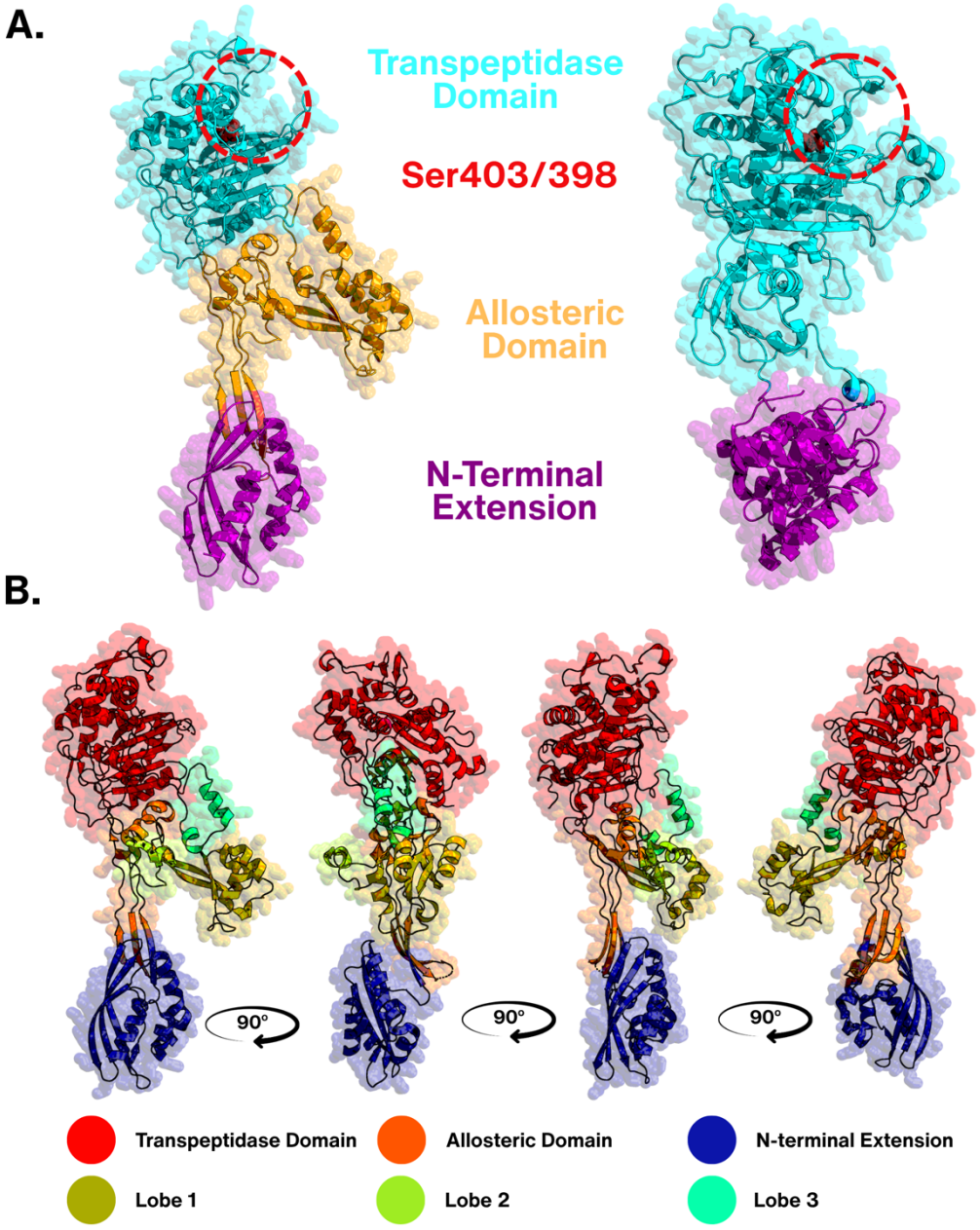

Figure 8: Comparison of the crystal structures of *Staphylococcus aureus* PBP2a (Left, PDB ID 1VQQ)[4] and PBP2 (Right, PDB ID 2OLU)[56] and PBP2a structural overview.

(A) Structural overview showing the major domains of PBP2a and PBP2. The canonical transpeptidase (TP) domain and N-terminal extension shared between the PBPs are coloured in cyan and purple, respectively, while the allosteric domain unique to PBP2a is shown in orange. The active-site serine residues (PBP2a: Ser403; PBP2: Ser398) are indicated by red spheres, with the active-site clefts encircled in red dashed lines for clarity. PBP2 displays a broader, more solvent-exposed catalytic groove with the active site serine (Ser398) accessible for catalysis. By contrast, in the absence of allosteric effectors, the PBP2a TP domain is more constricted, partially occluded by the adjacent "gatekeeper" α2-α3 and β3-β4 loops; resulting in a narrower entrance and a catalytic serine (Ser403) that remains shielded from effectors (e.g. β-lactam antibiotics). (B) Domain organisation of PBP2a with 90° rotations, highlighting allosteric domain substructures. Lobe 1 (olive), Lobe 2

(yellow), and Lobe 3 (cyan) are shown relative to the N-terminal extension (blue) and transpeptidase domain (red).

The PBP2a TP domain has a similar overall fold to those of other PBPs[54] with two distinct subdomains, one comprised of a five strand β-sheet crowned with three α-helices and the other containing an all-helical fold; with the active site residing at the interface of the two subdomains[89]. Three sequence motifs conserved among PBP TP active sites exist between these subdomains: SXXK, [K/H][S/T]G and [S/Y]X[N/C], with the SXXK serine as the catalytic serine[73]. However, in contrast to canonical PBPs, the TP domain of PBP2a is visibly distinct, wherein tactile placement of "gatekeeper" protein loops α2-α3 and β3-β4, in conjunction with an altered conformation of the serine nucleophile (Ser403), results in an active site which excludes β-lactam access in the absence of allosteric effector binding (Figure 9)[89]. The catalytic Ser403 of PBP2a is situated in a narrow crevice at the N-terminal end of helix α2 in the hallmark SXXK sequence motif proximal to strand β3 (Figure 9). In the absence of substrate, Ser403 remains sheltered within a tight groove, hydrogen-bonded to Lys406 which strengthens the nucleophilicity of its Oγ for catalysis[4,90].

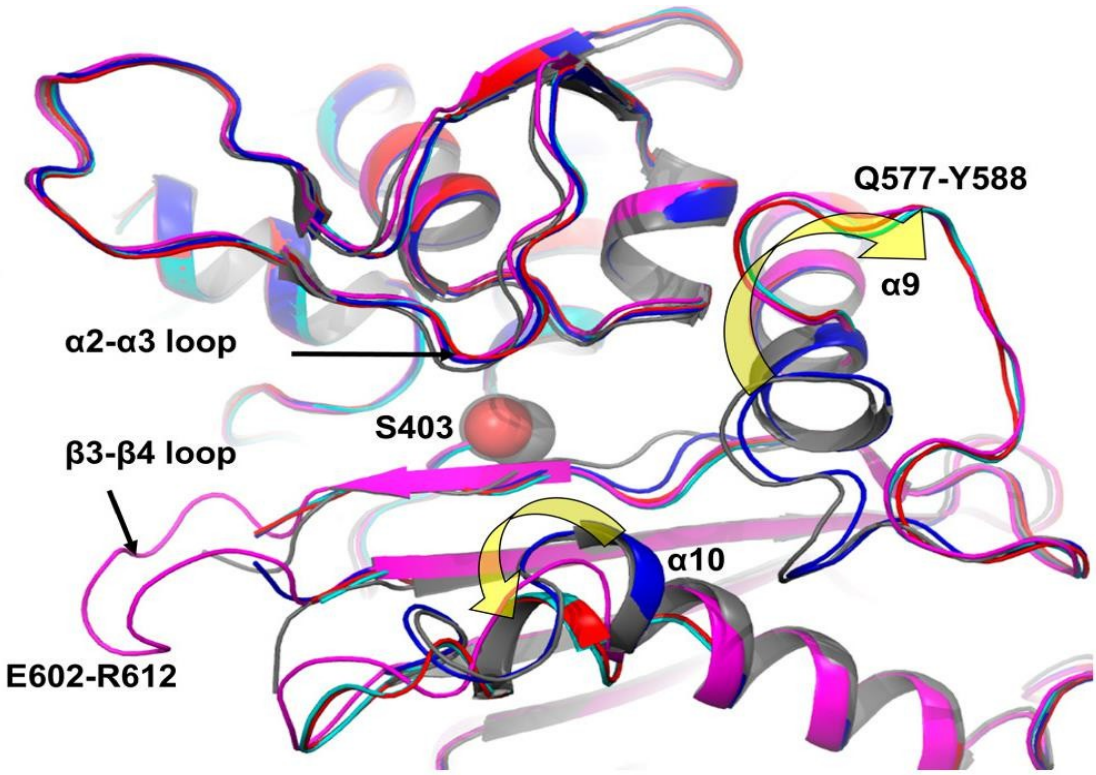

Figure 9: Structural distinctions between PBP2a transpeptidase domain in the unbound state and when bound to various antibiotics

Structural comparison of key features and movements of the apo (unliganded) PBP2a transpeptidase domain (active site) structure (Grey, PDB ID 1VQQ)[4] and in bound states with the following antibiotics: ceftazidime

(Blue – β-lactam), cefepime (Red – β-lactam), oxacillin (Cyan – β-lactam) and a quinazoline (Magenta, PDB ID 4CJN)[77]. Yellow arrows highlight the rearrangements of helices α9 and α10, which increase the volume of the active site to facilitate the occupancy of two peptidoglycan strands and access to the catalytic Ser403 (central sphere). Adapted from Mahasenan et al[89].

The active site of the PBP2a TP domain is distorted with respect to other β-lactam-susceptible PBPs, where it is hypothesised that, due to the sheltering of Ser403, the energetically costly rearrangement of β-lactams required for nucleophilic attack to sufficiently form a stable acyl-PBP intermediate underpins the basis of its resistance to β-lactams[4-6,89]. Additionally, PBP2a is the only *S. aureus* PBP to contain an allosteric domain (Figure 8 – orange). Comparisons of β-lactam binding kinetics between PBP2a and other β-lactam-sensitive PBPs suggest that, owing to the inaccessibility of the active site of PBP2a, poor ($t_{1/2}$ = 3-12 min) acylation rate constants mean that covalent modification of its catalytic serine (Ser403) occurs less readily, thus conferring resistance[8,91,92]. This is further supported by the significant effect which mutations in the catalytic centre of other β-lactam-susceptible PBPs have on the acylation rate[93,94], as well as the impact of structural differences between β-lactam compounds on their acylation rates with PBPs. An example of which is illustrated in the four-fold greater acylation rate seen in the cephalosporin nitrocefin comparative to penicillin G due to different contacts made within the active site owing to R2 groups with distinct structural differences[94]; underscoring the importance of stereochemistry within the PBP2a TP domain. Indeed, both methicillin and penicillin G have comparable K_d values, yet extremely poor acylation rates are seen in methicillin[91]. However, the kinetics of PBP2a inhibition change in the presence of some antibiotics and synthetic peptidoglycan fragments in a concentration-dependent manner, making PBP2a increasingly more available to β-lactam acylation at higher concentrations of either[92].

Allostery is a well-established regulatory feature of many proteins wherein conformational flexibility is central[95]. Allostery is made possible by the existence of multiple conformers, interchangeable over different timescales, comprised of specific residue networks which connect distal domains[7]. Crystal structures of apo PBP2a (PDB 1VQQ)[4] compared with the other structures of PBP2a in complex with a variety of effective (ceftobiprole, ceftaroline) and ineffective (methicillin, oxacillin, ceftazidime, cefepime, nitrocefin) antibiotics[4,5,12,89] reveal the occurrence of subtle conformational changes at helix α2 and at strand β3 for acylation to be achieved. Otero and colleagues[5] compared the crystal structures of PBP2a including a synthetic peptidoglycan bound within the allosteric domain (Complex 1) with that of PBP2a co-crystallised or soaked with ceftaroline (CFT; Complex 2), revealing conformational changes in the region between allosteric and transpeptidase domains; as well

as the reorientation of several loops within the active site. This conformational reorganisation of residues within the active site α2-α3 and β3-β4 loops result in a 500 $Å^3$ to 1300 $Å^3$ increase in volume, leaving Ser403 better-positioned for nucleophilic attack, facilitating both substrate catalysis and acylation by β-lactam antibiotics (Figure 9). Recent investigations have shown that ceftaroline-mediated acylation of the nucleophile Ser403 in the PBP2a catalytic domain is facilitated by binding of a second ceftaroline molecule within the allosteric domain[5]. It has been theorised that binding of the allosteric domain is key to PBP2a TP domain catalysis via the subsequent propagation of conformational rearrangements of critical residues that ultimately lend to the increased TP domain occupancy necessary for Ser403 accessibility[4-6,89]. Among the known structurally characterised PBPs, the only other example of allostery has been evidenced in PBP2x of *S. pneumoniae*[72,96]. PBP2x contains a similar overall architecture to PBP2a (Figure 10), containing a TP domain with the conserved SXXK, [K/H][S/T]G and [S/Y]X[N/C] motifs classical of HMM PBPs, a flexible N-terminal region of unclear function, and two PASTA domains which recognise uncrosslinked peptidoglycan and β-lactams, acting as sensor/anchor modules rather than catalytic sites, with evidence of importance in allosteric regulation[72,96].

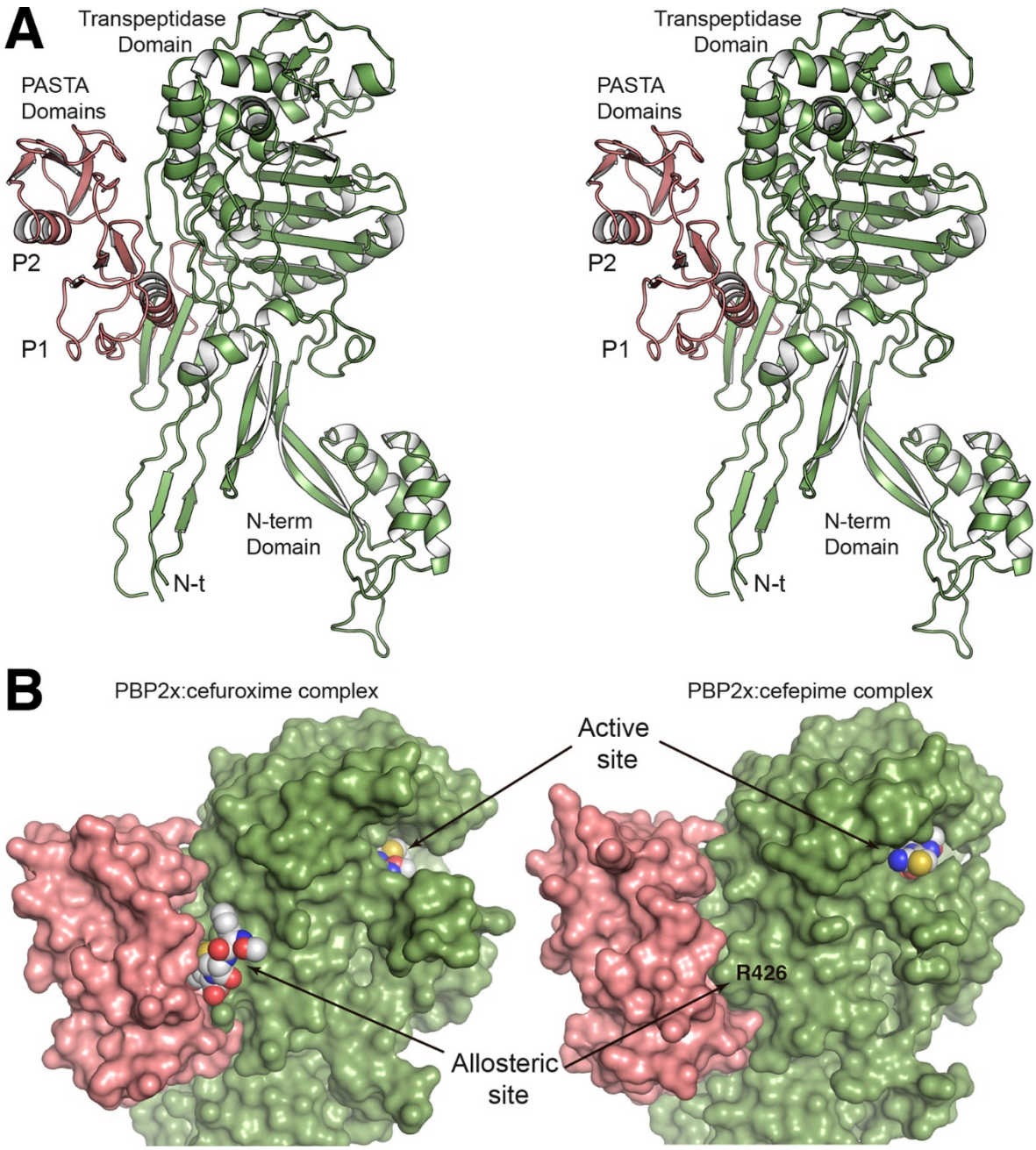

Figure 10: Comparison of crystal structures of PBP2x in complex with cefuroxime (left) and cefepime (right)

(A) Stereo view cartoon representation of apo PBP2x with the PASTA module (allosteric domain) in pink and the transpeptidase domain in green; the two PASTA domains (P1, P2) are labelled, and the catalytic Ser337 is indicated by an arrow. (B) Surface renderings of X-ray structures coloured as in (A). Left: previously published complex with cefuroxime, showing two antibiotic molecules (spheres) – one covalently acylated at the active site and a second bound non-covalently in the allosteric pocket. Right: the PBP2x:cefepime structure from present referenced work, in which the allosteric site adopts a closed conformation. Figure taken from Bernardo-García et al.[42].

Similar to PBP2a, previous work evidenced binding of one molecule of cefuroxime at the interface of the two PASTA domains, and another within the active site[72], whereas in structures of PBP2x in complex with cefepime, cefepime was only noted in the active site[96]. Accordingly, the PASTA domains of PBP2x are collectively referred to as the allosteric

domain; believed to function as a recognition site for nascent peptidoglycan (PG), guiding a donor PG into its TP domain prior to crosslinking with an acceptor PG strand. However, these mechanistic functions and structural features of the PBP2x allosteric domain are distinct from that of PBP2a which coordinates a series of salt-bridge interactions that increase the physical occupancy of its TP domain, de-shielding the catalytic serine (S403), facilitating the covalent formation of acyl-enzyme intermediates with β-lactams. Additionally, it is noteworthy that in structures of PBP2a co-crystallised with a synthetic peptidoglycan fragment comprised of a single NAG-NAM unit (complex 1), that complex 1 was only seen bound within the allosteric domain; not the transpeptidase domain[5]. Further, structures of PBP2a co-crystallised with one of two β-lactams retaining efficacy against MRSA (ceftobiprole or ceftaroline), ceftobiprole was only observed in the transpeptidase domain (active site)[12].

1.5 Allosteric Regulation of the PBP2a Active Site

The flexibility observed in Lobes 1 and 2 (Figure 8) which constitute the PBP2a allosteric domain in concert with that of the α2-α3 and β3-β4 loops of the active site are supportive of the suggested importance of allostery within PBP2a active site regulation[5-7,97]. Further, coordinates for PBP2a crystalised with a synthetic peptidoglycan fragment were resolved at 2.55 Å which was found perfectly accommodated between Lobes 1 and 2 (Figure 8)[5,7]. Ceftaroline (CFT) and ceftobiprole (CFB) are the only known β-lactam agents with anti-MRSA activity[9,10,98]. Crystal structures of PBP2a-CFT complexes (PDB IDs 3ZFZ and 3ZG0)[5] revealed an active site with S403 acylated by one CFT molecule as well as a second CFT molecule noncovalently bound within the allosteric domain[5], suggesting CFT binding in the allosteric site facilitates binding of CFT to the active site. The same is apparent for crystal structures of PBP2a in complex with CFT and a muropeptide (PDB ID 3ZG5)[5]. Resistance to CFT emerged shortly after its introduction to the clinic, where interestingly, two frequently encountered CFT-resistant MRSA variants (N146K/E150K and N146K/E150K/H351N) both harbour mutations pinpointed within the allosteric domain of PBP2a[5]. Indeed, introduction of these mutations into wild-type (ceftaroline-susceptible) PBP2a in *S. aureus* conferred CFT resistance. Activation of the allosteric domain is significant in the conformational changes within the 60 Å-distal transpeptidase domain required for Ser403 acylation, positing the allosteric domain as a potent principal regulator of both substrate catalysis and antibiotic binding upon binding of CFT[6]. For this to be possible, effector binding most likely induces a cascade of intermolecular interactions

originating in residues near Lobes 1-2 (Figure 8) which propagate (possibly via Lobe 3) to the β3-β4 loop of the TP domain active site, ultimately providing a more favourable structural environment for S403 catalysis.

Acebrón and colleagues used molecular dynamics simulations to suggest that a series of residues that form a salt-bridge network linking the allosteric and transpeptidase domains is responsible for signal transduction upon binding of a ligand to the allosteric domain[7]. It is proposed that 'domino-like' concerted motions within this residue network are responsible for the interdomain communication required for the opening of the active site, where an increased number of salt-bridge interactions following a 3 Å shortening between Lobes 1-2 (Figure 8) was observed when comparing simulations of apo-PBP2a (PDB ID 1VQQ)[4] (closed active site) and PBP2a-muropeptide structures (PDB ID 3ZG5)[5] (open active site). Similar investigations by Mahasenan and colleagues[89] computed 59 dynamic salt-bridge interactions (Figure 11A) using MD simulations as well as salt-bridges distinct to both open and closed conformations (Figure 11B). Iterations using the STRESS (STRucturally identified ESSential residues) program[99] against 24 PBP2a X-ray structures identified clusters of surface-critical residues (associated with allosteric-ligand recognition), the most notable of which localised precisely to the previously determined binding cleft of a peptidoglycan analogue within the allosteric domain[5]. STRESS predicts amino acids that mediate allosteric signalling using two modules: surface-critical residues for allosteric-ligand recognition and interior-critical residues for buried transmission[99]. For surface sites, it performs thousands of Monte Carlo trials in which a four-atom dummy ligand explores the protein surface (translation/rotation/angle moves), computing attractive and repulsive contact energies to identify recurrent high-affinity patches. Predicted sites are then scored by normal-mode analysis to gauge how local distortions couple to intrinsic protein motions, yielding ranked allosteric hotspots[99].

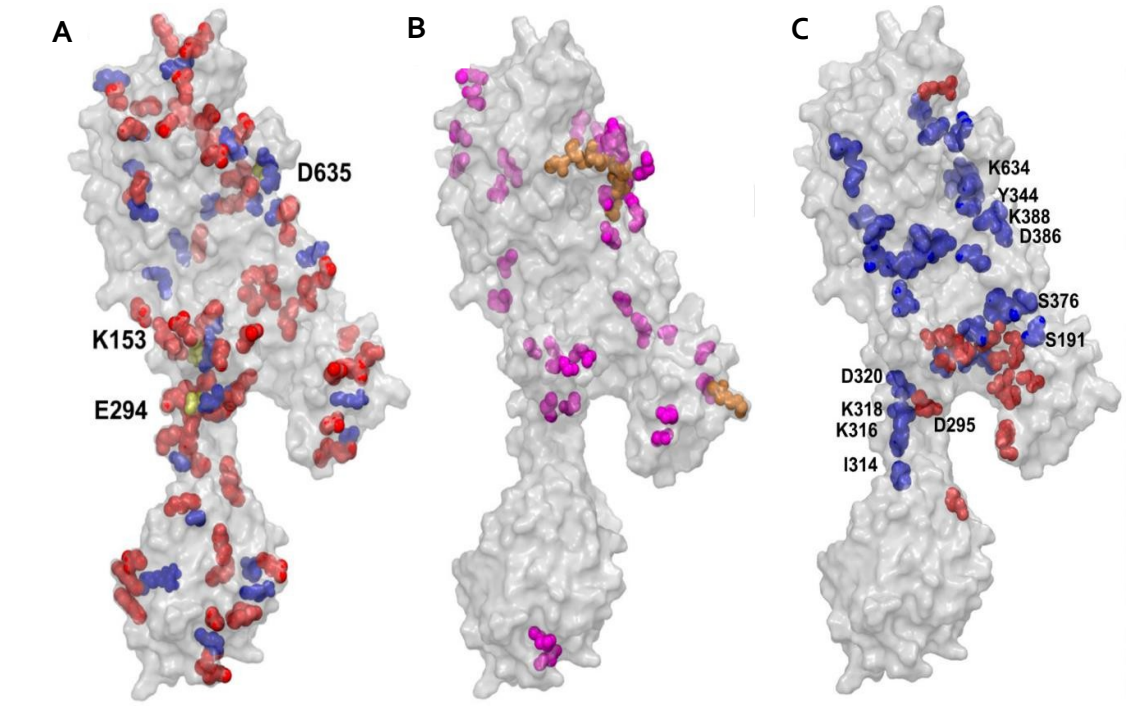

Figure 11: Computationally identified residues of a theorised salt-bridge network (A, B) and those critical to surface and interior signal propagation (C) contributing to allosteric regulation of the PBP2a transpeptidase domain of *Staphylococcus aureus.*

A: Residues participating in one (red), two (blue) or three (yellow) salt-bridge interactions. B: Residues involved in salt bridges unique to open (magenta) and closed (orange) conformations of *S. aureus* PBP2a. C: Surface (red) and interior (blue) residues critical to allosteric regulation of the PBP2a transpeptidase domain as determined by the STRESS (STRucturally identified ESSential residues)[99] program by Mahasenan et al. Figure adapted from Mahasenan et al.[89].

Additionally, numerous interior-critical residues that are likely involved in signal propagation from the allosteric to the catalytic domain were identified surrounding both domains and along their interconnecting regions (Figure 11C), with one residue cluster (N386, K388, Y344 and K634) apparently providing a (partial) direct path between both domains. An atomistic model of PG catalysis by PBP2a, created by docking two PG strands onto the CFT-acylated (open conformation) PBP2a structure (PDB ID 3ZG0[5]) via the GLIDE suite[89], suggested a four-stage catalytic cycle: (i) allosteric opening of the active site facilitates accommodation of the donor PG strand which acylates Ser403, (ii) opening of the alternate side of the active site permits entry of an acceptor PG strand and finally, (iii) following acyl-transfer to the acceptor PG strand stem peptide, S403 is liberated and both PG strands are crosslinked with the loss of the terminal D-Ala.

Interestingly, differences in protein reorganisation were observed in PBP2a bound with either CFT or the synthetic peptidoglycan, suggesting that conformational changes are

effector-specific[7]. Supporting this, abolished acylation was observed in two different PBP2a variants designed with point mutations in regions the identified signal transduction pathway (K387A-D635 and D343A-E389A-D635A) despite the overall protein fold remaining unaffected[5], highlighting the requirement of conformational change in regions removed from the active site for efficient catalysis. Furthermore, point mutations within the active site (e.g. Y466N and E477K) have been evidenced to have dramatic effects on CFT activation[14]. In contrast to CFT, β-lactams that do not inhibit PBP2a are thought to be unable to activate the allosteric site, preventing access to the active site catalytic serine.

1.6 Ceftobiprole and PBP2a

Ceftobiprole (CFB) is another cephalosporin antibiotic with activity against PBP2a that shares structural similarity and activity profiles with CFT, yet with structurally distinct mechanisms of action. As such, it is important not to conflate CFT and CFB as mechanistically equivalent, particularly with regard to allosteric engagement of PBP2a – a dependency established for CFT but neither evidenced nor implied in the case of ceftobiprole[12,16]. In contrast to CFT, which has seen increased clinical usage since its FDA approval in 2010, CFB has only been approved in European countries as late as 2017, with the US only receiving FDA approval for limited use in 2024. To date, only one structure of CFB with PBP2a has been resolved[12], where interestingly, there is no evidence of CFB occupancy within the allosteric domain, despite having an only subtly different R2 group to CFT (Figure 12).

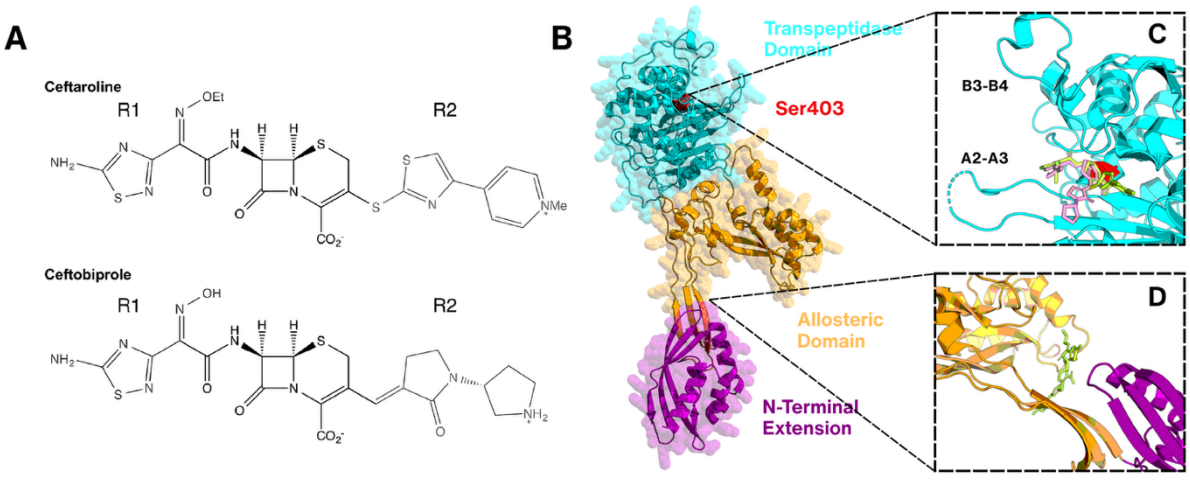

Figure 12: Ceftaroline and ceftobiprole have subtle structural differences but significant differences in PBP2a binding

A) Structural comparison of two fifth generation cephalosporin antibiotics with antibacterial activity against MRSA. Both share the same core cephem nucleus and aminothiazole R1 side chain, only differing by their respective R2 groups. Ceftaroline (CFT) possesses a thio-linked pyridylthiazole group contrasting with

ceftobiprole (CFB) which features a vinyl-pyrrolidinone ring linked to a pyrrolidine group. B) overall structure of PBP2a (PDB ID 4DKI[12]) with the N-terminal extension (purple), allosteric domain (orange), transpeptidase domain (cyan) and catalytic serine (S403, red) highlighted. C) PBP2a (4DKI[12]) transpeptidase domain with CFB (pink) and CFT (yellow – from PDB ID 3ZG0[5] aligned with 4DKI[12]) shown covalently bound to the catalytic serine (S403, red). D) Only CFT non-covalently associates with the PBP2a (3ZG0[5]) allosteric domain, as well as the transpeptidase domain. A ~70-80° difference in rotation is evident between the thiol and double bound R2 side chain linkages between CFT and CFB R2 side chains, likely accounting for their distinct interactions in the allosteric and transpeptidase domain(s) respectively.

Other structures of PBPs that are enzymatically homologous to PBP2a with CFB have been resolved (class B and C PBPs such as PBP3 *Pseudomonas aeruginosa* (6VJE[100]), PBP2 *Clostridioides difficile* (7RCY[101]), PBP4 *Staphylococcus aureus* (5TXI[102]), and PBP5 *Enterococcus faecium* (6G88[103])), however there are no CFB structures with another PBP that retains the distinctive allosteric domain seen in PBP2a. However, clinical isolates with resistance to CFT and CFB share several mutations within the allosteric domain (N146K, E239K, N146K-E150K-G246E and N146K-N204K-G246E) which would support CFB requiring similar activation of the allosteric site to CFT for PBP2a inhibition. Taken collectively, while considerable work has been made in characterising the allosteric domain, our knowledge of resistance to β-lactams in PBP2a remains incomplete. Multi-drug-resistant MRSA lineages are regularly isolated in the clinic and have represented >70% of *S. aureus* infections in some surveys[104,105], with some records evidencing CFB resistance pre-dating its clinical approval[20,105,106]. As such, greater molecular detail surrounding the role of allosteric communication in PBP2a and is interaction with CFB is vital for a better prognosis of this worldwide calamity.

1.7 NMR and Allostery

While X-ray crystallography and cryo-EM – including time-resolved and serial approaches – remain the benchmarks to providing high-resolution static protein structures and can capture ensembles of structural snapshots, these methods still observe selected states rather than the continuous dynamic processes. Many proteins interconvert between distinct conformations with different roles in their function, limiting the utility of such techniques in the detailing of the dynamic equilibrium that exists between these states[107]. By contrast, solution NMR directly quantifies conformational dynamics and exchange over pico- to second timescales, making it uniquely powerful for dissecting allosteric mechanisms. Indeed, a paradigm shift within structural biology from focusing on the ground states of proteins to one centred on understanding the functional implications of the landscape of potential protein conformers has been evident in recent times. Solution-state NMR spectroscopy is a well-established tool for studying protein dynamics[108] but has historically been limited to small proteins (~25 kDa)[109]. However, in recent decades, NMR has seen a

continuous stream of innovations such as advances in hardware, pulse programs (such as amide and methyl TROSY approaches)[110,111] and new combinations of isotopic labelling schemes[112], have made possible the delineation of protein structure-activity relationships as well as the mechanics underlying the binding, function and dynamics of molecular machines as large as 1 MDa[113]. NMR is highly sensitive to delicate changes in protein structure and the detailing of dynamic equilibria over a wide range (ps-sec) of timescales with atomistic resolution. This positions NMR as the preferred method for both the validation of computational predictions of molecular dynamics (MD) and ligand screening/docking, as well as probing the details of allosteric signalling pathways in complex protein structures. Although some insights into dynamics processes on similar timescales can be gleaned from other techniques such as cryo-electron microscopy and free-electron laser crystallography, these techniques lack the atomistic resolution of NMR and rely on the inference of solution-like behaviour from multiple static snapshots. By contrast, NMR is advantaged with the ability to quantitate dynamics across a broad array of timescales; and has been well-established in the characterisation of allostery and dynamics of large (>50 kDa) protein complexes in solution[114]. NMR studies have provided in-solution atomistic detail into key dynamic processes of highly flexible proteins, including substrate recognition/binding, protein-protein interactions and allosteric regulatory mechanisms[113,115,116].

Specific to PBP2a, such capabilities may help address the questions that static structures cannot: how a distal regulatory region communicates with the transpeptidase active site, on what timescale the enzyme exchanges between inactive and active-like states, and how ligands or resistance substitutions redistribute those populations. Methyl-TROSY methods on a perdeuterated background allow the mapping of long-range chemical-shift perturbations following the titration of existing efficacious ligands such as CFT or CFB onto the structure, building on the static structural detail already present[4,5,7] and probing recent computational predictions[89,97] further by adding critical detail to binding footprints and allosteric propagation pathways. Additionally, ^{13}C-methyl CPMG dispersion experiments directly quantify the μs-ms exchange that could contribute to the gating motion linking the allosteric and transpeptidase domains, with the potential to report how antibiotics with different susceptibility profiles (e.g., oxacillin vs CFB) modulate exchange rates and state populations[117]. As such, solution NMR observables are excellent experimental additions to convert static models into a kinetic and thermodynamic description of the allosteric network in PBP2a, thereby testing mechanistic hypotheses about signal transmission and resistance.

1.8 *de novo* Protein Binders

The recent development of deep learning methods, such as AlphaFold2[21,118] and RoseTTAFold, designed to predict the three-dimensional structure of proteins from their amino acid sequences has been exploited to drive the *de novo* design of small (<65 amino acids) protein binders[23,119]. Hyperstable protein binders with diverse shapes, sizes, and surface properties have been designed to bind to specific sites on the surfaces of target proteins with nanomolar to picomolar affinities, with crystal structures closely matching their corresponding computational design models[23,119]. Such *de novo* designed binders hold potential for inhibition of PBP2a or activation sufficient to allow for inactivation by antibiotics that otherwise cannot activate the protein. Briefly, a two-stage computational pipeline is used to address the challenge of binding to protein targets that lack distinct, high-energy interaction sites (Figure 13)[119]; wherein a broad, global search for potential solutions is performed first, followed by a focused, intensified search to refine the most promising candidates. The initial global search stage commences with the generation of a rotamer interaction field (RIF), which serves as a pre-calculated map of billions of favourable side-chain interactions with the target surface[119]. A large library of computationally designed and experimentally validated stable mini-protein scaffolds, ranging from 50 to 65 amino acids, is then docked against the target using the RIF to guide the placement of backbones into regions of high interaction potential[119]. Due to the vast number of resulting docked poses, a rapid pre-screening method using a simplified Rosetta energy function, termed the "Predictor," is employed to efficiently identify promising candidates[119]. These selected poses subsequently undergo a full combinatorial sequence design with an enhanced Rosetta protocol, specifically developed to maximise shape and chemical complementarity while avoiding common design failures such as buried, unsatisfied polar atoms[119]. To overcome the limitations inherent in such a vast and necessarily incomplete search, a second, focused

stage of "resampling" is implemented. In this stage, successful secondary structural motifs from the top-scoring designs of the global search are extracted and clustered.

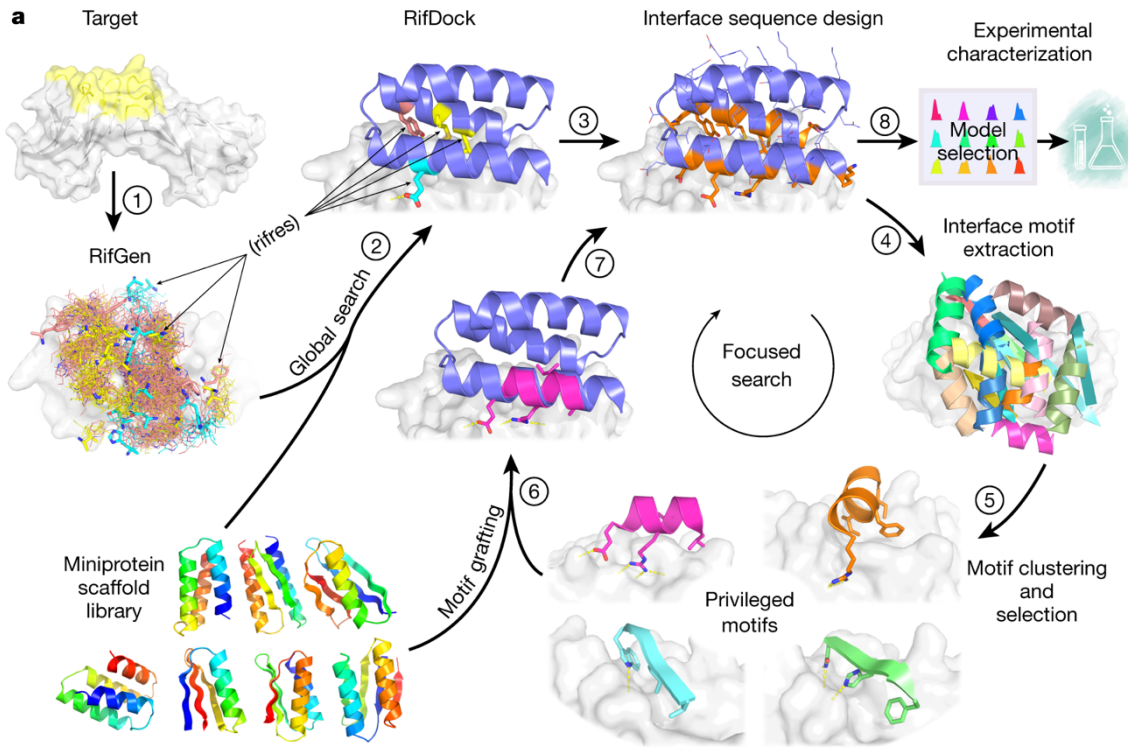

Figure 13: *de novo* protein binder design pathway overview.

Overview of the two-phase workflow. In the global search, RifGen docks billions of isolated side chains onto the chosen region of the target surface; favourable placements are stored as rif residues ("rifres") (step1). Mini-protein scaffolds are then positioned on the target guided by hotspot side-chain interactions (step 2). Interface sequences are optimised to maximize target interactions (step 3). In the focused search stage, interface structural motifs from successful models are extracted and clustered (steps 4-5). These recurrent, "privileged" motifs seed a second cycle of guided docking and design (steps 6-7). Designs are ranked by computational metrics and downselected for experimental testing (step 8). B: Sampling efficiency comparison of PatchDock, RifDock, and resampling protocols. The bar plot shows, across the three methods, the fraction of models in the top 1% by Rosetta ΔΔG and contact molecular surface, obtained by pooling equal-CPU dock-and-design trajectories for 13 target sites and averaging the per-target distributions. Adapted from Cao and colleagues[119].

The most favourable motif from each cluster is selected as a "privileged" interaction template[119]. These motifs are then used to guide a further round of design, wherein library scaffolds are superimposed onto the motif, and the sequence is re-optimised[119]. Crucially, this resampling protocol incorporates backbone flexibility, allowing for subtle conformational adjustments to achieve superior packing and complementarity with the target. Finally, designs originating from both the broad searching and the focused resampling stages are evaluated for experimental characterisation[119]. The final selection is based upon a suite of computational metrics, including predicted binding free energy (ΔΔG), folding

stability, and a purpose-built metric termed the contact molecular surface (CMS), which offers a more accurate quantification of interface packing quality than standard measures[119].

In their seminal publication, Cao and colleagues[119] validated the *de novo* designed binder technology against 13 native proteins spanning a variety of shapes and biological functions. The first class of targets consisted of extracellular proteins involved in signalling including fibroblast growth factor receptor 2 (FGFR2)[120], insulin receptor (IR)[121], tropomyosin receptor kinase A (TrkA)[122], epidermal growth factor receptor (EGFR)[123], platelet-derived growth factor receptor (PDGFR)[124], insulin-like growth factor 1 receptor (IGF1R)[125], interleukin-7 receptor-α (IL-7Rα)[126], transforming growth factor-β (TGFβ)[127], angiopoietin-1 receptor (TIE2)[128] and CD3 delta chain (CD3δ)[129]. Binders targeted at native ligand-binding sites - or surface regions proximal to native ligand binding sites – were obtained, with some binding affinities ranging from 1 nM (TrkA and FGFR2) to 860 nM (IGF1R). Additionally, competition experiments confirmed binding to target sites consistent with the computational design models. Further, strong inhibition of native agonist signalling was observed through FGFR2, EGFR and TrkA in cultured cells[119]. These receptor tyrosine kinases have been well-established as key regulators of cellular processes central to the progression and development of a variety of cancers[130], underscoring the potential therapeutic utility of *de novo* protein binders in important clinical diseases. Finally, IL-7 is crucial in the regulation of T and B cell development and homeostasis via its recruitment of the γc receptor following IL-7Rα binding[131], wherein a protein binder with picomolar affinity for the IL-7 binding site-targeting IL-7Rα successfully blocked IL-7-induced STAT5 signalling[119].

The second class of proteins targeted pathogen surface proteins including the VirB8-like protein from *Rickettsia typhi* (VirB8)[132], the SARS-CoV-2 coronavirus spike protein[133] and influenza A H3 haemagglutinin (H3)[134]. While the binding and neutralisation against the group 1 HA (influenza haemagglutinin – the main target for influenza A virus drugs and vaccines) stem region by protein[135], peptide[136] and small-molecule inhibitors[137] have successfully been demonstrated, various physicochemical challenges have made it difficult to achieve the same with group 2 HA. Cao and colleagues successfully designed binders with 28 nM to 320 nM affinities to deglycosylated and wild-type H3 HA (A/Hong Kong/1/1968), the main pandemic subtype of group 2 influenza virus[119]. Additionally, mini-proteins with picomolar affinities targeted at the receptor-binding domain of the SARS-CoV-

2 spike protein – a crucial virulence element of the devastating COVID-19 virus – have been developed[138], representing some of the most potent compounds capable of virus inhibition in cell culture; with potent protection evidenced in follow up animal experiments *in vivo*[139]. Finally, high affinity (510 pM) binders were developed against the causative agent of murine typhus VirB8, the prokaryotic pathogen protein; a key component of the *R.typhi* type IV secretion system[119].

This *de novo* protein design methodology offers unique advantage over conventional small molecule screens and other scaffold-based affinity reagents such as affimers. Unlike small-molecule drug discovery, affimers or antibody fragments which typically target pre-existing pockets or active sites with high-energy binding potential[140-142], *de novo* design can create binders to nearly any chosen surface on a target protein, including shallow, featureless regions ("undruggable" sites)[143]. This facilitates the discovery of inhibitors with novel modes of action, including allosteric modulators or binders that prevent the formation of protein-protein associations, as well as excellent thermodynamic stability and resistance to denaturation and proteolysis[119,144]. Additionally, the computational pipeline allows for the precise design of shape complementarity over extended surface areas and can be designed accurately, resulting in – as previously evidenced – exceptionally high-affinity (pM-nM) and highly specific interactions that are considerably more challenging with small molecule strategies.

The ability to design hyperstable proteins that bind to specific, pre-determined surface patches makes *de novo* binders uniquely powerful tools for dissecting complex allosteric systems. For PBP2a, this allows for the creation of molecular probes that can accomplish several key objectives. First, binders designed to target only the allosteric site to act solely as an agonist or antagonist, allowing for the isolation and characterisation of the allosteric effect in the absence of any active site chemistry. Second, binders designed to scaffold across/between both allosteric and transpeptidase domains to restrain PBP2a in a specific conformation, such as locking it in the "closed" conformation to prevent allosteric transition. This provides several novel approaches to investigating the function of PBP2a wherein assessing the impact of these binders on the susceptibility of MRSA to previously ineffective β-lactam antibiotics (e.g. oxacillin or methicillin) *in vivo* via minimum inhibitory concentration (MIC) assays and *in vitro* using solution-state NMR techniques, allows more detailed characterisation of PBP2a's regulatory network. Specifically, NMR-based chemical

shift perturbation (CSP) experiments can precisely map each binder's footprint onto the PBP2a surface, validating computational design and confirming engagement with intended sites. Additionally, Carr-Purcell-Meiboom-Gill (CPMG) relaxation dispersion experiments can provide insights into the dynamic regulation of PBP2a, revealing whether binders successfully dampen μs-ms timescale motions associated with allosteric conformational changes in the presence or absence of known effectors (e.g. ceftaroline or peptidoglycan). By correlating these detailed biophysical and structural data with the functional cellular outcomes from MIC testing, unprecedented insight into the linkage between allosteric site engagement, conformational dynamics, and the ultimate expression of antibiotic resistance are possible. Finally, development of binders that inhibit PBP2a directly or can activate it such that non-PBP2a active antibiotics can inhibit PBP2a has potential as either an alternative to antibiotics or an adjuvant to existing antibiotics to inactivate the existing resistance mechanism, thereby rejuvenating the usefulness of these antibiotics. This is particularly of interest for proteins such as PBP2a that do not require the binder to enter the cell to have its effect.

1.9 Present work aims and objectives

Methicillin-resistant *Staphylococcus aureus* (MRSA) owes its β-lactam resistance to PBP2a, a transpeptidase whose activity has long been postulated as solely due to modulation by long-range allosteric communication between a distal regulatory surface and its active site[5-7,89,97]. While several high-resolution structures have detailed PBP2a's architecture alone and in complex with various antibiotics, these static snapshots cannot quantify conformational substates or exchange kinetics in solution – features central to both catalysis and resistance. As such, though the prevailing allosteric model is widely accepted, it remains poorly characterised outside of a static context. This work integrates high-field solution NMR with structural and microbiological assays to further characterise the mechanism of PBP2a resistance to known antibiotics, probe the conformational flexibility of PBP2a in the apo and antibiotic bound state, and test whether rationally designed binders can restore β-lactam susceptibility as a study of the feasibility of such binders as potential adjuvants to existing antibiotics. This work therefore addresses three interconnected aims:

Aim 1 – Establish an NMR assignment of PBP2a spectra, enabling the use of NMR for characterisation of PBP2a structure, function and ligand binding.

PBP2a mediates β-lactam resistance through allosteric regulation however, structural insights derive primarily from static crystallographic snapshots and computational models. NMR spectroscopy is a versatile tool for studying protein dynamics which might therefore allow for a better understanding of the PBP2a-mediated mechanism of resistance. Furthermore, NMR spectroscopy is adept at identifying weak binding interactions, such as those expected from a first pass *de novo* designed binder and allows for the binding site to be identified. Therefore, NMR makes a good tool to allow for screening of binders. However, spectroscopic assignment is essential for both studies. Using $^{13}CH_3$-^{1}H-selective labelling of Ile δ1 methyl groups with SOFAST-HMQC detection, we assigned probes distributed throughout PBP2a, and across both transpeptidase and regulatory surfaces of previously determined clinical, structural and predicted relevance. This enabled robust mapping of chemical shift perturbations and µs-ms dynamics onto the 3D structure, establishing the experimental foundation for subsequent aims.

Aim 2 – Define how known ligands reshape the PBP2a landscape

Different ligands engage PBP2a with distinct susceptibility profiles and mechanisms. Discriminating their binding sites, modulation of conformational exchange and interaction interfaces is central to understanding allosteric control. Given the ambiguity in understanding of ceftobiprole binding and mechanism of action, this study aimed to determine the binding site for ceftobiprole binding to PBP2a and estimate the K_d of the interaction. The binding of other ligands both expected to bind to PBP2a and not to bind was also analysed. Given the allosteric mechanism of PBP2a activation in required in ceftaroline and peptidoglycan, this work also aimed to determine whether conformational flexibility of the protein was altered by ceftobiprole binding. Through methyl-SOFAST-HMQC titrations with ligands of varying efficacy, we quantified chemical shift perturbations and mapped binding footprints, allowing the binding sites of different ligands to be identified. ^{13}C-methyl CPMG relaxation-dispersion experiments added further context to binding dynamics by probing µs-ms exchange. Strikingly, ceftobiprole perturbed a narrow interface confined to the transpeptidase domain, in contrast to existing work evidencing the essentiality of ceftaroline's engagement with a salt-bridge dependent allosteric network to modulate the active site – despite their structural similarity. These solution-based measurements refine crystallographic models by highlighting dramatic mechanistic differences between two closely related ligands with subtle structural differences.

Aim 3 – Develop, test and characterise *de novo* binders that modulate PBP2a function

Rationally designed binders targeting allosteric surfaces could re-sensitise MRSA to β-lactams whilst directly probing allosteric circuitry. Effective candidates must demonstrate specific binding, favourable population shifts, and altered cellular susceptibility. We screened six computationally designed mini-proteins using methyl-HMQC CSP titrations to confirm binding and rank affinities. Parallel MIC assays in MRSA evaluated β-lactam susceptibility restoration. Integrating spectroscopic and phenotypic data revealed one candidate that produced clear CSPs at the targeted interface and – crucially – restored oxacillin susceptibility in MRSA at clinically relevant concentrations (8 μg/mL). This allowed for a proof of principle that *de novo* binders could function as effective antibiotic adjuvants to overcome PBP2a-mediated β-lactam resistance.

Taken together, these aims move from establishing a reliable spectroscopic handle on a challenging, aggregation-prone protein critical to clinical MRSA infections (Aim 1), through probing the effects of antibiotic binding in solution (Aim 2), to demonstrating that rationally designed binders can restore antibiotic susceptibility (Aim 3). The progression from method development through mechanistic characterisation to functional modulation provides both fundamental insights for understanding PBP2a allostery and informs future efforts to rationally re-sensitise resistant *S. aureus* to treatment.

Chapter 2 Materials and methods

2.1 Materials

2.1.1 Bacterial strains and plasmids

Table 1 illustrates the bacterial strains used in this study. All bacterial strains were stored at -80ºC as glycerol stocks in LB medium containing 20% (v/v) glycerol.

Table 2: Uses, source and genotype of bacterial strains used for the expression of PBP2a in this study

Strain	Use	Source
E. coli BL21-Star (DE3)	Recombinant protein expression of PBP2a: F⁻ *ompT hsdSB*(*rB*⁻ *mB*⁻) *gal dcm rne131* (DE3)	Thermo Fisher Scientific
E. coli BL21-Gold (DE3)	Recombinant protein expression of PBP2a and *de novo*-designed protein mini-binders: *E. coli* B F⁻ *ompT hsdS*(*rB*⁻ *mB*⁻) *dcm* Tet^R *gal* λ(DE3) *endA*I	Agilent Technologies
E. coli BL21-RosettaTM 2 pLysS (DE3)	Recombinant protein expression of PBP2a: F⁻ *ompT hsdSB*(*rB*⁻ *mB*⁻) *gal dcm* (DE3) pLysSRARE2 (Cam^R)	Merck Millipore
E. coli BL21-RosettaTM 2 (DE3)	Recombinant protein expression of PBP2a: F⁻ *ompT hsdSB*(*rB*⁻ *mB*⁻) *gal dcm* (DE3) pRARE2 (Cam^R)	Merck Millipore
E. coli BL21-CodonPlus(DE3)-RIL	Recombinant protein expression of PBP2a: *E. coli* B F⁻ *ompT hsdS*(*rB*⁻ *mB*⁻) *dcm* Tet^R *gal* λ(DE3) *endA*I [*argU ileY leuW* Cam^R]	Agilent Technologies
E. coli DH5α	High-efficiency cloning and high-yield plasmid prep of pSK-mecA mutants: F⁻ φ80*lacZ*ΔM15 Δ(*lacZYA-argF*)U169 *recA*1 *endA*1 *hsdR*17 (r_k^- m_k^+) *gyrA*96 *relA*1 λ⁻	Merck Millipore
S. aureus RN4220	Intermediate host to methylate plasmid DNA with the S. aureus pattern and bypass SauI restriction prior to transfer into experimental strains: *Sau*I *hsdR*⁻ (*r*⁻ *m*⁺)	Laboratory stock from S. Galarion
S. aureus NE1868 (USA300 JE2)	USA300 JE2 *mecA*::*Tn* (*bursa aurealis*, Erm^R); endogenous *mecA* inactivated; *SCCmec* context retained	BEI/NARSA (Nebraska Transposon Mutant Library)

Strain	Use	Source
S. aureus LAC (USA300)	USA300 community-associated MRSA parental strain for minimum inhibitory concentration (MIC) assays; ST8, spa type t008, SCCmec IVa, PVL positive, ACME positive; canonical USA300 laboratory background from which JE2 was derived	Laboratory stock from S. Galarion

To maximise soluble yield of PBP2a under both protonated and deuterated defined-media conditions, several BL21(DE3) derivatives were screened before settling on BL21-Star(DE3) for production. All strains share the BL21 background (deficient in the OmpT/Lon proteases) and the λDE3 lysogen encoding T7 RNA polymerase under *lacUV5* control, enabling high-level expression from T7 promoters. BL21-Star(DE3) carries the *rne131* mutation in RNase E, which increases mRNA half-life and commonly boosts expression of difficult or low-abundance transcripts – an advantage in slow-growing minimal/^{2}H media where transcription/translation are rate-limited. BL21-Gold(DE3) provides the same expression chassis with additional *endA* inactivation and high transformation efficiency, with yields comparable to BL21-Star(DE3)but without the mRNA-stability benefit. Two strains supplied rare tRNAs to alleviate codon-usage bias. BL21-CodonPlus(DE3)-RIL contains extra tRNAs for Arg (AGG/AGA), Ile (AUA) and Leu (CUA)), whereas BL21-Rosetta2(DE3)/Rosetta2(DE3)-pLysS strains contain a broader tRNA set on the included pRARE2 plasmid; the pLysS variant additionally expresses T7 lysozyme to suppress basal expression, which is often helpful for toxic targets. Rare-tRNA strains can improve expression of heterologous genes, however extra plasmid/antibiotic burden (in this case, from chloramphenicol) came at the cost of growth and yield in minimal ^{2}H media; performing worse than BL21-Star for PBP2a. Accordingly, BL21-Star(DE3) was selected for all final productions, balancing yield, culture robustness, and simplicity of antibiotic selection.

For plasmid construction and transfer of *mecA* variants into *S. aureus*, we used a three-host pipeline chosen to maximise plasmid yield, protect constructs from staphylococcal restriction systems, and enable *mecA*-null but SCCmec-contextual testing *in vivo*. *E. coli* DH5α was used for site-directed mutagenesis and high-quality, high-copy plasmid production using a pSK shuttle vector; its recombination deficiency (*recA1*) and nuclease deficiency (*endA1*) minimise unwanted rearrangements and improve plasmid prep quality.

Plasmids were then passed through *S. aureus* RN4220, a restriction-deficient laboratory strain commonly used as an intermediate host to overcome *SauI* restriction barriers. Growth in RN4220 deposits a staphylococcal methylation pattern on the plasmid, allowing efficient transformation. For phenotypic testing we used NE1868 (USA300 JE2 background) from the Nebraska transposon library: a *mecA::Tn* (Erm^R) strain in which *mecA* function is ablated while the SCCmec context remains, providing a clean, near-native background to assess β-lactam susceptibility conferred solely by the plasmid-borne *mecA* variants. This combination yielded reliable plasmid production, efficient interspecies transfer, and interpretable MIC readouts uncontaminated by endogenous PBP2a.

A pET-28a(+) plasmid modified to include a TEV protease cleavage site and cloned with a truncated *mecA* insert encoding PBP2a residues 22-668 ($pET\text{-}28a(+)_{PBP2a}$), thereby excluding the N-terminal transmembrane anchor, was used for recombinant expression of PBP2a in *E. coli* (Figure 14 and Table 3).

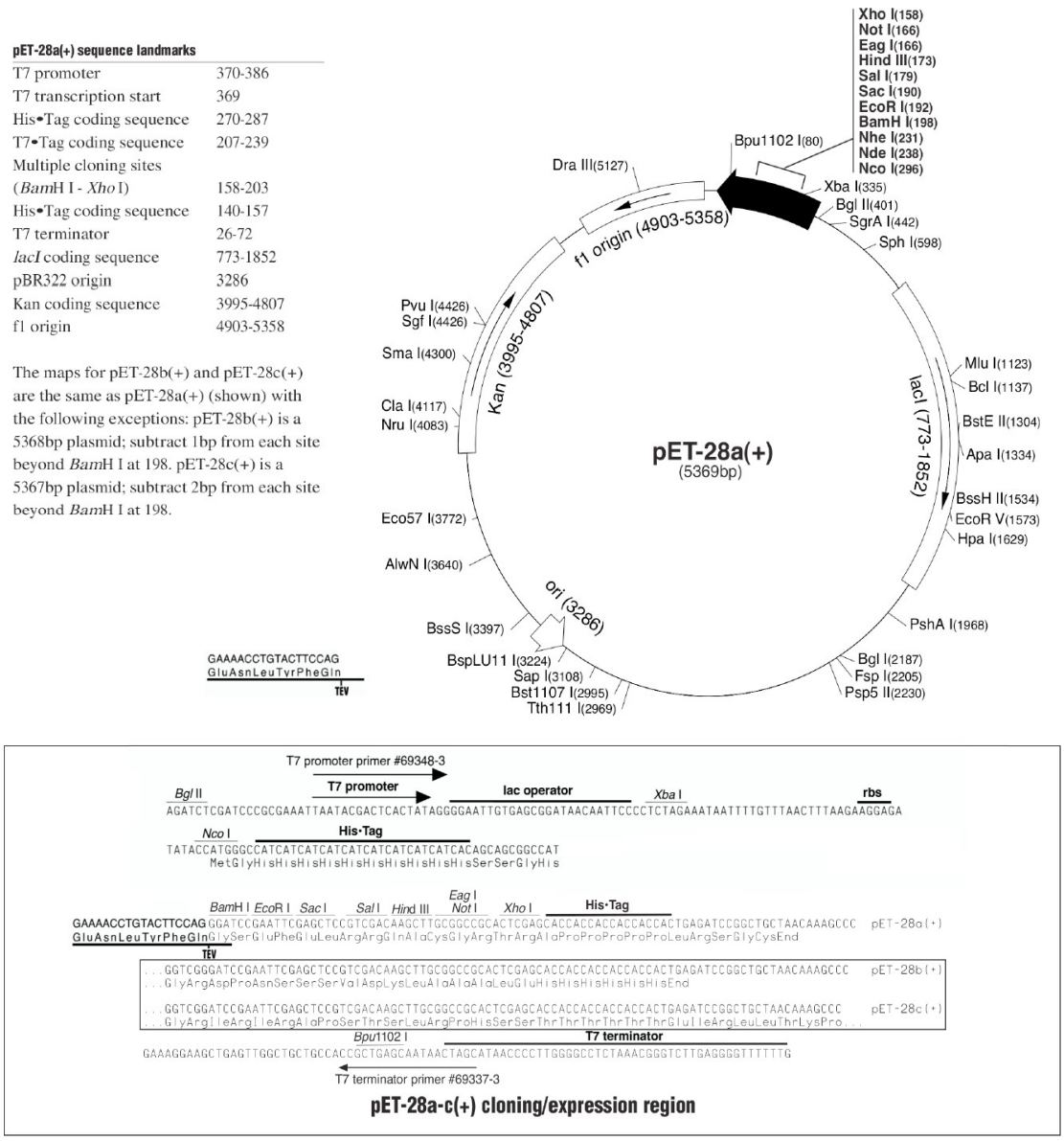

Figure 14: Map of the pET-28a(+) plasmid utilised for the expression of PBP2a in this study[145].

In addition to the wild-type PBP2a construct, selectively mutated PBP2a constructs were generated for NMR resonance assignment by Ile/Val selective mutagenesis (Table 3). These constructs encoded the same truncated PBP2a region as the wild-type expression construct, with incorporation of the relevant Ile and Val substitutions, and were expressed from a pET-28a(+) based vector containing an N-terminal His-tag and TEV protease cleavage site. Separate *de novo*-designed mini-protein binder constructs encoding P18, P21, P49, P60, P66 and P74 (pET28-PX - Table 3; where 'X' denotes each binder number) were also used for recombinant expression in *E. coli*. These binder constructs encoded the full designed binder sequences shown in Table 9 and contained an N-terminal polyhistidine tag with a TEV protease cleavage site for affinity purification and optional tag removal.

Table 3: DNA constructs used for recombinant protein expression in this study.

Construct	Encoded Protein	Expression Vector	Host Strain(s) Used	Insert / Expressed Region	Tag / Fusion Features	Selection Marker	Purpose
pET28a-PBP2a	PBP2a	pET-28a(+)	*E. coli* BL21 variants (Table 1)	PBP2a with transmembrane anchor removed (Δ1-22).	N-terminal His tag (MG**HHHHHHHHHH**SSGHENLYFQGS) and C-terminal His Tag (LE**HHHHHH**)	Kan	Recombinant expression and purification of WT PBP2a
pET28a-PBP2a	PBP2a (Ile and Val mutants)	pET-28a(+)	*E. coli* BL21-Gold (Table 1)	PBP2a with transmembrane anchor removed (Δ1-22).	N-terminal His tag (MGSS**HHHHHH**SSGENLYFQG) – commercially synthesised by Twist Bioscience	Kan	Recombinant expression and purification of Ile/Val PBP2a mutants
pET28-PX	*De novo* designed mini protein binders P18, P21, P49, P60, P66, P74 (Table 9)	Modified pET-28 vector	*E. coli* BL21-Gold (Table 1)	Full designed binder coding sequence (Table 9)	N-terminal His tag (MG**HHHHHH**SSGENLYFQG)	Kan	Recombinant expression and purification of *de novo*-designed mini protein binders

2.1.2 Media

Commercially made Luria-Bertani (LB) media broth (Sigma-Aldrich, United States) used in *E. coli* cultures was prepared according to manufacturer recommendations. M9 minimal media for used in *E. coli* liquid cultures was prepared by the addition of the following components (Table 4) into appropriate culture vessels.

Table 4: Required reagents for the preparation of 1 litre of M9 defined media for the culture of PBP2a-expressing *E. coli*.

Stock Solutions	Stock Preparation	Volume/1 L Media
D_2O*	Membrane-filtered (0.2 µm) prior to use	862.1 mL
M9 Salts (10 x)	Per 200 mL: 13.52 g $NaHPO_4$, 6.0 g KH_2PO_4 and 1.0 g NaCl were solubilised in D_2O to a final volume of 200 mL and filter sterilised (0.22 µm).	100 mL
(^{13}C) Glucose** (20 % w/v)	Per 20 mL: 4.0 g glucose was solubilised in D_2O to a final volume of 20 mL and filter sterilised (0.22 µm).	20 mL
(^{15}N) NH_4Cl (25 % w/v)	Per 10 mL: 2.5 g NH_4Cl was solubilised in D_2O to a final volume of 10 mL and filter sterilised (0.22 µm).	4 mL
$MgSO_4$ (1 M)	Per 10 mL: 1.2 g $MgSO_4$ was solubilised in D_2O to a final volume of 10 mL and filter sterilised (0.22 µm).	2 mL
Trace Elements (1000 x)	Per 1000 mL: 1 g $FeSO_4 \cdot 7H_2O$, 8.8 g $ZnSO_4 \cdot 7H_2O$, 0.4 g $CuSO_4 \cdot 7H_2O$, 0.15 g $MnSO_4 \cdot 4H_2O$, 0.1 g $Na_2B_4O_7 \cdot 10H2O$, 0.05 g $(NH_4)_6Mo_7O_{24} \cdot 4H_2O$ was solubilised in 1 L H_2O with 200 µL HCl (6 M) before autoclaving.	1 mL
$FeCl(III) \cdot 6H_2O$	Per 10 mL: 0.5 g $FeCl(III) \cdot 6H_2O$ was solubilised in D_2O to a final volume of 10 mL and filter sterilised (0.22 µm).	800 µL
MEM Vitamins (100 x)	Pre-purchased from Invitrogen (Cat No. 11120052).	10 mL
$CaCl_2$ (1M)	Per 10 mL: 1.1 g CaCl2 was solubilised in D_2O to a final volume of 10 mL and filter sterilised (0.22 µm).	100 µL

*For protonated media, filter-sterile (0.22 µm) dH2O was used. **For uniform labelling in deuterated media, ^{13}C was used. For uniform labelling in protonated media, ^{12}C was used. For methyl-selective labelling, $^{12}C^2H$ was used.

Following the addition of all media components (Table 4), culture vessels were autoclaved (121°C for 16 minutes at 1.4 bar pressure). For expression of perdeuterated proteins for NMR studies, D_2O was used in place of dH_2O for each component of the M9 media ($M9^D$). Enrichment of proteins with ^{13}C and ^{15}N isotopes for NMR studies was achieved by replacing (^{12}C) Glucose and (^{14}N) NH_4Cl with (^{13}C) Glucose and (^{15}N) NH_4Cl (Cambridge Isotope Laboratories, United States) respectively

2.1.3 Protein purification and experimentation buffers

The following buffers (Table 3) were used for the purification of PBP2a from *E. coli* via Ni-NTA affinity chromatography and size exclusion chromatography:

Table 5: Composition of buffers used for the routine purification of PBP2a from *E. coli* in this study.

Buffer	Composition	Use
Lysis/Binding Buffer	10 mM Imidazole, 300 mM NaCl, 50 mM NaH_2PO_4, pH 8.0	Ni-NTA Chromatography
Wash Buffer	20 mM Imidazole, 300 mM NaCl, 50 mM NaH_2PO_4, pH 8.0	Ni-NTA Chromatography
Elution Buffer	500 mM Imidazole, 300 mM NaCl, 50 mM NaH_2PO_4, pH 8.0	Ni-NTA Chromatography
Size Exclusion Buffer	300 mM NaCl, 50 mM NaH_2PO_4, Glycerol (10% v/v), pH 8.0	Size Exclusion Chromatography

All buffers were solubilised in dH_2O and filtered through a 0.22 µm PES membrane before use. In addition, the Size Exclusion Buffer was de-gassed.The following buffers (Table 4) were used for the various downstream applications of recombinant PBP2a purified as previously described:

Table 6: Composition of buffers used for all downstream experimentation of PBP2a in this study.

All buffers were solubilised in dH_2O and filtered through a 0.22 µm PES membrane before use.

Buffer	Composition	Use
NMR Buffer	300 mM NaCl, 50 mM NaH_2PO_4, 10% (v/v) D_2O, cOmplete Protease Inhibitor Cocktail (1 tablet/50 mL), pH 8.0	NMR Spectroscopy
Native Buffer	300 mM NaCl, 50 mM NaH_2PO_4, cOmplete Protease Inhibitor Cocktail (1 tablet/50 mL), pH 8.0	Unlabelled protein experiments
CD Buffer	300 mM Sodium Sulfate, 50 mM NaH_2PO_4, 10% (v/v) D_2O, cOmplete Protease Inhibitor Cocktail (1 tablet/50 mL), pH 8.0	Circular Dichroism

2.2 Methods

2.2.1 Molecular biology techniques

2.2.1.1 Purification of plasmid DNA

Plasmid DNA was purified from LB cultures grown from freeze-dried stocks of *E. coli* (DE3) Rosetta™ containing the pET-28a(+)$_{PBP2a}$ construct using a QIAprep Spin Miniprep Kit (Qiagen, Germany) in accordance with manufacturer instructions.

2.2.1.2 Preparation of chemically competent bacteria

2.2.1.2.1 E. coli

Large stocks of chemically competent cells were made from commercially bought untransformed *E. coli* ultracompetent cells (Table 1). Briefly, a small amount of frozen competent cells was scraped, spread on LB agar plates and cultured overnight in a static incubator at 37°C. A single colony was inoculated into 5 mL LB media and cultured overnight at 37°C, shaking at 250 rpm. 1 mL of saturated culture was used to inoculate 100 mL LB media in a 250 mL baffled flask and cultured at 37°C for 2 hours, shaking at 250 rpm. Cultures were placed on ice for 10 minutes before being harvested by centrifugation at 4500 x *g* for 3 minutes at 4°C before being placed on ice. All subsequent steps outside of

centrifugation were strictly maintained on ice. The supernatant was discarded, and the cells gently resuspended in 10 mL ice-cold 0.1 M CaCl before being left to incubate on ice for 20 minutes. Cells were centrifugation at 4500 x *g* for 3 minutes, the supernatant discarded, and cells gently resuspended in 0.1 M CaCl supplemented with 15% (v/v) glycerol. 300 µL of competent cells were aliquoted into pre-chilled microtubes, snap-frozen in liquid nitrogen and stored at -80ºC.

2.2.1.2.2 S. aureus

Electrocompetent cells for NE1868 and RN4220 were prepared from untransformed cultures as follows. A scrape of electrocompetent cells was spread on TSB agar plates and cultured overnight in a static incubator at 37ºC. A single colony was inoculated into 5 mL TSB supplemented with 2.5% (w/v) yeast extract (filter-sterilised) and grown overnight at 37ºC, 200 rpm. The next day, 1 mL of the saturated culture was used to inoculate 25 mL TSB supplemented with 2.5% yeast extract (autoclaved) and incubated at 37ºC, 200 rpm until OD_{600} = 0.5-0.6. Cultures were chilled on ice, and all subsequent manipulations were performed cold. Cells were harvested by centrifugation at 4000 × *g* for 10 min at 4ºC, the supernatant discarded, and the pellet gently resuspended in 25 mL ice-cold sterile deionised water. This water wash was repeated 1-3 times. Cells were then exchanged into a low-conductivity buffer by washing with 5 mL ice-cold 10% (v/v) glycerol, followed by resuspension in 2.5 mL ice-cold 10% glycerol and incubation on ice for 15 min. Cells were re-pelleted by centrifugation at 4500 x *g* for 3 minutes and finally resuspended in 800 µL 10% glycerol, aliquoted in 50 µL portions into pre-chilled microtubes, snap-cooled, and stored at -80ºC. Electrocompetent stocks generally performed best after at least one freeze at -80ºC.

2.2.1.3 Generation of pRMC2$_{mecA}$ mutants in E. coli

A panel of *mecA* (USA300) mutants in the anhydrotetracycline-inducible *E. coli/S. aureus* shuttle vector pRMC2 were commercially synthesised and procured from NBS Biologicals (Huntingdon, UK). The point mutants created were: S403A, K153A, E294A, K265A, D226A, K316A, T348A, S376A, K382A, I492A, K604A, K634A, and D635A. These mutations were selected based on previous studies that identified residues critical for catalysis or acylation[7] or those predicted to be functionally important by computational analysis[89]. The purpose of this work was to sub-clone each *mecA* mutant into pSK to assess their resistance phenotypes in the *mecA*-naïve MRSA strain NE1868 (Table 1).

Each mutant *mecA* open reading frame was PCR-amplified from its pRMC2 template using a Phusion HF polymerase (New England Biolabs, UK) and primers introducing 5′ EcoRI and 3′ KpnI sites (FOR_mecA_KpnI and REV_mecA_EcoRI; Table 5).

Table 7: Composition of primers used for cloning in this study.

Primer	Sequence	Use
REV_pSK KpnI	GTTGTTGAATTCACTCCTTATATAA GACTACATTTGTAG	pSK vector preparation
FOR_pSK KpnI	GTTGTTGGTACCAATCCGTAACGAT GGTTGC	pSK vector preparation
REV_ mecA EcoRI	GTTGTTGGTACCCTTCACTGTTTTGT TATTCATCTATATC	Mutant *mecA* insert generation
FOR_mecA EcoRI	GTTGTTGAATTCATGAAAAAGATAA AAATTGTTCCACT	Mutant *mecA* insert generation

Each 50 µL reaction mixture consisted of 10 µL of 5x Phusion HF Buffer, 1.5 µL of 10 mM dNTPs, 2.5 µL of forward primer (10 µM), 2.5 µL of reverse primer (10 µM), 1.5 µL of 50 mM $MgCl_2$, 1.5 µL of DMSO, 20 ng of template pDNA, 0.5 µL of Phusion DNA Polymerase (2 U/µL), and nuclease-free water to a final volume of 50 µL. All reagents were sourced from New England Biolabs, Hertfordshire, UK. The thermal cycling conditions were performed on a CFX96 Touch Real-Time Thermal Cycler (Bio-Rad) and consisted of an initial denaturation step at 98°C for 30 seconds; followed by 30 cycles of denaturation at 98ºC for 10 seconds, annealing at 60ºC for 30 seconds, and extension at 72ºC (1.7 min per kb); and a final extension step at 72ºC for 10 minutes before holding at 4ºC. Following PCR amplification, to remove the parental, methylated template DNA, each reaction was digested via the addition of 1 µL of DpnI (20,000 U/mL) and subsequent incubation at 37ºC for 2 hours.

The pSK vector was PCR-linearised to remove the existing wild-type *mecA* insert (legacy construct supplied by Dr L. Galarion and Dr M. Mohhamed) and to append EcoRI and KpnI sites compatible with the inserts. Primers REV_pSK KpnI and FOR_pSK KpnI (Table 7) were used with LongAmp Taq (NEB) polymerase. Each 50 µL reaction mixture contained 10 µL of (5x) LongAmp Taq Reaction Buffer, 1.5 µL of 10 mM dNTP mix, 2.5 µL of 10

µM forward primer, 2.5 µL of 10 µM reverse primer, 50 ng of pSK template DNA, and 2 µL of LongAmp Taq DNA Polymerase (5,000 U/mL). All reagents were sourced from New England Biolabs (Hertfordshire, UK), and nuclease-free water was added to bring the final volume to 50 µL. The thermal cycling conditions were performed on a CFX96 Touch Real-Time Thermal Cycler (Bio-Rad) and consisted of an initial denaturation at 94ºC for 1 minute, followed by 32 cycles of denaturation at 94ºC for 30 seconds, annealing at 58ºC for 2 minutes, and extension at 65ºC for (1 min per kb), with a final extension at 65ºC for 10 minutes before holding at 4ºC. Following PCR amplification, to remove the parental, methylated template DNA, each reaction was DpnI-digested as above.

2.2.1.4 E. coli to S. aureus cloning and subcloning

Insert amplicons and the linear pSK backbone were double-digested with EcoRI-HF and KpnI-HF (NEB). Each digestion reaction included: 50 µL pDNA, 6 µL (10X) CutSmart® Buffer (New England Biolabs, Cat No. B7204S), 2 µL of EcoRI-HF (New England Biolabs, Cat No. R3101S), and 2 µL of KpnI-HF (New England Biolabs, Cat No. R3142S). Digestions were incubated at 37ºC for 2 hours. Following digestion, the digested inserts and vector were purified by separation via agarose gel electrophoresis on a 1.0% (w/v) agarose gel in 1X TAE buffer, followed by excision of the bands corresponding to the expected length of mutant insert DNA and pSK respectively and DNA extraction using a QIAquick Gel Extraction Kit (Qiagen, Cat No. 28704) according to the manufacturer's protocol.

The digested and purified (mutated) insert and vector were ligated using T4 DNA Ligase (NEB, Cat No. M0202S). The ligation reaction included 50 ng of digested vector, a 7:1 molar ratio of insert (mutated fragment) to vector (pSK), 2 µL of (10X) T4 DNA Ligase Reaction Buffer (New England Biolabs, Cat No. B0202S), 1 µL of T4 DNA Ligase (New England Biolabs, Cat No. M0202T), and nuclease-free water to a final volume of 20 µL. The ligation reaction was incubated at 16ºC overnight in a static incubator. Ligation products (containing each mecA mutant cloned into its own pSK vector) were then transformed into chemically competent *E. coli* DH5*α* by heat-shock. Briefly, 50 µL of chemically competent DH5α cells were inoculated with 5 µL of ligation product before being mixed gently and left on ice for 30 minutes. Cells were heat-shocked in a dry block set at 42ºC for 45 seconds, rested on ice for 2 minutes, and recovered via the addition of 800 µL of sterile S.O.C medium (Thermo Fisher Scientific, UK; Cat No. 15544034) and subsequent incubation at 37ºC, shaking at 250 rpm, for 60-90 minutes. 150 µL of the recovered cells were spread onto LB agar plates

supplemented with 100 µg/mL ampicillin and incubated at 37°C overnight (12-16 hours) in a static incubator. Resulting colonies containing the desired mecA mutations within the pSK shuttle vector were picked, inoculated into LB broth supplemented with 50 µg/mL kanamycin and incubated at 37°C, shaking at 220 rpm, for 12-16 hours (overnight). Cultures were centrifuged for 10 minutes at 4800 x g at room temperature and plasmid DNA was isolated from cell pellets using a QIAprep Spin Miniprep Kit (Qiagen, Cat No. 27104) according to the manufacturer's protocol. The presence of all desired mutations was confirmed by Sanger sequencing by a third-party commercial company (Genewiz, Azenta, Germany). All plasmid constructs produced in this study were sequenced this way. This plasmid is hereafter referred to as pSK_{mecA}.

2.2.1.5 E. coli to S. aureus cloning and subcloning

To impart the appropriate *Staphylococcus aureus* methylation pattern, the recombinant plasmid pSK_{mecA}, isolated from *E. coli* DH5α, was first transformed into the restriction-deficient *S. aureus* strain RN4220.

For electroporation, 50 uL of electrocompetent RN4220 cells were mixed with 500 ng of pSK_{mecA} plasmid DNA in a pre-chilled 1 mm electroporation cuvette (Geneflow, Elmhurst, UK). Electroporation was performed using a MicroPulser electroporator (Bio-Rad, Cat. 165-2100) with a single pulse with the following settings: 21 kV/cm, 100 Ω, and 25 µF. Immediately following the pulse, 1 mL of TSB supplemented with 0.5 M (filter-sterile) sucrose was added to the cuvette, mixed gently, transferred to a 25 mL sterile universal tube and incubated at 37°C, shaking at 220 rpm for 1 hour. 150 µL of the recovered cells were then spread onto TSB agar supplemented with appropriate antibiotics for selection, which were then incubated at 37°C overnight.

Single colonies from pSK_{mecA}-containing RN4220 were selected and cultured in 5 mL of TSB containing 10 µg/mL chloramphenicol at 37°C overnight, shaking at 250 rpm. Plasmid DNA was then isolated using the QIAprep Spin Miniprep Kit (Qiagen, Cat No. 27104), with the following modifications for more robust lysis of S. aureus: cell pellets were resuspended in Buffer P1 containing 50 µg/mL lysostaphin (produced by recombinant expression and purified in house by J. Clarke) and incubated at 37°C for 45 minutes before proceeding with Buffer P2 as per the manufacturer's protocol. The isolated plasmid was quantified using a NanoDrop One spectrophotometer.

The RN4220-modified pSK$_{mecA}$ plasmid DNA was subsequently transformed into a *mecA*-naïve *S. aureus* strain NE1868 (Table 1). For electroporation, 50 µL of electrocompetent NE1868 cells were mixed with 200-500 ng of the RN4220-modified pSK$_{mecA}$ plasmid and electroporated, recovered and grown overnight as previously described for RN4220. Successful transformants carrying the pSK$_{mecA}$ point mutants in NE1868 were then selected for further study.

2.2.2 Over-expression and purification of PBP2a

2.2.2.1 Overexpression in rich media

A single colony – irrespective of liquid media volume – of *E. coli* transformed with pET-28a(+)$_{PBP2A}$, grown on LB agar, was inoculated into LB media supplemented with 30 µg/mL kanamycin, and grown at 37ºC, 220 rpm until an OD_{600} of 0.8 was reached. Protein expression was induced via the addition of 1.0 mM IPTG, following which, cultures were incubated at 25ºC for 18 hours, shaking at 200 rpm. Prior to induction, 1 mL of each culture from each colony was retained and stored at -80ºC as a 20% glycerol stock to select for highly expressing constructs. Cells were harvested via centrifugation at 4800 x *g* for 10 minutes at 4ºC and resuspended in ice-cold Lysis Buffer (Table 3 – 10 mL per 4-5 g cell pellet) supplemented with cOmplete™ Protease Inhibitor Cocktail (Roche, Germany) and ~1 mg lysozyme (Sigma-Aldrich, UK). For small cultures (5-10 mL), resuspended cell pellets were lysed via 4 rounds of freeze thaw lysis at -80ºC. For large scale cultures (>10 mL), resuspended cell pellets were maintained on ice and lysed via sonication by 8 x 15 second pulses at 55 % amplitude, each alternated with a 45 s rest interval. Total cell protein was harvested from cell lysate via centrifugation at 21 000 x g for 40 minutes at 4ºC and the supernatant retained for purification.

Expression levels were confirmed by SDS-PAGE. A 1:1 mixture of supernatant and (2X) SDS Loading Buffer was denatured for 5 minutes at 95ºC and loaded into 4-12% RunBlueTM Bis-Tris Protein Gels (Expedeon, United Kingdom). Gels were run at 200 V for 40 minutes, in (1X) MOPS Buffer, and then subsequently stained with InstantBlue™ Coomassie Protein Stain (Expedeon, United Kingdom) until sufficiently stained.

2.2.2.2 Overexpression in defined media

A scrape from frozen glycerol stocks of successfully expressing transformants retained in 2.2.2.1 were streaked onto M9 agar plates. The composition of all M9 growth media can be found in Table 4. Single colonies were inoculated into M9 media supplemented with 30 µg/mL kanamycin, and grown at 37ºC, shaking at 220 rpm until an OD600 of 0.8 was reached. Protein expression was induced via the addition of 1.0 mM IPTG, following which, cultures were incubated at 25ºC for 24-26 hours, shaking at 220 rpm. Prior to induction, 1 mL of each culture from each colony was retained, combined with sterile 50% glycerol solution and stored at -80ºC to select for highly expressing constructs. Cells were harvested via centrifugation at 4000 x *g* for 10 minutes at 4ºC, lysed and expression yields qualitatively assessed as previously described in rich media.

2.2.2.3 Acclimation of E.coli strains to deuterated growth media

Three fresh individual colonies from LB agar plates of *E. coli* transformed with pET-28a(+)$_{PBP2A}$ selected for the most abundant expression levels were streaked on M9 minimal media agar plates, containing 30% deuterium oxide, supplemented with 30 µg/mL kanamycin, and grown in a static incubator at 37ºC overnight. This process was repeated on M9 minimal media agar containing 50%, 70%, 90% and 100% deuterium respectively with single colonies selected from the preceding concentration of D_2O, facilitating the selection for colonies progressively adapted to deuterium, as per previous methods[146]. Slower growth rates at 100% deuterium typically required 16-36 hours incubation time.

Three single colonies from M9 agar plates containing 100% deuterium were subcultured onto fresh individual 100% deuterium M9 agar plates and incubated. Single colonies from each subcultured 100% deuterium M9 agar plate were inoculated into 5 mL 100% deuterium M9 media supplemented with 30 µg/mL kanamycin, and grown at 37oC, 220 rpm until an OD600 of 0.8 was reached. Protein expression was induced via the addition of 1.0 mM IPTG, following which, cultures were incubated at 25oC for 32-36 hours, shaking at 220 rpm, in 50 mL sterile Falcon tubes. Prior to induction, 1 mL of each culture from each colony was retained, combined with sterile 50% glycerol solution and stored at -80oC. Cells were harvested, lysed and expression yields qualitatively assessed as previously described in rich and defined media.

This process was repeated for a total of three bouts of subculturing, with the strongest performing colonies being carried through each time, and a final deuterated M9 ($M9^{D2O}$) expression-optimised strain stored at -80°C for further study.

2.2.2.4 Overexpression in perdeuterated $^{13}C/^{15}N$ uniformly-labelled defined media

A scrape of glycerol stock from $M9^{D2O}$ expression optimised transformants was streaked out on LB agar and incubated overnight at 37°C. A single colony was inoculated into 200 mL of LB media supplemented with 30 µg/mL kanamycin, in a baffled flask, and grown at 37°C, shaking at 220 rpm until an OD_{600} of 0.8 was reached. Cultures were centrifuged for 5 minutes at 4000 x *g*, at room temperature, and the cell pellet gently resuspended in 50 mL of $M9^{D2O}$ Media I supplemented with 30 µg/mL kanamycin, in 250 mL bottom-baffled Erlenmeyer flasks (Simax®, KAVALIERGLASS a.s., Sázava, Czech Republic; Cat No. FLA1012) and incubated for 45-60 minutes, at 37°C, shaking at 220 rpm to exhaust any residual ^{12}C and re-acclimate to deuterated media. It is worthy of note that bottom baffled flasks improved the consistency and reliability of recombinant protein expression yields in deuterated media. Protein expression was induced via the addition of 1.0 mM IPTG, following which, cultures were incubated at 18°C for 32-36 hours, shaking at 220 rpm. Cultures were centrifuged for 10 minutes at 4800 x *g*, at 4°C, and cell pellets stored at -80°C unless immediately required for NMR study.

2.2.2.5 Overexpression in media selective for Ile δCH^3 labelling

A scrape of glycerol stock from $M9^{D2O}$ expression optimised transformants was streaked out on LB agar and incubated overnight at 37°C. A single colony was inoculated into 200 mL of LB media supplemented with 30 µg/mL kanamycin, in a baffled flask, and grown at 37°C, shaking at 220 rpm until an OD_{600} of 0.8 was reached. Cultures were centrifuged for 5 minutes at 4000 x *g*, at room temperature, and the cell pellet gently resuspended in 50 mL of $M9^{D2O}$ Media II supplemented with 30 µg/mL kanamycin, in a 250 mL bottom baffled Erlenmeyer flask, and incubated for 45-60 minutes, at 37°C, shaking at 220 rpm to exhaust any residual ^{12}C and re-acclimate to deuterated media. Cultures were supplemented with [methyl-^{13}C, 3,3-D_2]-α-ketobutyrate (70 mg/L) and incubated for an additional 45-60 minutes, at 37°C, shaking at 220 rpm to provide the precursors selective for Ile $\delta 1CH_3$ labelling. Protein expression was induced via the addition of 1.0 mM IPTG, following which, cultures were incubated at 18°C for 32-36 hours, shaking at 220 rpm. For ILVA labelling,

samples were U-^{2}H, U-^{15}N with selective $^{13}CH_3$-^{1}H labelling of Ile δ1, Leu/Val γ CH_3 and Ala β introduced via α-ketoacid precursors [3,3-D_2, 3-^{13}C]-α-ketoisovalerate (120 mg L^{-1}), [^{13}C]-L-Alanine (800 mg/L), and [^{13}C]-succinic acid (2.5 g/L) in addition to [methyl-^{13}C, 3,3-D_2]-α-ketobutyrate (70 mg/L) for Ile. Cultures were centrifuged for 10 minutes at 4800 x *g*, at 4°C, and cell pellets stored at -80°C unless immediately required for NMR study.

Table 8: **Composition of media used for the routine culture and overexpression of PBP2a from *E. coli* in this study.**

Media	Composition	Use
LB Media	20 g Luria Broth (Lennox; Sigma-Aldrich, UK) per 1 L dH_2O	Unlabelled growth and expression in protonated rich media
M9 Media	As described in Table 4 with ^{12}C glucose and ^{14}N NH_4Cl and all reagents solubilised in dH_2O instead of D_2O	Unlabelled growth and expression in protonated defined media
$M9^{D2O}$ Media I	As described in Table 4 with D-Glucose (1-^{13}C, 98-99%; Cambridge Isotopes, Cat No. CLM-420) and ^{15}N NH_4Cl (99%; Cambridge Isotopes, Cat No. NLM-467-10)	Uniformly labelled growth and expression in deuterated, defined media
$M9^{D2O}$ Media II	As described in Table 4 with $^{12}C^{2}H$ D-Glucose (1,2,3,4,5,6,6-D_7, 97-98%; Cambridge Isotopes, Cat No. DLM-2062) and ^{14}N NH_4Cl (Sigma-Aldrich, UK)	Methyl-selective labelled growth and expression in deuterated, defined media

2.2.2.6 IMAC

Cell pellets were resuspended in 5 mL ice-cold Lysis Buffer (Table 3) supplemented with cOmplete™ Protease Inhibitor Cocktail (Roche, Germany) and ~1 mg lysozyme. For small cultures (5-10 mL), resuspended cell pellets were lysed via 4 rounds of freeze thaw lysis at -80°C. For large scale cultures (>10 mL), resuspended cell pellets were maintained on ice and lysed via sonication by 8 x 15 second pulses at 55 % amplitude, each alternated with a 45 s rest interval. Total cell protein was harvested from cell lysate via centrifugation at 21,000 x g for 40 minutes at 4°C and the supernatant retained for purification.

The supernatant was filtered through a 0.22 μm syringe filter pre-washed with Binding Buffer (Table 3) before being loaded onto a His SpinTrap (Cytiva Life Sciences, Marlborough, MA, USA) column washed and equilibrated with Binding Buffer, in a microfuge pre-chilled to 4ºC. All subsequent steps were performed at 4ºC, and one column was used per 50 mL of cell culture. The original manufacturer protocol was initially followed. Columns were first equilibrated with 600 μL Binding Buffer and centrifuged for 60 s at 70-100 x *g*. Up to 600 μL sample was then applied and the column centrifuged 60 s at 70-100 x *g*. Additional 600 μL applications were performed sequentially as needed without exceeding column capacity until all sample was loaded. Columns were washed with 600 μL Binding Buffer and centrifuged 60 s at 70-100 x *g*. Bound protein was eluted in two steps by adding 200 μL Elution Buffer, centrifuging for 60 s at 70-100 x g, collecting the fraction in a fresh microtube. This step was repeated once. The manufacturer notes that the first 200 μL contains most of the target protein. The protocol was then optimised as follows. Columns were equilibrated with 800 μL Binding Buffer and centrifuged for 60 s at 70-100 x g. This step was repeated once. Up to 600 μL sample was then applied and the column centrifuged 60 s at 70-100 x g. Additional 600 μL applications were performed sequentially as needed without exceeding column capacity until all sample was loaded. Columns were washed with the addition of 800 μL Wash Buffer (Table 3) and centrifuged at 100 x g for 45-60 seconds. This step was repeated once. Target proteins were eluted by loading 800 μL Elution Buffer (Table 3) and centrifuging at 100 x g for 45-60 seconds, collecting the fraction in a fresh microtube. This step was repeated six times.

Identification of target protein-containing fractions were determined by SDS-PAGE as described previously, and subsequently pooled and concentrated using a centrifugal concentrator with a MWCO ~2.5x less than the target protein molecular weight (30 000 Da MWCO for PBP2a, 5000 Da MWCO for *de novo* designed protein binders), pre-washed with NMR Buffer (Table 4) at 12ºC. Concentrators were centrifuged in 10-15 minute intervals, between which, concentrator membranes were carefully washed, and the solution gently resuspended to avoid aggregation.

2.2.2.7 Size Exclusion Chromatography

A pre-packed HiLoad Superdex 200 pg size exclusion column (GE Healthcare, United Kingdom) was equilibrated with 1.20 x CV Size Exclusion Buffer (Table 3) using a ÄKTA Pure Protein Purification System (GE Healthcare, United States) until a stable conductivity

was reached. Concentrated Ni-NTA-purified protein was loaded onto the column via an injection loop and eluted in 3 mL fractions, following which, protein-containing fractions were retained, individually pooled and analysed via SDS-PAGE.

2.2.2.8 Buffer optimisation

Buffer conditions for PBP2a were optimised using the ThermoFluor™ thermal shift assay, a well-established technique for the assessment of the stability of proteins in different chemical and thermal environments by monitoring the fluorescence of SYPRO™ Orange, which binds to exposed hydrophobic regions during protein unfolding with increasing temperature. The screen evaluated protein stability in various buffers, pH conditions, salt concentrations, and with different additives. Core buffers included Sodium Phosphate ($NaHPO_4$, pH 5.5-8.0), HEPES (pH 6.8-8.2), PIPES (pH 6.1-7.5), Citric Acid Phosphate buffer ($CaNaHPO_4$, pH 5.0-7.0), MES (pH 5.5-6.7), and BisTris (6.0-7.2), each tested across their respective buffering ranges in ~0.5 pH unit increments. For every buffer and pH combination, NaCl concentrations of 0, 100, 200, or 300 mM were assessed. These conditions were further evaluated with or without additive either Glycerol (2.5%, 3.5%, or 5.0% v/v), 50 mM L-Arginine (Arg), 50 mM L-Glutamic acid (Glu), or a combination of 50 mM Arg and 50 mM Glu.

Each well contained a final reaction volume of 50 µL, consisting of 3.3 µL non-isotopically enriched PBP2a at a final concentration of 2.5 µM, 4 µL (12.5x) SYPRO™ Orange dye (ThermoFisher Scientific, Cat No. S-6651), and 42.7 µL buffer (containing buffer, pH, NaCl, and additive). Control wells contained the protein in its storage buffer with and without SYPRO™ Orange, as well as SYPRO™ Orange without protein (1x in dH2O). Plates were sealed with optical-quality sealing tape and gently agitated for 2 minutes on a microplate shaker, and fluorescence intensity was monitored as a function of temperature using a CFX96 Touch Real-Time Thermal Cycler (Bio-Rad). The temperature was ramped from 20°C to 95°C at a rate of 1.0°C/minute, with the thermocycler lid heated to 95°C to avoid condensation effects. Fluorescence from SYPRO™ Orange was monitored using the instrument's native CFX Maestro software. SYPR™ Orange was excited at ~470 nm and emission were collected at ~570 nm, as specified by the dye manufacturer.

Fluorescence-temperature traces exported from CFX Maestro (CFX96 Touch) were analysed in Microsoft Excel. Raw fluorescence for each well was first corrected by

subtracting the dye-only control at each temperature, after which signals were normalised to the dynamic range of the run by setting the mean of the pre-transition baseline to 0 and the post-transition plateau to 1. For each technical replicate, the melting temperature (T_m) was obtained in two equivalent ways. In the derivative method, the first derivative dF/dT was computed by centred finite differences over neighbouring points, and T_m was taken as the temperature at the maximum of *dF/dT*; for numerical stability a short (5-7 point) moving average was applied before differentiation, and a local quadratic fit to the three points around the peak was used to refine the maximum. In the model-based method, each normalised trace was fitted by non-linear least squares (Excel Solver, GRG) to a four-parameter Boltzmann function:

$$F(T) = \frac{F_{\mathrm{low}} + (F_{high} - F_{\mathrm{low}})}{1 + exp\frac{(T_m - T)}{k}},$$

where F_{low} and F_{high} are the pre- and post-transition baselines and k describes the slope; initial values were taken from the observed baselines, an approximate inflection temperature, and a slope yielding a visually similar transition width. For each condition, the change in melting temperature, $\Delta T_m = T_{m,condition} - T_{m,reference}$, was assessed relative to PBP2a in its reference buffer (50 mM $NaPO_4$, 300 mM NaCl, pH 7.0). Conditions yielding a ΔT_m greater than 2°C were considered significantly stabilising.

2.2.3 Overexpression of *de novo* protein binders

The details of each *de* novo designed binder are included below (Table 9):

Table 9: Physicochemical properties of protein binders *de novo* designed using Alpha Fold for this study

Binder	Length	MW (Da)	Theoretical pI	Ext. Coefficient	Sequence
P18	84	9779	7.02	7450	*MGHHHHHHSSGENLYFQGNPLKPLEDFFNSVYNTFDSDEEAKEALVKGQKYLRNPSLPKPDIKAISLAQAYRDYMRRQVLLNQP
P21	84	9757	6.02	7450	MGHHHHHHSSGENLYFQGDPLKSLKEFFDSIYNSFDSKEEADEALVKGQAYLRDPSLPKPDIRAISLAEAYRDYMRRQVLLNQP
P49	84	9610	6.02	11920	MGHHHHHHSSGENLYFQGKIGSYYEKLLNSIYLTYDSDEEAKEALVRGQKYLRDPSEPGVTLRDISLAEAYLNYMRAQNLANGP
P60	91	10151	5.84	7450	MGHHHHHHSSGENLYFQGKAKELIKKLVEEIVAEVKANPSTTQESIDEVKEVGEIALKETEKVGGYSYAIERANSIYRYAEALIAKDEGKA
P66	109	11012	9.26	4470	MGHHHHHHSSGENLYFQGAEVAKLTAEQAKKVIDAAVAARKTGAAGAAKARDVAVAAYDKVAAAGTPEVAREFALAARYAVLAAENAANADALLAKAKAAAEKAIAAAK
P74	133	14793	6.09	14900	MGHHHHHHSSGENLYFQGGEEEKLAKEAKKLGEEAVKAEKESGLAALNGNYEEAKKYDEKADEALKKLEKLAEEAKKKGLYNAAAEAYNALAEAYFKRAQVYMGNPDYSEEKALESANKGQKALALANYYARL

*Leader sequences are underlined which include the His-tag

A single colony of *E. coli* (BL21-Gold (DE3)) transformed with each protein binder on a pET28 vector backbone (prepared in house by Dr B. Schriffin), grown on LB agar, was inoculated into LB media supplemented with 50 µg/mL kanamycin, and grown at 37ºC, 220 rpm until an OD_{600} of 0.8 was reached. Protein expression was induced via the addition of 1.0 mM IPTG, following which, cultures were incubated at 37ºC for 4 hours, shaking at 200 rpm. Cells were harvested via centrifugation at 4800 x *g* for 10 minutes at 4ºC and resuspended in ice-cold Lysis Buffer (Table 3 – 10 mL per 4-5 g cell pellet) supplemented with cOmplete™ Protease Inhibitor Cocktail (Roche, Germany). Resuspended cell pellets were maintained on ice and lysed via sonication by 8 x 15 second pulses at 55 % amplitude, each alternated with a 45 s rest interval. Total cell protein was harvested from cell lysate via centrifugation at 21 000 x *g* for 40 minutes at 4ºC and the supernatant retained for purification. Expression levels were confirmed by SDS-PAGE as previously described using a PageRuler™ Plus Prestained Protein Ladder (ThermoFisher Scientific, UK; Cat No. 26619).

2.2.4 Antimicrobial susceptibility testing of *de novo* protein binders against PBP2a

Antimicrobial susceptibility testing was performed using *S. aureus* USA300 (prepared in house by Dr L. Galarion) which was routinely cultured in Mueller-Hinton Broth (MHB; Sigma-Aldrich, St. Louis, MO, USA) or on Mueller-Hinton Agar (MHA; Sigma-Aldrich, St. Louis, MO, USA) at 37ºC. Oxacillin sodium salt (Sigma-Aldrich, St. Louis, MO, USA) was dissolved in sterile, deionised water to create a stock solution of 1 mM, which was filter-sterilised and stored at -20ºC. Each de novo designed protein binder was expressed and purified as previously described (Section 2.2.3), and buffer exchanged into Native Buffer (Table 4) to a stock concentration of 1 mM and stored at 4ºC for a maximum length of 48 hours.

The minimum inhibitory concentrations (MICs) of each protein binder against PBP2a, and its efficacy towards *S. aureus* USA300 in the presence of oxacillin, was determined using the broth microdilution technique in flat-bottom 96-well sterile microtiter plates, according to previously established guidelines[147]. An inoculum of *S. aureus* USA300 was prepared by suspending colonies from an overnight MHA plate into MHB to match a 0.5 McFarland standard (1.5 x 108 CFU/mL) by serial dilution, and this suspension was further diluted in MHB to achieve a final inoculum density of approximately 5 x 105 CFU/mL in each well.

The final volume in each well was 100 µL. Wells contained the bacterial inoculum, MHB, oxacillin at a fixed final concentration of 8 µg/mL, and the protein binders at varying final concentrations (50 µM down to 0.39 µM). The oxacillin concentration was selected in the context of the CLSI clinical resistance breakpoint for *S. aureus* (≥4 µg/mL), thereby providing a stringent challenge to assess the ability of the de novo protein binders to restore antibiotic susceptibility.

A comprehensive set of controls was included in each assay plate: media only (MHB); MHB with 8 µg/mL oxacillin; MHB with *S. aureus* USA300; MHB with *S. aureus* USA300 and 50 µM of binder without oxacillin; MHB with 50 µM of binder without bacteria or oxacillin; and MHB with 50 µM of binder and 8 µg/mL oxacillin without bacteria.

The 96-well plates were covered with Parafilm M® to prevent evaporation and incubated at 37°C for 16-20 hours (as per CLSI guidelines for *S. aureus*) in a standing incubator with shaking at 250 rpm. Following incubation, bacterial growth was assessed both visually and by measuring the optical density at 600 nm using a FLUOstar Omega microplate reader (BMG Labtech, United Kingdom). The MIC was defined as the lowest concentration of the protein binder (or oxacillin in relevant controls) that completely inhibited visible growth of *S. aureus* USA300. The MICs of *de novo* designed protein binders designed against PBP2a were determined using the broth microdilution technique according to previously established guidelines[147,148]. Bacterial inoculum of 1 x 10^5 colony forming units (CFU) were used to determine the effect of each protein binder on PBP2a via their impact on the bacterial growth of *S. aureus* USA300 *in vivo*.

2.2.5 Structural and functional validation

2.2.5.1 Circular Dichroism

Circular dichroism (CD) spectroscopy was employed to characterise the secondary structure of PBP2a and as a primary assessment of protein folding. PBP2a was exchanged into CD Buffer (Table 4) using a centrifugal concentrator at a final concentration of 20 µM. Far-UV CD spectra were acquired over the range 180 nm down to 260 nm on a Chirascan Plus (Applied Photophysics, United Kingdom) spectrophotometer using a quartz cuvette with a path length of 1.0 mm. Measurements were performed at 20°C. For each spectrum, 2 scans were acquired and averaged. The data were collected with a wavelength step of 1.0 nm and a bandwidth (slit width) of 2.0 nm. The time-per-point (sampling integration time) was set

to 1.0 second. The output signal was recorded in millidegrees (mdeg). A corresponding buffer baseline spectrum was recorded under identical conditions (using the same cuvette and parameters) and was subtracted from each sample spectrum during data processing. Secondary structure content (α-helix, β-sheet, random coil, etc.) was estimated from the processed far-UV CD spectra using the deconvolution program CDSSTR, accessible via the DichroWeb server.

2.2.5.2 Mass Spectrometry

Measurements were performed in house by facility staff as a commercial service. Protein desalting and mass analysis was performed by LC-MS using an M-class ACQUITY UPLC (Waters UK, Manchester, UK) interfaced to a Xevo QToF G2-XS mass spectrometer (Waters UK, Manchester, UK). Samples were diluted to 1µM using 0.1% TFA. 1 µL of the 1 µM sample was run on an Acquity UPLC Protein BEH C4 column (300 Å, 1.7 µm, 2.1 mm × 100 mm, Waters UK) with an Acquity UPLC Protein BEH VanGuard Pre-Column (300 Å, 1.7 µm, 2.1 mm × 5 mm, Waters UK). Buffer A was 0.1% formic acid in water, and buffer B was 0.1% formic acid in AcN (v/v basis). System flowrate was kept constant at 50 µl/min. Protein sample was loaded on to the trap column in 20% acetonitrile/0.1% formic acid and washed for 5 min. Following valve switching, the bound protein was eluted by a gradient of 20-95% solvent B in A over 10 min. The column was subsequently washed with 95 % solvent B in A for 5 min before re-equilibration at 20% solvent B in A ready for the next injection. The mass spectrometer was calibrated using a separate injection of glu-fibrinopeptide. Data were processed using MassLynx 4.2.

2.2.5.3 Validation of catalytically competent PBP2a

Acylation of the catalytic serine by β-lactams converts nitrocefin to its ring-opened chromophore, yielding a time-dependent increase in absorbance near 500 nm, serving as a simple assay to determine if purified PBP2a was catalytically competent. The acylation of the active site serine (S403) of PBP2a, wherein the acyl-enzyme species undergoes slow deacylation, is described as follows:

$$PBP + \text{ß-lactam} \overset{K_M}{\leftrightarrows} \underset{\text{[Michaelis complex]}}{\text{PBP} \cdot \text{ß-lactam}} \overset{k_2}{\longrightarrow} \underset{\text{[acyl-enzyme]}}{\text{PBP} - \text{ß-lactam}} \overset{k_3}{\underset{H_2O}{\longrightarrow}} \underset{\text{[hydrolysed]}}{\text{PBP} + \text{ß-lactam}}$$

where E represents PBP2a, EI is the noncovalent preacylation complex, and E-I is the covalent acyl-enzyme species. Acylation rates (k2) were determined by monitoring the change in absorbance at 500 nm for 45 minutes using nitrocefin as a reporter molecule, as previously described[149].

Reactions (300 µL) were assembled in clear 96-well plates in 25 mM HEPES, 1.0 M NaCl, pH 7.0 at 37°C. The optical density at 500 nm was measured immediately at time 0 and then approximately every 60 s for 45 min using a FLUOstar Omega microplate reader (BMG Labtech, UK). The PBP2a concentration (20 µM) was kept constant across conditions (matching the nitrocefin-only control), while nitrocefin was assayed at 20, 50, 100 and 200 µM. Control wells contained PBP2a without nitrocefin (in buffer; Table 4– Native Buffer), nitrocefin without enzyme (in buffer; Table 4 – Native Buffer), or buffer alone.

Time-dependent A_{500} traces (nitrocefin) were corrected by subtracting dye-only and buffer-only controls. Initial rates (v_0) were computed as the average per-minute increase over the first 8-12 min using Microsoft Excel, reported in mOD/min. PBP2a was considered catalytically competent if rates increased monotonically with enzyme concentration, and where controls remained flat.

2.2.5.4 NMR spectroscopy

Unless otherwise stated, all NMR spectroscopy was conducted in NMR Buffer (Table 4). All data were initially processed in NMRPipe[150] or TopSpin 3.5 prior to assignment and visualised using CCPN Analysis[151], often using NMRbox[152].

2.2.5.4.1 1H-15N HSQC

Uniformly ^{2}H-^{13}C-^{15}N-labelled PBP2a was prepared as above and exchanged into NMR buffer (Table 4) at 300 µM using a 30 000 MWCO centrifugal concentrator. 2D ^{1}H-^{15}N correlation spectra were recorded for PBP2a using a 950 MHz Ascend Aeon™ NMR spectrometer (Bruker, United States) fitted with a 5 mm TXO-cryoprobe or a 3 mm TCI-cryoprobe at 25-30°C. A TROSY-HSQC pulse program[153] using Echo-Antiecho gradient selection with sensitivity enhancement was used.

2.2.5.4.2 1H-13C HMQC

For methyl spectra, 2D ^{1}H-^{13}C correlation spectra were recorded for 300 µM uniformly ^{2}H-^{13}C-^{15}N-labelled PBP2a using a 950 MHz Ascend Aeon™ NMR Spectrometer (Bruker, United States) fitted with a 5 mm TXO-cryoprobe. An IBS C SOFAST- HMQC pulse program[46] with decoupling during acquisition was used. For Ile mutants used for assignment via selective mutagenesis, only δ1 methyls of Ile side chains were ^{1}H,^{13}C,^{15}N-labelled, with remaining PBP2a residues labelled as ^{2}H-^{12}C-^{15}N. These experiments were conducted at 15ºC (mutagenesis experiments) or 25ºC on a 950 MHz Ascend Aeon™ NMR spectrometer (Bruker, United States) fitted with a 3 mm TCI-cryoprobe using a protein concentration of 100-300 µM.

2.2.5.4.3 Titration of de novo protein binders and antibiotic ligands

For chemical shift perturbation (CSPs) analyses of both *de novo* designed protein binders and antibiotic ligands, a baseline 2D ^{1}H-^{13}C correlation spectrum of 20-110 µM PBP2a with only δ1 methyl of Ile side chains labelled with ^{1}H-^{13}C-^{15}N (as above) using an IBS C SOFAST- HMQC pulse program[154] with decoupling was acquired at 15ºC. Following which, spectra for each increasing concentration of protein binder or antibiotic were sequentially acquired at 0.5-5.0 times the molar ratio of PBP2a. Data were processed in NMRPipe before measurement of CSPs[155] by CCPN Analysis 3.2.2[151]. CSPs were calculated as the weighted Euclidean distance for methyl correlations,

$$\Delta\delta_w = \sqrt{(\Delta\delta_{1H})^2 + (0.25\,\Delta\delta_{13C})^2}$$

where $\Delta\delta^{1}$H and $\Delta\delta^{13}$C are the changes in ppm relative to the reference spectrum, with weighting for the nucleus type as follows (H = 1.0, C = 0.25)[151]. CSPs were considered significant if the CSP was greater than 1 standard deviation (SD) of the average CSP for all residues. Kds of interactions were determined by fitting curves of CSP vs ligand concentration for residues showing significant (>1SD) CSPs to the following equation:

$$Y = B_{max}\frac{\left(T + x + K_d - \sqrt{(T + x + K_d)^2 - 4T_x}\right)}{2T}$$

Where Y represents the observed binding response at a given ligand concentration, B_{max} is the maximum binding amplitude, T is the total protein concentration (µM), x is the total

ligand concentration (μM), and K_d is the apparent dissociation constant describing the equilibrium between bound and free states.

2.2.5.4.4 TROSY-HNCO

Uniformly ^{2}H-^{13}C-^{15}N-labelled PBP2a (300 μM) was prepared as above and exchanged into NMR buffer (Table 4). Samples (300 μM) were used to record spectra at 30°C on a 950 MHz Bruker Ascend Aeon™ equipped with a 5 mm TXO cryoprobe. A gradient-selected, water-flip-back TROSY-HNCO (no ^{15}N decoupling during acquisition) was used to correlate H^N/N(*i*) with C'(*i*$^{-1}$), providing directional sequential anchors and well-dispersed carbonyl shifts for initiating backbone walks. Non-uniform sampling (NUS) was used was used throughout all 3D experiments at 21% unless otherwise specified and processed with IST/SMILE reconstruction in NMRPipe.

2.2.5.4.5 TROSY-HNCA

To observe Cα(*i*) together with weaker Cα(*i*$^{-1}$) correlations from each amide, a gradient-selected, water-flip-back TROSY-HNCA was acquired using uniformly ^{2}H-^{13}C-^{15}N-labelled PBP2a (300 μM). Spectra were recorded at 30°C on a 950 MHz Bruker Ascend Aeon™ equipped with a 5 mm TXO cryoprobe.

2.2.5.4.6 TROSY-HNCA(CO)

To isolate the sequential Cα(*i*$^{-1}$) pathway and suppress intra-residue Cα(*i*), TROSY-HNCA(CO) spectra were recorded with ^{2}H-^{13}C-^{15}N-labelled PBP2a (300 μM). Spectra were recorded at 30°C on a 950 MHz Bruker Ascend Aeon™ equipped with a 5 mm TXO cryoprobe.

2.2.5.4.7 TROSY-HNCACB

TROSY-HNCACB spectra (gradient selection, water flip-back, broadband ^{13}C decoupling during acquisition as per implementation) were acquired with ^{2}H-^{13}C-^{15}N-labelled PBP2a (300 μM) to correlate H^N/N with Cα/Cβ(*i*) and Cα/Cβ(*i*-1), enabling residue-type discrimination and confirmation of sequential connectivities when combined with HNCA/HNCA(CO). Spectra were recorded at 30°C on a 950 MHz Bruker Ascend Aeon™ equipped with a 5 mm TXO cryoprobe. Uniform sampling was used throughout, and data were processed in NMRPipe[150] prior to analysis using CCPN Analysis 3.2.2[151].

2.2.5.4.8 NOESY

Samples were U-^{2}H, U-^{15}N with selective $^{13}CH_3$-^{1}H labelling of Ile δ1, Leu/Val γ CH_3 and Ala β, exchanged into the NMR buffer (Table 4). Spectra were acquired at 30ºC on a 950 MHz Bruker Ascend Aeon™ equipped with a 3 mm TCI cryoprobe. A gradient-selected 3D ^{13}C-edited NOESY-^{1}H-^{13}C HSQC optimised for aliphatic methyls was used to detect methyl-methyl NOEs suitable for topology-based assignment with MAGMA/MAGIC[156,157]. Non-uniform sampling (NUS) at 40% (Poisson-gap schedule) was employed to limit experiment time. Data were initially processed in NMRPipe[150] using IST reconstruction prior to analysis in CCPN Analysis 3.2.2[151].

2.2.5.4.9 CPMG

Methyl ^{1}H-^{13}C multi-quantum CPMG relaxation-dispersion experiments were recorded at 15ºC on a 950 MHz Bruker Ascend Aeon™ equipped with a 3 mm TCI cryoprobe using the pulse program of Korzhnevet al.[117]. ~110 µM PBP2a with U-2H, U-15N with selective 13CH3-1H labelling of Ile were used. Spectra were recorded with a T2 mixing time of 24 ms and CPMG field strengths (ν_{CPMG} frequencies) of 62.5, 83.3 (repeated), 166.7, 333.3, 666.7 and 1000 Hz. Errors were estimated from variation between repeated data points. Uncertainties in $R_{2,eff}$ were estimated from the duplicate ν_{CPMG} measurement.

Spectra were processed using nmrPipe and peak heights integrated in CCPN Analysis 3.2.2. For each methyl resonance, the effective transverse relaxation rate was computed as:

$$R_{2,eff}(\nu_{CPMG}) = -\frac{1}{T}\ln\left(\frac{I(\nu_{CPMG})}{I_{ref}}\right),$$

with T = 24 ms and I_{ref} the intensity from an interleaved reference acquired without the CPMG refocusing train. Methyl groups were classified as showing dispersion when ΔR2eff = $\max R_{2,eff} - \min R_{2,eff} \geq 1$ s-1 across the ν_{CPMG} series. Peaks that were overlapped were excluded from analysis.

Chapter 3 Assignment of PBP2a by NMR spectroscopy

3.1 Abstract

This chapter outlines the progressive development of a nuclear magnetic resonance (NMR) framework to obtain a partial resonance assignment of the ~76 kDa penicillin-binding protein 2a (PBP2a) from methicillin-resistant *Staphylococcus aureus*, a key determinant of methicillin resistance[4]. The overarching aim was to establish residue-level probes to enable future investigation of allosteric regulation and ligand binding within this large, multi-domain enzyme.

Initial efforts focused on amide-detected triple-resonance experiments to pursue full backbone assignment. Although 2D TROSY-HSQC spectra demonstrated good folding and dispersion, higher-dimensional datasets suffered from progressive signal loss due to rapid transverse relaxation, limited sample stability, and intrinsic conformational exchange. Even after extensive optimisation of buffer composition, temperature, and ionic strength, full backbone assignment proved experimentally unfeasible.

Accordingly, the workflow transitioned to a methyl-detection strategy, exploiting the slower relaxation and superior sensitivity of ILVA methyl groups. Selective $^{13}CH_3$-labelling produced well-resolved spectra suitable for downstream analysis, but non-uniform sampling-assisted methyl-NOESY experiments failed to yield sufficient long-range cross-peaks for automated assignment. A site-directed mutagenesis approach was subsequently implemented to assign 34 Ile>Gly mutants strategically distributed across the PBP2a structure. Comparison of wild-type and mutant HMQC spectra enabled confident identification of 23 individual isoleucine resonances, achieving a distributed partial assignment encompassing all major domains.

This integrated approach demonstrates that while amide-based strategies are impractical for PBP2a, combining selective methyl labelling with targeted mutagenic validation provides a robust and tractable means of establishing residue-specific probes. These residues provide a robust experimental foundation for subsequent chemical-shift perturbation and relaxation analyses aimed at furthering detailing the molecular basis of allostery, catalysis, and β-lactam resistance in PBP2a.

3.2 Introduction

High-resolution structural biology depends fundamentally on the availability of sufficient quantities of homogeneous, stable, and isotopically appropriate protein. Regardless of method – be it X-ray crystallography, cryo-electron microscopy, or nuclear magnetic resonance (NMR) – the underlying requirements are universal: the protein must be pure, correctly folded, and conformationally stable under experimental conditions[158]. To generate interpretable NMR spectra, the sample must remain soluble and monodisperse at high concentrations (typically 0.1-1 mM), resist aggregation over the course of long acquisitions, and be free of contaminating species that would obscure resonances or cause line broadening[158,159]. NMR uniquely provides atom-specific, solution-state information, but to do so each resonance observed in the spectrum must be unambiguously linked to a specific nucleus within the protein – the process known as assignment[109,160,161]. Without this, chemical shifts are anonymous signals rather than molecular reporters. Thus, every step of NMR sample preparation – from construct design and isotopic labelling to purification and buffer formulation – exists to meet the simple but demanding goal of obtaining pure, plentiful, stable, and interpretable protein.

NMR relies on the magnetic properties of nuclei such as ^{1}H, ^{13}C, and ^{15}N. Because the natural abundance of ^{13}C (1.1%) and ^{15}N (0.37%) is too low for efficient detection, isotopic enrichment is essential. Uniform labelling with ^{13}C and ^{15}N in minimal media enables the acquisition of heteronuclear correlation spectra (e.g. HSQC, HNCO, HNCA) that form the basis of resonance assignment by amide backbones[95,146]. However, as molecular size increases, transverse relaxation and dipolar coupling broaden resonances, dramatically reducing both sensitivity and resolution[160,162]. To mitigate this, proteins are typically expressed in perdeuterated (U-^{2}H) media, replacing most ^{1}H atoms with ^{2}H to decrease dipolar relaxation and extend transverse relaxation times (T_2)[163]. However, although perdeuteration is critical for large proteins, its implementation is non-trivial. Growth in D_2O minimal media introduces kinetic isotope effects that slow enzymatic rates, alter macromolecular assembly, and increase cellular stress[164]. As such, bacteria used for the routine production of recombinant proteins such as *E. coli* must adapt to the use of deuterated metabolites, which can impair translation and protein folding, resulting in reduced yield and solubility[164]. Stepwise adaptation or "grow-exchange" protocols are often required to sustain healthy growth and maintain correct folding in deuterated systems, wherein expression hosts

are progressively adapted by subculturing in defined media with progressive increases in deuterium content[146]. Additionally, expression challenges are compounded when point mutants are introduced – either for selective labelling (e.g. ILV methyl systems) or for mutagenesis-based assignment – by the additional biosynthetic and folding burden each substitution imposes on cells already stressed with suboptimal substrates[111,160]. These combined effects often make expression optimisation for perdeuterated samples one of the most time- and resource-intensive stages of NMR study, particularly for large, multi-domain proteins such as PBP2a.

This enables the use of TROSY (transverse relaxation-optimised spectroscopy), which selectively retains the slowly relaxing component of coupled multiplets, providing sharper, more sensitive peaks for high-molecular-weight systems[110,153]. For small and moderately sized proteins (<30 kDa), standard triple-resonance experiments (HNCO, HNCA, HNCACB, HN(CA)CO, etc.) typically allow complete backbone assignment by correlating amide protons to adjacent carbonyl and α/β carbons through scalar couplings. When molecular weight exceeds ~40 kDa, however, amide resonances become broad and weak despite TROSY optimisation, and spectral crowding renders assignment by amide backbones alone intractable[109,160,161]. These data can often be supplemented with NOESY (Nuclear Overhauser Effect Spectroscopy) experiments to map through-space correlations to compliment amide backbone experiments however, for many systems, this is still insufficient[153]. Several alternative approaches have been developed to address the size bottleneck of large proteins that are persistently challenging. Methyl-TROSY spectroscopy, uses selectively protonated methyl groups ($^{13}CH_3$) in a perdeuterated background, dramatically improving the sensitivity and resolution for large systems. Automated NOE-based assignment tools such as MAGMA[156], MAGIC[157], and MAP-XSII[165] which can extract side-chain connectivity patterns from NOESY data to map methyl resonances to structure when coordinated with existing crystal structures. Finally, assignment by selective mutagenesis of specific residues – typically Ile, Leu, Val, Ala, Met and Thr– and provides a pragmatic route when backbone or automated strategies fail, wherein individual residue substitutions, deletions, or selective unlabelling produce diagnostic chemical-shift changes, revealing the identity of specific resonances[146].

Penicillin-binding protein 2a (PBP2a) of Staphylococcus aureus is an especially demanding NMR target. It is a large (>76 kDa), multi-domain, and conformationally dynamic protein,

containing a transpeptidase (TP) domain, an allosteric regulatory domain (AD), and an N-terminal extension (NTE) connected by flexible inter-domain linkers[4-7], where line broadening and dynamic exchange are expected to add significant challenge to traditional amide detection methods. These structural features are essential for its function, wherein ligand activation of the AD induces long-range rearrangements that open the TP domain to fulfil its native function (transpeptidation of peptidoglycan) or antibiotic binding[5-7]. PBP2a's highly complex fold with highly interrelated domains (Figure 8) would likely render it susceptible to unfolding and/or disrupted inter-domain coupling if attempted to study its domains in isolation, rendering them non-representative of the native enzyme. Additionally, the functional loops (α_2-α_3 and β_3-β_4) of the TP domain and several regions within the AD and NTE have been predicted to have high intrinsic and conformation-dependent dynamics[89]. As such, pronounced μs-ms exchange motions likely add further challenge for assignment by further compounding spectral complexity, limiting the viability of uniform backbone assignment strategies.

To overcome these inherent limitations, a selective methyl-labelling strategy was implemented. PBP2a was expressed in *E. coli* using a perdeuterated, uniformly ^{12}C-labelled background with selective $^{13}CH_3$-^{1}H labelling at Ile δ_1 methyl positions, introduced via α-ketoacid precursors. This approach retains high sensitivity while suppressing unwanted proton relaxation pathways, enabling observation of sharp, well-resolved methyl-TROSY spectra even for a >76 kDa system. Complete assignment of all methyl resonances in a protein of this size is often unachievable. Instead, we pursued a tactically designed partial assignment, selecting isoleucine residues that (i) were structurally dispersed across the NTE, AD, and TP domains; (ii) lay near predicted functional interfaces; and (iii) could be uniquely verified through targeted mutagenesis and cross-referencing with structural models. This targeted approach provided a set of well-distributed probes suitable for quantitative analysis of ligand binding (chemical-shift perturbations, CSPs), conformational exchange (methyl-CPMG), and inter-domain coupling effects to overcome the intractable requirements of assignment by backbone amides. This work establishes a practical platform for probing the molecular mechanisms of allostery, catalysis, and antibiotic resistance in PBP2a at residue-level resolution.

3.3 Aims

The objective of this chapter is to establish a reliable, residue-specific NMR framework suitable for probing the structure, dynamics, and ligand interactions of PBP2a in solution. Achieving this required overcoming the considerable technical challenges posed by the size, multi-domain organisation, and intrinsic flexibility of the protein.

Specifically, this chapter aims to:

Aim 1 – Optimise isotopic labelling and expression of PBP2a for solution-state NMR

To generate perdeuterated, ^{15}N-labelled, and selectively $^{13}CH_3$-^{1}H methyl-labelled samples of PBP2a that were correctly folded, stable, and of sufficient yield and purity for high-field NMR spectroscopy.

Aim 2 – Acquire and process high-quality NMR spectra for assignment

To record TROSY-based correlation spectra suitable for large molecular systems, assess spectral quality, and determine experimental conditions (field strength, temperature, buffer composition) that maximised signal dispersion and stability.

Aim 3 – Obtain a partial residue-level assignment of PBP2a using a targeted strategy

To employ a combination of selective isotope labelling, targeted site-directed mutagenesis, and structure-guided inference to identify a strategically distributed subset of isoleucine δ_1 resonances across the N-terminal, allosteric, and transpeptidase domains.

Aim 4 – Establish a probe set for downstream mechanistic studies

To define a validated set of residue-specific methyl reporters capable of detecting local and long-range structural changes, forming the basis for subsequent chemical-shift perturbation and relaxation-dispersion experiments in later chapters.

Broadly, this chapter aims to generate a robust, information-rich partial assignment that enables the dynamic and functional analyses necessary to further understand the molecular mechanisms of β-lactam resistance in PBP2a.

3.4 Results & Discussion

3.4.1 Expression and purification of isotopically labelled PBP2a for NMR study

3.4.1.1 Expression in Rich Media

Expression in LB media was used to validate the initial expression of recombinant proteins in *E.coli*. The expression of PBP2a from Rosetta^{TM}(DE3) *E.coli* transformed with the pET-28a(+)$_{PBP2a}$ construct under different temperatures (16ºC and 25ºC) and IPTG concentrations (0.4 mM and 1.0 mM) was evaluated (Figure 15):

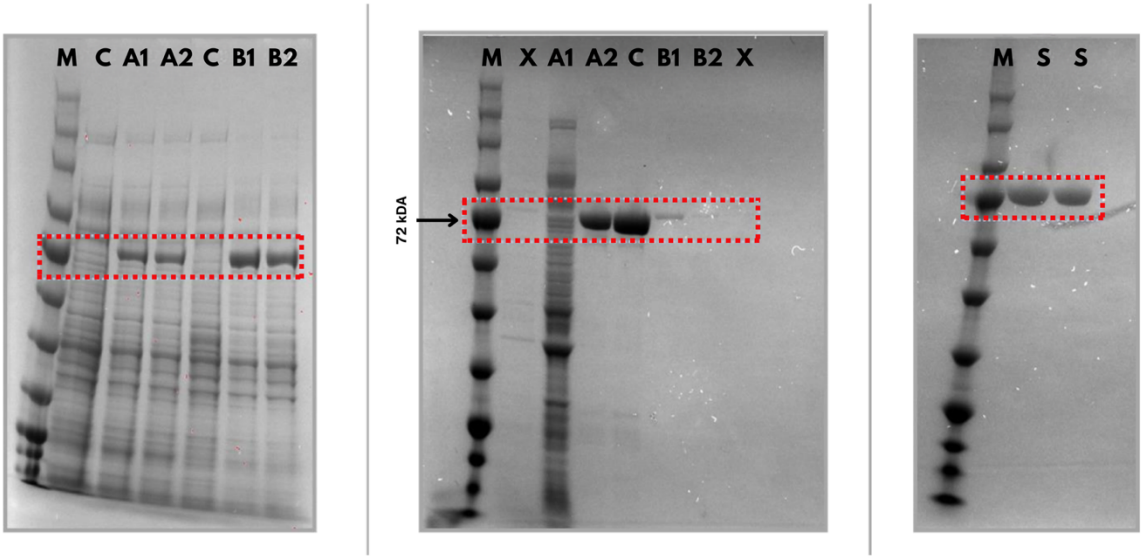

Figure 15: Expression and purification of PBP2a in rich media

Left: small scale **(5 mL)** expression in LB media **for 20 hours**. M: 11-250 kDa protein standard**. C**: uninduced control**, A1:** induced with 0.4 mM IPTG at 16ºC, **A2**: induced with 1.0 mM IPTG at 16ºC, **B1**: induced with 0.4 mM IPTG at 25ºC, **B2**: induced with 1.0 mM IPTG at 25ºC. Middle: Ni-NTA purification of large-scale expression in LB media. M: 11-250 kDa protein standard**.** E: elution fractions, **X**: empty lane. Right: PBP2a purified by size exclusion chromatography (SEC). Expected migration region for PBP2a **(~76.5 kDa)** highlighted by the **red** box.

Expression at 25ºC significantly increased levels of PBP2a expression, whereas no significant difference in expression was noted between *E. coli* induced with 0.4 mM and 1.0 mM IPTG, yielding 2000 µL of 300 µM purified PBP2a following purification via Ni-NTA and size exclusion chromatography.

3.4.1.2 Expression in Protonated Defined Media

Defined media sources are necessary for the expression of proteins for investigation by NMR spectroscopy due to the allowing of the selective incorporation of isotopes via specialised media components such as glucose containing only ^{13}C or ammonium chloride containing only ^{15}N, both of which have a very low natural abundance.

Yields from initial attempts to express PBP2a in protonated M9 media ($^{12}C/^{14}N$) using the conditions deemed suitable for rich media were impractically low to justify large scale production of deuterated and isotopically labelled protein. As such, additional optimisations were explored including temperature (16°C and 25°C), IPTG concentration (0.05, 0.1, 0.4, 0.7 and 1.0 mM), induction length (16, 18, 20, 24, 28, 30, 32 and 48 hours), culture saturation (OD_{600} of 0.6, 0.8 and 1.0) and glucose concentration (0.5, 1.0, 1.5, 2.0, 3.0 and 4.0 g/L), as well as alternative *E. coli* expression hosts (BL21- Star(DE3), BL21-Gold(DE3), BL21-Rosetta^{TM}2(DE3)$_{pLysS}$ and BL21-CodonPlus(DE3)-RIL *E. coli*) in addition to Rosetta^{TM}(DE3). Optimised conditions for the expression of PBP2a from each strain transformed with the pET-28a(+)$_{PBP2a}$ were as follows (Figure 16):

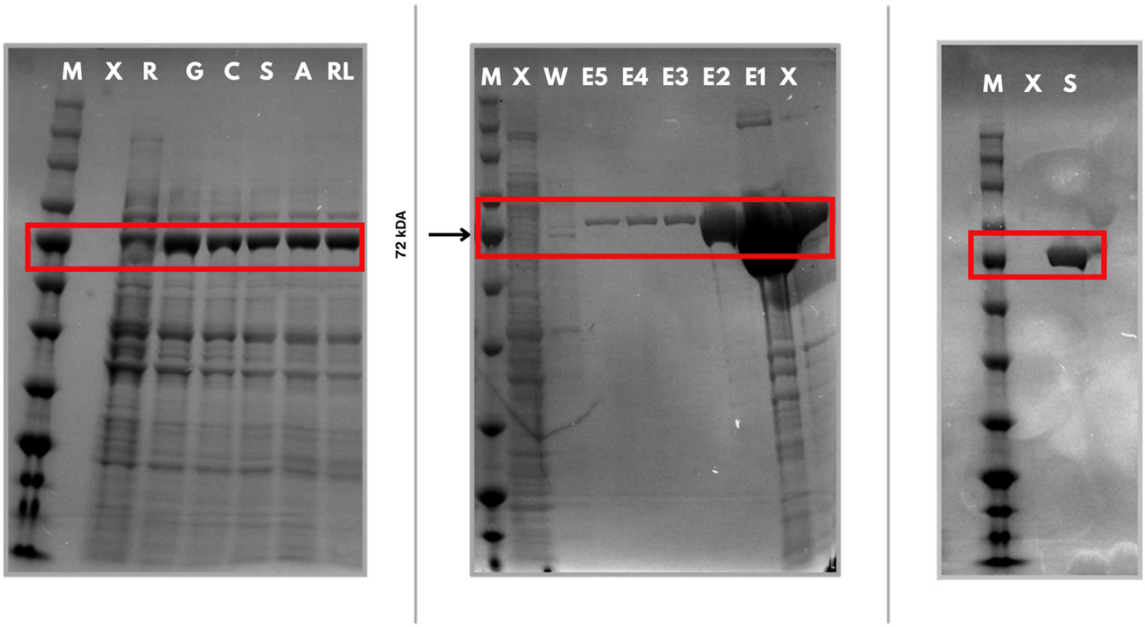

Figure 16: **Expression and purification of PBP2a in protonated, defined media**

Left: small scale expression in M9 media in different *E. coli* strains. x: empty lane, R: Rosetta(DE3), G: BL21(DE3)-Gold, C: BL21(DE3)-CodonPlus-RIPL, S: BL21(DE3)-Star, A: BL21(DE3)-ArcticExpress, RL: Rosetta- pLysS. Middle: Ni-NTA purification of large scale expression in M9 media. F: flow through, W: wash fractions, E: elution fractions, X: empty lane. Right: PBP2a purified by size exclusion chromatography (SEC). Expected migration region for PBP2a highlighted by the red box. M: 11-250 kDa protein standard.

Expression of PBP2a at 25°C for 24 hours, induced with 1.0 mM IPTG, in M9 medium containing 4.0 g/L glucose, in all strains but Rosetta™(DE3) yielded the best – comparative with one another – results. No significant difference in PBP2a expression levels were noted when expression was induced at optical densities of 0.6, 0.8 or 1.0. For convenience, BL21-Star(DE3) was selected to proceed for deuterated expression.

3.4.2 Validation of kinetically active PBP2a

3.4.2.1 Mass spectrometry

The identity of PBP2a was verified by accurate mass measurement by LC-MS via the mass spectrometry facility at The University of Leeds (Figure 17):

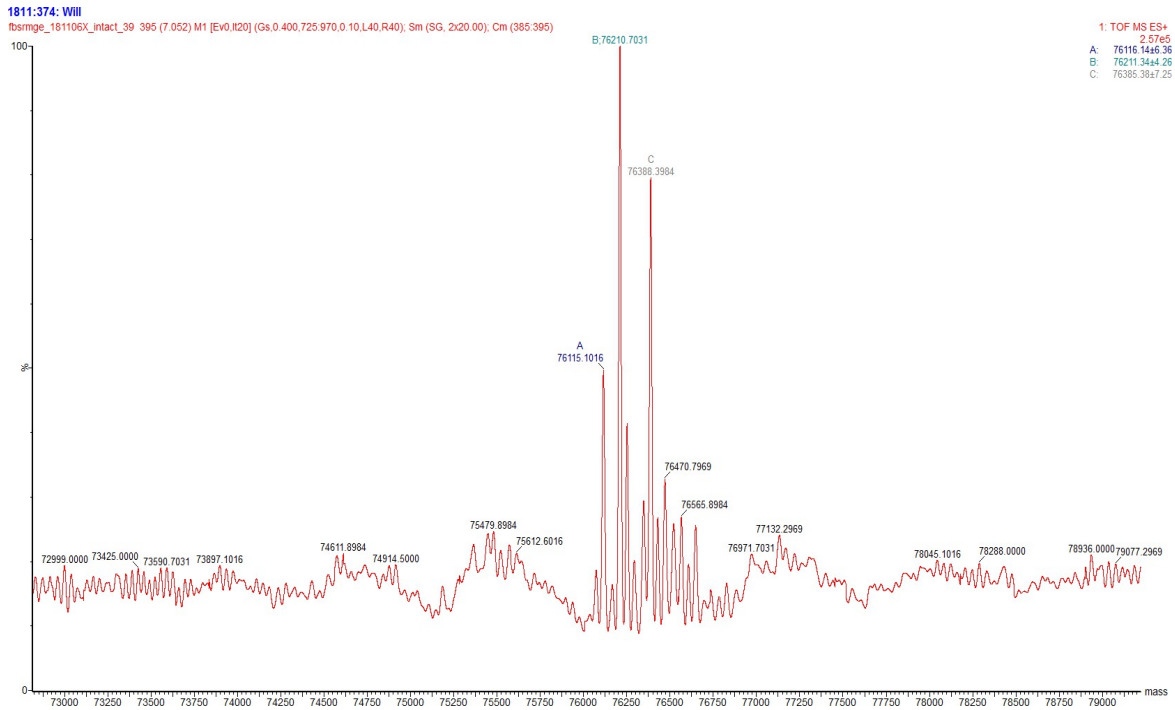

Figure 17: Intact-mass ESI–QTOF of ΔTM PBP2a from PBP2a$_{pET28a}$ (Synapt HDMS).

The deconvoluted mass spectrum confirmed the expected molecular weight of the intact ΔTM (residues 1-22) PBP2a-His$_{10}$ construct acquired on a Synapt HDMS (Q-TOF) under denaturing conditions. A dominant peak is evident at ~76.76 kDa (B), with neighbouring lower-intensity species at ~76.39 kDa (C) and ~76.12 kDa (A), with a series of small shoulders.

The predicted mass of His$_{10}$-tagged PBP2a with the N-terminal membrane anchor removed is 76 537.36 Da[166] where Figure 17 suggests the dominant species (A-C) are reflective of intact, monomeric PBP2a. The small differences between the theoretical predicted molecular mass in the dominant and satellite species are consistent with expected minor proteoforms and/or adduct heterogeneity (e.g. Na^+/K^+, buffer/imidazole), limited N/C-terminal micro-processing, or in-source loss of labile adducts. The -149 Da smaller 76 388 Da species (C)

may correspond to PBP2a minus its N-terminal methionine residue, a modification which commonly occurs in recombinant proteins produced in *E. coli* explained by the activities of endogenous *E. coli* methionine aminopeptidase[167]. The 76 210 Da species (B) may correspond to PBP2a subject to both N-terminal methionine cleavage as well as the loss of its C-terminal glutamic acid by nucleophilic attack on the adjacent residue carbonyl carbon via the C-terminal or side chain carboxylate group of the C-terminal glutamic acid residue[168]. The absence of higher-mass envelopes indicates the sample is predominantly monomeric and that the construct is suitable for continuation for further study.

3.4.2.2 Circular dichroism

Far-UV circular dichroism (CD) spectra were acquired for PBP2a (Figure 18) to assess secondary structure content and solution integrity under similar conditions to those used for downstream biophysical characterisation. Samples were prepared in CD Buffer (Table 4 – which uses Na_2SO_4 instead of NaCl to avoid noise artefacts) and measured in a 1 mm quartz cuvette at 3 µM, with spectra recorded over 180–260 nm on a Chirascan spectropolarimeter (Applied Photophysics) at 25°C. A matched buffer baseline was collected and subtracted prior to averaging (Figure 18).

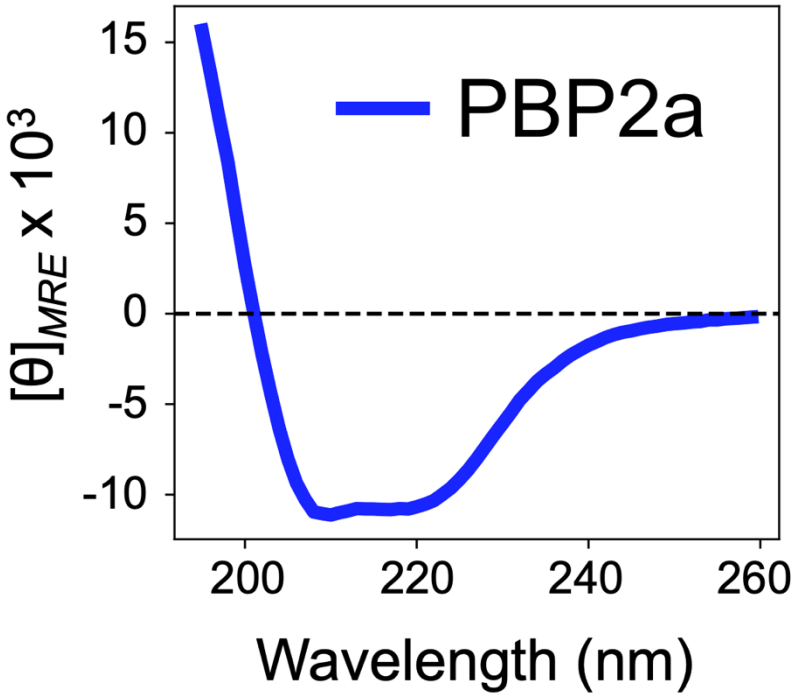

Figure 18: **Far-UV circular dichroism spectra of PBP2a (0.2 mg·mL⁻¹; ~2.6 µM; 1.0-mm pathlength) in CD Buffer**.

The dominant ~210-nm negative band with only a weak 222-nm shoulder is consistent with the expected secondary character – a β-enriched α-helical dominant mixed secondary structure – of PBP2a, suggesting a well-folded protein.

The line shape is consistent with a protein that is not predominantly α-helical (which would show well-resolved 208/222-nm double minima) but instead contains a substantial proportion of β-sheet and/or β-rich/heterogeneous secondary structure, in agreement with the known mixed architecture of PBP2a. Qualitative inspection suggests the protein is correctly folded in the CD Buffer, as no features characteristic of fully disordered polypeptide (strong ~198-nm minimum, near-zero long-wavelength ellipticity) are observed. Collectively, the CD data support that PBP2a retained its expected conformation and that similar buffer conditions were suitable for subsequent experiments.

3.4.2.3 PBP2a kinetic activity assay

To verify that purified PBP2a was active in the buffer conditions which further experiments were conducted, 20, 50, 100 and 200 µM of the chromogenic cephalosporin nitrocefin were incubated with PBP2a (2.5 µM) and the change absorbance at 500 nm monitored over 45 minutes (Figure 19) which occurs following the opening of the β-lactam ring of nitrocefin during the formation of the acyl-PBP intermediate[149]:

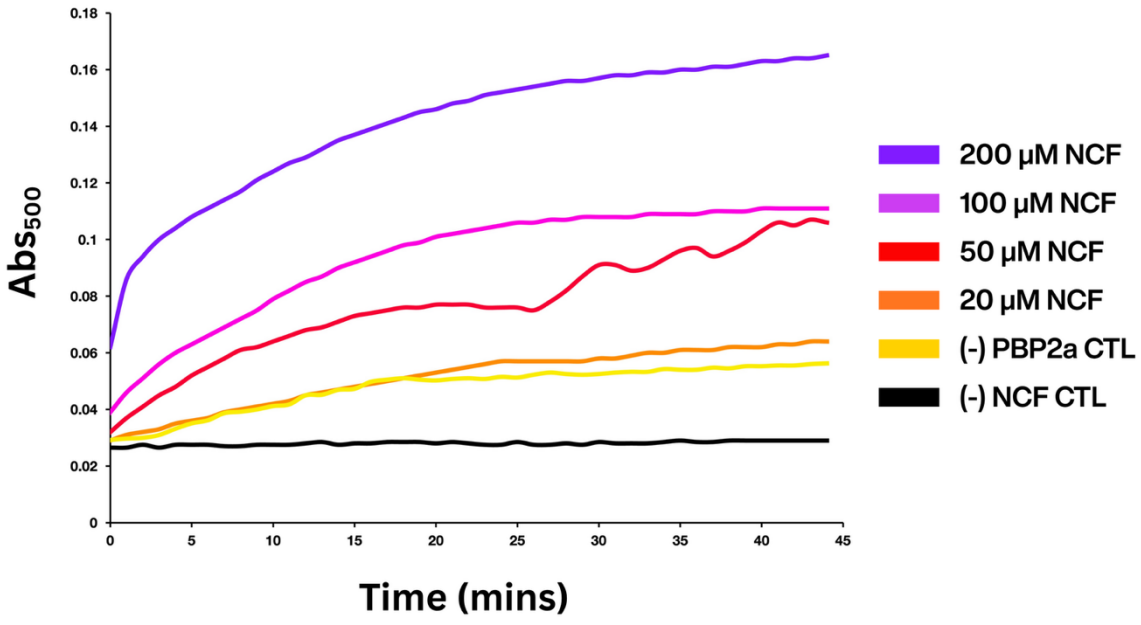

Figure 19: Binding kinetics of PBP2a and the chromogenic β-lactam antibiotic nitrocefin.

The change in absorbance at 500 nm reflects the rate of formation of an acyl-enzyme intermediate in PBP2a (2.5 µM) transpeptidase domain following acylation by varying concentrations of nitrocefin (NCF – coloured lines). Control samples contained buffer in the absence of PBP2a (yellow) and absence of nitrocefin (black) respectively.

Progressive increases in acylation rate were observed for each nitrocefin concentration with hyperbolic curves consistent with expected Michaelis-Menton kinetics observed, displaying a progressive increase in acyl-PBP2a complex formation, suggestive of an active protein.

3.4.3 Expression in Deuterated Defined Media

Initial attempts to express PBP2a from BL21-Star(DE3) *E. coli* in deuterated M9 media labelled with ^{13}C and ^{15}N isotopes ($M9^{D}$) using the conditions optimised for (unlabelled) defined media expression were unsatisfactory. As such, BL21-Star(DE3) transformed with $pET28a_{PBP2a}$ was acclimated to deuterated M9 media by successive subculture on a series of M9 agar comprised of progressively increasing proportions of deuterium content (30, 50, 70 and 100 %). It was surmised that the earlier phases of the stepwise adaptation procedure (10 % to 50 %) may have been too steep for sufficient adaptation. To validate potential deleterious effects of background basal expression of PBP2a on cell viability, Rosetta^{TM}(DE3)pLysS was selected for further investigations. pLysS strains reduce basal expression of recombinant proteins via the inhibition of basal levels of T7 RNA polymerase by the constitutive expression of low levels of T7 lysozyme; stabilising pET expression hosts encoding target proteins with a deleterious impact on cell growth and viability[169,170]. Expression in RosettaTM(DE3)pLysS was trialled in each of the conditions investigated for existing expression hosts as per 3.4.1.2. Small scale expression trials noted substantial variability in expression levels, however large-scale expression trials did not result in yields practical for further NMR study. The incorporation of isotopically-labelled (^{13}C and ^{15}N) and deuterated Celtone Complete Medium (10% v/v) (Cambridge Isotope Laboratories Inc., United States of America) – a commercially-available rich bacterial growth medium derived from algal sources reported to facilitate growth rates and protein expression yields comparable to LB media – was next trialled. However, while the inclusion of Celtone improved growth rates substantially, no improvements in expression yields were observed in either RosettaTM(DE3)pLysS or BL21-Star(DE3). Further work was continued in BL21-Star(DE3) strains to minimise any unnecessary potential toxicity from antibiotic burden, due to RosettaTM(DE3)pLysS pRARE plasmid requiring chloramphenicol for selection.

Work by Cai and colleagues[171]. employing a novel adaptation and expression protocol, utilising rich (LB) media in the primary phases of adaptation to deuterated conditions followed by adaptation to partially and fully deuterated defined (M9) media, was trialled. This procedure employed a modified M9 salt ('M9+') stock to facilitate the culture of expression hosts at high densities (OD_{600} ~20.0) prior to induction, with published data evidencing a tenfold increase in protein expression for an equivalent volume of deuterated growth media used with conventional expression procedures. However, no significant

improvements in PBP2a expression were observed. In *E. coli*, growth in deuterated media (D_2O) slows growth and reduces the glucose consumption rate during exponential phase[172,173], plausibly leaving higher residual extracellular glucose prior to induction. Elevated glucose maintains glucose-mediated repression of the lac system predominantly via inducer exclusion – dephosphorylated EIIA(Glc) inhibition of LacY and subsequent reduction of IPTG uptake - thereby sustaining LacI repression at both the chromosomal lacUV5-controlled T7 RNAP locus and the T7-lac promoter on pET-28aPBP2a[174,175]. To test whether LacI-mediated repression of *mecA* limiting recombinant protein expression, all expression trials in deuterated M9 media were repeated with lower (2 g/L and 3 g/L) glucose concentrations. A direct correlation between glucose concentration and PBP2a expression was observed, mirroring our results in protonated M9 medium. Given that longer induction times are often required for robust expression in deuterated media, induction lengths of 24, 28, 30, 32, 36, and 40 h were evaluated. Like previous investigations in protonated M9 media, substantial differences in PBP2a expression levels were noted at different induction lengths, wherein 30 to 32 hours presented the best performance.

Further efforts to evaluate the potential loss of plasmid during adaptation to deuterated conditions, where BL21-Star(DE3) competent cells were progressively adapted to deuterated conditions (as previously mentioned) prior to transformation with the pET-28a(+)PBP2a plasmid. Cells adapted in this manner cultured effectively in kanamycin-containing deuterated growth media selecting for pET-28a(+)PBP2a however, with no discernible improvements in PBP2a expression in small or large scale deuterated M9 media. Additionally, expression of PBP2a in BL21-Star(DE3) was induced at each phase of adaptation in complimentary media (i.e. protein expression was induced in 30 % deuterated M9 media from cultures adapted to 30 % deuterated M9 media), where an inverse correlation between PBP2a expression and the proportion of deuterium in the media was observed.
Inspired by previous procedures documented by Cai et al.[171], BL21-Star(DE3) adapted to deuterated conditions on a series of M9 agar of progressively increasing deuterium content (30, 50, 70 and 100 %) were cultured in large volumes (5 x 400 mL conical flasks) of LB media to mid-/late-log phase (OD600 0.8-1.0), centrifuged briefly at room temperature, cell pellets resuspended in a fourfold smaller volume of fully-deuterated, isotopically-labelled M9 media, incubated for 30 minutes (37°C, shaking at 220 rpm) to exhaust any residual LB media, and induced with 1.0 mM IPTG; in order to both decrease the challenge of deuterated conditions on cell viability while providing a greater quantity of hosts (OD_{600} 4.0) for

expression. Successful and reproducible expression of large quantities of PBP2a were possible with this approach (Figure 20) following induction with 1.0 mM IPTG at 25°C for 30-32 hours.

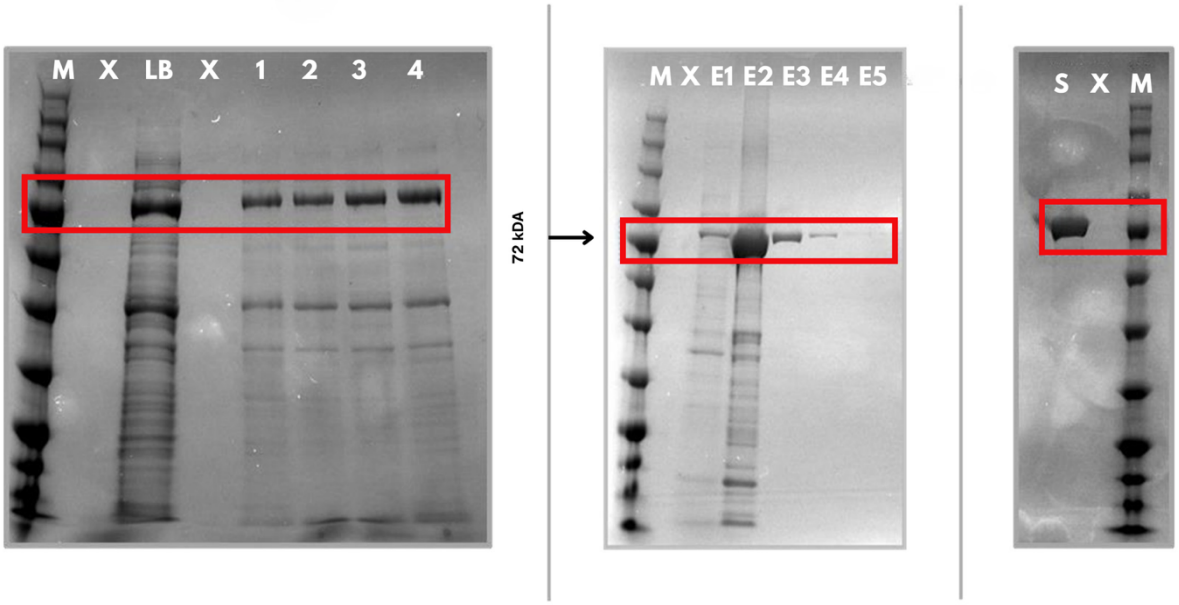

Figure 20: **Expression and purification of PBP2a in perdeuterated, defined media**

Left: small scale expression of PBP2a in deuterated M9 media in BL21-Star *E. coli* adapted to deuterium via successively subculturing on M9 agar plates with a series of progressively increasing (30-100%) proportions of D2O/H2O. x: empty lane, LB: un-adapted BL21-Star expression in LB media, 1: BL21-Star adapted with one round of selection at 100% D2O, 2: BL21-Star adapted with one round of selection at 100% D2O, 3: BL21-Star adapted with two rounds of selection at 100% D2O, 4: BL21-Star adapted with two rounds of selection at 100% D2O. Middle: Ni-NTA purification of large scale expression in deuterated M9 media. E: elution fractions, x: empty lane. Right: PBP2a purified by size exclusion chromatography (SEC). Expected migration region for PBP2a highlighted by the blue box. M: 11-250 kDa protein standard.

The average yield per 400 mL flask of deuterated M9 media was 500-600 µL of purified ^{2}H-^{13}C-^{15}N-labelled PBP2a at a concentration of 300 µM, approximately 40 % lower yield than that obtained through expression protonated M9 media. Such decreases in protein yield are typically expected when producing isotopically labelled proteins in deuterated media.

3.4.4 Resonance assignment via amide backbone experiments

NMR is a uniquely positioned biophysical technique capable of observing the dynamic behaviour of proteins in near native in-solution contexts with atomistic detail[108,112,115,154,155]. However, a significant bottleneck for the utility of NMR with large proteins is the difficulty in the relation of resonances observed in NMR spectra to residue-specific atoms within the target protein[109,161,162]; also known as resonance assignment. Resonance assignment is essential for a meaningful interpretation of NMR data for functional studies. This is

commonly achieved by conducting experiments that correlate the backbone and side-chain nuclei within and between residues[160,161]. Resonance assignment via backbone amide-detected NMR spectroscopy (2D TROSY-HSQC and 3D TROSY-based HNCO/HNCA/HNCACB suites) remains the gold standard for residue-specific assignment. Given the primary objectives of (i) characterising conformational dynamics underlying allosteric regulation in PBP2a and (ii) benchmarking ligand-induced perturbations with residue-level precision, an amide-first strategy was the logical starting point. As a large (>76 kDa) globular but anisotropic protein, PBP2a folds into a well-defined multidomain architecture with elongated dimensions rather than a compact spherical shape, placing it near the upper practical limit for solution-state NMR assignment[4-7]. The effective molecular weight threshold for reliable backbone assignment under standard conditions typically falls around 60-80 kDa, beyond which extensive deuteration and advanced TROSY-based approaches become essential to maintain spectral resolution and sensitivity[158,176,177]. Despite these challenges, previous studies have successfully obtained partial or full backbone assignments for proteins of comparable size and complexity using such strategies[178-180]. Given that conventional backbone assignment – if achievable – provides the most direct and systematic mapping of resonances, it was pursued initially before adopting alternative approaches such as mutational or selective methyl labelling for residue identification.

3.4.4.1 ^{1}H-^{13}C HMQC

To assess whether methyl-detected NMR offered a viable route for studying PBP2a, an initial exploratory ^{2}H-^{13}C-^{15}N uniformly labelled ^{1}H-^{13}C HMQC spectrum was recorded. The sample was prepared using "poor man's deuteration," a cost-effective strategy in which the protein is expressed in D_2O-based minimal medium supplemented with protonated carbon sources (e.g. ^{1}H-^{13}C labelled glucose). This partial deuteration attenuates dipolar relaxation pathways and improves signal lifetimes compared with fully protonated samples, while avoiding the substantial cost and reduced growth rates associated with complete deuteration. A ^{1}H-^{13}C SOFAST-HMQC was acquired for 62 minutes for ^{1}H-^{13}C-^{15}N uniformly labelled PBP2a (300 μM) with at 30^{o}C at 950 MHz (Figure 21).

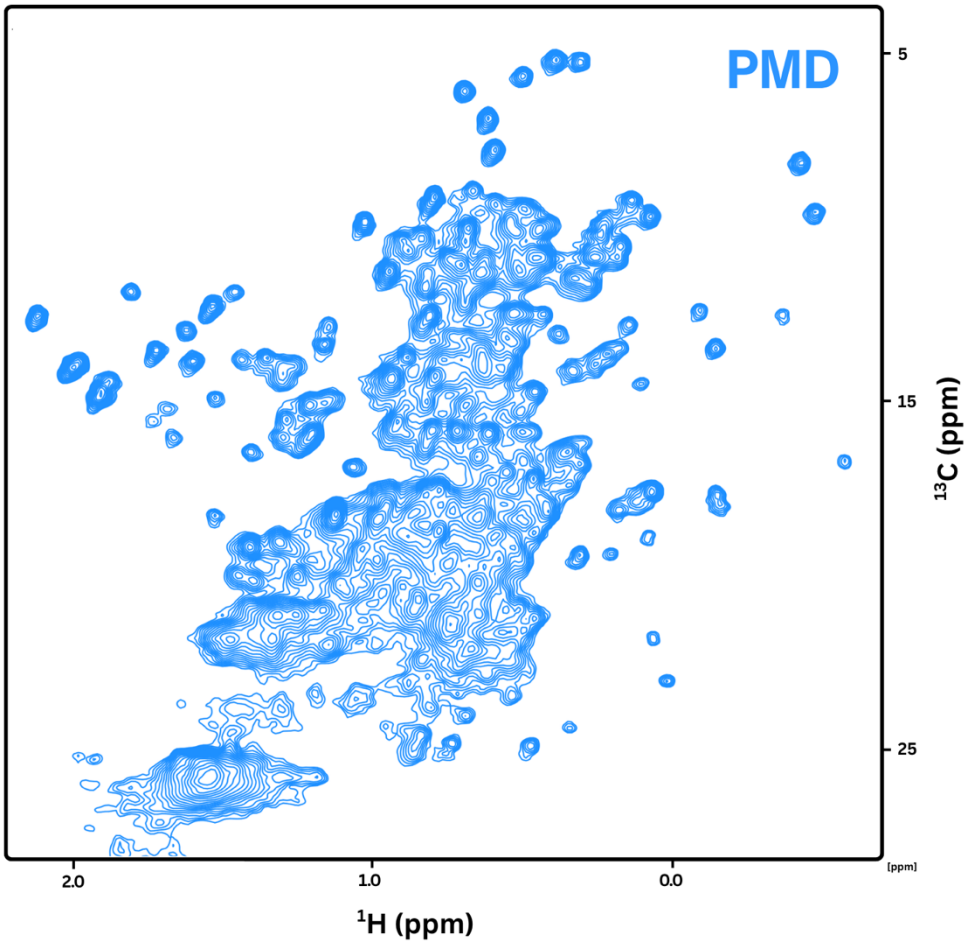

Figure 21: ^{1}H-^{13}C SOFAST-HMQC spectrum of PBP2a with non-selective deuteration.

The spectrum was acquired from a 300 µM sample labelled with a "poor man's deuteration" strategy at 30°C on a 950 MHz spectrometer. All the expected cross-peaks for the available methyl-containing residues within PBP2a are observed but with significant overlap between regions characteristic of specific residue signatures.

The resulting spectrum exhibited approximately 293 methyl resonances of the ~269 expected PBP2a methyls (Ala = 27, Leu = 45, Ile = 55, Val = 33, Thr = 31; with two methyl groups for Leu δ_1/δ_1 and Val γ_1/γ_2). Although the spectrum confirmed that PBP2a's methyl environments were detectable with adequate sensitivity, as shown in Figure 21, the substantial peak breadth and extensive overlap – particularly in the densely populated upfield region dominated by leucine and valine methyls – prevented unambiguous peak resolution. This crowding is characteristic of uniform, non-selective methyl labelling, where the simultaneous enrichment of all methyl-bearing residues leads to spectral degeneracy. Selective labelling of specific residues – such as using α-ketoacid precursors for Ile δ1, Leu/Val proS and Ala β labelling – in perdeuterated media would likely result in better resolved spectra. However, this exploratory dataset demonstrated that PBP2a methyls were detected with sufficient sensitivity to justify considering alternative assignment strategies

using methyl-based methods should assignment not be possible via amide backbone approaches.

3.4.4.2 1H-15N-HSQC

A preliminary ^{1}H-^{15}N HSQC-TROSY spectrum was acquired to assess the feasibility of using solution-state NMR for PBP2a backbone assignment, since a 2D amide fingerprint provides a rapid indication of overall protein fold, spectral quality, and whether sufficient dispersion and signal intensity exist to justify more complex multidimensional experiments. The spectrum was acquired for 18 hours and 24 minutes for PBP2a (300 µM) at 25°C at 950 MHz to provide a peak for each non-proline residue amide in PBP2a (Figure 22):

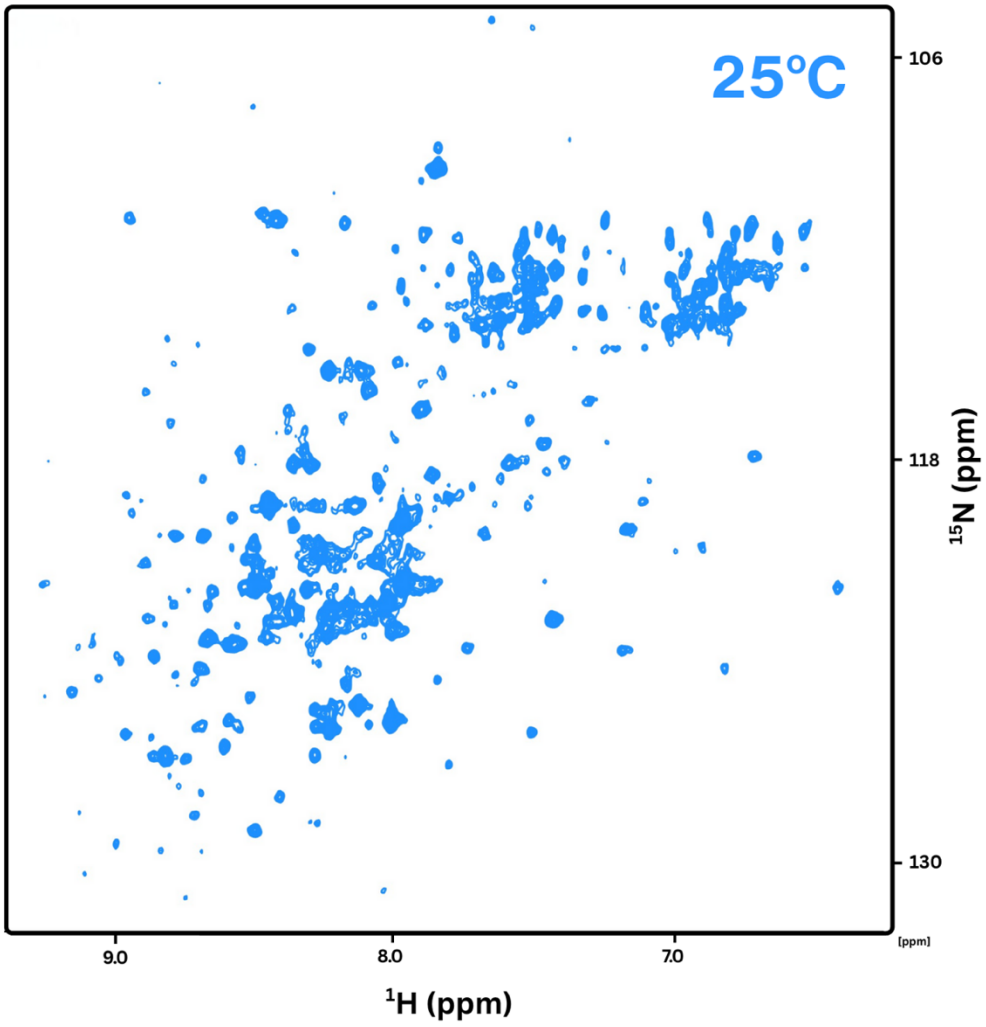

Figure 22: 2D ^{1}H-^{15}N HSQC-TROSY of PBP2a (300 µM) at 25°C displaying peaks for each non-proline residue amide.

The spectrum shows well-dispersed cross-peaks, consistent with a correctly folded tertiary structure, but only 457 of the 668 expected amide resonances were detected, indicating incomplete spectral coverage and suboptimal data quality for subsequent 3D backbone assignment. The missing resonances likely reflect line broadening from µs-ms conformational exchange, rapid solvent exchange of surface-accessible amides, and

signal loss due to incomplete deuteration or local unfolding events, consistent with prior reports for large (~76 kDa) multidomain proteins such as PBP2a

Despite well-dispersed peaks suggesting that the protein remained folded under these conditions, only 457 of the 668 expected amide resonances were detected, indicating incomplete spectral coverage and suboptimal data quality to proceed with more complex 3D experiments required for full backbone assignment. A combination of factors may account for this, including conformational exchange broadening from µs-ms dynamics (previously documented in PBP2a[89,97]), rapid solvent exchange of surface-exposed amides, and reduced signal intensity from incomplete deuteration or local unfolding events[158,176,177]. The extended acquisition time required to achieve this level of resolution reflects a low overall signal-to-noise ratio, suggesting that the current buffer conditions and acquisition parameters needed to be optimised to improve spectral quality before progressing to higher-dimensional NMR experiments with more complex resonance transfers.

Increasing the temperature to 30^{o}C was intended to improve molecular tumbling and reduce transverse relaxation, thereby sharpening amide resonances and enhancing spectral resolution. A ^{1}H-^{15}N HSQC-TROSY spectrum recorded over 16 hours at 30oC showed a clear improvement in overall spectral quality, with reduced peak broadening and greater dispersion across both proton and nitrogen dimensions (Figure 23):

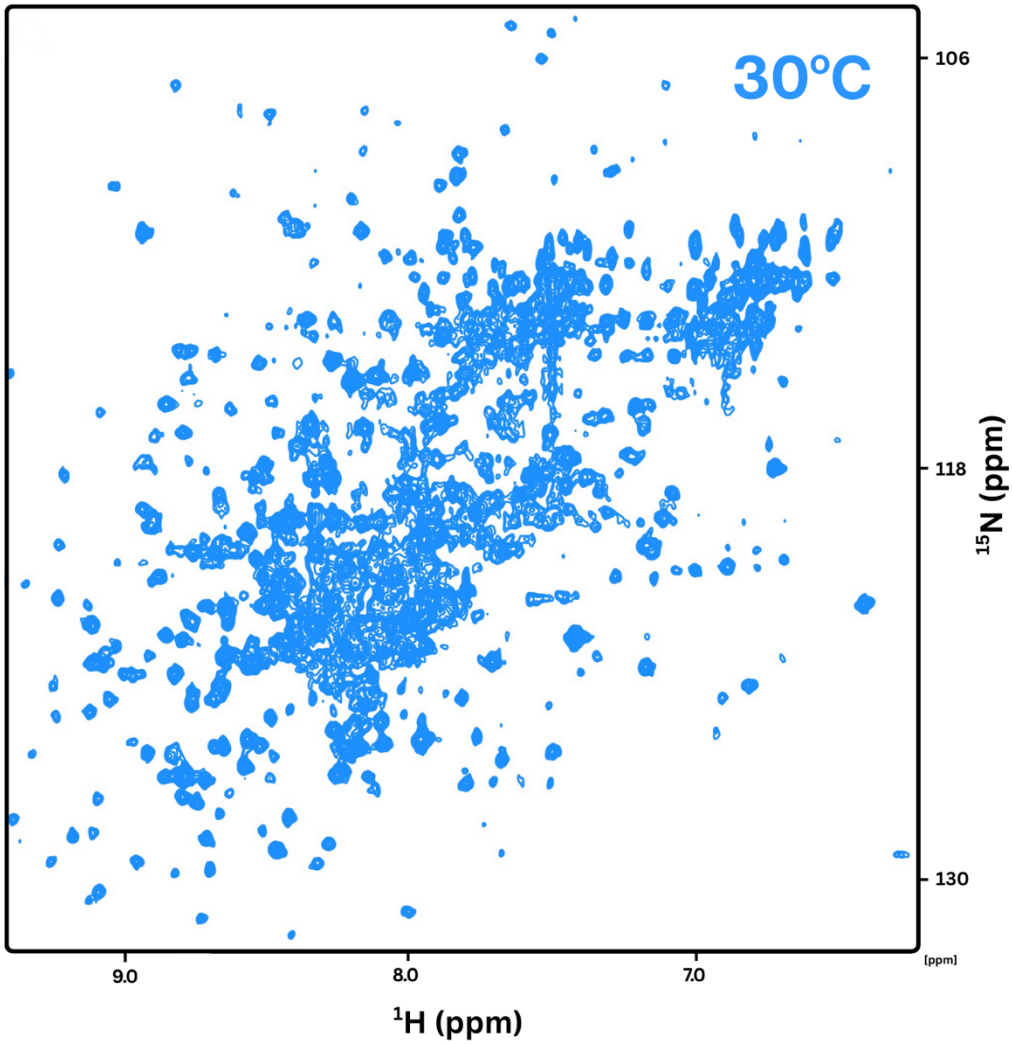

Figure 23: **2D ^{1}H-^{15}N HSQC-TROSY of PBP2a (300 µM) at 30°C 950 MHz displaying peaks for each non-proline residue amide.**

This spectrum produced 639 of the 668 expected amide resonances, representing a marked improvement in spectral completeness compared to the 25°C dataset. The enhanced resonance detection is likely explained by improved molecular tumbling, reduced transverse relaxation, and partial stabilisation of dynamic regions within the protein.

These data showed substantial improvement in the number of identifiable amide resonances, with 639 of the expected 668 amide resonances now detectable. The increased number of observable peaks likely reflects a combination of improved molecular tumbling and partial alleviation of line broadening as well as the possible stabilisation of previously dynamic regions within PBP2a. These findings are consistent with PBP2a's expected intrinsic flexibility, particularly within regions implicated in the allosteric regulation of access to the TP domain. While considerable overlap and crowding remains in some regions of the spectrum (Figure 23, e.g. ^{1}H: 7.8-8.5 ppm; ^{13}C: 119-125 ppm) – expected for a protein of this size – the data nonetheless confirmed adequate dispersion and sensitivity to justify more complex 3D experiments. However, the fact that each HSQC required overnight acquisition

provided early indications that multidimensional backbone assignment would likely be challenging, as long acquisition times exacerbate relaxation losses and sample instability in large systems. To address these limitations, a systematic optimisation step was introduced prior to commencing the 3D experimental series to minimise signal loss, line broadening, and precipitation which threaten to compromise the quality and reproducibility of the longer triple-resonance experiments. Consequently, a buffer optimisation campaign was undertaken to enhance both spectral sensitivity and sample longevity by identifying solution conditions that balanced structural stability with minimal electrical conductivity. This step was essential because cryogenically cooled probes – while delivering substantial sensitivity gains – are highly sensitive to sample composition. The optimisation therefore sought to refine buffer composition, pH, and additive content to preserve PBP2a's folded, monomeric state while maximising probe efficiency, enabling extended 3D data collection without compromising spectral quality.

3.4.4.3 TROSY-HNCO

With optimised sample conditions established, a systematic and progressive strategy was adopted for the subsequent 3D experiments. The approach began with the most sensitive triple-resonance experiments to establish amide-carbonyl connectivities before progressing to the more demanding Cα/Cβ correlation experiments. A TROSY-HNCO experiment was selected as the initial 3D dataset, providing the most direct and sensitive link between each amide proton-nitrogen pair and its preceding carbonyl carbon, thereby serving as the foundation for subsequent backbone assignment experiments. A ^{1}H-^{15}N TROSY-HNCO was acquired for 22 hours and 28 minutes for ^{2}H-^{13}C-^{15}N uniformly labelled perdeuterated PBP2a (300 μM) at 30°C at 950 MHz to provide resonances for each $^{15}N^{H}$-^{13}CO (on residues *i* and i^{-1} respectively) non-proline PBP2a residues (Figure 24).

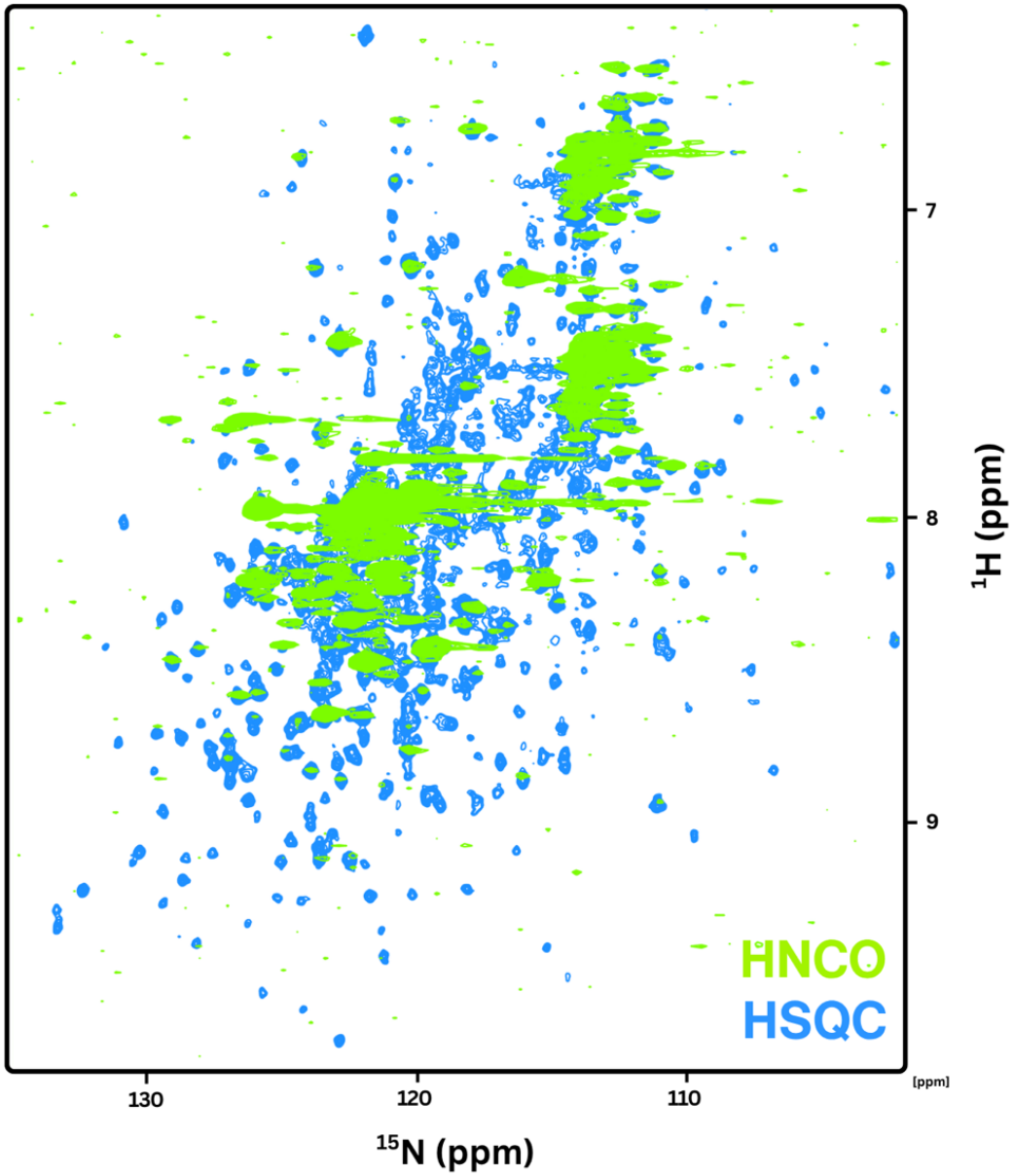

Figure 24: 3D ^{1}H-^{15}N HNCO spectrum of 300 µM ^{2}H-^{15}N-^{13}C-labelled PBP2a acquired at 30°C on a 950 MHz spectrometer.

Overlay of a ^{1}H-^{15}N TROSY-HSQC (blue) ^{1}H-^{15}N plane of the 3D TROSY-HNCO for PBP2a. Both spectra were acquired at 30°C on a 950 MHz spectrometer with ~73% peak correlation, establishing a modest number of ^{15}NH(i) to ^{13}CO(i^{-1}) connectivities sufficient to proceed with further sequential backbone assignment experiments.

These TROSY-HNCO measurements accurately pair with the amide resonances detected in Figure 23 (Figure 24) with modest ~73% peak coverage. The TROSY-HNCO spectrum provided essential ^{15}NH(i) to ^{13}CO(i^{-1}) links making it possible to proceed with further 3D experiments to obtain Cα and Cβ chemical shifts, which are critical for identifying amino acid types and confirming sequential walks. To this end, a TROSY-HN(CO)CA was the next 3D experiment selected.

3.4.4.4 Optimisation of buffer and purification conditions

The production of high-quality protein samples for NMR study is not a trivial task, where many experiments – e.g. CPMG, NOESY, chemical shift perturbations via titrations – demand stable sample conditions for long experimental times (several days in some instances), often at near physiological temperatures, placing additional demands on the thermal stability of the sample. Additionally, NMR studies have a limited tolerance for sample heterogeneity, where solubility and monodispersity are crucial for quality spectra, making the due diligence in suitable buffer selection an essential rather than recommended practice[159]. This is further complicated by the requirement of buffer conditions to not only sustain a homogenous population of well-folded proteins but also limit/avoid interference with the signals of the protein[181]. Over the past few decades, technological advances in NMR spectroscopy – including the introduction of higher magnetic field strengths, cryogenically cooled probes, enhanced preamplifier design, and continual pulse-sequence innovation – have led to a dramatic improvement in experimental sensitivity[108,155,158,182]. As a result, NMR spectroscopy can now be applied to an increasingly broad range of proteins encompassing greater molecular size, structural complexity, and functional diversity than was previously accessible. Among these developments, the introduction of cryogenically cooled probes has been especially transformative, delivering a 3-4-fold increase in experimental sensitivity by markedly reducing the thermal noise of the radiofrequency (RF) receiver circuitry[144,181]. Cooling the receiver coils to 15-30 K substantially lowers their electrical resistance, thereby amplifying signal strength and improving the signal-to-noise (S/N) ratio[144,181]. However, the performance gains achievable with cryoprobes are inversely related to the electrical conductivity of the sample: highly conductive buffers increase resistive losses within the coil, diminishing sensitivity[181]. By contrast, samples with low conductivity – composed of electrically insulating materials – are ideal for NMR because they do not generate eddy currents in response to the applied RF field[181]. The absence of these currents ensures uniform field penetration, maintains the probe's high quality factor (Q factor), and prevents both signal attenuation and line broadening, ultimately yielding spectra of superior resolution and sensitivity[181].

However, many proteins studied by solution-state NMR require buffered solutions to maintain a constant pH, defined protonation state, and native fold, where sample optimisation represents a delicate balance between experimental sensitivity and structural stability, often involving trade-offs that influence both data quality and the feasible duration

of acquisition[181]. The concentration and combination of different buffer excipients have dramatic impacts on osmolality, pH stability, protein unfolding, precipitation, aggregation, adsorption and chemical modification potential[159]. Additionally, the inclusion of common buffering components – particularly salts – can significantly impact the performance of cryogenic probes, as ionic species increase solution conductivity and thereby reduce sensitivity[159]. Even modest salt concentrations (100-150 mM NaCl) have been shown to reduce the sensitivity advantage of cryoprobes by as much as 50 % compared with equivalent low-conductivity samples[144,181]. Nevertheless, salts such as NaCl or KCl are frequently indispensable for maintaining colloidal stability by screening surface charges and preventing non-specific aggregation[181,183]. pH control represents another critical factor in NMR sample optimisation, as it governs the protonation state of ionisable residues and thus modulates electrostatic interactions, hydrogen-bond networks, and overall protein conformation[181,183]. Importantly, at more extreme pH values (>7.0 or <6.0), acid- and base-catalysed proton exchange accelerates, leading to increased line broadening and signal loss[159]. Maintaining a stable pH is therefore essential to obtain reproducible spectra and avoid artefacts arising from conformational or chemical exchange. Core buffering agents such as sodium phosphate and Tris are widely used for this purpose and are fundamental for preserving native protein structure and function during data collection. However, these buffers vary considerably in electrical conductivity, adding another layer of complexity to the optimisation process[181]. Co-solvents such as glycerol are sometimes included to enhance protein solubility and thermal stability or to act as cryoprotectants during low-temperature acquisitions[144,183]. Despite these benefits, glycerol's abundant proton resonances can overlap with protein signals, complicating spectral interpretation and reducing its suitability for high-resolution NMR studies[184].

Kozak and colleagues evidenced a clear link between experimental sensitivity on the conductivity of a given sample, as a function of both ion mobility and ion concentration[159]. As such, buffers with components of a variety of ionic strengths were explored to find an optimal combination of sample stability and experimental sensitivity. Additionally, the inclusion of additives has shown success in improving protein stability by providing low conductivity alternatives to screen surface charges that might otherwise drive self-association/aggregation[185]. The simultaneous addition of charged amino acids L-Arginine and L-Glutamate to protein buffers has previously been shown to dramatically increase the maximum achievable concentration, long-term stability and resistance to proteolytic

degradation of several proteins[185]. Additionally, lower pH buffers have the potential to improve spectral resolution via alteration of the protonation/deprotonation susceptibility of NH groups via acid-/base-dominant exchange regimes, increasing exchange rates[183].

The fluorescence-based thermal-shift assay (ThermoFluor®) – also referred to as differential scanning fluorimetry (DSF)[159,183] – is a high-throughput approach for screening buffer conditions that has, in recent times, become considered one of the gold standards for rapid assessment of protein stability. The thermal shift assay utilises a fluorescent hydrophobic dye with a high affinity for hydrophobic protein regions as a reporter that enables the monitoring of protein unfolding upon thermal denaturation and has been successfully utilised in the identification of buffer conditions of challenging proteins suitable for NMR study[159]. Indeed, Kozak and colleagues[159] successfully utilised ThermoFluor™ in the optimisation of buffer conditions that improved the conformational stability, peak intensity homogeneity, and number of well-resolved detectable peaks of both RTT109 and Protein "BA" (an adenylation domain of a non-ribosomal peptide synthase). As such, a sequential screening strategy using a ThermoFluor® based buffer screening protocol inspired by Kozak and colleagues[159] implemented to optimise buffer composition for PBP2a for NMR experimentation.

Buffer selections were prioritised on the basis of low electrical conductivity and favourable sensitivity characteristics for cryogenic NMR probes[159,181]. In such probes, the achievable signal-to-noise ratio depends strongly on the quality factor (Q) of the receiver coil, which decreases when the sample has high ionic conductivity. The sensitivity factor (L) describes the ratio of the signal intensity of a loaded probe relative to the unloaded state, where highly conductive solutions reduce L by introducing resistive losses that increase thermal noise. Thus, buffers that maintain low ionic strength and contain ions of low mobility are expected to produce higher Q and therefore greater sensitivity[159,181]. Optimising buffer composition for PBP2a was therefore driven by the dual aim of improving thermal stability while preserving conditions conducive to high-quality NMR data acquisition; with selections guided by previous reports[159,181]. Primary screening was undertaken to establish a baseline range of conditions suitable for subsequent refinement. Buffers tested included PIPES, MES, HEPES, CHES, Bis-Tris, and citric acid-$NaHPO_4$, each formulated with 300 mM NaCl to standardise ionic strength. The reference condition – chosen by the previous student working on PBP2a (Dr F. Salama) – was 50 mM $NaHPO_4$, 300 mM NaCl, pH 7.0, produced a melting

temperature (T_m) of 44.5°C. As such, in this initial screen, a T_m above 41°C was used as the threshold for retention. All buffers met this criterion except CHES, which was excluded from further analysis owing to its lower apparent stability.

A follow-up screen explored the effects of ionic strength, pH, and low-salt additives to define the limits of conductivity reduction without compromising stability (Figure 25). NaCl was varied between 0 mM and 500 mM, across a broad pH range encompassing both acidic and near-neutral conditions. Samples were also prepared with 50 mM L-arginine, 50 mM L-glutamic acid, or 50 mM of each in combination, as these additives have previously been reported to improve solubility and reduce aggregation under low-salt conditions[185]. The goal of this screen was to determine whether lower-salt conditions could confer sufficient thermal stability to justify the expected improvement in NMR sensitivity by a reduction in conductivity[185], or conversely, whether higher ionic strength was necessary to stabilise the protein during long acquisitions. At the same time, exploring lower and higher pH values allowed assessment of conditions that might reduce amide exchange, thereby improving signal-to-noise in amide-detected experiments[183]. The reference buffer (50 mM $NaHPO_4$, 300 mM NaCl, pH 7.0) was included as a control in all runs.

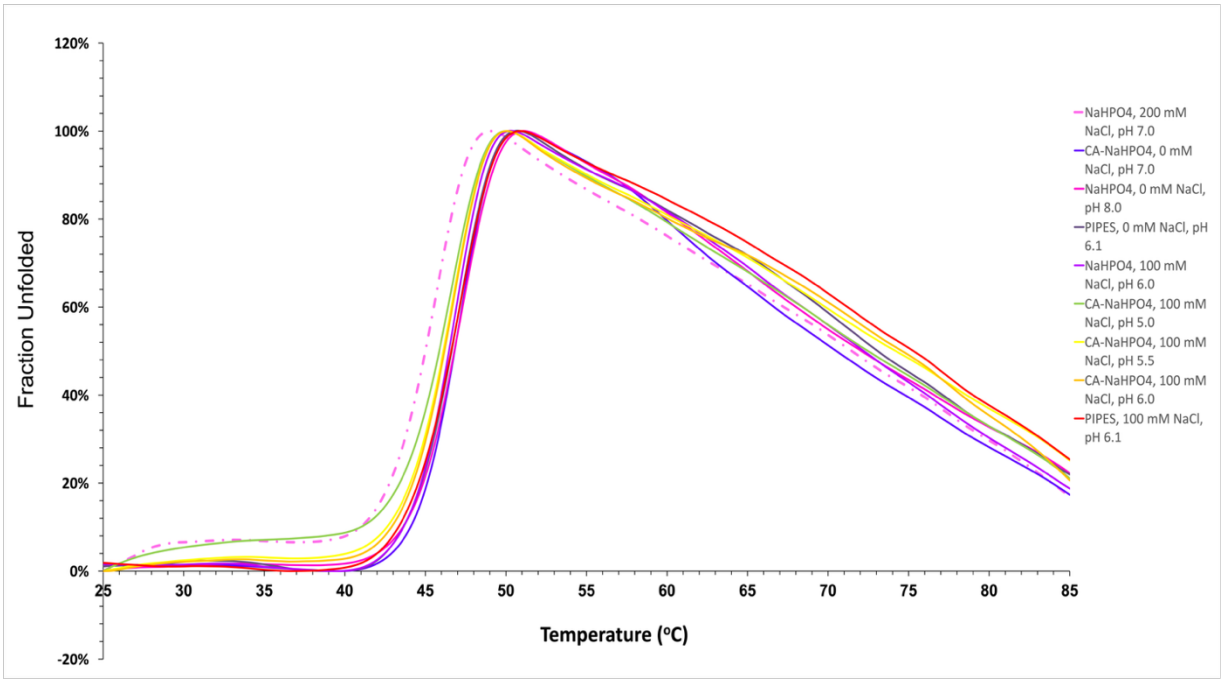

Figure 25: Thermal stability screening of PBP2a across buffer conditions using ThermoFluor™ analysis

Thermal unfolding profiles of PBP2a recorded under various buffer formulations, with fluorescence intensity monitored as a function of temperature using a qPCR thermocycler. The dotted pink line represents the melting transition (T_m = 44.5°C) of PBP2a in the reference buffer (50 mM $NaHPO_4$, 300 mM NaCl, pH 7.0). Alternative buffer systems exhibiting an increase in T_m >1°C relative to reference buffer were selected for further NMR

evaluation and optimisation. These stabilising conditions were considered to reflect improved protein conformational stability and resistance to thermal denaturation under experimental conditions.

Conditions were advanced for further consideration if they produced a T_m improvement of at least 1.5°C greater than the reference. Although the inclusion of L-arginine and L-glutamate was hypothesised to confer stabilisation at lower ionic strength, all additive-containing samples displayed reduced stability relative to their additive-free counterparts. These results contrast with reports from other proteins where these amino acids improved solubility, suggesting that in PBP2a they may disrupt essential electrostatic interactions required to maintain the native fold.

A final optimisation screen focused on the most promising buffer systems – PIPES, MES, $NaHPO_4$, and citric acid-NaHPO4 – across NaCl concentrations of 0-300 mM within their individually optimised pH windows, testing also the effects of glycerol at 2.5%, 3.5%, and 5.0% (Figure 26). Glycerol is frequently used as a cryoprotectant and stabiliser because it increases the viscosity of the solvent, thereby reducing protein unfolding and aggregation[186], but it also marginally decreases NMR sensitivity by increasing dielectric losses and adding proton background signals[187]. Lower concentrations are generally tolerated however without substantial detriment to signal-to-noise, with previous reports showing success in long (~4.5 days) 3D acquisitions in buffers containing up to 11% glycerol[184].

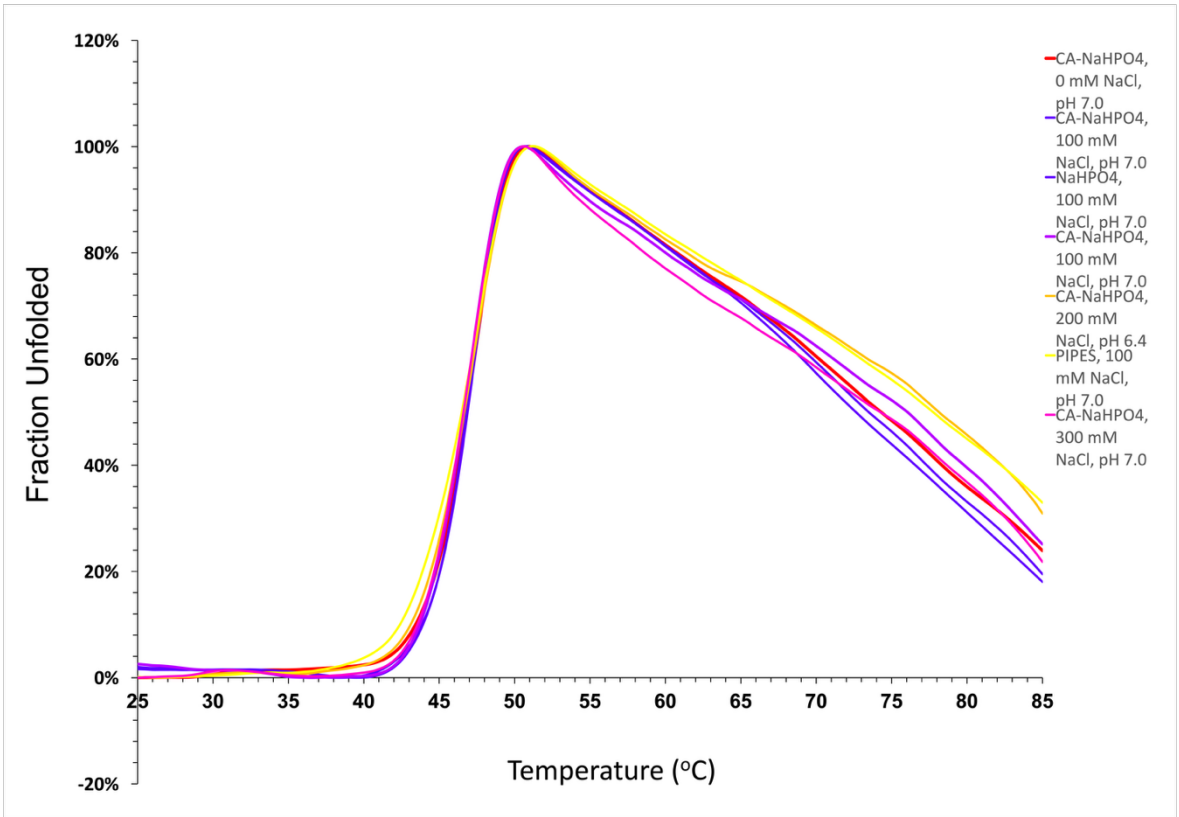

Figure 26: Thermal stability screening of PBP2a across buffer conditions using ThermoFluor™ analysis

Thermal unfolding profiles of PBP2a recorded under various buffer formulations, with fluorescence intensity monitored as a function of temperature using a qPCR thermocycler. Alternative buffer systems exhibiting an increase in T_m >1.5°C relative to reference buffer (T_m 44.5°C) were selected for further NMR evaluation and optimisation. These stabilising conditions were considered to reflect improved protein conformational stability and resistance to thermal denaturation under experimental conditions.

Glycerol-containing buffers represented several of the top-performing conditions; however, the differences compared with matched glycerol-free buffers were not statistically significant, and no concentration-dependent trend was observed. The best-performing formulation across all three screens were combinations using the citric acid-$NaHPO_4$ buffer, several of which exhibited T_m of 46°C. Notably, citric acid-$NaHPO_4$ consistently conferred the greatest tolerance to reduced pH and lower NaCl concentration, with many maintaining a thermal stability advantage of approximately +1.5°C relative to the reference buffer even at 0 mM NaCl (pH 7.0) or 100 mM NaCl (pH 5.5). Because this formulation combined improved thermal stability with lower conductivity and reduced pH, it was selected as the first optimised buffer to be tested in NMR experiments. A 2D ^{1}H-^{15}N TROSY-HSQC was acquired to test the viability of the citric acid-$NaHPO_4$ variants (Figure 27):

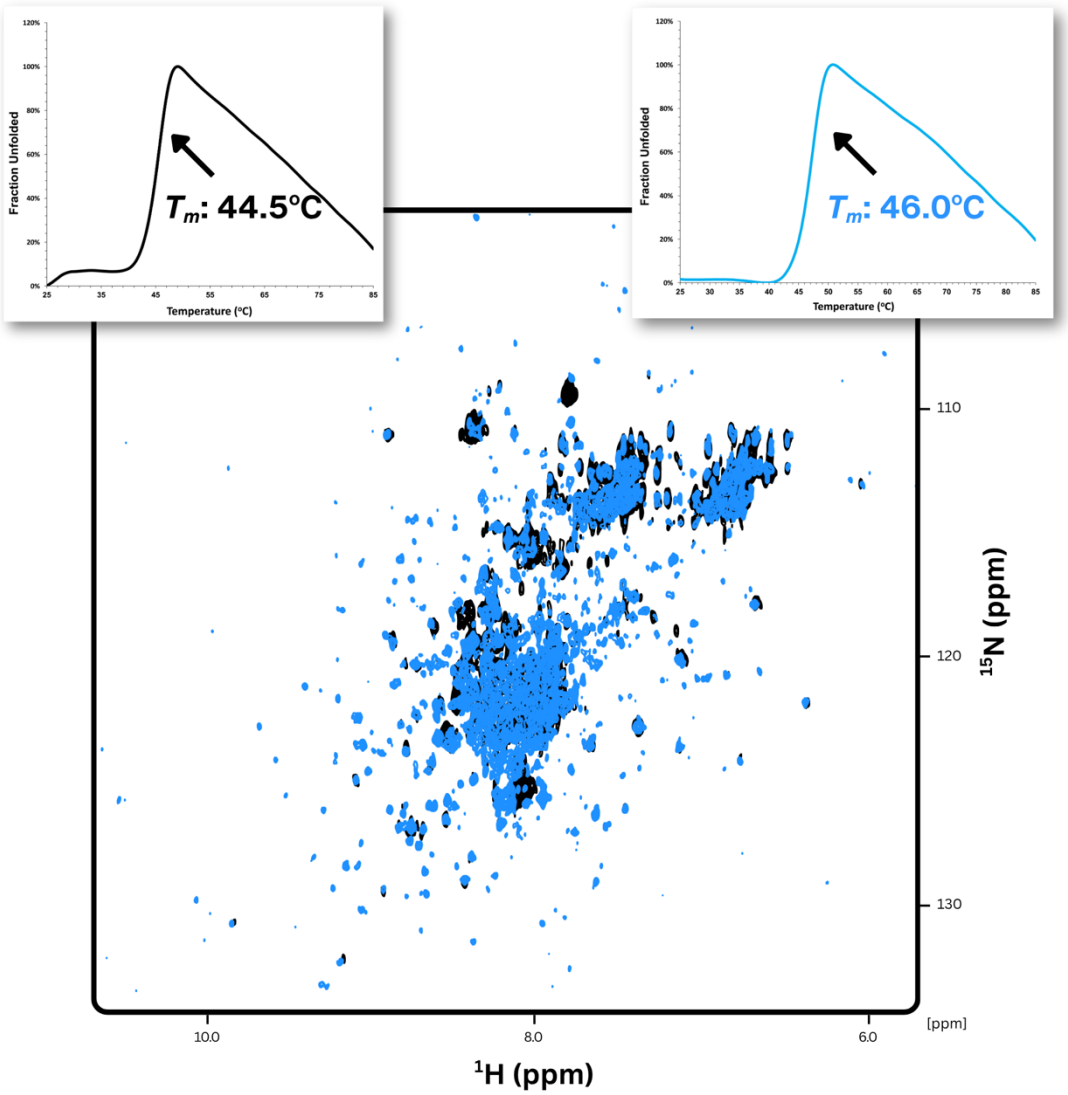

Figure 27: 2D ^{1}H-^{15}N TROSY-HSQC comparison of PBP2a in the reference buffer (50 mM $NaHPO_4$, 300 mM NaCl, pH 7.0; T_m = 44.5°C) and citric acid-$NaHPO_4$ buffer (100 mM NaCl, pH 6.1; T_m = 46°C).

Spectra were recorded at 30°C on a 950 MHz spectrometer over 2.5 hr. The citric acid-$NaHPO_4$ condition (blue) exhibits improved signal-to-noise and reduced linewidths, indicating enhanced stability and lower sample conductivity relative to the reference buffer (black).

The resulting spectrum showed visibly improved signal-to-noise and sharper linewidths in the citric acid-$NaHPO_4$ buffer (100 mM NaCl, pH 6.1, T_m = 46°C; Figure 27 – blue) compared to the reference buffer (50 mM $NaHPO_4$, 300 mM NaCl, pH 7.0 T_m = 44.5°C; Figure 27 – black), consistent with both reduced ionic conductivity and increased protein stability. Despite these improvements, the benefits did not extend to longer 3D acquisitions. A 3 day 15 hr TROSY-HNCO recorded under the same conditions as previous showed visible precipitation by the end of the experiment, and the follow-up HSQC confirmed significant signal loss and spectral deterioration. Although the ThermoFluor™ data,

acquired at 25 μM protein concentration, suggested a stable folded state, the substantially higher concentrations required for amide experiments (300 μM) imposed additional colloidal and thermodynamic stresses. To evaluate this, the best-performing buffer candidates (T_m = 46ºC) were tested under static incubation at 30ºC for seven days at 150-750 μM, with samples inspected microscopically every 24 hr. The purpose of this screen was to assess whether either buffer could confer greater stability at higher protein concentrations as a means of reducing experiment duration and subsequent stability losses. The reference buffer consistently outperformed both the citric acid-$NaHPO_4$ and PIPES conditions, remaining visually monodisperse for approximately two days longer. At 500 μM protein, PBP2a remained stable for roughly five days in 50 mM $NaHPO_4$ containing 0-100 mM NaCl at pH 6.0, in 50 mM $NaHPO_4$ containing 200 mM NaCl at pH 7.0, and in the original reference formulation containing 50 mM $NaHPO_4$ containing 300 mM NaCl at pH 7.0.

However, a repeat HNCO performed at 500 μM in the reference buffer yielded comparable signal-to-noise as previous attempts with similar unfolding noted following acquisitions after 4 days at 30ºC, confirming that buffer optimisation alone could not overcome the intrinsic relaxation and exchange limitations imposed by the size and dynamic behaviour of PBP2a during prolonged 3D acquisitions. Consequently, subsequent experiments were performed in the reference buffer (50 mM $NaHPO_4$, 300 mM NaCl, pH 7.0) at 300 μM.

3.4.4.5 TROSY-HN(CO)CA

A 3D ^{1}H-^{15}N TROSY-HN(CO)CA experiment was acquired for 3 days 15 hours and 36 minutes for PBP2a (300 μM) at 30ºC at 950 MHz with 21% non-uniform sampling (NUS) to establish correlations between each amide group (residue *i*) and the α-carbon of the preceding residue (i^{-1}) (Figure 28). This experiment represents a critical step in sequential backbone assignment, linking amide and intra-residue carbon correlations to build residue connectivity.

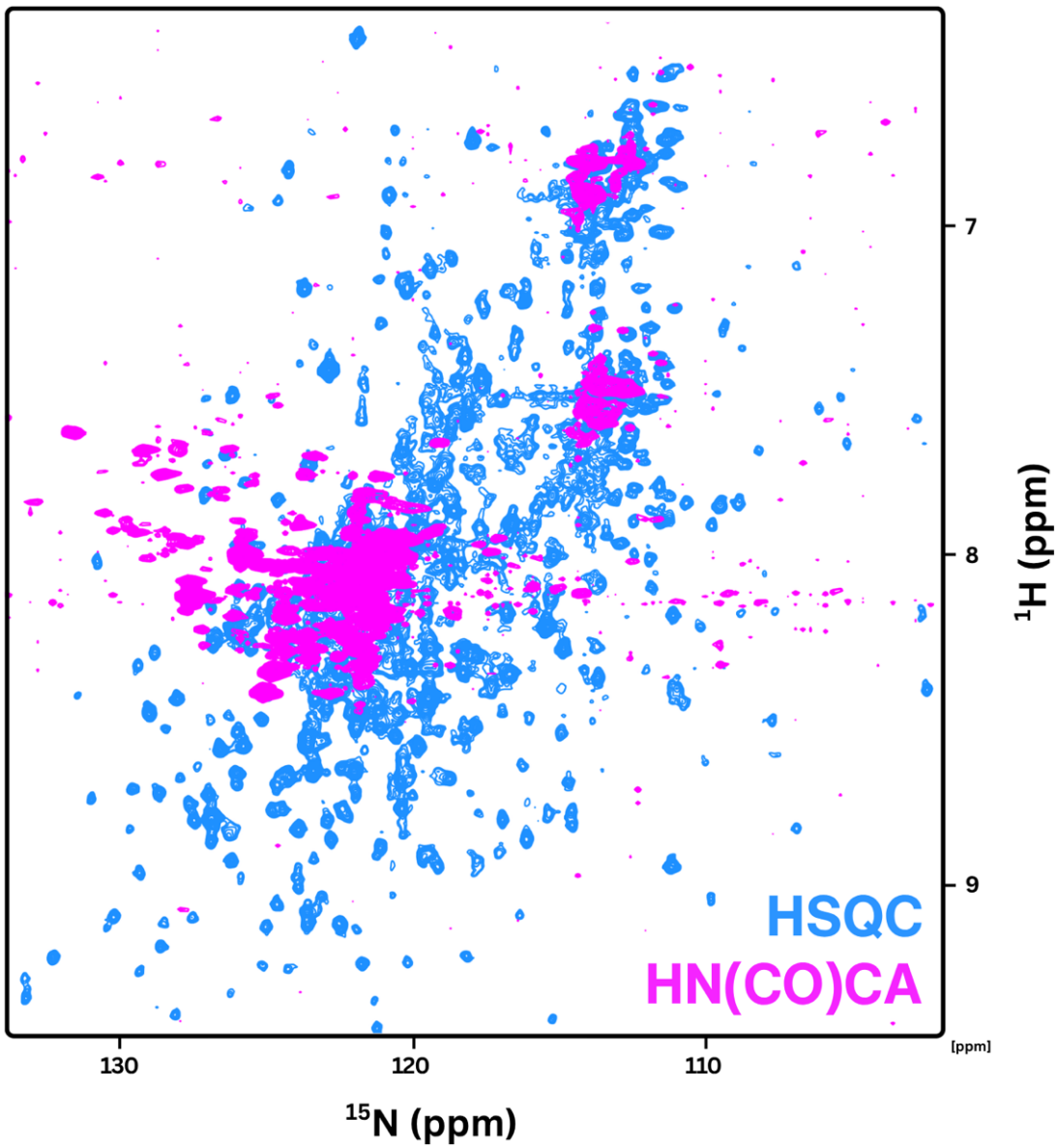

Figure 28: 3D ^{1}H-^{15}N TROSY-HN(CO)CA spectrum of 300 µM ^{2}H-^{15}N-^{13}C-labelled PBP2a acquired at 30°C on a 950 MHz spectrometer.

Overlay of a ^{1}H-^{15}N TROSY-HSQC (blue) with the ^{1}H-^{15}N plane of the 3D TROSY-HN(CO)CA for PBP2a. A low ~40% of the expected correlations were detected, evidencing a steep reduction in experimental sensitivity associated with extended coherence-transfer pathways due to rapid transverse relaxation and potential conformational exchange with the <76 kDa PBP2a; precluding its use for sequential backbone assignment.

The resulting spectrum (Figure 28) exhibited poor sensitivity with only 40% of the expected correlations detected, with many expected peaks falling below the noise threshold, leaving too few identifiable correlations for reliable sequential assignment. This outcome indicates that, although PBP2a remained stably folded at 30°C, its molecular size and slow tumbling rate imposed a fundamental sensitivity limit on extended triple-resonance experiments under the current labelling and concentration conditions. The already long acquisition time made

it impractical to improve spectral quality through additional scans or increments, and increasing protein concentration was not viable owing to visible unfolding being observed at concentrations above 400 μM at 25°C. Further, the limited signal-to-noise ratio was likely a byproduct rather than the cause of the poor spectral quality, wherein the dominant constraint was likely rapid transverse relaxation leading to severe coherence loss during the long transfer delays required for triple-resonance experiments in a large (>76 kDa) protein. To further assess the feasibility of obtaining Cα correlations under more favourable magnetisation-transfer conditions, a TROSY-HNCA experiment was next performed. This experiment, being somewhat less demanding than HN(CO)CA or HNCACB, was designed as a diagnostic test to determine whether intra-residue and sequential Cα connectivities could be detected at usable sensitivity, rather than to achieve complete assignment

3.4.4.6 TROSY-HNCA

A 3D ^{1}H-^{15}N TROSY-HNCA experiment was acquired over 3 days and 34 minutes for PBP2a (300 μM) at 30°C on a 950 MHz spectrometer to correlate the amide group of each residue (*i*) with the α-carbons of both its own and the preceding residue (^{15}NH(*i*) to ^{13}Cα(*i*) and ^{13}Cα(i^{-1})) (Figure 29). This experiment was selected as a less demanding alternative to the HN(CO)CA, as it omits the intermediate transfer via the carbonyl carbon, involving fewer coherence-transfer steps and shorter magnetisation delays. These features make the HNCA comparatively more tolerant to the rapid transverse relaxation and coherence decay that severely limit sensitivity in high-molecular-weight proteins such as PBP2a.

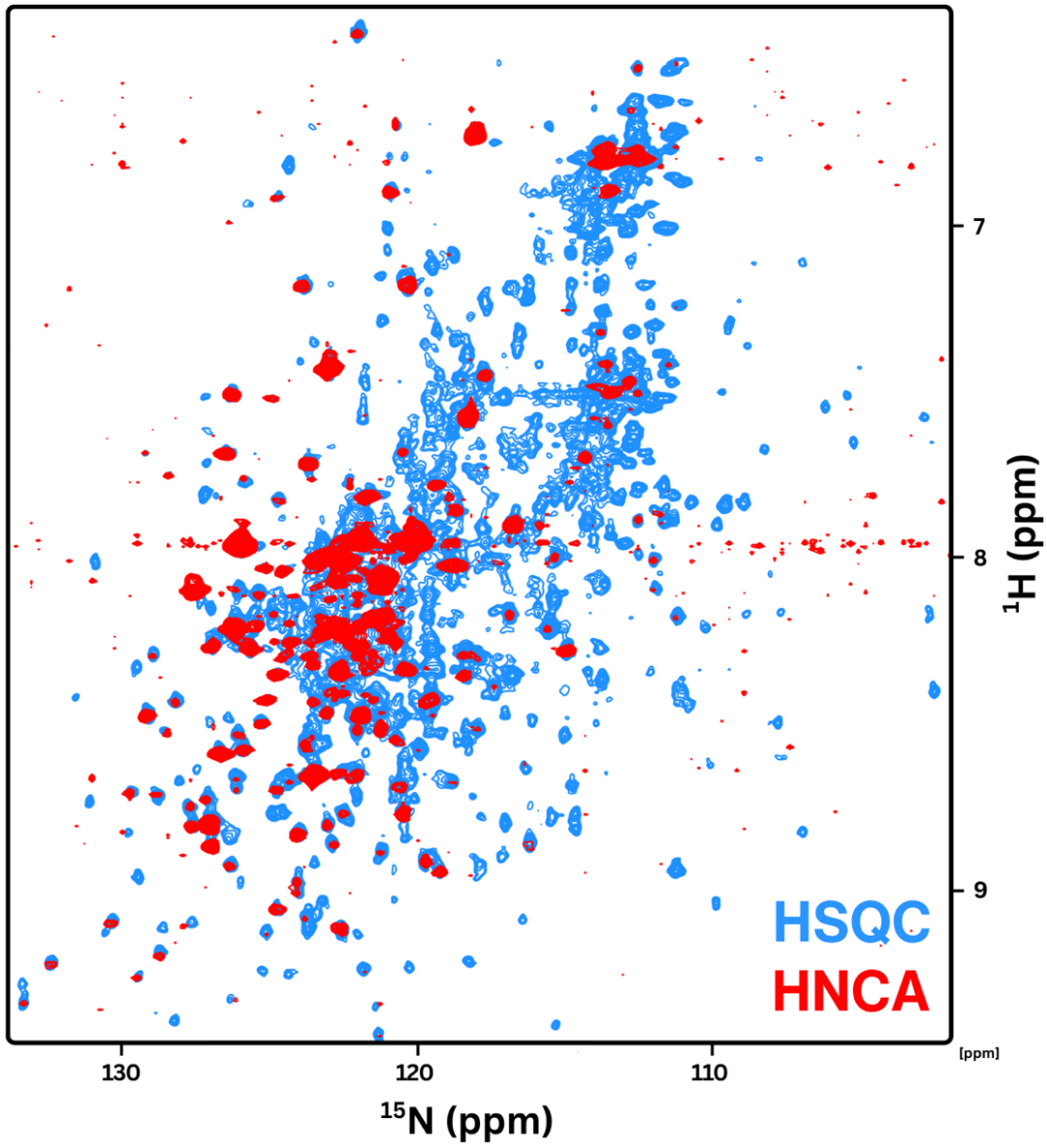

Figure 29: 3D ^{1}H-^{15}N TROSY-HNCA spectrum of 300 µM ^{2}H-^{15}N-^{13}C-labelled PBP2a acquired at 30°C on a 950 MHz spectrometer.

Overlay of a ^{1}H-^{15}N TROSY-HSQC (blue) with the ^{1}H-^{15}N plane of the 3D TROSY-HNCA for PBP2a. Despite overlaying well with the HSQC and a lower complexity transfer then the HN(CO)CA dataset, only ~61% of the expected correlations were detected.

The resulting spectrum (Figure 29) exhibited poor signal-to-noise and marked reduction of expected peaks correlated with the 2D TROSY-HSQC (~61%). Some partial sample unfolding was also evident over the course of the acquisition, consistent with marginal stability at the high concentrations and the extended experiment times and temperatures required for 3D data collection. Collectively, these findings confirmed that backbone assignment by amide-detected NMR was not tractable under the present conditions,

reinforcing the need to transition toward methyl-selective labelling strategies to enable residue-specific analysis of PBP2a dynamics.

3.4.4.7 TROSY-HNCACB

To confirm that all Cα/Cβ-based correlation pathways were likewise intractable, a final, short TROSY-HNCACB experiment was performed. The sequence correlates the amide group of each residue with both its intra- and inter-residue Cα and Cβ nuclei (^{15}NH(i) to ^{13}Cα/β(i) and ^{13}Cα/β(i^{-1})) where although a longer transfer series, theoretically provides richer assignment information. A 3D ^{1}H-^{15}N TROSY-HNCACB experiment (Figure 30) was acquired for 1 day 15 hours and 30 minutes for PBP2a (300 µM) at 30°C at 950 MHz with 21% non-uniform sampling (NUS). This rapid acquisition was not intended to yield a complete assignment but to serve as a diagnostic test.

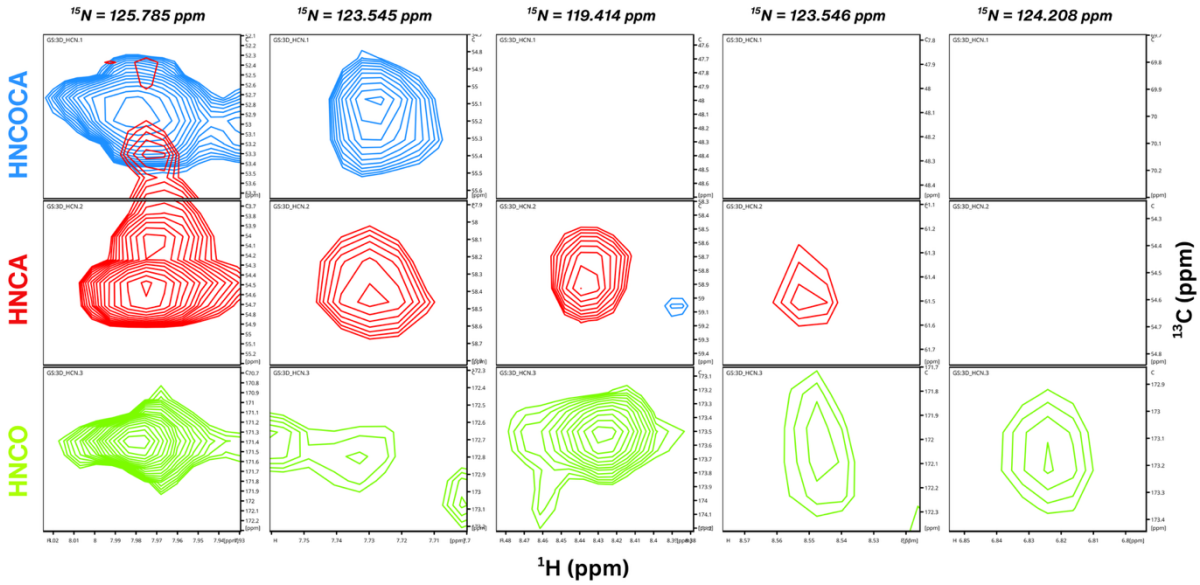

Figure 30: Comparison of representative strip plots from sequential triple-resonance experiments (HNCO, HNCA, and HN(CO)CA) recorded for perdeuterated PBP2a at 30°C on a 950 MHz spectrometer.

Each panel displays corresponding strips for selected residues illustrating the progressive loss of sensitivity and signal definition with increasing experimental complexity. The HNCO experiment (green) demonstrates the highest quality spectra, with clear, well-defined peaks and an estimated 73% correspondence to resonances observed in the 2D TROSY-HSQC. In contrast, signal intensity and peak definition decline markedly in the HNCA (~61% correspondence; red) and the HN(CO)CA spectra (blue). These data collectively illustrate the steep reduction in experimental sensitivity associated with extended coherence-transfer pathways in large molecular-weight systems such as PBP2a.

As expected for a protein of this size, the additional coherence-transfer steps of the HNCACB experiment further compromised sensitivity, resulting in extremely weak signal intensity with only a few discernible peaks above baseline and extensive noise throughout the 3D dataset. The progressive disappearance of resonances across experiments followed

the predicted relaxation-weighted order – HNCO > HNCA > HN(CO)CA/HNCACB – reflecting the cumulative effects of longer transfer delays and coherence pathways, which exacerbated the already severe transverse relaxation losses inherent to a >76 kDa system, even under TROSY and perdeuterated conditions. The markedly improved spectral quality in 2D HSQC-TROSY experiments (Figure 22-Figure 23) increasing the temperature from 25ºC to 30ºC – yielding over 200 additional resonances and significantly reduced line broadening – meant considering lower temperatures would not be a practical means of improving sample longevity. High concentrations (>300 μM), necessary to achieve adequate signal-to-noise, likely promoted non-specific self-association across hydrophobic surface patches. This was consistent with the precipitation and unfolding signatures observed following the longest 3D experiments, indicating marginal thermodynamic and colloidal stability during prolonged acquisitions at elevated temperatures. Attempts to enhance sensitivity by lowering ionic strength (< 200 mM NaCl) or increasing protein concentration (>300 μM) repeatedly resulted in visible aggregation over experiments of comparable duration.

However, despite the apparent improvement in thermal stability observed in the ThermoFluor™ screening – where the best optimised buffer formulation produced a >4ºC increase in melting temperature (T_m) and yielded improved retention of native folding in 2D TROSY-HSQC spectra acquired following 3D experiments – these optimisations were insufficient to overcome the fundamental relaxation and exchange limitations inherent to PBP2a's size and dynamics in 3D backbone experiments. Although the buffer adjustments enhanced thermostability and marginally delayed unfolding, they did not measurably improve sample longevity or signal-to-noise during extended multidimensional acquisitions and were insufficient to overcome the intrinsic relaxation and exchange limitations imposed by PBP2a's molecular weight and anisotropic tumbling. Additionally, they were unable to allow higher concentrations (~500 μM) to be maintained without visible aggregation or precipitation, where subsequent HNCO experiments conducted using T_m-optimised buffers showed no further improvement in spectral sensitivity or stability. To rationalise these observations, a structure-guided hydropathy and solvent-accessible surface area (SASA) analysis of PBP2a was performed (Figure 31). This identified short, solvent-exposed hydrophobic segments primarily around the active-site cleft (residues ~409-410), the Ω-loop edge (~467-469), and a C-terminal helical face (~527-529), along with smaller hydrophobic clusters near residues ~360, 385-390, 498-503, 558-563, and 597-601. These patches

coincide with regions of conformational mobility and interdomain interfaces, suggesting that transient "breathing" between partially open and closed conformers intermittently exposes hydrophobic cores, promoting reversible self-association under the high concentrations and long acquisition times required for amide 3D experiments.

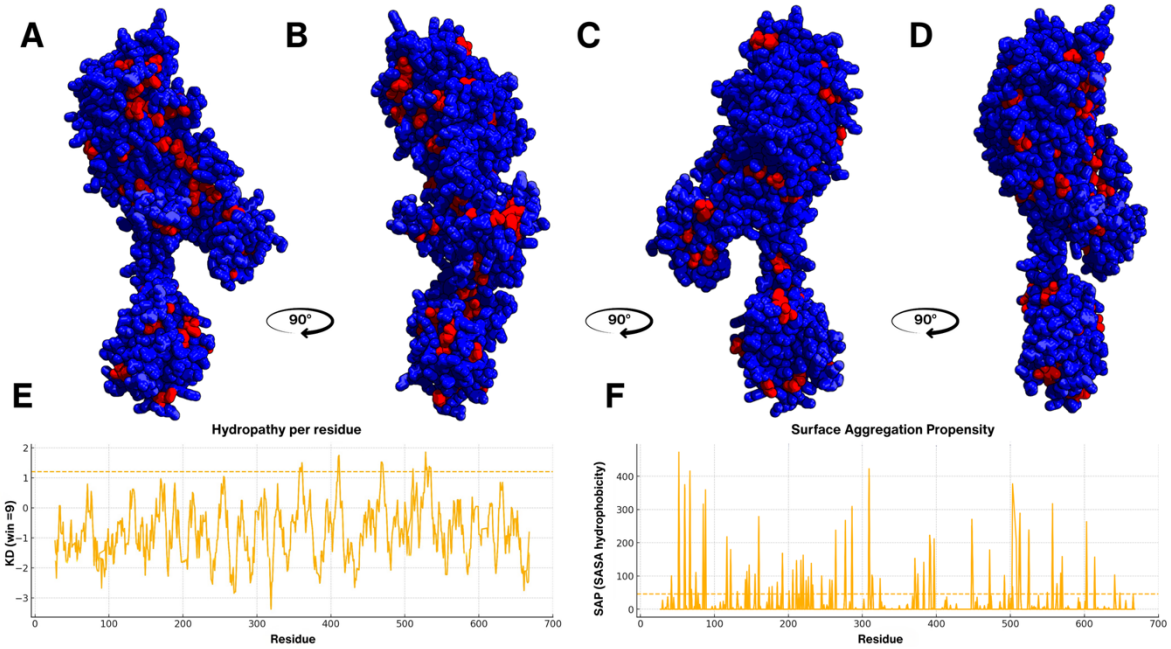

Figure 31: Hydrophobicity and surface-aggregation hot spots in PBP2a (1VQQ)[4]

Composite figure showing hydrophobic features that rationalise colloidal instability. A-D: Molecular surface coloured by a surface aggregation propensity (SAP) proxy; red marks residues in the top 10% of SAP. E: Smoothed Kyte–Doolittle hydropathy (9-residue window); the dashed line at KD = +1.2 indicates hydrophobic enrichment. F: SAP proxy (SAP = SASA × KD^{+}), where SASA is per-residue solvent-accessible surface area from a Shrake-Rupley calculation (1.4 Å probe; 60 points/$atom^{-1}$) and KD^{+} is the positive (hydrophobic) component of the KD score; the dashed line denotes the 90th percentile threshold used to define hot spots. Peaks in E-F map to the red patches in A-D highlighting discrete solvent-exposed hydrophobic segments that likely drive reversible self-association during long NMR acquisitions, with notably high density around allosteric domain binding interface (B) in the NTE and the core of the TP domain (A).

Compared with an average globular protein of similar molecular weight, PBP2a displays a slightly elevated aggregation propensity. This reflects its functional architecture: an elongated, multidomain fold with several surface-exposed hydrophobic grooves associated with its transpeptidase and allosteric sites. Whereas most cytosolic enzymes of comparable size bury 85-90 % of their hydrophobic surface area, PBP2a retains multiple exposed hydrophobic patches, likely to accommodate dynamic domain rearrangements necessary for allosteric signalling and catalysis. These features, while essential for function, render PBP2a more prone to self-association under concentrated or low-salt conditions, particularly during extended NMR acquisition where even minor unfolding or conformational sampling can nucleate aggregation. Clusters of positively charged residues within these same regions further exacerbate colloidal interactions when electrostatic screening is insufficient,

consistent with the aggregation observed at lower ionic strengths. Taken together, the instability and progressive signal attrition observed experimentally are best explained by a combination of (i) size-driven relaxation constraints, (ii) intermediate exchange dynamics within key flexible regions, and (iii) aggregation nucleated by discrete hydrophobic patches exposed during conformational fluctuations. While the foundational TROSY-HNCO 3D experiment yielded high-quality data, any experiment requiring coherence transfer to Cα and/or Cβ nuclei (HNCACB, HN(CO)CA, HNCA) failed irrespective of transfer pathway or acquisition duration. Their direct comparison (Figure 29) illustrates that the deleterious effects of transverse relaxation during longer, more complex pulse sequences are the principal limiting factor. This systematic loss of signal across all Cα-based experiments established that full backbone assignment using amide-detected approaches was impractical for this large, anisotropic system. Consequently, the experimental strategy was redirected toward methyl-selective labelling and assignment by targeted mutagenesis, which offered substantially higher sensitivity and tractability for a protein of this molecular weight which exploit the slower relaxation properties of methyl probes.

3.4.5 Methyl assignment strategies

Although the experimental strategy for resonance assignment in PBP2a considered both amide- and methyl-detected approaches, backbone (amide) assignment was prioritised initially because, if successful, it would not only provide residue-level structural information but also facilitate the straightforward assignment of methyl resonances via TOCSY-based correlations from the backbone – a far more efficient route than *de novo* methyl assignment. Several alternative strategies have been developed for the resonance assignment of large, complex proteins. These include combining assignments from smaller protein fragments[188,189], the monitoring of spectral changes following selective residue mutation[190], or correlating crystal structure coordinates with intermethyl distance restraints obtained from NOE (nuclear Overhauser enhancement) experiments[191]. However, PBP2a's architecture poses challenges for such methods. Its three domains are not discrete but are interwoven through long stretches of continuous sequence, meaning that truncation into smaller constructs would almost certainly disrupt folding and destabilise interdomain contacts, resulting in a functionally benign construct unsuitable for further study. Similarly, sequential assignment through residue-specific mutagenesis – while conceptually viable – is labour-intensive, expensive, and risks perturbing protein folding, solubility, or aggregation behaviour via the introduction of each mutagenic probe.

In recent years, automated algorithms such as MAP-XSII, FLAMEnGO2.0, MAGIC, and MAGMA have proven highly effective in assigning methyl groups of large proteins by integrating high-resolution structural models with solution-state NOE data. Among these, Methyl Assignment by Graph Matching (MAGMA) has demonstrated near-complete accuracy (up to 89% of assignable resonances) for complexes as large as 360 kDa[156], making it a particularly powerful tool for high-molecular-weight systems like PBP2a. Therefore, the next logical step was to pursue methyl-based assignment via NOESY experiments, which, if sufficient spectral quality could be achieved, would provide a more tractable and informative route to residue-specific mapping compared with mutational assignment.

3.4.5.1 1H-13C HMQC

The initial uniformly labelled spectrum (Figure 21) provided valuable proof-of-concept for methyl detection in PBP2a but was hindered by extensive overlap from all methyl-bearing residues, particularly leucine and valine. To overcome this limitation and achieve the spectral resolution required for assignment, a selective methyl-labelling strategy was implemented. PBP2a was expressed in D_2O-based minimal medium supplemented with a defined mixture of isotope-labelled precursors – [$^{13}CH_3$]-L-Alanine, [^{13}C,^{1}H]-α-ketobutyric acid, and [^{13}C,^{1}H]-α-ketoisovalerate – alongside ^{2}H,^{12}C-glucose as a carbon source (see 2.2.2.5). This scheme restricts $^{13}CH_3$ incorporation to the δ_1-methyl of isoleucine, the proS-methyls of leucine and valine, and the β-methyl of alanine, while deuterating all other non-exchangeable sites. A ^{1}H-^{13}C SOFAST-HMQC was acquired for 25 minutes for PBP2a (300 μM) with at 25°C on a 950 MHz spectrometer (Figure 32).

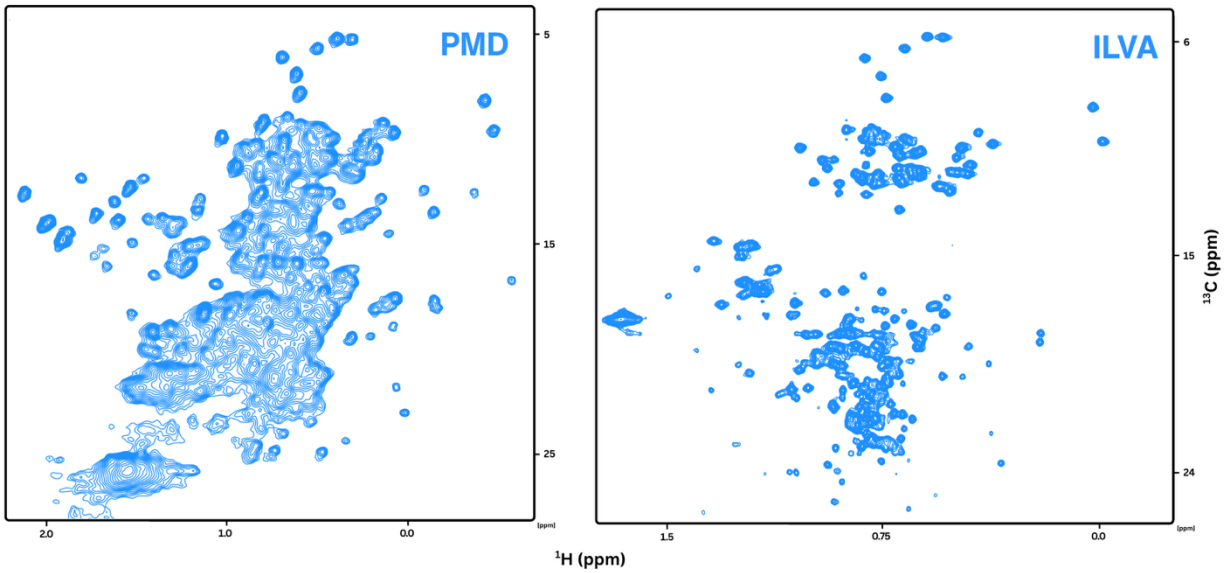

Figure 32: Comparison of ^{1}H-^{13}C SOFAST-HMQC spectrum of PBP2a with non-selective deuteration and ILVA selective labelling.

Spectra acquired for PBP2a at 30°C on a 950 MHz spectrometer. Left: uniformly ^{13}C-^{15}N-labelled PBP2a produced with "poor-man's" partial deuteration (PMD), showing extensive spectral congestion and overlap between residue-specific methyl regions (Leu/Val/Ile/Thr/Met). Right: selectively ILVA-labelled sample (ILVA), prepared using α-ketoacid precursors on a U-^{2}H background, showing markedly reduced peak density and sharper, better-resolved resonances suitable for quantitative analysis.

This targeted labelling substantially simplified the resulting spectrum by reducing the number of NMR-active methyl groups, eliminating stereochemical ambiguity, and improving relaxation properties, yielding sharper, well-separated peaks across the spectral window relative to initial non-selective labelling (Figure 32, Left). Moreover, the absence of heterogeneous CH_2D and CHD_2 isotopomers – which, in the uniformly labelled sample, produced mixed couplings and subtle chemical-shift dispersion – further enhanced spectral homogeneity and consistency of cross-peak positions. The combination of reduced isotopic heterogeneity, improved sensitivity, cleaner dispersion, and faster acquisition (25 min vs >16 h) established this ILVA-selective approach as the optimal labelling strategy for subsequent methyl-methyl NOE experiments and quantitative analyses of ligand-induced chemical-shift perturbations.

3.4.5.2 NOESY

To obtain inter-residue distance information for structural mapping and methyl resonance assignment, a three-dimensional ^{13}C-edited NOESY-HSQC was acquired for PBP2a (150 µM) with the same labelling scheme as Figure 32 at 25°C for 4 days and 18 hours on a 950

MHz spectrometer with 40% non-uniform sampling (NUS) (Figure 33). This experiment detects through-space ^{1}H-^{1}H nuclear Overhauser effects (NOEs) between methyl groups while using ^{13}C editing to selectively include only those protons bound to ^{13}C atoms, effectively isolating methyl-methyl cross-peaks. Given the availability of multiple high-resolution crystal structures of PBP2a (e.g. 1VQQ[4]), these NOE-derived distance correlations were intended to be used for structure-based methyl assignment via comparison with predicted inter-methyl distances calculated from PDB coordinates using MAGMA or related computational methods for automated assignment. Methyl NOEs are particularly valuable in large molecular systems such as PBP2a, as methyl groups retain favourable relaxation properties even at high molecular weights. Their rotational freedom allows longer transverse relaxation times (T_2), while their relatively short correlation times (τ_c) and slow dipolar relaxation enable the detection of cross-peaks that remain visible when most amide signals are broadened beyond detection.

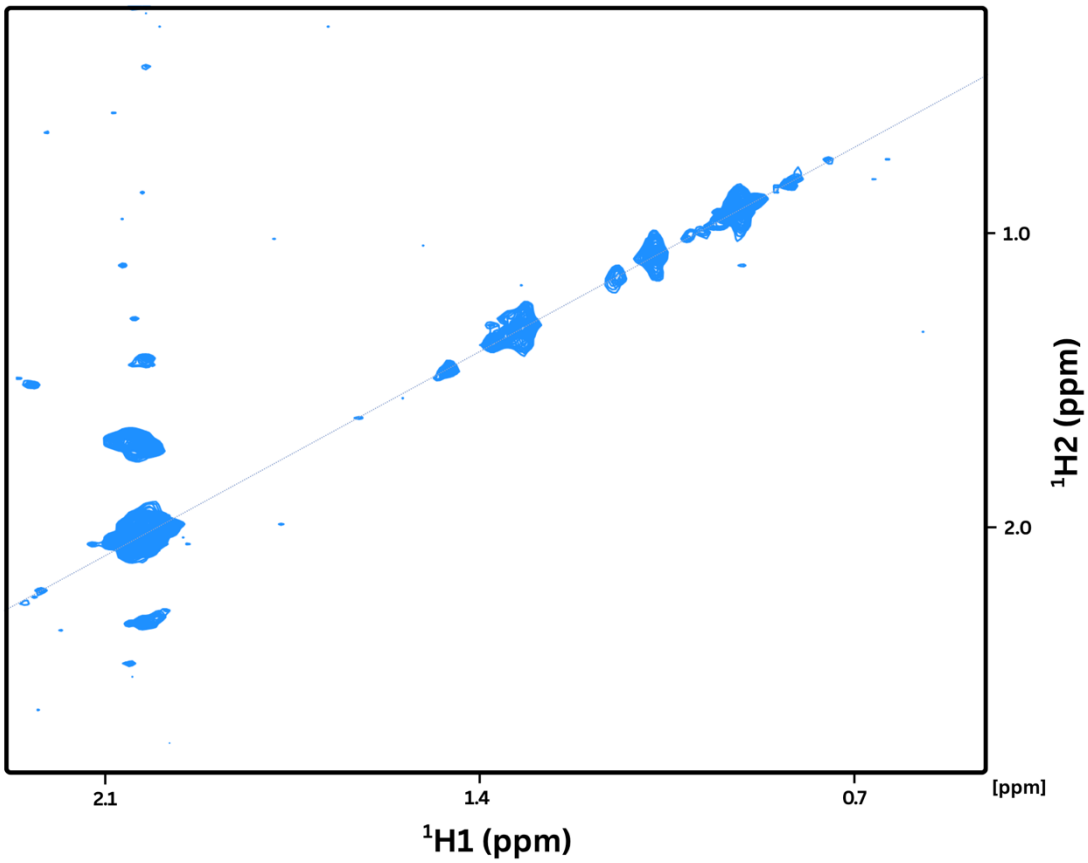

Figure 33: ^{13}C-edited NOESY-HSQC spectrum of ILVA-labelled PBP2a showing limited inter-methyl NOE connectivity despite extended acquisition

A ^{13}C-edited NOESY-HSQC recorded for ILVA-labelled PBP2a (300 µM) at 25ºC on a 950 MHz spectrometer, with 40% non-uniform sampling (NUS) to improve digital resolution and reduce acquisition time. The experiment was acquired over 4 days and 18 hours with a mixing time optimised for methyl-methyl NOE detection. An insufficient number of off-diagonal cross-peaks corresponding to through-space ^{1}H-^{1}H NOE interactions between spatially proximal methyl groups were observed for further automated assignment.

Although strong diagonal peaks are seen, almost no discernible off-diagonal cross-peaks are evident, indicating an absence of detectable inter-methyl NOEs. This limited cross-relaxation efficiency likely reflects the combination of slow molecular tumbling, rapid transverse relaxation, and incomplete magnetisation transfer inherent to a >76 kDa system, even under perdeuterated and selectively labelled conditions. Despite prior optimisation of temperature, buffer composition, and ionic strength, as well as implementation of NUS to enhance sensitivity, the experiment failed to yield sufficient cross-peak density for structure-based methyl assignment. Efficient NOE build-up depends critically on three factors: (i) sufficient overall sensitivity, (ii) optimal NOE mixing times long enough to permit cross-relaxation but short enough to avoid relaxation losses, and (iii) stable, monodisperse protein throughout prolonged data collection. In the case of PBP2a, the combination of extended acquisition periods, long mixing times, and intrinsically slow molecular tumbling markedly exacerbated transverse relaxation. As a result, only a handful of off-diagonal peaks were observed following NUS reconstruction, many of which were weak, distorted, or inconsistent across replicate points. The final cross-peak network fell well below the density threshold required for structure-based methyl assignment tools such as MAGMA or MAGIC, both of which rely on a sufficiently connected NOE matrix to resolve unique solutions.

This loss of inter-methyl connectivity was likely compounded by strained sample stability under the required conditions. As established during earlier backbone assignment attempts, despite buffer optimisations, PBP2a displayed slow aggregation at concentrations ≥300 μM and for long acquisitions (>48 hr), evident from progressive loss of dispersion and signal collapse into the random-coil region (^{1}H ≈ 8.0-8.5 ppm). Even at more modest temperatures 25^{o}C or lower concentrations (150 μM), subtle unfolding over the four-day acquisition likely altered relaxation properties and line shapes over time. Because non-uniform sampling (NUS) reconstruction assumes static line shapes, any time-dependent changes in peak intensity or width can introduce artefacts and missing peaks, reducing reconstruction fidelity. NUS is particularly effective for sparse spectra with adequate signal-to-noise (S/N), however, in this experiment, low S/N ratio in the ^{13}C dimension likely limited the recovery of weak NOEs. Consequently, the reconstructed spectrum was dominated by strong diagonal peaks, while weaker, longer-range NOEs were lost or obscured by noise. The resulting dataset therefore lacked sufficient information for automated assignment and distance restraint generation. Collectively, these findings confirmed that despite prior optimisation of

labelling, temperature, buffer, and acquisition parameters, the size and relaxation behaviour of PBP2a impose fundamental limitations on 3D NOE-based approaches. The experiment nonetheless provided valuable insight into the boundaries of feasible NMR strategies for this system, justifying the transition to selective mutagenesis of isoleucine residues for targeted methyl assignment and downstream functional studies.

3.4.6 Partial assignment of PBP2a via isoleucine-selective $^{13}C_{\partial 1}$ labelling

3.4.6.1 Protein expression and purification for methyl assignment

Given the substantial challenges encountered in assigning PBP2a using both conventional amide-based and alternative methyl-NOESY approaches, a single-residue substitution strategy was adopted to facilitate targeted assignment of methyl resonances. Isoleucine residues were chosen as the focus of this approach, representing the most numerous of the ILVA methyl-bearing species (n = 55). Additionally, their widespread distribution across the structure also positioned them well as reporters of domain-specific dynamics and ligand-induced conformational change. Several isoleucine sites are located in regions of recognised structural or mechanistic significance – such as I314, adjacent to R297 and the ceftaroline-binding interface within the allosteric domain, and I407, proximal to the catalytic S403 in the transpeptidase (TP) active site – making them valuable probes for mechanistic mapping.

Due to budgetary constraints, 34 of the 55 isoleucine residues were targeted for mutation to glycine (Ile to Gly), ensuring representative coverage across all major structural domains while prioritising residues with either computationally predicted functional relevance or prior clinical association with resistance phenotypes. Codon-optimised plasmids encoding

each single mutant were synthesised by a commercial provider (Twist Bioscience, San Francisco, USA; Figure 34).

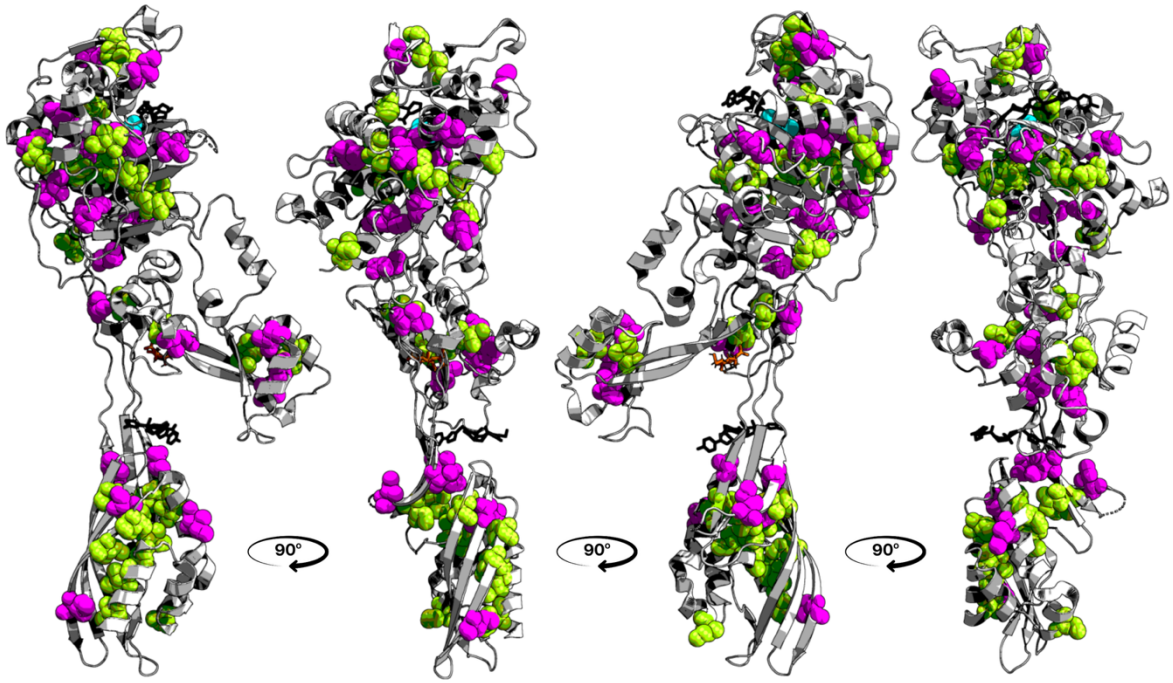

Figure 34: Spatial distribution and sequence positions of isoleucine residues in PBP2a (PDB ID: 1VQQ)[4].

360° Cartoon representations of PBP2a displaying all assigned (magenta) and unassigned (green) isoleucine residues displayed as spheres. The catalytic serine (Ser403) is displayed as spheres (cyan), ceftaroline is displayed as black sticks non-covalently-bound in the allosteric domain and covalently-bound in the active site, and muramic acid is displayed as orange sticks near the inter-domain hinge in the core of the allosteric domain between lobes 1 and 2. Ceftaroline and muramic acid are modelled from aligning 3VG0[5] with the apo structure, 1VQQ).

For higher throughput expression to compensate for the limited stability of PBP2a over extended experimental periods, the protein expression and purification workflow was redesigned to maximise yield and processing speed. Purification was performed using His SpinTrap™ centrifugal affinity columns (Cytiva Life Sciences, 28401353) following a modified manufacturer protocol (see 2.2.2.6), allowing rapid purification of multiple mutants in parallel and prompt preparation of fresh, high-purity protein samples for NMR analysis (Figure 35):

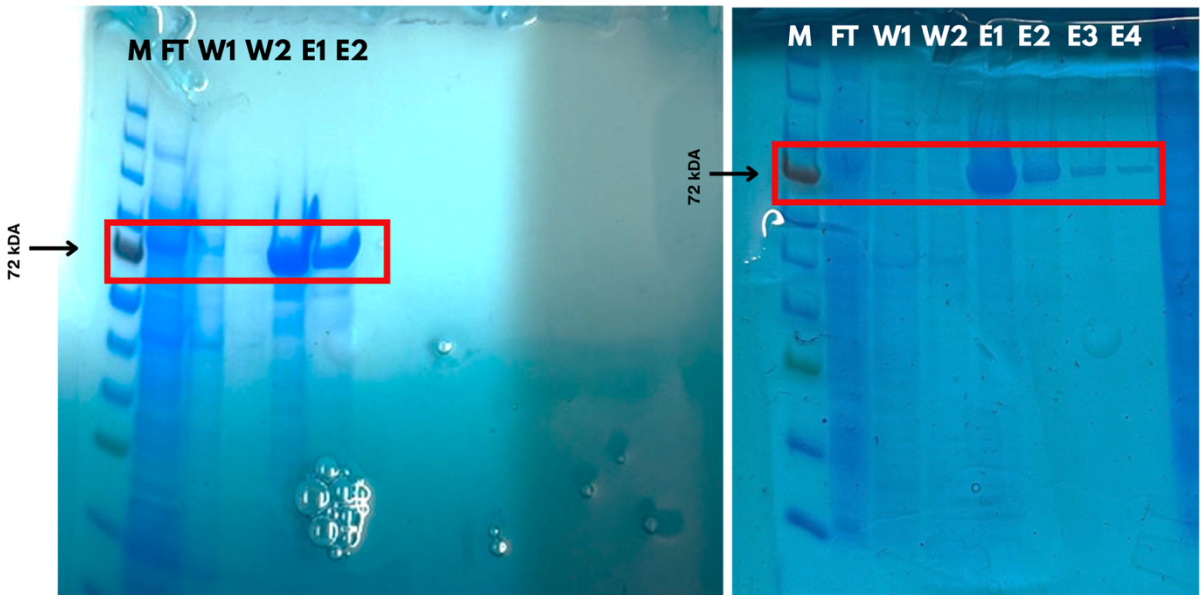

Figure 35: SDS-PAGE of modified His SpinTrap™ Ni-NTA purification of selectively labelled isoleucine mutants of PBP2a for assignment by selective mutagenesis

Comparison of SDS-PAGE pre-/post-optimisation (left/right) displaying enhanced protein elution following the modified (right) Vs manufacturer (left) protocol. M: 11-250 kDa protein standard, FT: flow through, W: wash fractions, E: elution fractions. Expected migration region for PBP2a highlighted by the red box.

Each Ile mutant was expressed as a 50 mL culture for efficiency and cost management. The typical yield following the purification of 50 mL of culture grown in fully deuterated media with selective ^{13}C-^{1}H labelling for Ile δ_1-CH_3 post-purification was ≈ 2.4 mg of purified PBP2a, sufficient to produce 300-330 µL samples at 90-110 µM. Using the modified purification protocol allowed for the complete purification and preparation of PBP2a for further study via NMR spectroscopy within 4-5 hours with a two-step workflow, as opposed to previous methods which utilised an AKTA-driven Ni-NTA primary purification step and a secondary size exclusion chromatography (HiLoad® 26/600 Superdex® 200 pg) step which required considerably greater time due to larger volumes from both size exclusion and of sample requiring buffer exchange and concentration. The modified protocol minimised protein loss between stages, produced sufficiently pure protein, and enhanced sample longevity, resulting in higher quality spectra.

For each single isoleucine-to-glycine (Ile>Gly) mutant, a 2D ^{1}H-^{13}C SOFAST-HMQC spectra were recorded at 15°C on a 950 MHz spectrometer with ~90-110 µM of perdeuterated PBP2a with selective ^{1}H-^{13}C labelling at the Ile δ_1. The acquisition temperature was optimised to 15 °C to maximise sample longevity over multi-hour measurements. Unlike amide-detected experiments, methyl detection is insensitive to backbone amide exchange

and, in a perdeuterated background, benefits from more favourable T_2 relaxation rates. A wild-type reference spectrum was recorded as a baseline (Figure 36):

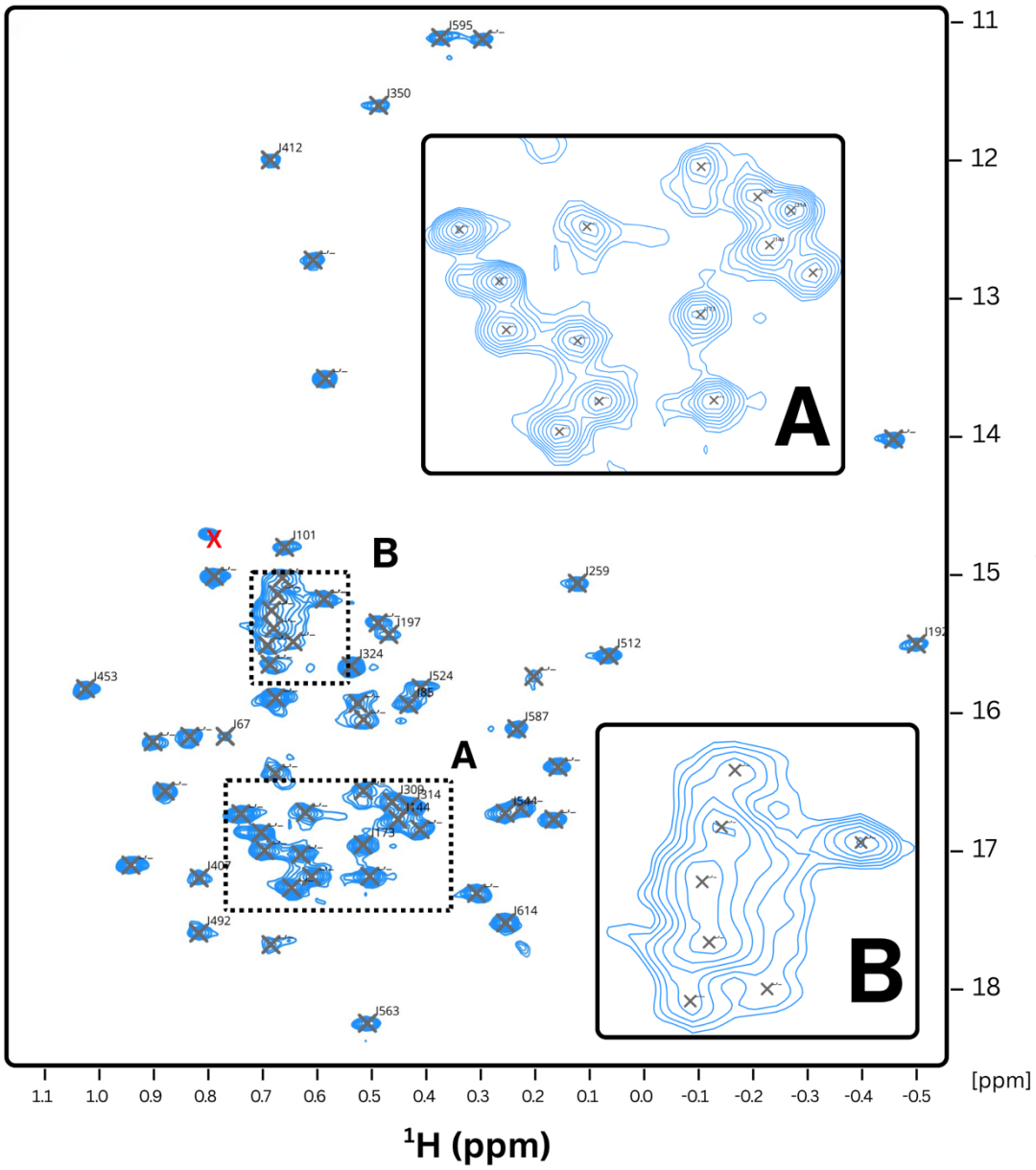

Figure 36: Wild-type 2D ^{1}H-^{13}C SOFAST-HMQC (methyl-optimised) spectrum of Ile δ1-labeled PBP2a.

2D ^{1}H-^{13}C SOFAST-HMQC spectrum of wild-type PBP2a (110 µM; Ile δ_1-^{1}H^{13}CH$_3$ labelling) recorded at 15°C at 950 MHz, in NMR buffer (Table 4). Peaks with confident assignments are annotated with single letter code. Insets show representative crowded regions (A/B). A pseudo peak that is inconsistent with previous WT spectra is highlighted with a red cross and is to be disregarded hereafter.

The reference spectrum showed excellent dispersion with minimal overlap, consistent with a well-folded protein and efficient precursor incorporation. A total of 61 Ile δ_1 resonances were observed of the 55 expected, most plausibly from some crowded regions with

significant overlap (e.g. Figure 36A). Typical acquisitions (~4 hr) yielded sufficient signal-to-noise for robust WT-mutant comparisons.

The principle underlying a selective mutagenesis strategy is straightforward: by systematically substituting individual isoleucine residues with glycine, the resonance corresponding to that specific isoleucine is selectively removed from the ^{1}H-^{13}C HMQC spectrum as only Ile δ_1 groups have been ^{1}H-^{13}C labelled. Each mutant spectrum is subsequently compared directly with that of the wild type under identical conditions, and the absence or attenuation of a single peak identifies the resonance position of the substituted residue, resulting in unambiguous residue identification. By repeating this process across multiple mutants, individual isoleucine resonances can be sequentially assigned throughout the structure, providing a set of well-distributed, site-specific probes suitable for subsequent ligand-binding and dynamics experiments. The first mutant I67 provides a straightforward assignment (Figure 37):

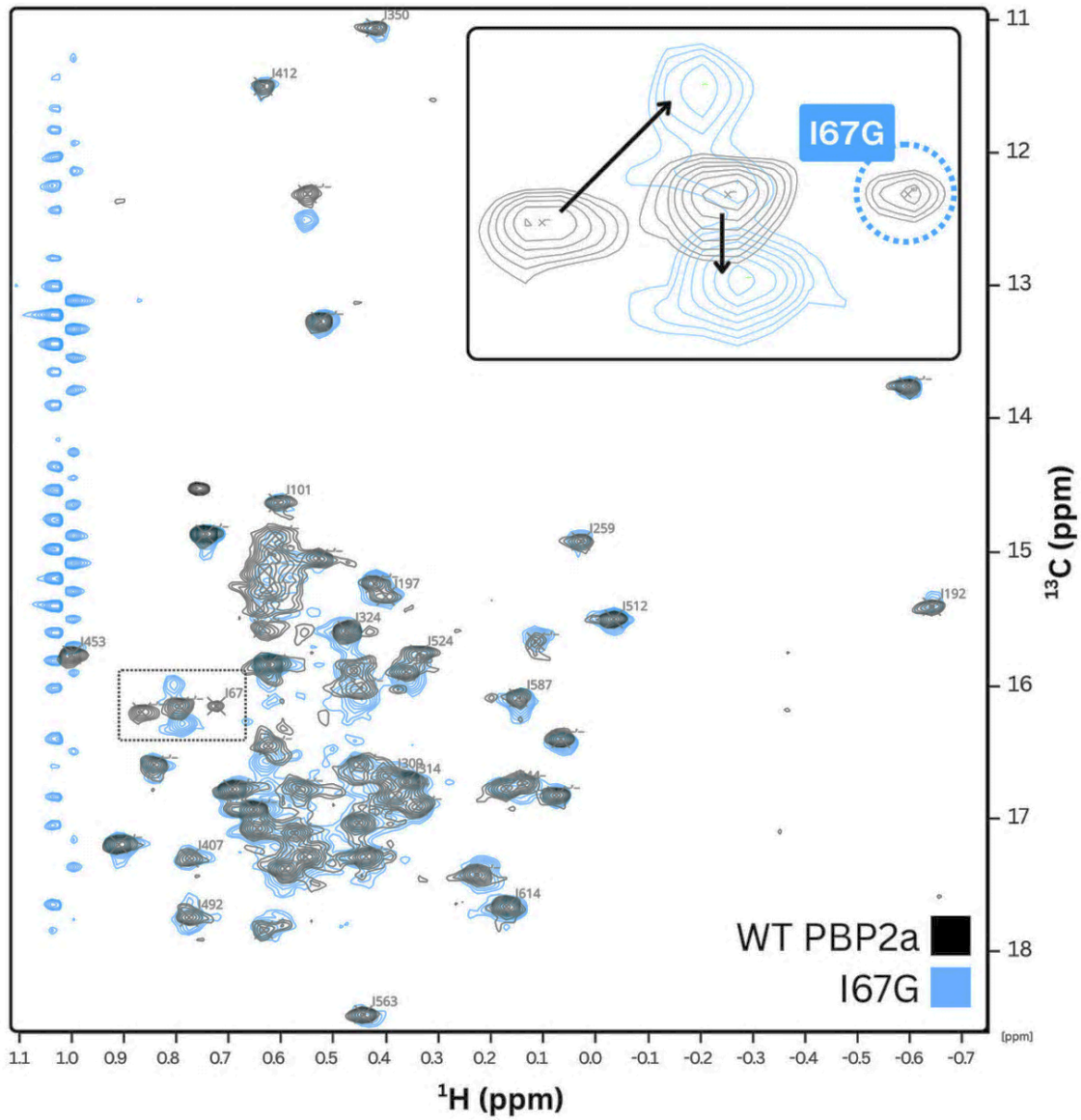

Figure 37: Assignment by selective mutagenesis (I67G) shows disappearance of a single Ile δ^1 peak in SOFAST-HMQC

Overlay of wild-type (black) and I67G mutant (blue) 2D ^{1}H-^{13}C SOFAST-HMQC spectra (110 µM; Ile δ_1-^{1}H^{13}CH$_3$ labelling) recorded at 15°C at 950 MHz, in NMR buffer. All subsequent mutants can be assumed as being treated the same, unless stated otherwise. Peaks with confident assignments are annotated with single letter code. The WT peak at δ^{1}H = 0.76 ppm, δ^{13}C = 16.34 ppm (circled) is not visible in the I67G spectrum while all other peaks are present, giving a clear assignment. Arrows mark minor CSPs for nearby Ile sites which are noted but not used for this assignment.

Overall, the I67G spectra overlaid closely with the wild-type reference, indicating that the amino acid substitution did not induce any major structural perturbations or compromise the global fold of PBP2a. Unless otherwise stated, this is assumed for each mutant unless otherwise stated. The WT peak at δ^{1}H = 0.76 ppm, δ^{13}C = 16.34 ppm (circled) is not visible in the I67G spectra while all other peaks remain visible, providing a clear indication that this peak originates from I67G. The peak can therefore be confidently assigned as that residue. Additionally, two unassigned WT peaks (δ^{1}H = 0.888 ppm, δ^{13}C = 16.385 ppm and δ^{1}H =

0.822 ppm, $\delta^{13}C$ = 16.346 ppm) showed chemical shift perturbations (CSPs) in the I67G mutant but retained peak intensity, consistent with indirect local perturbations (Figure 38):

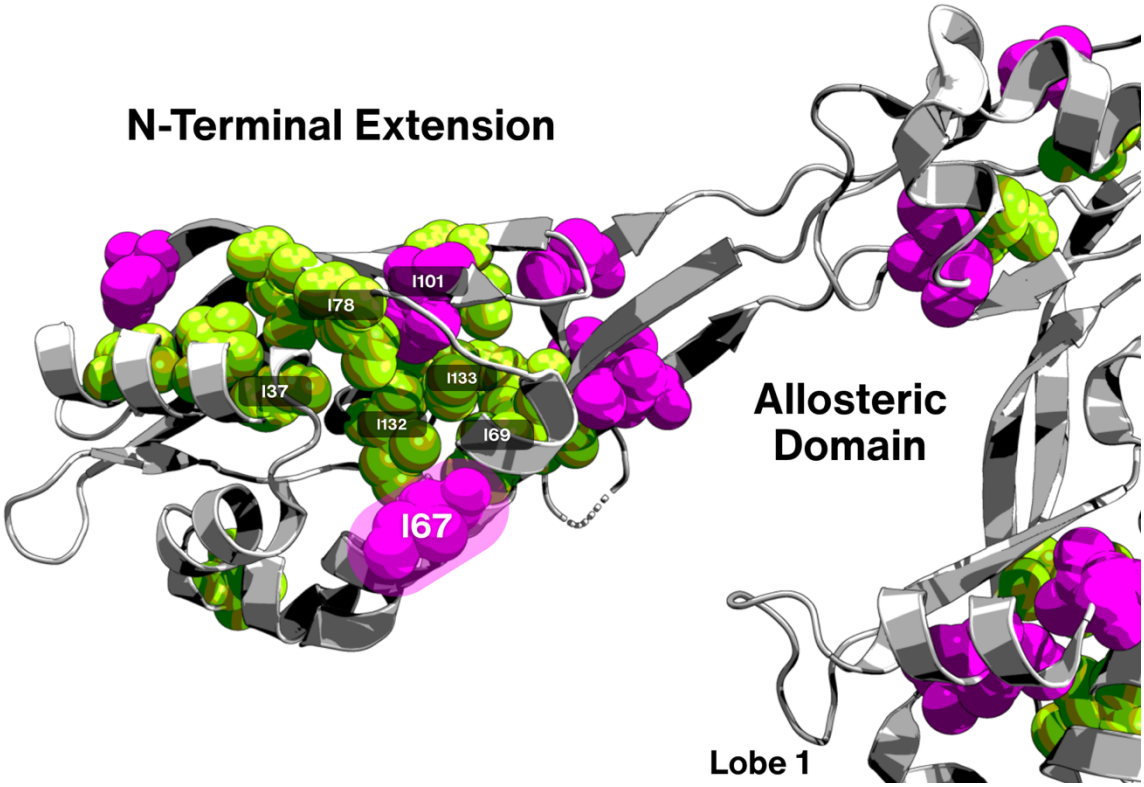

Figure 38: Structural mapping of potential assignment candidates for resonances with chemical shift perturbations nearby the I67G mutant of PBP2a (PDB ID: 1VQQ)[4].

Assigned (magenta) and unassigned (green) isoleucines are displayed as spheres. This colouring can be assumed for all assignment visualisations unless otherwise stated. I67 is highlighted in a magenta hue. Isoleucines <15 Å (Cα-Cα) of I67 are annotated as potential candidates for other peaks with significant CSPs noted in Figure 36. I69 (5.5 Å) and I132 (9.5 Å) are the closest in proximity and the most likely candidates.

Several residues are nearby (<15 Å) residue I67, therefore it is possible that those peaks showing CPSs may represent residues I37, I69, I78, I101, I132, and I133; with I69 (5.5 Å) and I132 (9.5 Å) being closest in proximity. It is most likely that these two residues correspond to the two other unassigned resonances exhibiting significant CSPs unassigned in Figure 37, however it is not possible to unambiguously determine which peak is from which residue from the existing data. I85G provided another unambiguous assignment (Figure 39):

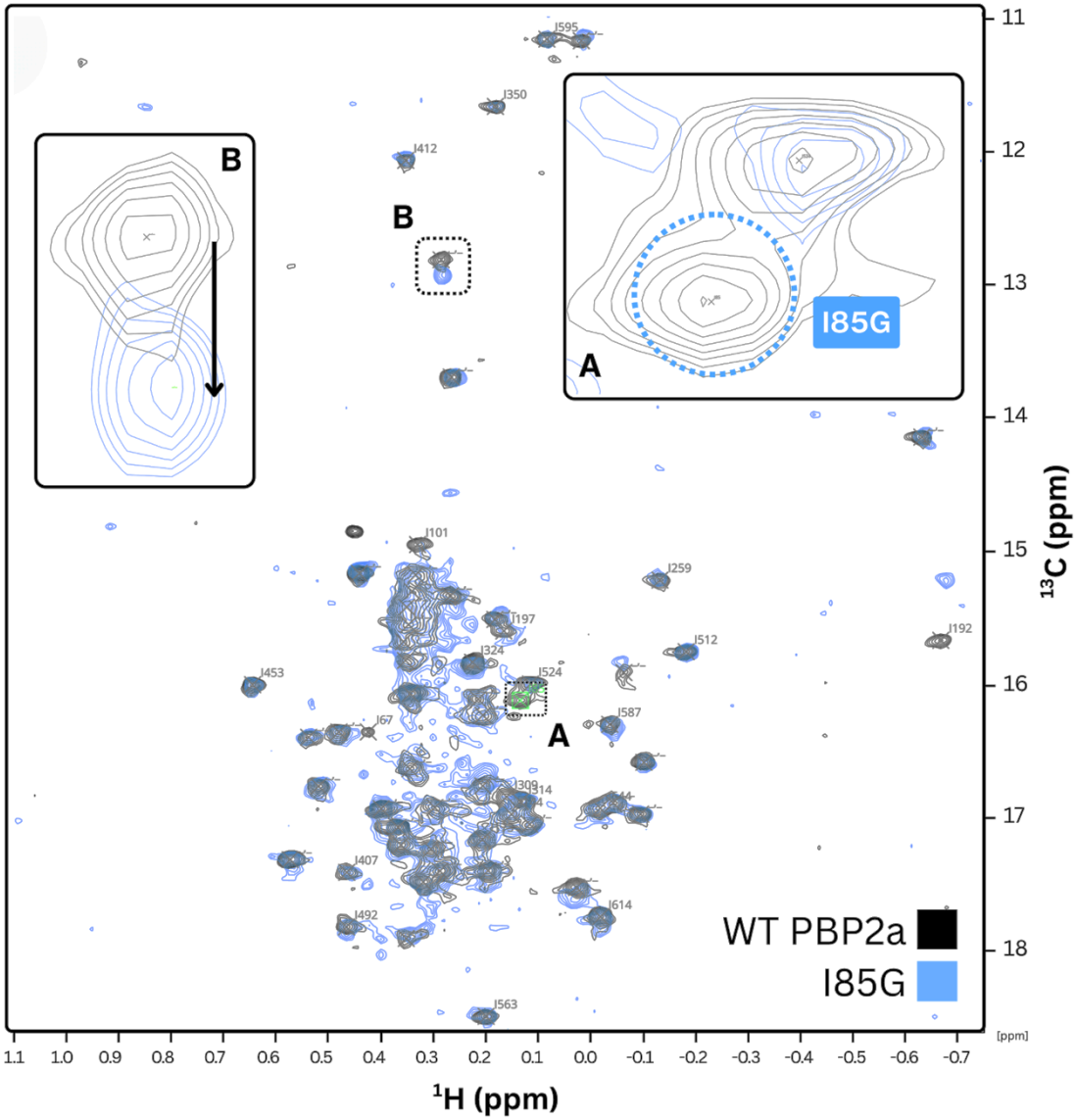

Figure 39: Assignment by selective mutagenesis (I85G) shows disappearance of a single Ile δ1 peak in SOFAST-HMQC

Overlay of wild-type (black) and I85G mutant (blue) 2D ^{1}H-^{13}C SOFAST-HMQC spectra. Peaks with confident assignments are annotated with single letter code. Insets display A, the WT peak at δ^{1}H = 0.423 ppm, δ^{13}C = 16.109 ppm (circled) disappears in I85G, giving a clear assignment, and B, an unassigned peak with a notable CSP at δ^{1}H = 0.597 ppm, δ^{13}C = 12.810 ppm with arrows marking the CSP.

The WT peak at δ^{1}H = 0.423 ppm, δ^{13}C = 16.109 ppm disappears unambiguously (Figure 39 – inset A) and is the only peak evident to do so in the mutant spectrum, providing a definitive assignment for I85G. The peak assigned to I192 displays a notable CSP however it is not close in structure nor does I85 see any CSPs in either of the I173G, I192G or I197V spectra. Additionally, one peak (δ^{1}H = 0.591 ppm, δ^{13}C = 12.926 ppm, Figure 39 - inset B) in the I85G spectrum shows a CSP relative to the WT (δ^{1}H = 0.597 ppm, δ^{13}C = 12.810 ppm where closer inspection of nearby unassigned Ile residues provides further context (Figure 40):

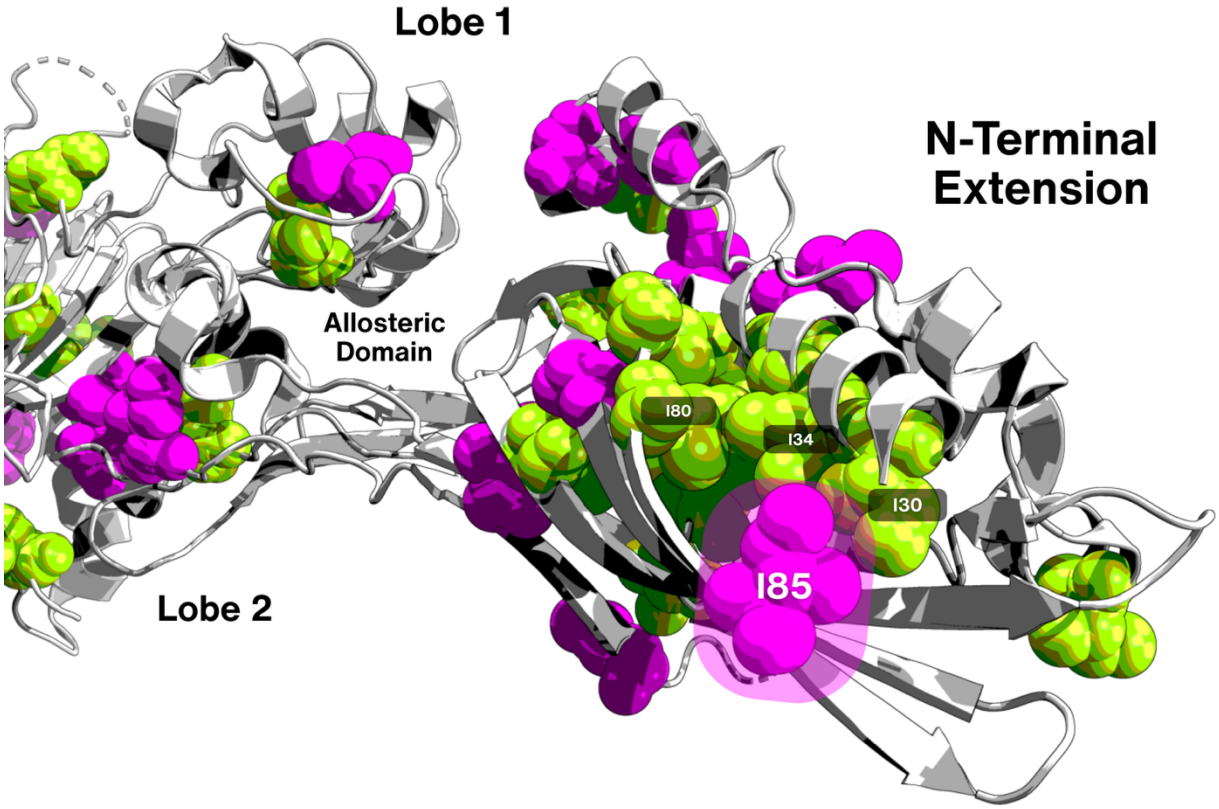

Figure 40: Structural mapping of potential assignment candidates for resonances with chemical shift perturbations nearby the I85G mutant of PBP2a (PDB ID: 1VQQ)[4].

I85 is highlighted in a magenta hue. Isoleucines <15 Å (Cα-Cα) of I85 are annotated as potential candidates for other peaks with significant CSPs noted in Figure 39. I30 (9.0 Å) and I34 (11.6 Å) are the closest in proximity and the most likely candidates.

Several residues are nearby (<15 Å) residue I85 (Figure 40), where it is likely that the remaining unassigned CSP in Figure 39 may be either I30, I34, or I80; with I30 (9.0 Å) and I34 (11.6 Å) being closest in proximity. It is likely that this resonance is one of these two candidates, however it is not possible to unambiguously determine which peak is from which residue without further analyses. I101G provided another unambiguous assignment (Figure 41):

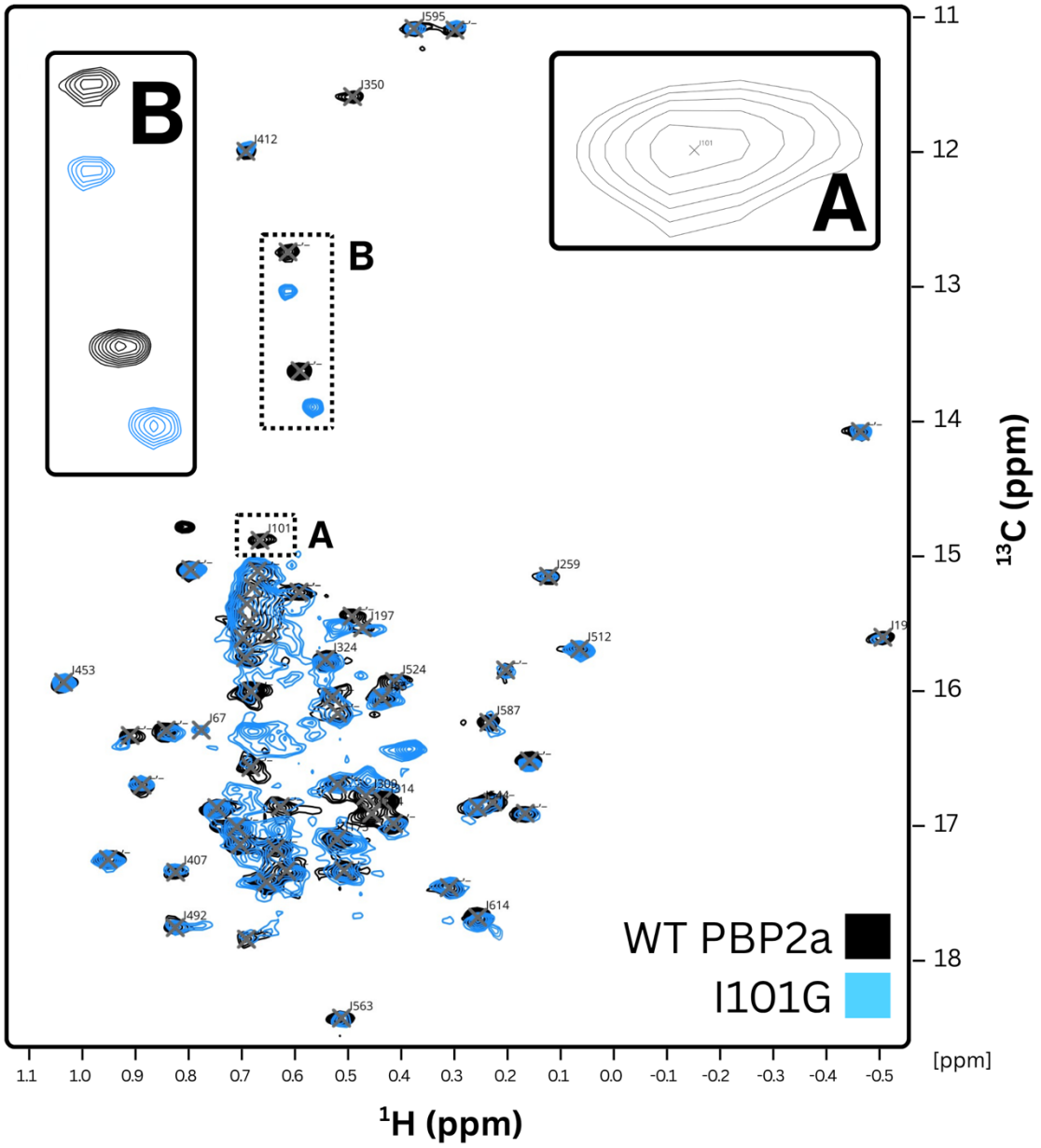

Figure 41: Assignment by selective mutagenesis (I101G) shows disappearance of a single Ile δ1 peak in SOFAST-HMQC

Overlay of wild-type (black) and I101G mutant (green) 2D ^{1}H-^{13}C SOFAST-HMQC spectra. Peaks with confident assignments are annotated with single letter code. Insets display A, the WT peak at $\delta^{1}H = 0.649$ ppm, $\delta^{13}C = 14.942$ ppm (circled) disappears in I101G, giving a clear assignment, and B, two unassigned peaks with notable CSPs from the WT peaks at $\delta^{1}H = 0.575$ ppm, $\delta^{13}C = 13.689$ ppm and $\delta^{1}H = 0.597$ ppm, $\delta^{13}C = 12.810$ ppm with arrows marking the CSPs.

The WT peak at $\delta^{1}H = 0.649$ ppm, $\delta^{13}C = 14.942$ ppm disappears (Figure 41 – inset A), and although the peak assigned to I350 has disappeared, this has been confidently assigned elsewhere, providing an clear assignment for I101G. I350 was found to be a particularly weak peak under the acquisition times used for these spectra and is to be considered accordingly for future spectra moving forward. Additionally, two peaks are noted in the I101G mutant spectra with notable CSPs relative from their WT equivalents at $\delta^{1}H = 0.575$

ppm, $\delta^{13}C$ = 13.689 ppm and $\delta^{1}H$ = 0.597 ppm, $\delta^{13}C$ = 12.810 ppm. Inspection of the WT PBP2a structure reveals several potential nearby iles which could be candidates for these peaks (Figure 42):

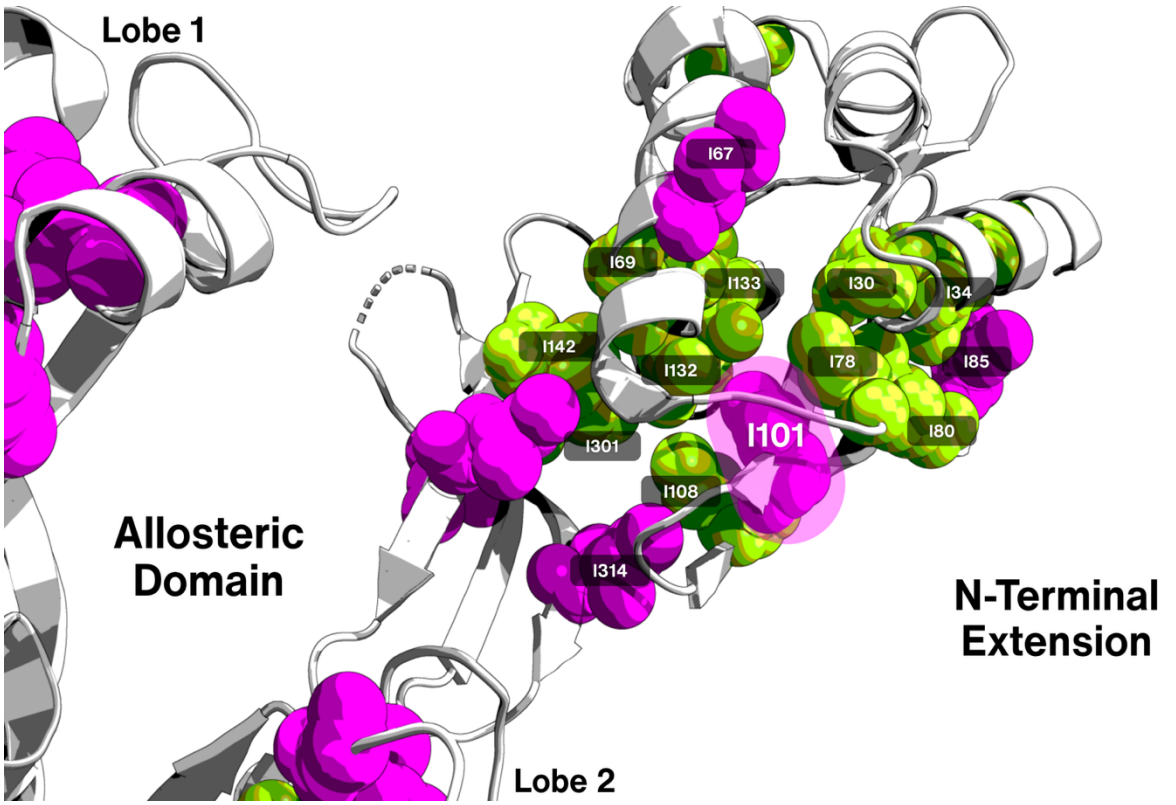

Figure 42: Structural mapping of potential assignment candidates for resonances with chemical shift perturbations nearby the I101G mutant of PBP2a (PDB ID: 1VQQ)[4].

I101 is highlighted in a magenta hue. Isoleucines <15 Å (Cα-Cα) of I101 are annotated as potential candidates for other peaks with significant CSPs noted in Figure 41. I78 (4.6 Å) and I108 (4.6 Å) are the closest in proximity.

Several unassigned Ile residues are nearby (<15 Å) I101, including (in decreasing order of distance) I301, I67, I142, I34, I69, I37, I314, I132, I133, I80, I78, and I108. Notably, CSPs are observed in the peak at δ^1H = 0.597 ppm, $\delta^{13}C$ = 12.810 ppm (WT position) in both I85G and I101G mutant spectra with a larger CSP observed in the I101G spectra relative to I85G ($\delta^{13}C$ = +0.300 ppm and $\delta^{13}C$ = +0.115 ppm relative to the WT respectively). As such, given that Ile residues I78 (I101: 4.6 Å, I85: 17.5 Å) and I80 (I101: 8.5 Å, I85: 11 Å) have the closest shared proximity, relative to other nearby unassigned Ile residues, it is possible that this resonance corresponds with one of these two candidates; with I80 potentially being the more likely candidate considering it being directly on the path between I101G and I85G. Potential candidates for the other WT peak at δ^1H = 0.575 ppm, $\delta^{13}C$ = 13.689 ppm with a notable CSP is most likely I108 being closest in proximity (4.6 Å – Figure 42). Residues I30 or I34 are less likely candidates, owing to similar CSPs noted in I44 (Figure 48), I309 (Figure 49) and I314 (Figure 50) which are further removed from I101, and are therefore more ambiguous choices for assignments. However, these putative assignments suggested require further verification. The spectra for the I173G, I192G, and I197V mutants each showed well-resolved spectra with the disappearance of a single, clearly identifiable cross-peak, enabling

unambiguous assignment of these residues. All three spectra exhibited CSPs in highly similar regions, where given close spatial proximity of I173, I192, and I197, these mutants were analysed collectively to interpret local structural coupling effects. The disappearance of a single peak was noted in the I173G spectrum (Figure 43):

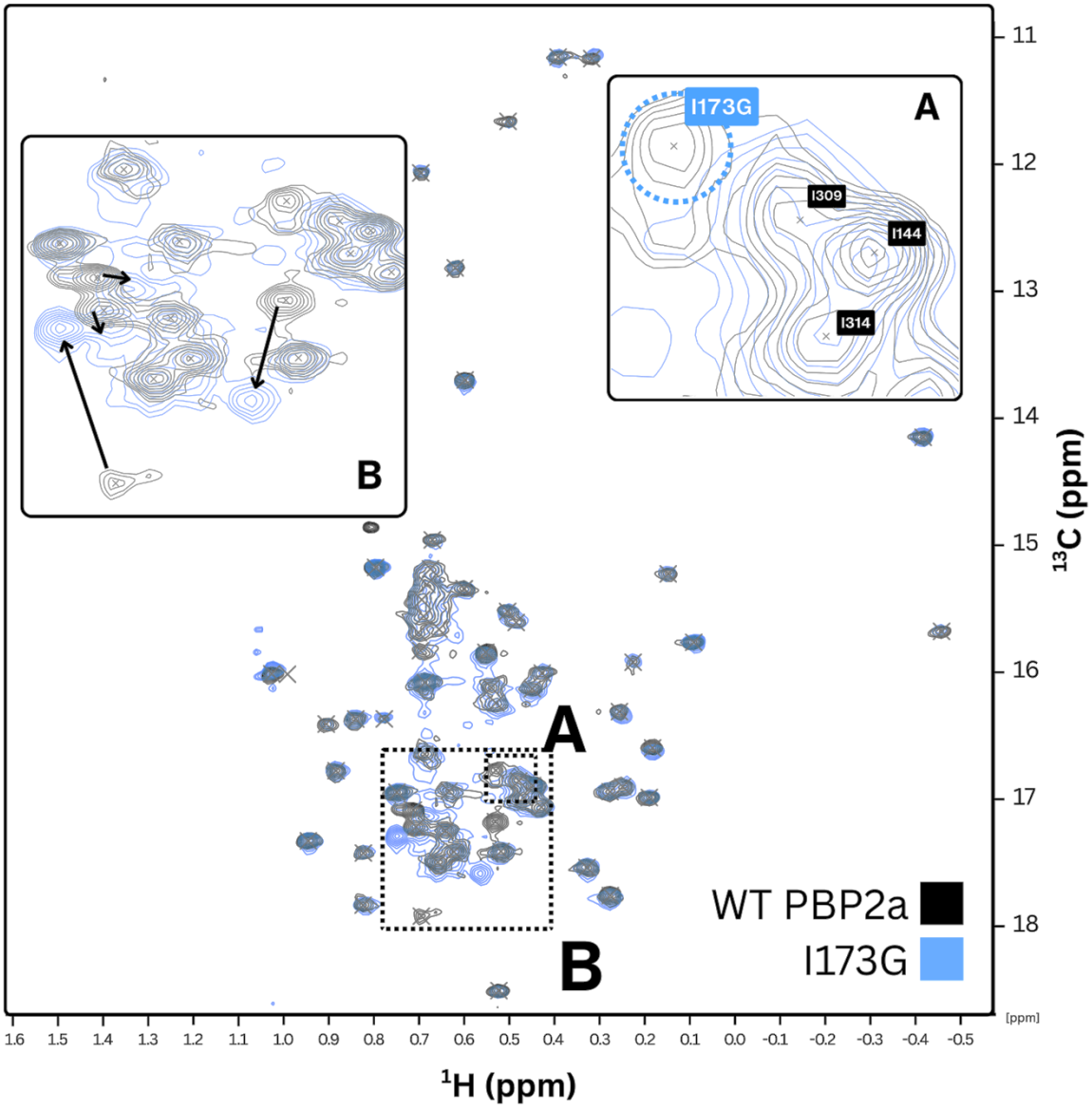

Figure 43: Assignment by selective mutagenesis (I173G) shows disappearance of a single Ile δ1 peak in SOFAST-HMQC

Overlay of wild-type (black) and I173G mutant (blue) 2D ^{1}H-^{13}C SOFAST-HMQC spectra. Peaks with confident assignments are annotated with single letter code. Insets display A, the WT peak at δ^{1}H = 0.506 ppm, δ^{13}C = 16.748 ppm (circled) disappears in I173G, giving a clear assignment, and B, several notable CSPs are noted in four unassigned Ile resonances, marked with arrows.

The WT peak at δ^{1}H = 0.506 ppm, δ^{13}C = 16.748 ppm (Figure 43 – inset A) disappears in the I173G spectrum and is confidently assigned as I173G as all other peaks are visible. Additionally, several other CSPs are evident (Figure 43 – inset B) in similar resonances in both I192G (Figure 44) and I197V (Figure 45) mutant spectra, as discussed below:

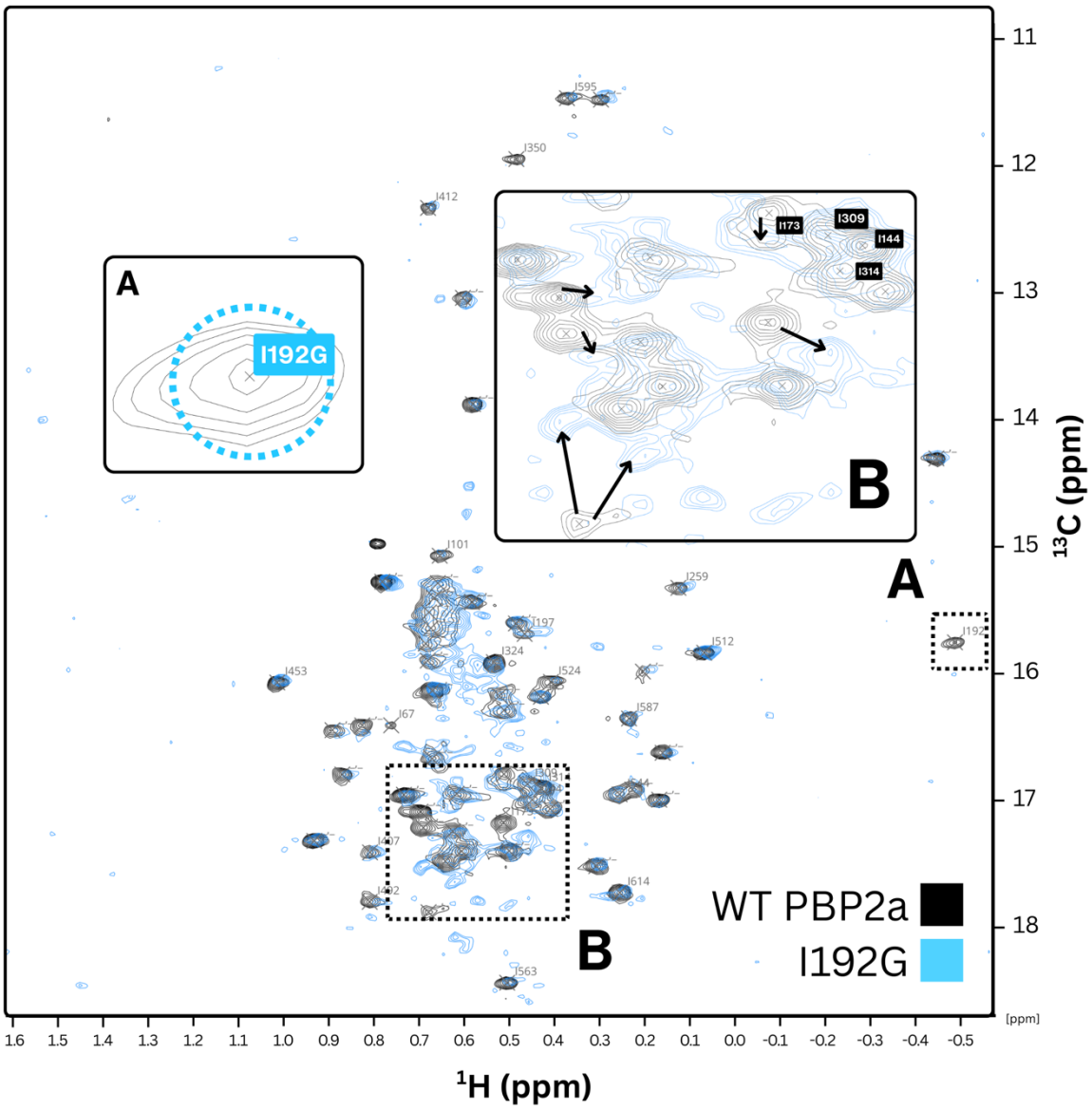

Figure 44: Assignment by selective mutagenesis (I192G) shows disappearance of a single Ile δ1 peak in SOFAST-HMQC

Overlay of wild-type (black) and I192G mutant (blue) 2D ^{1}H-^{13}C SOFAST-HMQC spectra. Peaks with confident assignments are annotated with single letter code. Insets display A, the WT peak at $\delta^{1}H$ = -0.501 ppm, $\delta^{13}C$ = 15.659 ppm (circled) disappears in I192G, giving a clear assignment, B, several notable CSPs are noted in four unassigned Ile resonances, marked with arrows.

The WT peak at $\delta^{1}H$ = -0.501 ppm, $\delta^{13}C$ = 15.659 ppm (circled) is not present in the I192G spectrum, providing an unambiguous assignment of that peak for I192 (Figure 44 – inset A). A notable CSP is observed in the previously assigned residue I173G (Figure 44 – inset B), and a small CSP is seen in I197, consistent with the close structural proximity between I192 and I173 (7.32 Å) and I197 (7 Å). Additionally, several CSPs are evident (Figure 44 – inset B) among unassigned Ile residues shared with the I173G (Figure 43) and I197V (Figure 45) mutant spectra, the latter of which also shows a clear assignment:

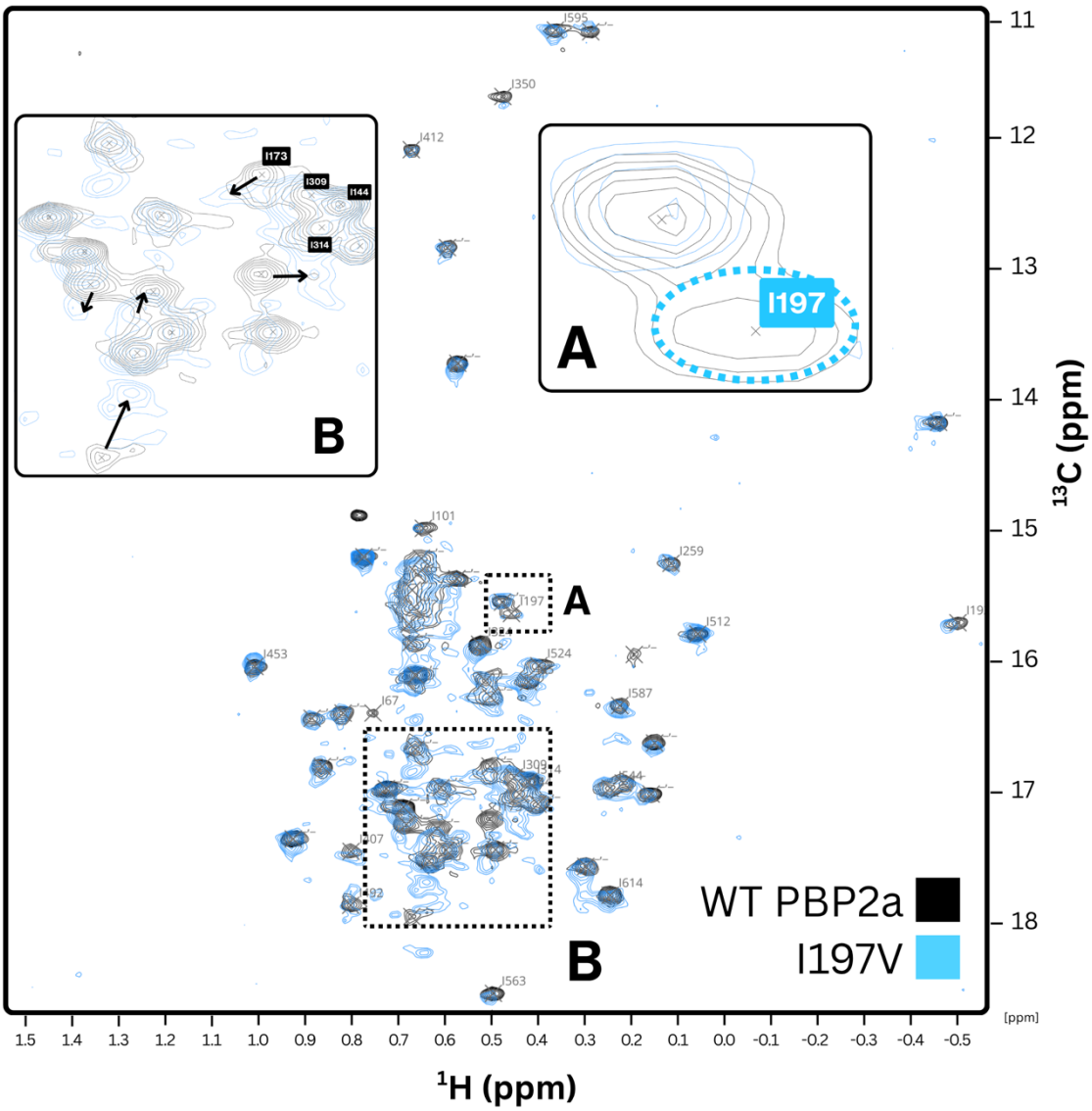

Figure 45: Assignment by selective mutagenesis (I197V) shows disappearance of a single Ile δ1 peak in SOFAST-HMQC

Overlay of wild-type (black) and I197V mutant (blue) 2D ^{1}H-^{13}C SOFAST-HMQC spectra. Peaks with confident assignments are annotated with single letter code. Insets display A, the WT peak at δ^{1}H = 0.459 ppm, δ^{13}C = 15.589 ppm (circled) disappears in I197V, giving a clear assignment.

The WT peak at δ^{1}H = 0.459 ppm, δ^{13}C = 15.589 ppm (circled) disappears in the I197V spectrum, providing an unambiguous assignment (Figure 45 – inset A). A notable CSP is observed in residue I173G (Figure 45 – inset B), consistent with the close structural proximity between I173 and I197 (5.00 Å). No CSP is noted for I192 in this spectrum, likely due to the more conservative I>V substitution. However, interestingly, the I173G spectra does not show CSPs for either I197 or I192. Additionally, notable CSPs are observed in four unassigned Ile peaks (Figure 45 – inset B), most of which are shared with I173G and I192G mutant spectra. Structural analysis reveals two potential assignment candidates nearby (Figure 46):

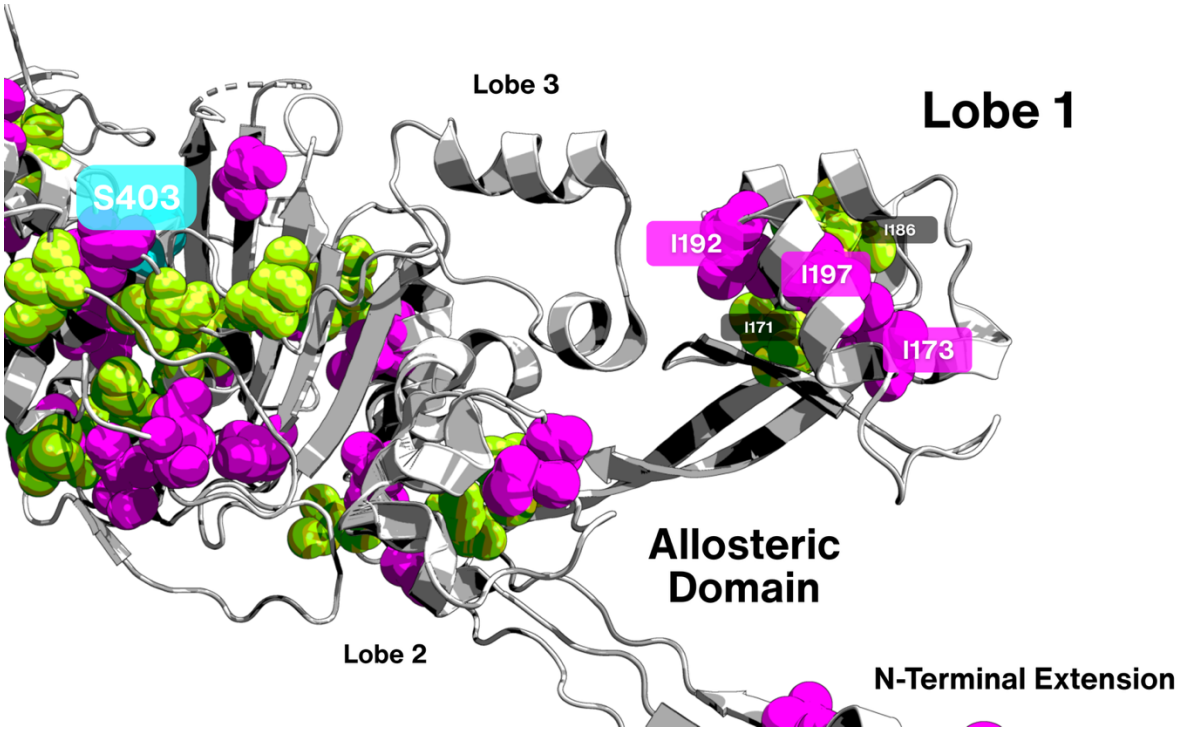

Figure 46: Structural mapping of potential assignment candidates for resonances with chemical shift perturbations nearby assigned residues I173, I192 and I197 of PBP2a (PDB ID: 1VQQ)[4].

I192, I173 and I197 are shown as spheres (magenta), with neighbouring Ile residues as likely candidates for the CSPs noted within Figure 45 (I171 and I186) annotated on green spheres.

Given that four notable CSPs are evident between the I173G, I192G and I197V mutant spectra, it is difficult to make definitive estimations of which CSPs are attributable to the two unassigned residues within close spatial proximity (I171; <12 Å and I186; <10 Å). However, given that the largest CSPs shared between spectra are evident in peaks $\delta^{1}H$ = -0.506 ppm, $\delta^{13}C$ = 17.150 ppm and $\delta^{1}H$ = 0.674 ppm, $\delta^{13}C$ = 17.891 ppm, it is likely that these two are potential candidates. The remaining peaks are likely attributable to global architectural changes, given the considerable flexibility noted in Lobe 1 following binding with peptidoglycan and/or ceftaroline noted by previous authors[5-7], as well as recent simulations that have evidenced Lobe 1 as a key dynamic region with significant RMSF differences between apo and ceftaroline-bound PBP2a in both open and closed states[97]. The I259G spectra provided another unambiguous assignment (Figure 47):

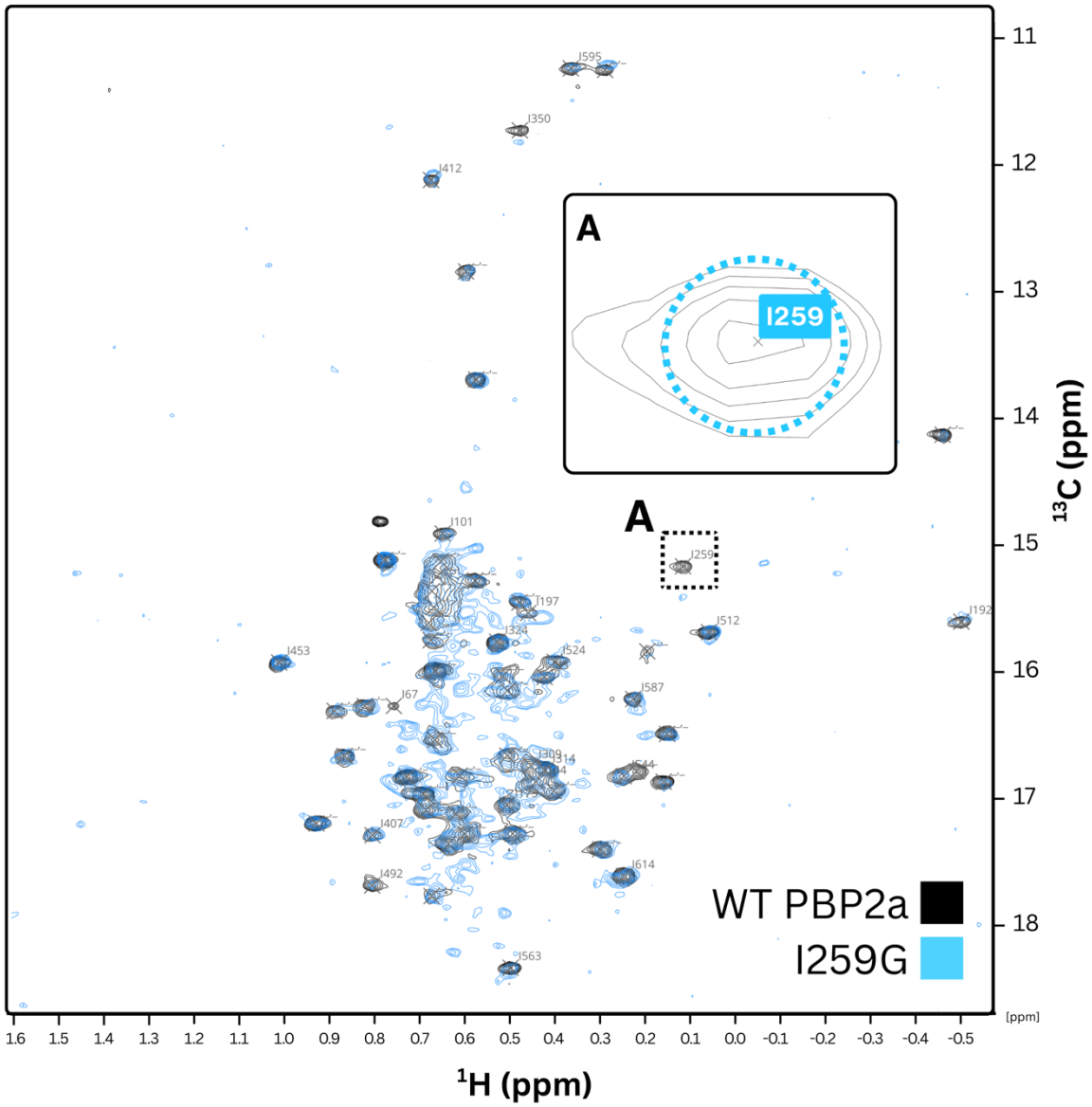

Figure 47: Assignment by selective mutagenesis (I259G) shows disappearance of a single Ile δ1 peak in SOFAST-HMQC

Overlay of wild-type (black) and I259G mutant (blue) 2D ^{1}H-^{13}C SOFAST-HMQC spectra. Peaks with confident assignments are annotated with single letter code. Insets display A, the WT peak at δ^{1}H = 0.116 ppm, δ^{13}C = 15.208 ppm (circled) disappears in I259G, giving a clear assignment.

Albeit a weaker spectrum with less signal-to-noise versus other mutants, likely due to a lower concentration sample (73 µM), the I259G spectra compares well with the WT spectrum. The WT peak at δ^{1}H = 0.116 ppm, δ^{13}C = 15.208 ppm disappears unambiguously (Figure 47–inset A), providing a definitive assignment for I259G. Initial attempts to express I144G were unsuccessful, wherein, owing to the proximity of I144 to the ceftaroline binding interface (Figure 8), an alternative mutant was commercially developed – I144V – guided by *in silico* mutagenesis mapping of conservative mutations (Figure 71) and it was unambiguously assigned (Figure 48):

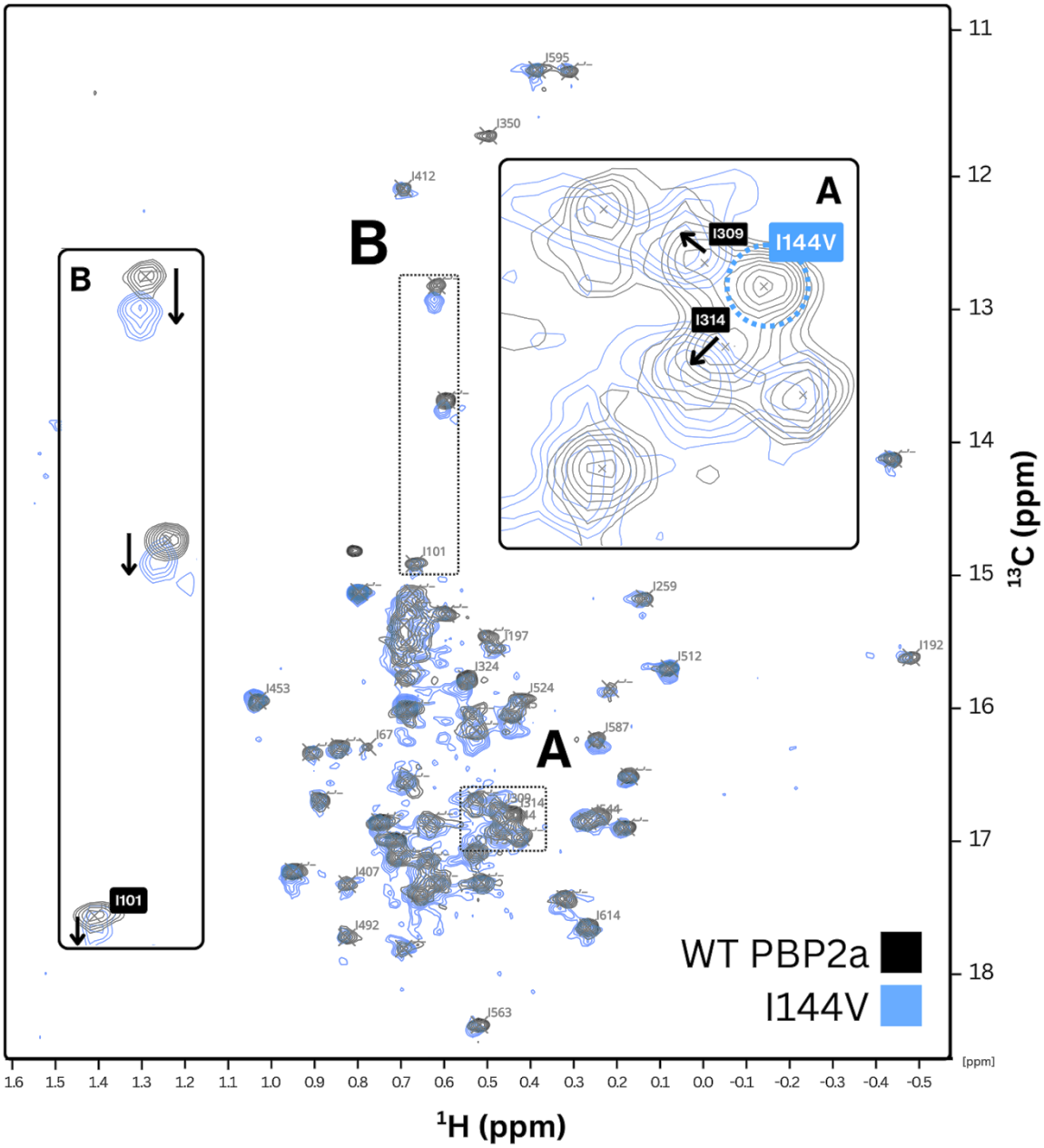

Figure 48: Assignment by selective mutagenesis (I144V) shows disappearance of a single Ile δ1 peak in SOFAST-HMQC

Overlay of wild-type (black) and I144VG mutant (blue) 2D ^{1}H-^{13}C SOFAST-HMQC spectra. Peaks with confident assignments are annotated with single letter code. Insets display A, the WT peak at $\delta^{1}H = 0.423$ ppm, $\delta^{13}C = 16.868$ ppm (circled) disappears in I144V, giving a clear assignment, and B, two unassigned peaks with notable CSPs at $\delta^{1}H = 0.597$ ppm, $\delta^{13}C = 12.810$ ppm and $\delta^{1}H = 0.575$ ppm, $\delta^{13}C = 13.689$ ppm, and another assigned peak (I101) with a smaller CSP with arrows marking the CSPs.

The WT peak at $\delta^{1}H = 0.423$ ppm, $\delta^{13}C = 16.868$ ppm (circled) disappears in the I144V spectrum, providing an unambiguous assignment (Figure 48 – inset A). Although I350 appears absent, this is due to contour level adjustment to remove noise. Notable CSPs are observed in two peaks (Figure 48 – inset B) that are similar to those observed in the spectra

of the I101G (Figure 41), I309G (Figure 49) and I314V (Figure 50) mutants spectra, discussed below.

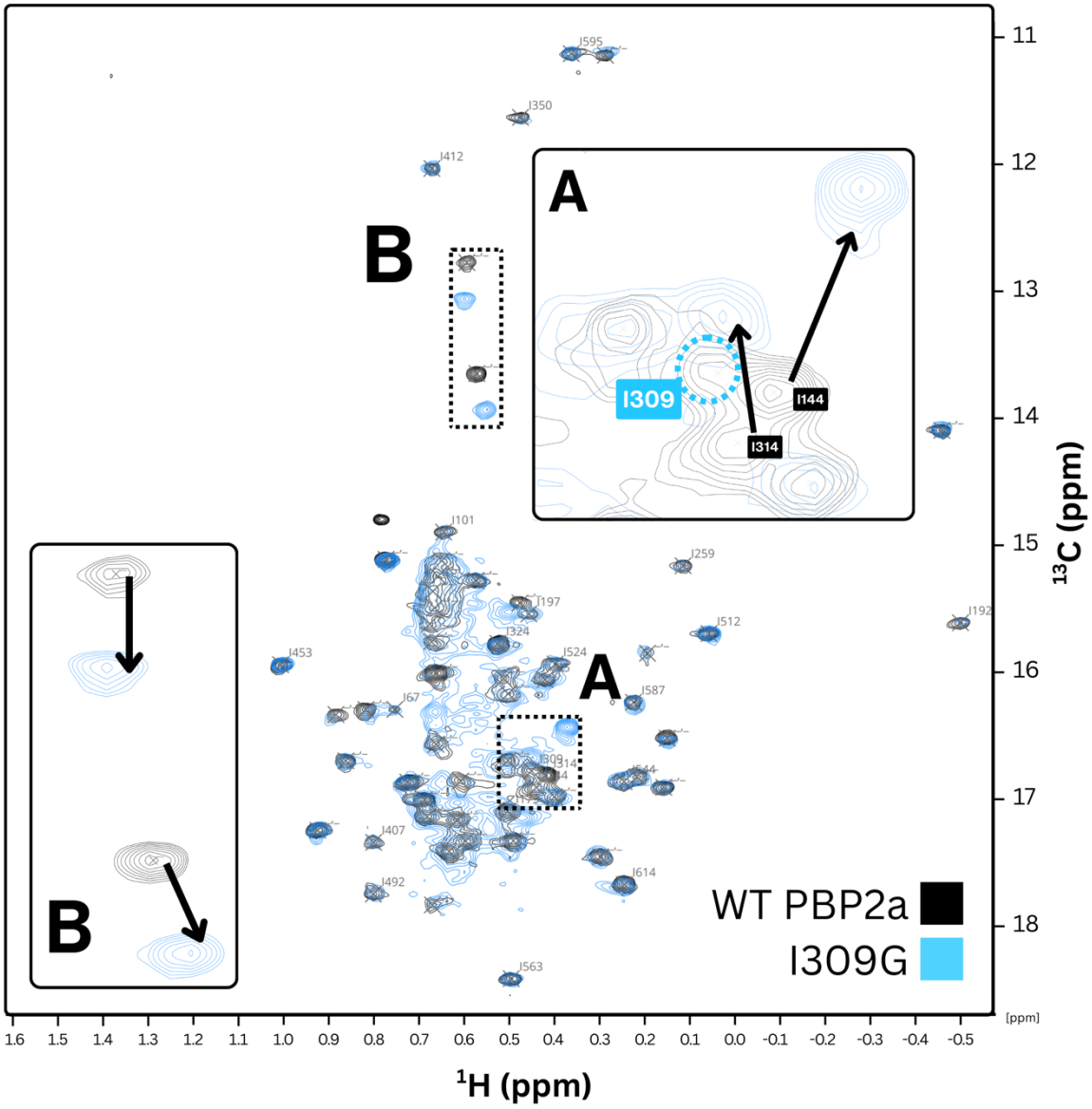

Figure 49: Assignment by selective mutagenesis (I309G) shows disappearance of a single Ile δ1 peak in SOFAST-HMQC

Overlay of wild-type (black) and I309G mutant (blue) 2D ^{1}H-^{13}C SOFAST-HMQC spectra. Peaks with confident assignments are annotated with single letter code. Insets display A, the WT peak at δ^{1}H = 0.453 ppm, δ^{13}C = 16.831 ppm (circled) disappears in the I309G mutant spectrum with two other assigned peaks (I314 and I144) showing notable CSPs, owing to their close structural proximity. Inset B shows two unassigned peaks with notable CSPs at δ^{1}H = 0.597 ppm, δ^{13}C = 12.810 ppm and δ^{1}H = 0.575 ppm, δ^{13}C = 13.689 ppm, with arrows marking the CSPs that appear in spectra of other nearby assigned residues.

Some noise is evident in the central region of the spectrum however this is likely signal-to-noise related which isn't evident at higher contour levels and each resonance is in good keeping with the reference spectrum. The WT peak at δ^{1}H = 0.453 ppm, δ^{13}C = 16.831 ppm (circled) disappears in the I309G spectrum, notable CSPs are observed in two assigned peaks (I144 and I314; Figure 49 – inset A) as well as two peaks (Figure 49 – inset B) that are shared

in I101G (Figure 41), I144V (Figure 46) and I314V (Figure 50) mutant spectra, one of which ($\delta^{13}C$ = ~13 ppm) is also seen in I67G (Figure 37) and I85G (Figure 37). Further confidence in the I309G assignment is derived from the I314V spectrum (Figure 50):

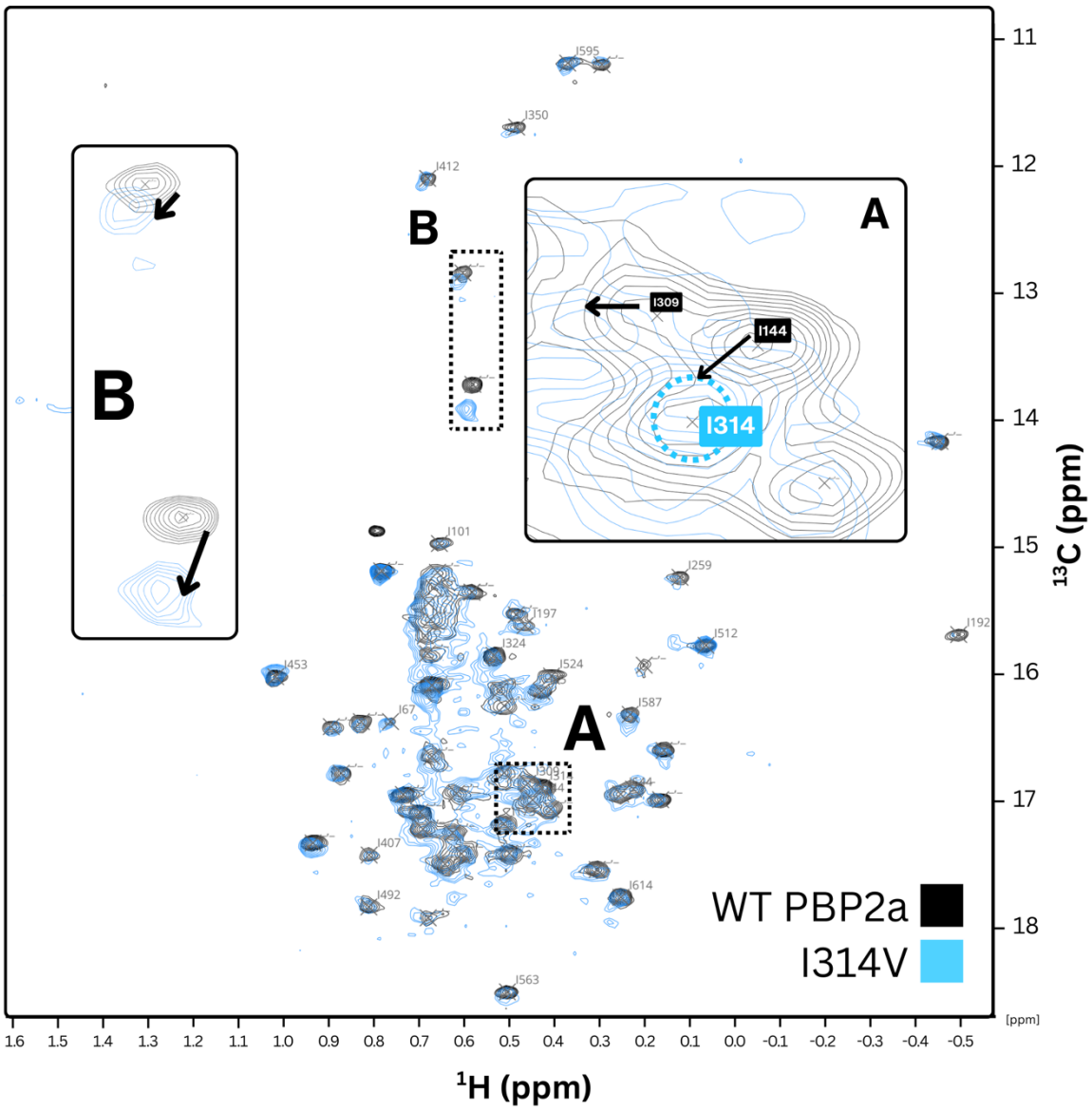

Figure 50: Assignment by selective mutagenesis (I314V) shows disappearance of a single Ile δ1 peak in SOFAST-HMQC

Overlay of wild-type (black) and I314V mutant (blue) 2D ^{1}H-^{13}C SOFAST-HMQC spectra. Peaks with confident assignments are annotated with single letter code. Insets display A, the WT peak at $\delta^{1}H$ = 0.443 ppm, $\delta^{13}C$ = 16.961 ppm (circled) disappears in I314V, in concert with the I144 peak shifting into its position, and B, two unassigned peaks with notable CSPs at $\delta^{1}H$ = 0.597 ppm, $\delta^{13}C$ = 12.810 ppm and $\delta^{1}H$ = 0.575 ppm, $\delta^{13}C$ = 13.689 ppm, with arrows marking the CSPs.

The WT peak at $\delta^{1}H$ = 0.443 ppm, $\delta^{13}C$ = 16.961 ppm (circled) disappears in the I314V spectra, whilst the I144 peak shifts approximately to its same position (Figure 50– inset A). Closer inspection of their spatial proximity provides further justification for the I144, I309 and I314 assignments (Figure 51):

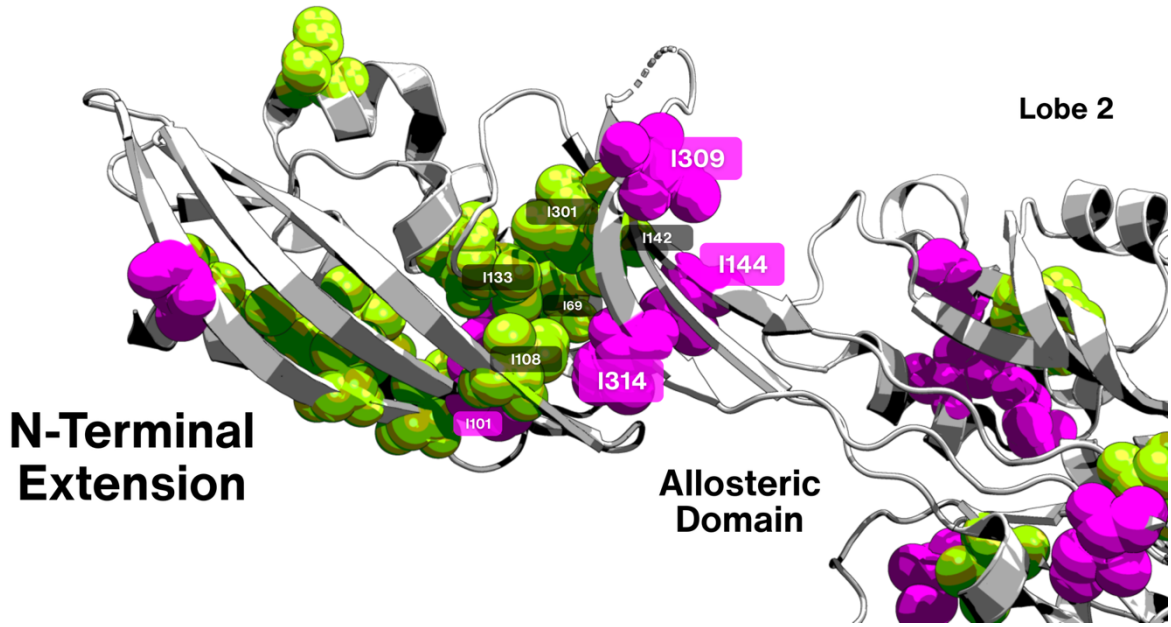

Figure 51: Structural mapping of potential assignment candidates for resonances with chemical shift perturbations nearby the I144V mutant of PBP2a (PDB ID: 1VQQ)[4].

I144, I314 and I309 are shown as spheres (magenta), with neighbouring Ile residues as likely candidates for the CSPs noted with neighbouring Ile residues as likely candidates for the CSPs shared between their respective spectra (I108, I69, I133, I142 and I301) annotated on green spheres.

I144, I309 and I314 are arranged in a triangle <10 Å of one another, with I309 and I314 lying at opposite ends of the same β-strand at the bottom of a three β-strand stack, with I144 on a the top strand. The I309G spectrum is the shows dramatic CSPs for both I314 and I144. By contrast, in both I144V and I314V spectra, subtle CSPs are noted for the other two unmutated residues (Figure 52). This is likely explained by the more conservative I>V substitutions which are expected to be less destabilising, supported by *in silico* mutagenesis simulations (Figure 71). Additionally, in both I309G and I314V spectra, the I144 peak shifts in opposite directions, supporting its likely central position to them structurally. Larger CSPs are also noted in the I101G spectrum for I144 and I314V resonances relative to I309G which correlate with their structural proximity. These observations collectively support their respective assignments.

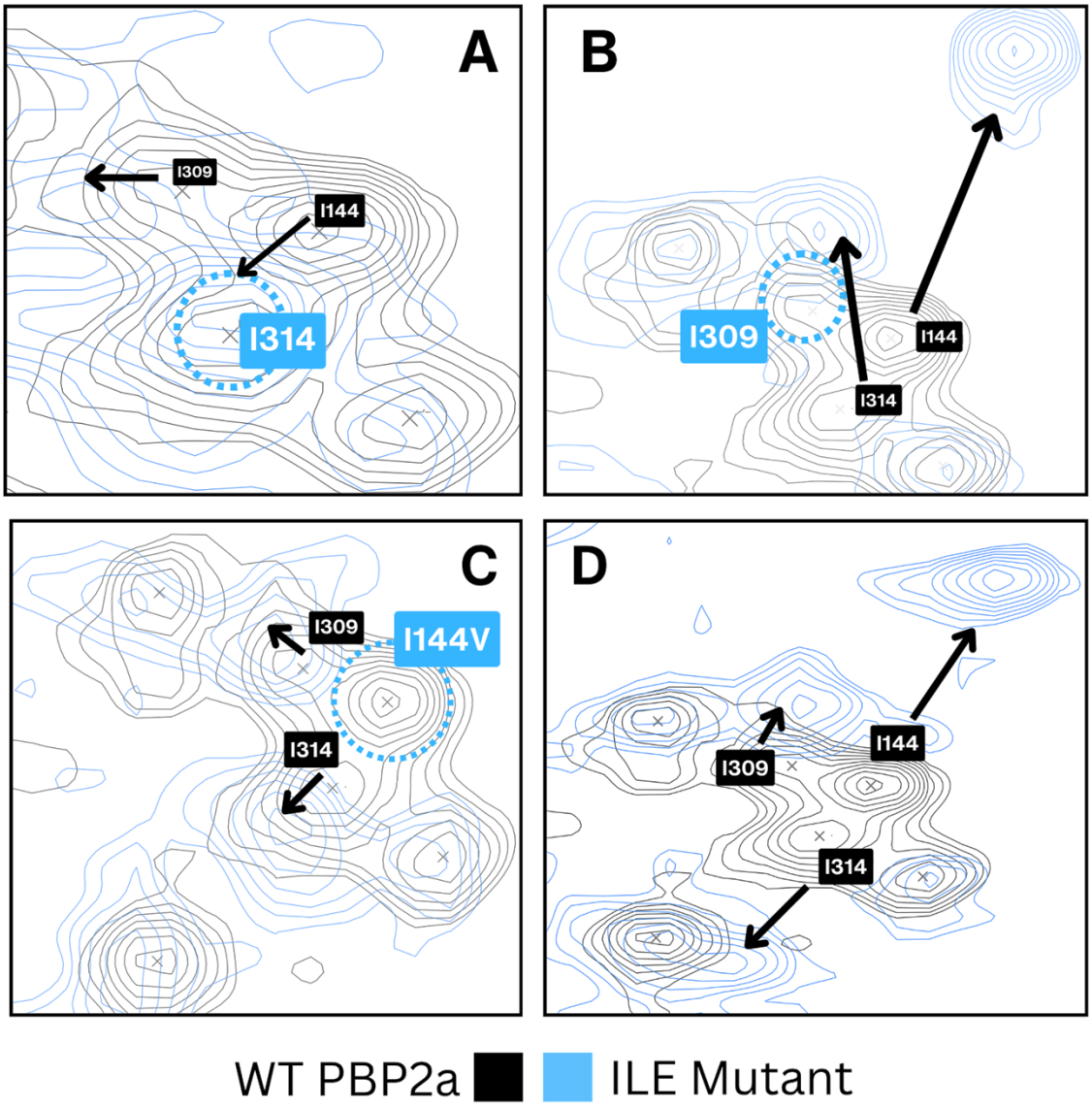

Figure 52: Comparison of regions showing related CSPs in I144V, I309G, I314V and I101G

CSPs are marked with arrows. Spectra are as follows: A) I314V, B) I309G, C) I144V and D) I101G.

Additionally, notable CSPs are observed in two peaks (Figure 50 – inset B) that are shared in I101G (Figure 41), I144V (Figure 46) and I309G (Figure 49) mutant spectra.

Observing the CSPs of the WT peak at $\delta^{1}H$ = 0.575 ppm, $\delta^{13}C$ = 13.689 ppm across the I309G, I144V, I101G and I314V mutant spectra, the largest CSPs are noted in the I101G and I309G spectra, followed by I314V and then I144V; consistent with their spatial proximity (Figure 50). Given their spatial proximity, it is likely that I69, I133, I108, I142 and I301 are possible candidates for the assignment of the peak showing this CSP. Regarding the CSPs observed in the WT peak at $\delta^{1}H$ = 0.597 ppm, $\delta^{13}C$ = 12.810 ppm seen across I309G, I144V, I101G, I85G and I314V mutant spectra, while Ile residues I78 and I80 remain suitable candidates given their proximity from I101 (4.55 Å and 8.50 Å respectively); the data from Figure 48, Figure 49 and Figure 50 also position I133, I108 and I301 as suitable

candidates owing to similar CSPs across a range of spectra, however these remain putative suggestions for further analyses.

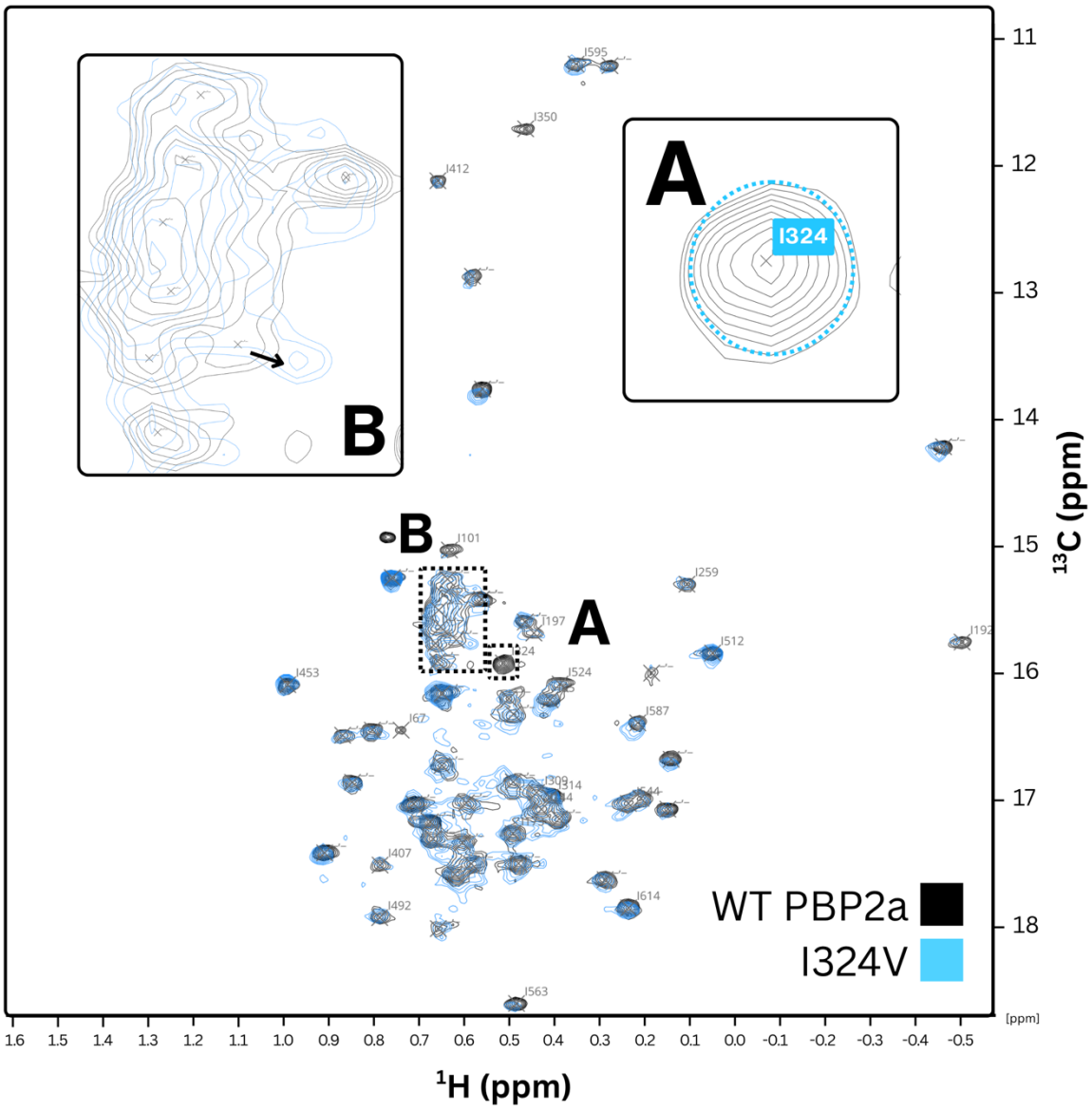

Figure 53: Assignment by selective mutagenesis (I324V) shows disappearance of a single Ile δ1 peak in SOFAST-HMQC

Overlay of wild-type (black) and I324V mutant (blue) 2D ^{1}H-^{13}C SOFAST-HMQC spectra. Peaks with confident assignments are annotated with single letter code. Insets display A, the WT peak at δ^{1}H = 0.528 ppm, δ^{13}C = 15.823 ppm (circled) disappears in I324V, giving a clear assignment, and B, an unassigned Ile peak at δ^{1}H = 0.634 ppm, δ^{13}C = 15.643 ppm with a notable CSP is marked with arrow.

The WT peak at δ^{1}H = 0.528 ppm, δ^{13}C = 15.823 ppm disappears unambiguously (Figure 47 – inset A) and is the only peak evident to do so in the mutant spectrum, providing a definitive assignment for I324V. Additionally, a notable CSP relative to the WT peak at δ^{1}H = 0.634 ppm, δ^{13}C = 15.643 ppm is observed in an unassigned Ile resonance in the I324V mutant spectrum.

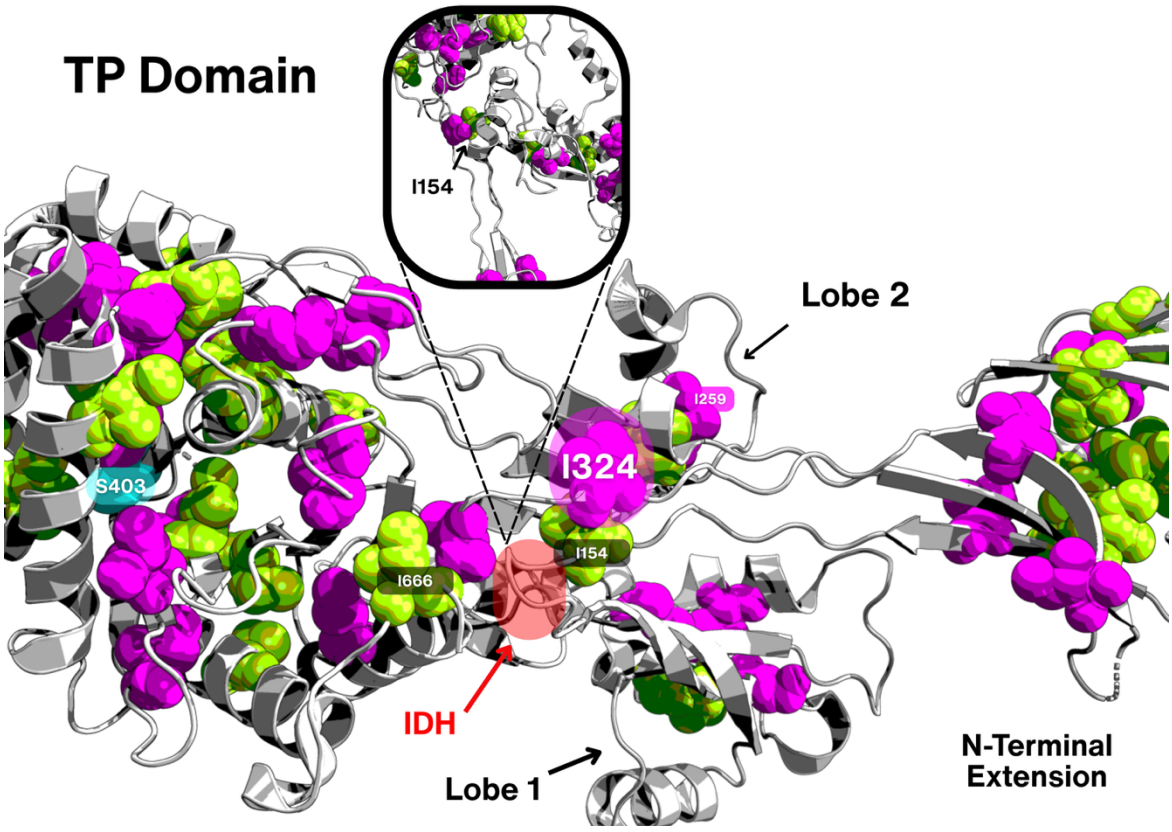

Figure 54: Structural mapping of potential assignment candidates for resonances with chemical shift perturbations nearby I324 of PBP2a (PDB ID: 1VQQ)[4].

Assigned residue I324 is shown as spheres highlighted in a magenta hue, with neighbouring unassigned Ile residues as likely candidates for the CSP noted within annotated as green spheres. The inset figure denotes the location of I154 on the interdomain hinge (IDH) highlighted with a red hue and arrow. The catalytic serine (S403) is highlighted in cyan hue for clarity.

Structural analysis reveals the only unassigned Ile residue nearby I324 is I154 (6.23 Å), making this a potential candidate for the peak observed at $\delta^{1}H$ = 0.634 ppm, $\delta^{13}C$ = 15.643 ppm (WT position) as there are no other unassigned Ile residues within 15 Å of I324. However, owing to the significant overlap in the $\delta^{1}H$ = 0.5-0.7 ppm, $\delta^{13}C$ = 15-16 ppm region, this cannot be confirmed without subsequent analyses. Additionally, expression yields of I154G were significantly lower (~1.0 mg/50 mL culture) than other mutants and 2D ^{1}H-^{13}C SOFAST-HMQC spectra indicated severe unfolding with most peaks collapsing into the $\delta^{1}H$ = 0.4-0.8 ppm window. Given its structural proximity near the interdomain hinge (IDH; Figure 54 – inset figure) between Lobe 1 and the Lobe 2/N-terminal extension, I154 is likely important to PBP2a folding and function. This is supported by previous analyses where I154 lies central to computationally simulated trajectories of the allosteric domain to TP domain communication network[89,97]. The I350G spectrum provides another clear assignment (Figure 55):

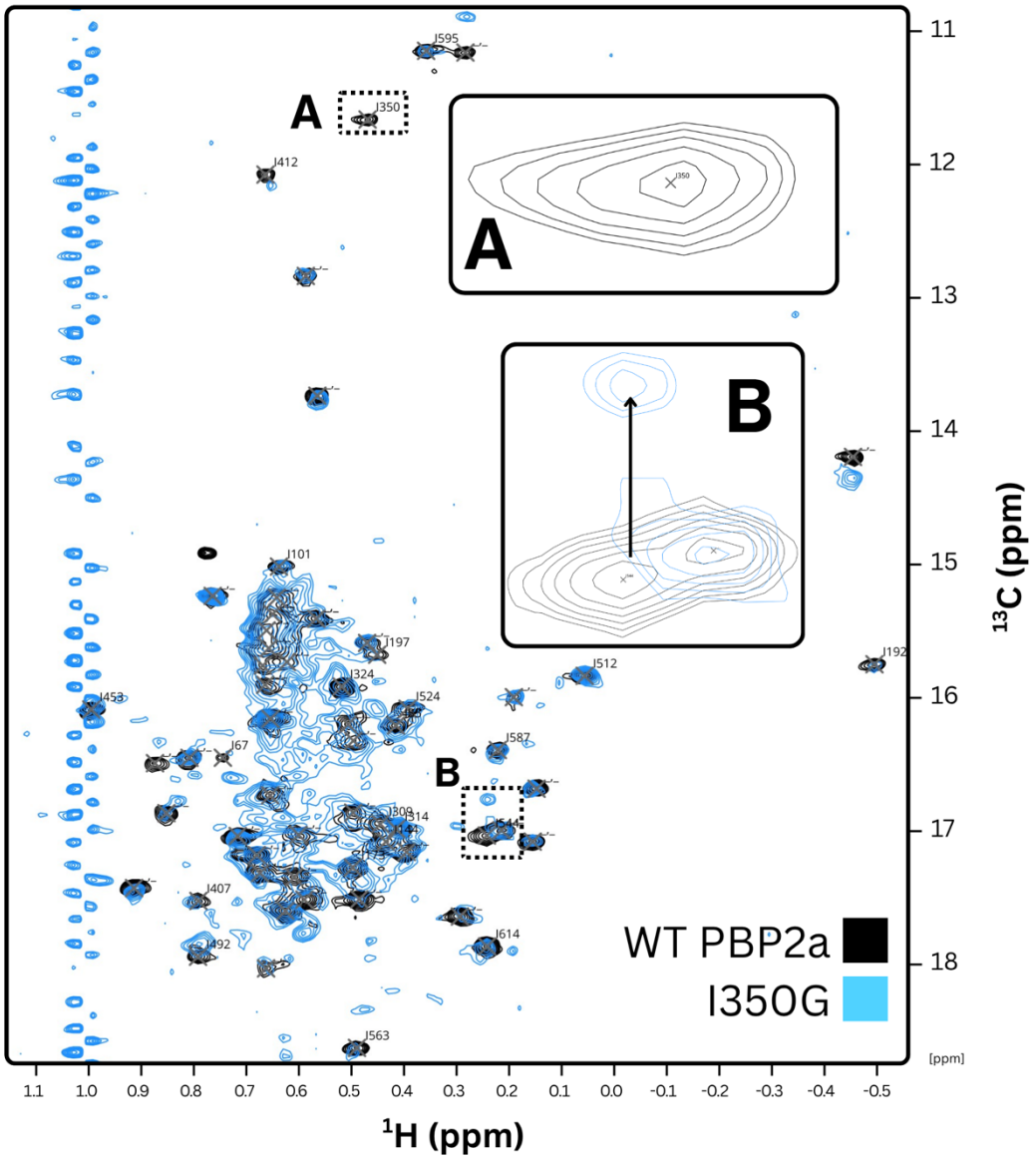

Figure 55: Assignment by selective mutagenesis (I350G) shows disappearance of a single Ile δ1 peak in SOFAST-HMQC

Overlay of wild-type (black) and I350G mutant (blue) 2D ^{1}H-^{13}C SOFAST-HMQC spectra. Peaks with confident assignments are annotated with single letter code. Insets display A, the WT peak at $\delta^{1}H = 0.478$ ppm, $\delta^{13}C = 17.396$ ppm (circled) disappears in I350G, giving a clear assignment, and B, several assigned and unassigned Ile resonances show notable CSPs relative to the WT spectra, indicated with arrows.

A single peak disappears relative to the WT spectrum at $\delta^{1}H = 0.478$ ppm, $\delta^{13}C = 11.662$ ppm, providing a clear assignment (Figure 55 – inset A). Considerable noise and overlap is noted in the central region of the spectrum likely due to lower signal-to-noise, however the spectra overlays well with the WT. Additionally, several assigned and unassigned Ile resonances show minor CSPs relative to the WT, reflective of I350's central position in the TP domain on the periphery of the β_2 strand in the core β-sheet stack with nine neighbouring isoleucines within <15 Å, including I544 which sees a $\delta^{1}H = -0.264$ ppm shift (Figure 55 – inset B) supporting this assignment. The I544G spectra shows a complimentary CSP for I350, supporting their proximity (Figure 56):

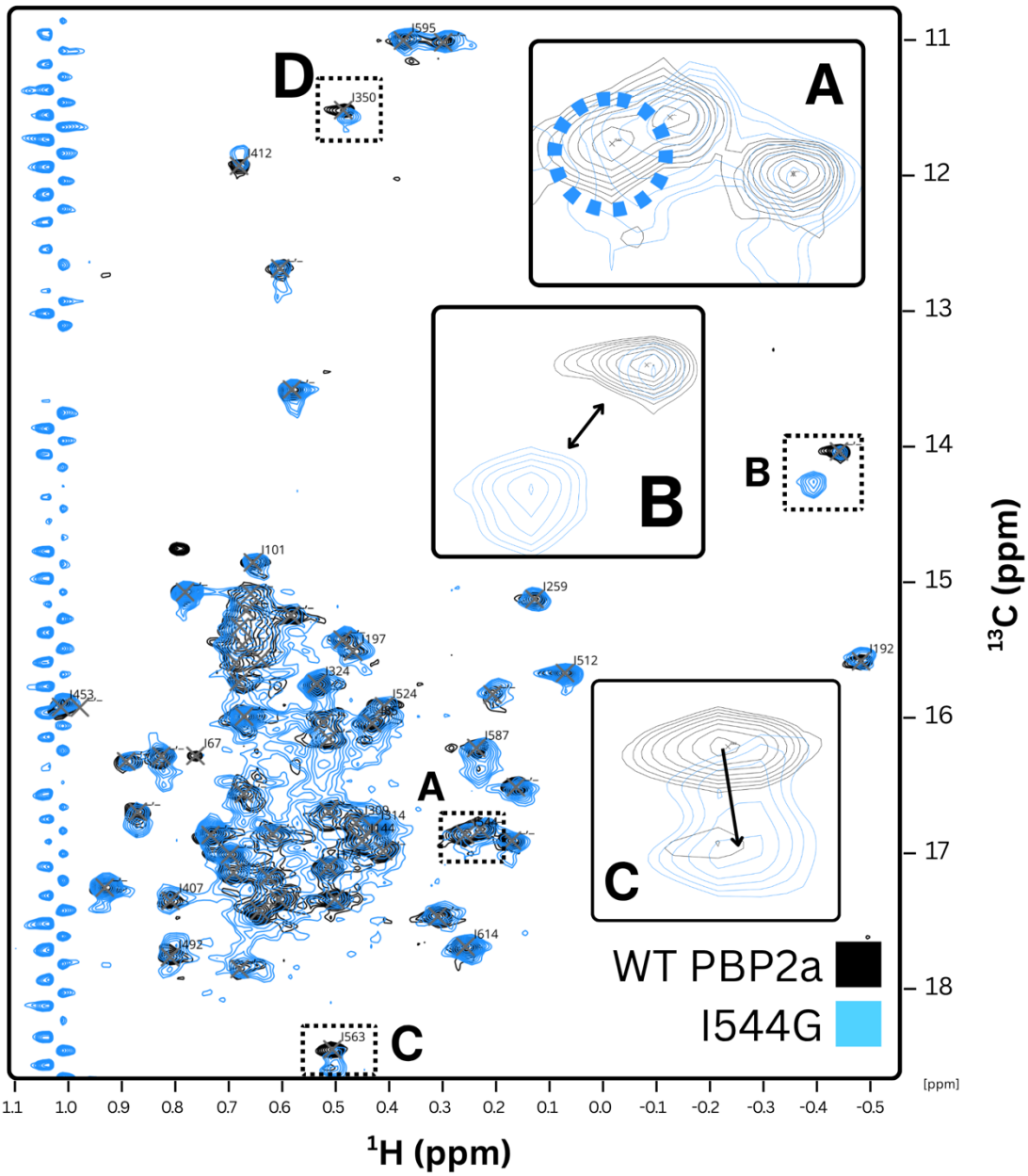

Figure 56: Assignment by selective mutagenesis (I544G) shows disappearance of a single Ile δ1 peak in SOFAST-HMQC

Overlay of wild-type (black) and I544G mutant (blue) 2D ^{1}H-^{13}C SOFAST-HMQC spectra. Peaks with confident assignments are annotated with single letter code. Insets display A, the WT peak at $\delta^{1}H = 0.248$ ppm, $\delta^{13}C = 16.916$ ppm (circled, inset A) disappears in I544G, giving a clear assignment, and B-D show several assigned and unassigned Ile resonances with notable CSPs relative to the WT spectra, indicated with arrows.

A single peak disappears relative to the WT spectrum at $\delta^{1}H = 0.248$ ppm, $\delta^{13}C = 16.916$ ppm, providing a clear assignment. Additionally, peaks assigned to I350 (Figure 56 – inset D) and I563 (Figure 56 – inset C) see notable CSPs, reflective of their close proximity (11.6 Å and 9.9 Å respectively). Notably, an additional unassigned peak (Figure 56 – inset B) has exhibits slow exchange in the I544G mutant, likely as a result of increased conformational freedom from the removal of the influence of the bulky isoleucine side chain. An inspection of isoleucines nearby I544 provides further context (Figure 63):

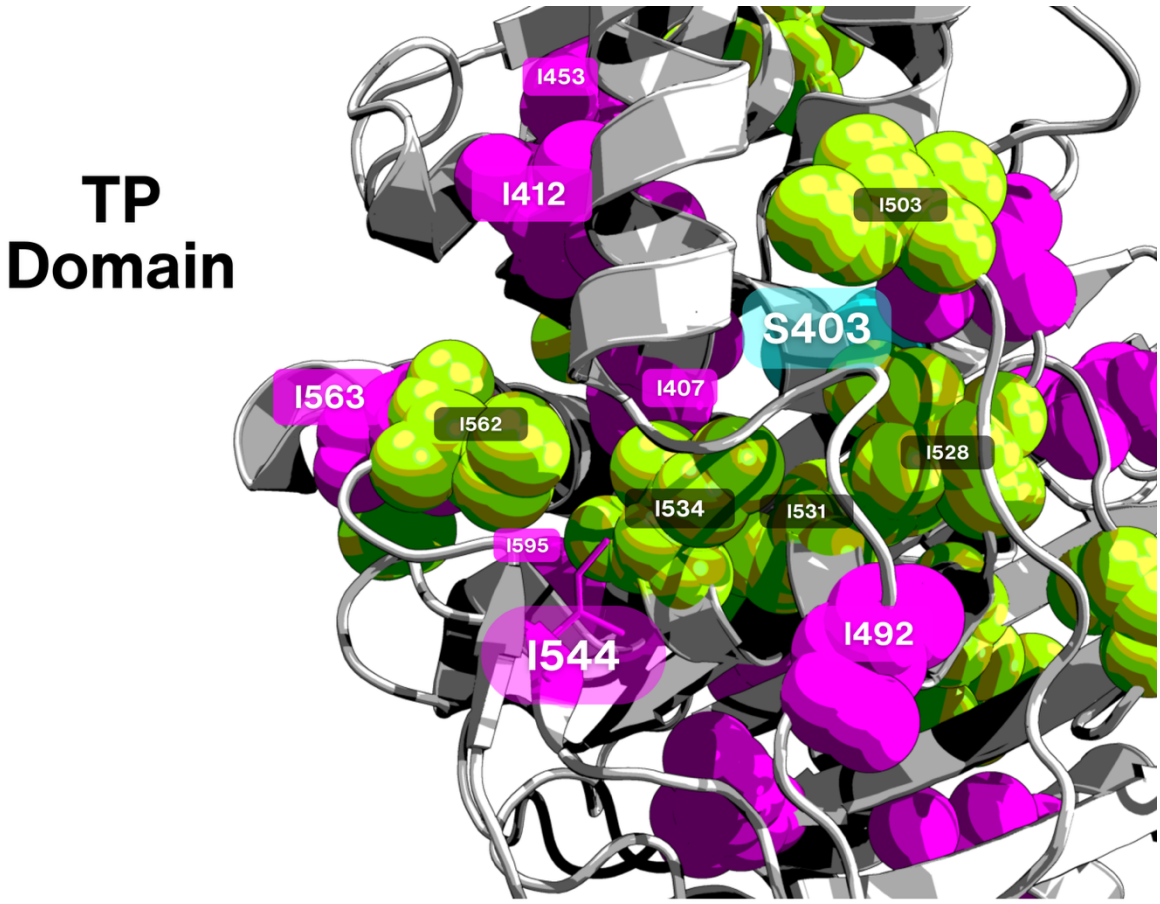

Figure 57: Structural mapping of potential assignment candidates for resonances with chemical shift perturbations nearby the I544G mutant of PBP2a (PDB ID: 1VQQ)[4].

I544 is highlighted in a magenta hue and displayed at sticks to best display its side chain. Isoleucines <15 Å (Cα-Cα) of I101 are annotated as potential candidates for other peaks

The I544 side chain projects into the core of the TP domain, densely packed with other assigned and unassigned isoleucine residues, nine of which are <15 Å to I544, with several at the back face of the S403-containing catalytic core of the TP domain. The buried and most proximal I534 stands the most likely residue to correspond to the unassigned resonance in Figure 56 inset B. Further examination of the I407G (Figure 58) and I412G (Figure 59) spectra lend further support to this:

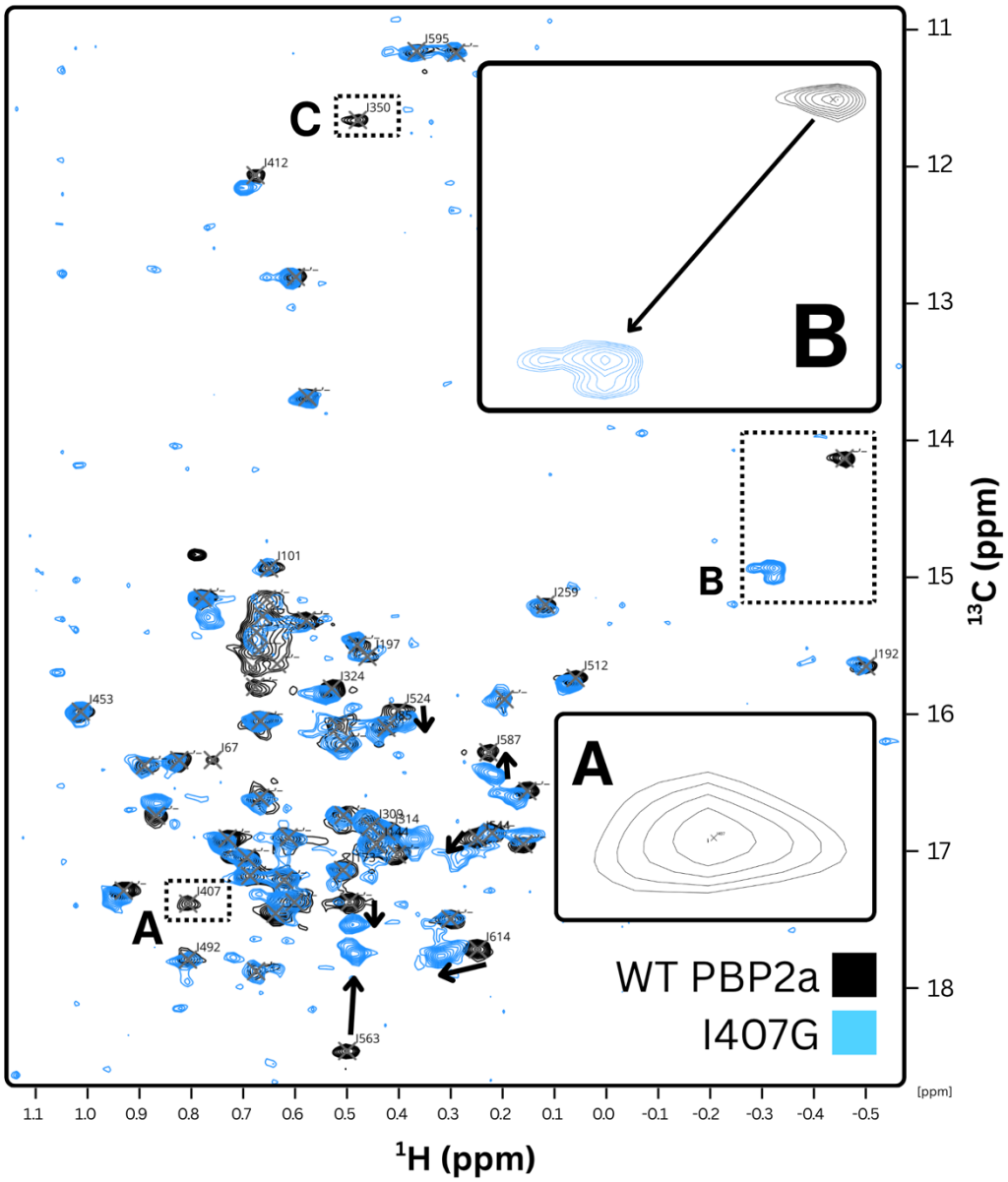

Figure 58: Assignment by selective mutagenesis (I407G) shows disappearance of a single Ile δ1 peak in SOFAST-HMQC

Overlay of wild-type (black) and I407G mutant (blue) 2D ^{1}H-^{13}C SOFAST-HMQC spectra. Peaks with confident assignments are annotated with single letter code. Insets display A, the WT peak at $\delta^{1}H = 0.805$ ppm, $\delta^{13}C = 17.396$ ppm (circled) disappears in I407G, giving a clear assignment, and B, a peak with the most notable CSP relative to the WT spectra, indicated with arrows that is shared with other nearby Ile spectra I412G and I544G. Other notable CSPs are noted by arrows.

Three peaks disappear relative to the WT spectrum, one at $\delta^{1}H = 0.805$ ppm, $\delta^{13}C = 17.396$ ppm, another at $\delta^{1}H = 0.675$ ppm, $\delta^{13}C = 12.066$ ppm, and another at another at $\delta^{1}H = 0.478$ ppm, $\delta^{13}C = 11.662$ ppm. However, I350G has been confidently assigned (Figure 55) providing a confident assignment for I407 (inset A). Additionally, several assigned and unassigned Ile resonances show notable CSPs relative to the WT, reflective of large number of isoleucines in the nearby environment of I407G (n = 14 <15 Å). I407 is buried deep within the catalytic centre of the TP domain (Figure 57), just 4.4 Å distal to the catalytic serine

S403 where substitution of its bulky side chain likely resulted in substantial subtle structural rearrangements. Many of the same CSPs are seen in the I412G spectrum, providing further support, given their spatial proximity (8.7 Å) (Figure 59):

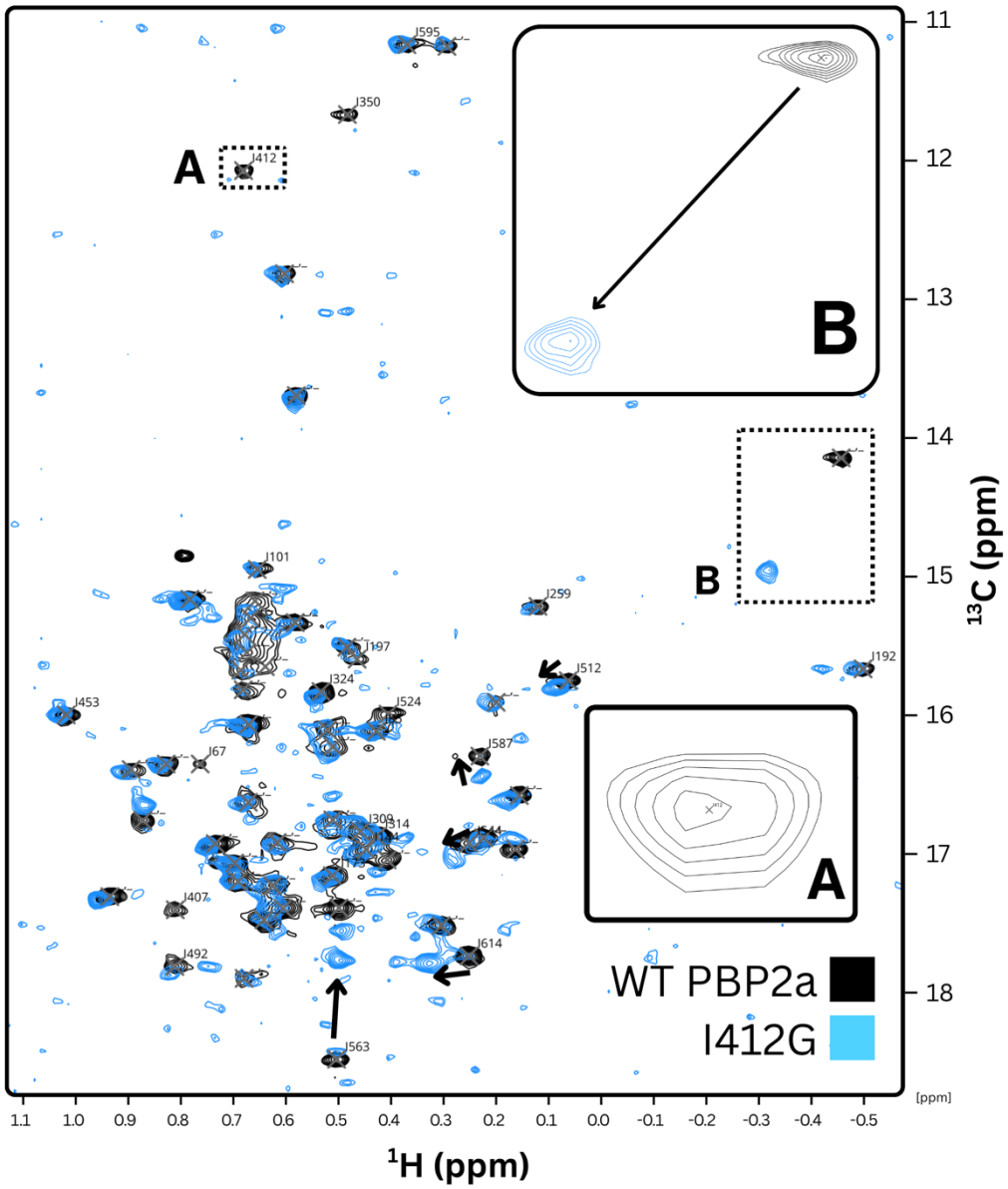

Figure 59: Assignment by selective mutagenesis (I412G) shows disappearance of a single Ile δ1 peak in SOFAST-HMQC

Overlay of wild-type (black) and I412G mutant (blue) 2D ^{1}H-^{13}C SOFAST-HMQC spectra. Peaks with confident assignments are annotated with single letter code. Insets display A, the WT peak at $\delta^{1}H = 0.675$ ppm, $\delta^{13}C = 12.066$ ppm (circled) disappears in I412G, giving a clear assignment, and B, a peak with the most notable CSP relative to the WT spectra, indicated with arrows that is shared with other nearby Ile spectra I407G and I544G.

Three peaks disappear relative to the WT spectrum, one at $\delta^{1}H = 0.805$ ppm, $\delta^{13}C = 17.396$ ppm, another at $\delta^{1}H = 0.675$ ppm, $\delta^{13}C = 12.066$ ppm (Figure 59 – inset A), and another at another at $\delta^{1}H = 0.478$ ppm, $\delta^{13}C = 11.662$ ppm. However, both I350 (Figure 55) and I407 (Figure 58) have been confidently assigned providing a clear assignment for I412G.

Additionally, several assigned and unassigned Ile resonances show notable CSPs relative to the WT, reflective of large number of isoleucines in the nearby environment of I412G. I412 lies on the same helix as I407 (Figure 57) wherein, given the TP domain's capacity to increase its occupancy from 500 $Å^3$ to 1300 $Å^3$ following effector binding[7], likely reflects a key stabilising/coordinating structural element. Finally, given the significant (δ^1H = ~+0.130 ppm; $\delta^{13}C$ = ~+0.800 ppm) CSPs in both I412G and I407G spectra and their respective proximity to I534 (I412: 7.2 Å, I407: 6.2Å), this lends further support to its potential correlation as the resonance in inset B. I453 provides a more straightforward assignment (Figure 60):

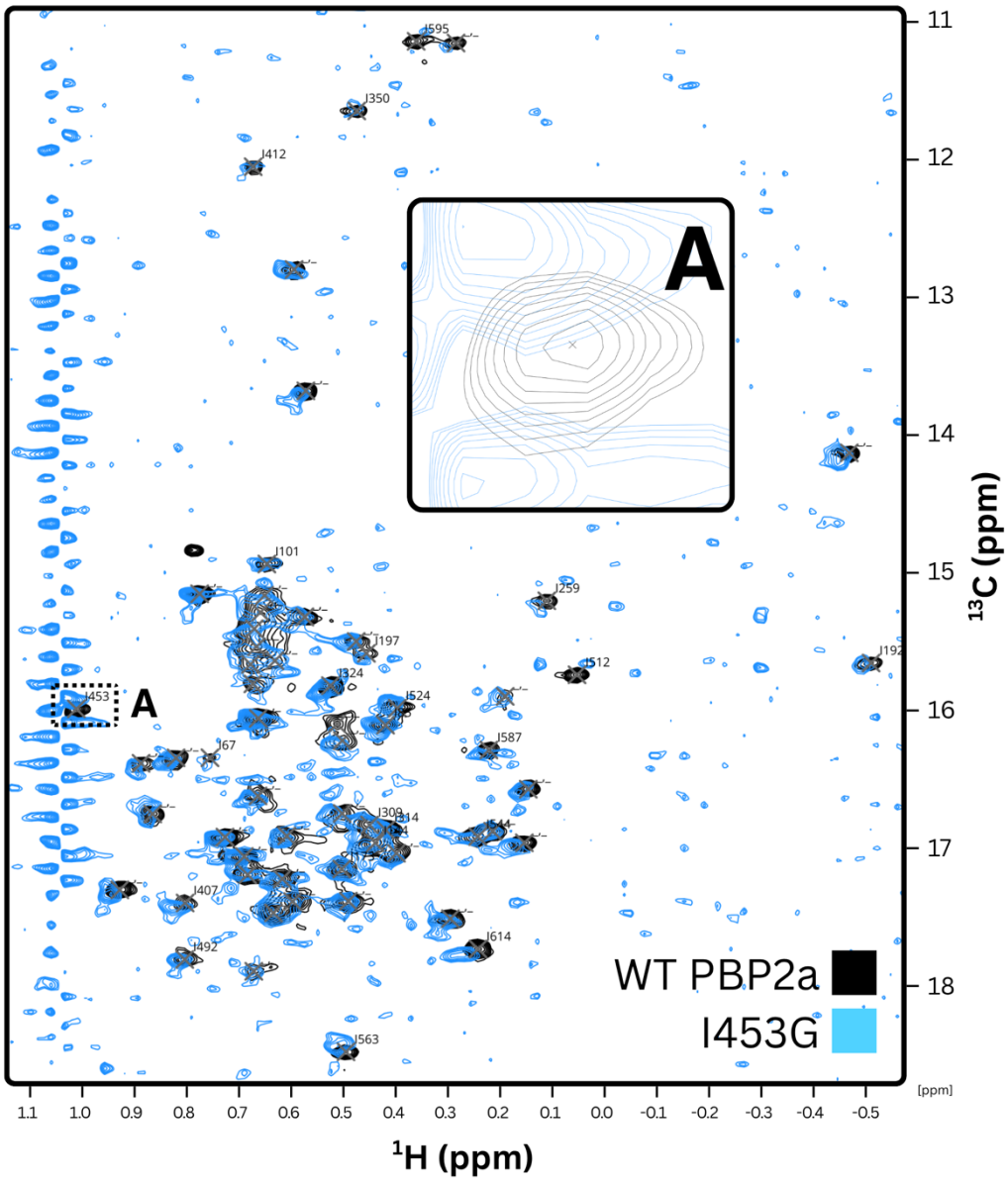

Figure 60: Assignment by selective mutagenesis (I453G) shows disappearance of a single Ile δ1 peak in SOFAST-HMQC

Overlay of wild-type (black) and I453G mutant (blue) 2D ^1H-^{13}C SOFAST-HMQC spectra. Peaks with confident assignments are annotated with single letter code. Insets display A, the WT peak at δ^1H = 1.012 ppm,

$\delta^{13}C$ = 15.991 ppm disappears in I453G with no other peaks disappearing in this spectrum, which despite the low signal-to-noise and noise line, makes this the only clear option and a confident assignment.

The I453G spectrum poorer signal-to-noise versus other mutants, likely due to a lower concentration sample (73 µM), however remains in good agreement with the WT spectrum. However, only one peak clearly disappears at $\delta^{1}H$ = 1.012 ppm, $\delta^{13}C$ = 15.991 ppm, making this the only confident choice for assignment. Additionally, the same peak appears in several other mutant spectra where the noise line is absent. I492G provided another unambiguous assignment (Figure 61):

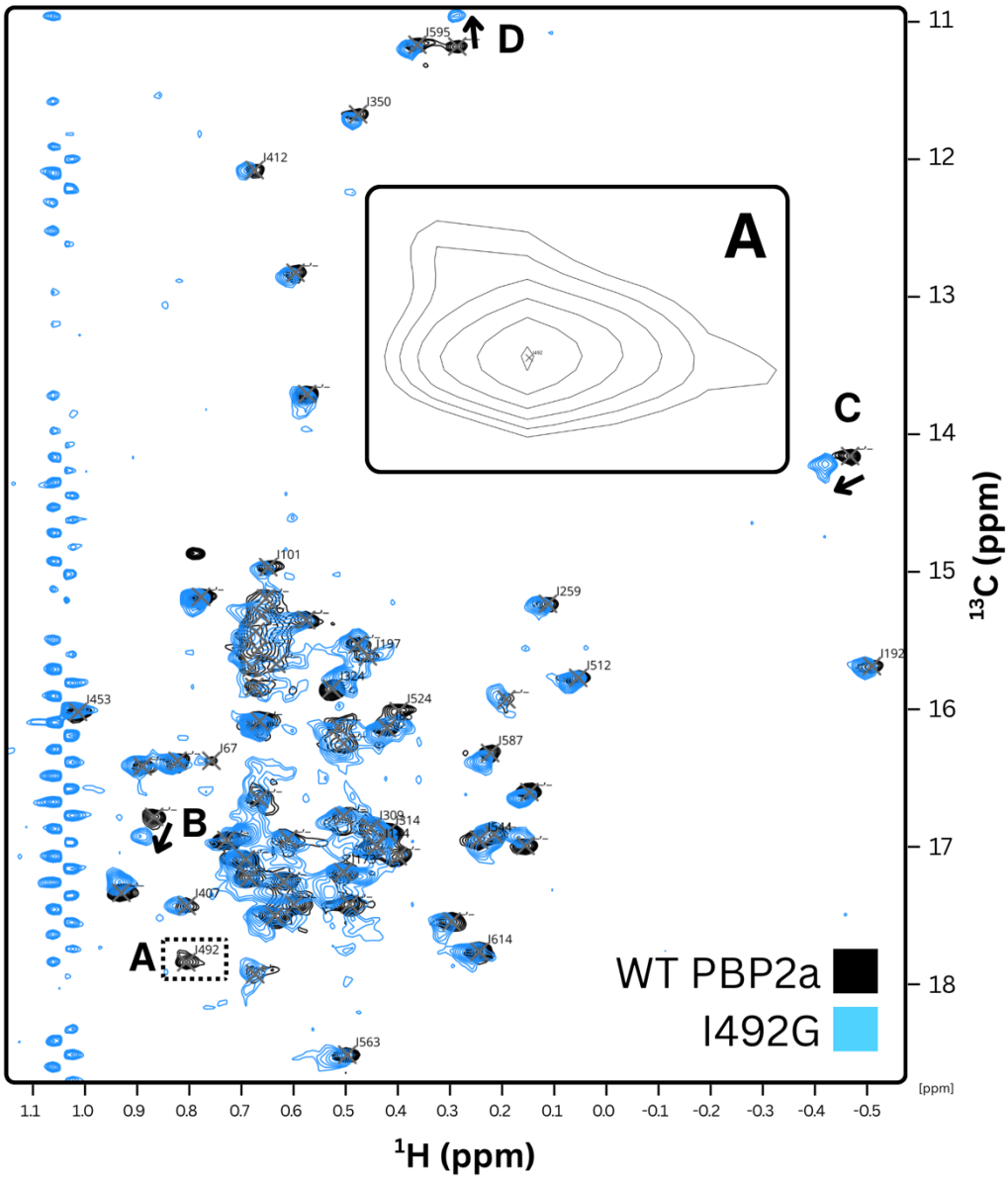

Figure 61: Assignment by selective mutagenesis (I492G) shows disappearance of a single Ile δ1 peak in SOFAST-HMQC

Overlay of wild-type (black) and I492G mutant (blue) 2D ^{1}H-^{13}C SOFAST-HMQC spectra. Peaks with confident assignments are annotated with single letter code. Inset A displays the disappearance of the WT peak at $\delta^{1}H$ = 0.805 ppm, $\delta^{13}C$ = 17.805 ppm with no other peaks disappearing in this spectrum. Arrows B-D indicate the most significant CSPs

A single peak disappears at $\delta^{1}H = 0.805$ ppm, $\delta^{13}C = 17.805$ ppm, giving a clear assignment for I492G (Figure 61 – inset A). Several other peaks (B-D) exhibit significant CSPs, with peak C lending further support to I534 being a potential candidate given its proximity (9.5 Å) and peaks B and D potentially corresponding with either I503 (12.5 Å) or I526 (6.5 Å) (Figure 57). The I614G spectrum provided a similarly clear assignment (Figure 62):

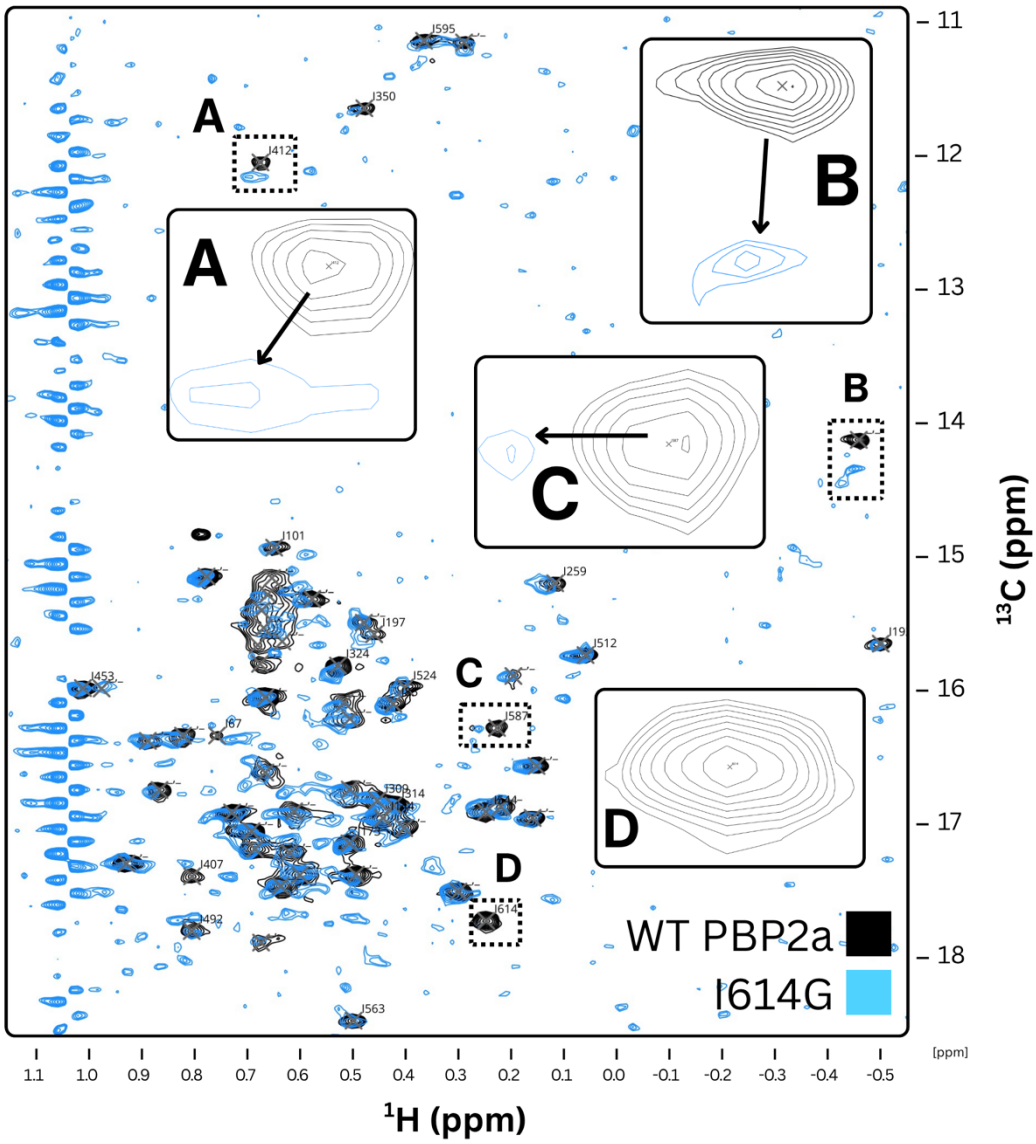

Figure 62: Assignment by selective mutagenesis (I614G) shows disappearance of a single Ile δ1 peak in SOFAST-HMQC

Overlay of wild-type (black) and I614G mutant (blue) 2D ^{1}H-^{13}C SOFAST-HMQC spectra. Peaks with confident assignments are annotated with single letter code. Insets display A-C, and D the WT peak at $\delta^{1}H = 0.247$ ppm, $\delta^{13}C = 17.729$ ppm which disappears in I614G, giving a clear assignment.

Albeit a weaker spectrum with less signal-to-noise versus other mutants, due to a lower concentration sample (73 µM) because of lower expression yields (~1.3 mg/50 mL culture), the I614G spectra compares well with the WT spectrum. The WT peak at $\delta^{1}H = 0.247$ ppm,

$\delta^{13}C$ = 17.729 ppm disappears unambiguously (Figure 62 – inset A) and is the only peak evident to do so in the mutant spectra, providing a definitive assignment for I614G. Additionally, several resonances show notable CSPs relative to the WT, reflective of the nearby environment of I614G with five other assigned and unassigned isoleucine residues <15 Å (Figure 63):

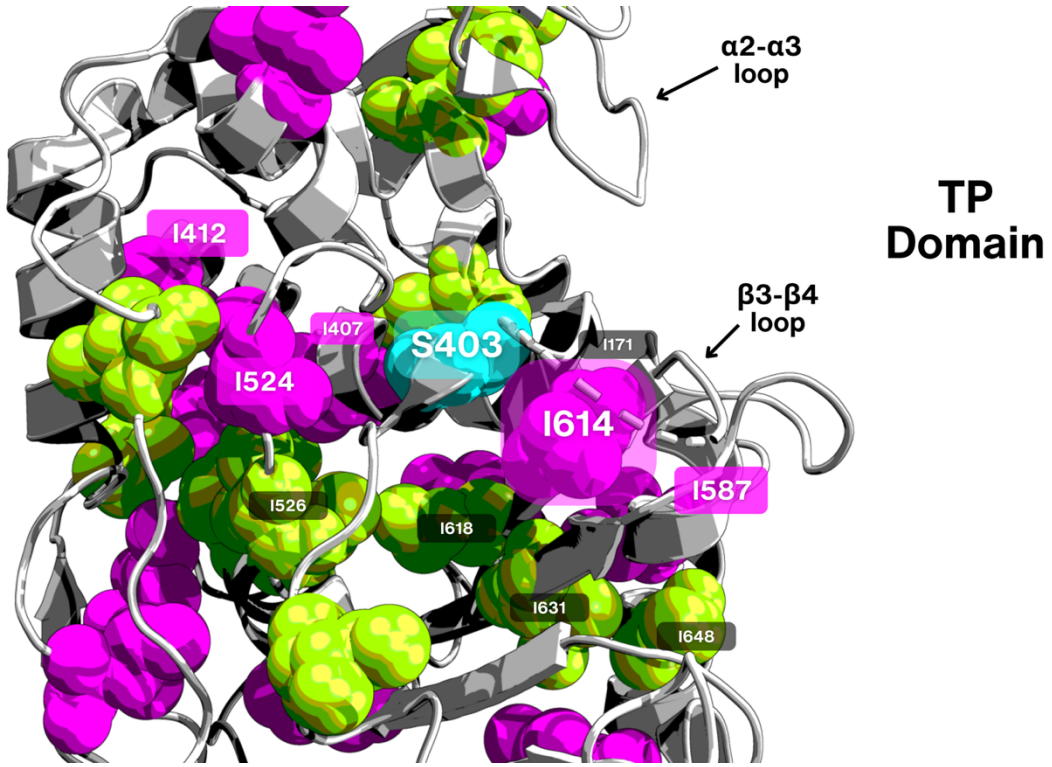

Figure 63: Structural mapping of potential assignment candidates for resonances with chemical shift perturbations nearby the I614G mutant of PBP2a (PDB ID: 1VQQ)[4].

I614 is highlighted in a magenta hue. Isoleucines <15 Å (Cα-Cα) of I614 are annotated as potential candidates for other peaks

Structural analysis reveals the only unassigned Ile residue nearby I324 is I154 (6.23 Å), making this a potential candidate for the peak observed at $\delta^{1}H$ = 0.634 ppm, $\delta^{13}C$ = 15.643 ppm (WT position). I587G provided another unambiguous assignment (Figure 64):

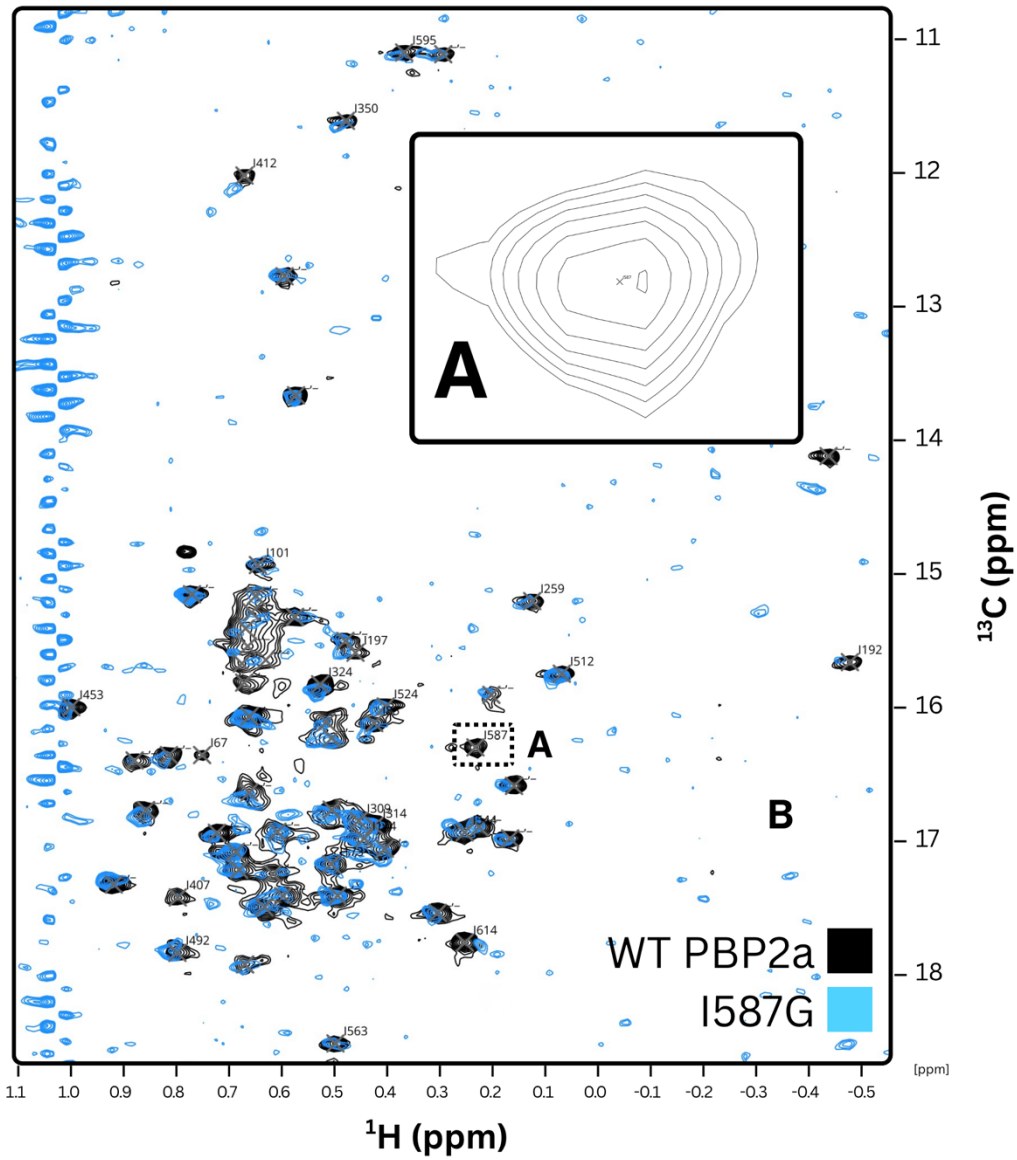

Figure 64: Assignment by selective mutagenesis (I587G) shows disappearance of a single Ile δ1 peak in SOFAST-HMQC

Overlay of wild-type (black) and I587G mutant (blue) 2D ^{1}H-^{13}C SOFAST-HMQC spectra. Peaks with confident assignments are annotated with single letter code. Insets display A, the WT peak at δ^{1}H = 0.227 ppm, δ^{13}C = 16.288 ppm (inset A) disappears in I587G, giving a clear assignment.

Albeit a weaker spectrum with less signal-to-noise versus other mutants, due to a lower concentration sample (73 µM) because of lower expression yields (~1.3 mg/50 mL culture), the I587G spectra compares well with the WT spectrum. The WT peak at δ^{1}H = 0.227 ppm, δ^{13}C = 16.288 ppm disappears unambiguously (Figure 64– inset A) and is the only peak evident to do so in the mutant spectra, providing a definitive assignment for I587G. Several peaks that are not as apparent reappear at lower contour levels.

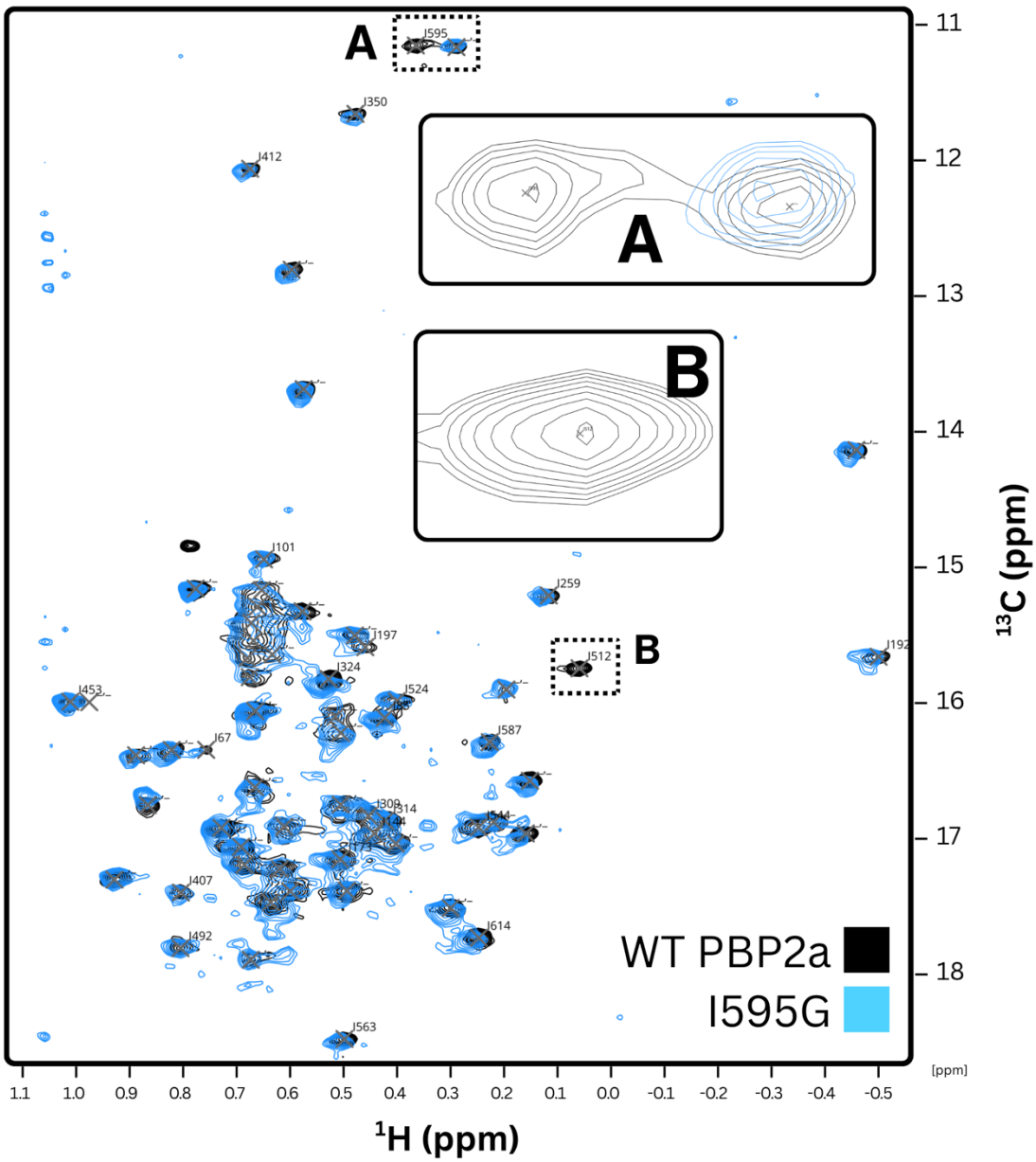

Figure 65: Assignment by selective mutagenesis (I595G) shows disappearance of a single Ile δ1 peak in SOFAST-HMQC

Overlay of wild-type (black) and I595G mutant (blue) 2D ^{1}H-^{13}C SOFAST-HMQC spectra. Peaks with confident assignments are annotated with single letter code. Insets display A, the WT peak at δ^{1}H = 0.42 ppm, δ^{13}C = 16.11 ppm (circled) disappears in I614G, giving a clear assignment.

Two WT peaks disappear at δ^{1}H = 0.365 ppm, δ^{13}C = 11.158 ppm (Figure 65A) and δ^{1}H = 0.059 ppm, δ^{13}C = 15.744 ppm (Figure 65B). The I512G spectra reveals CSPs for the same peaks (Figure 66):

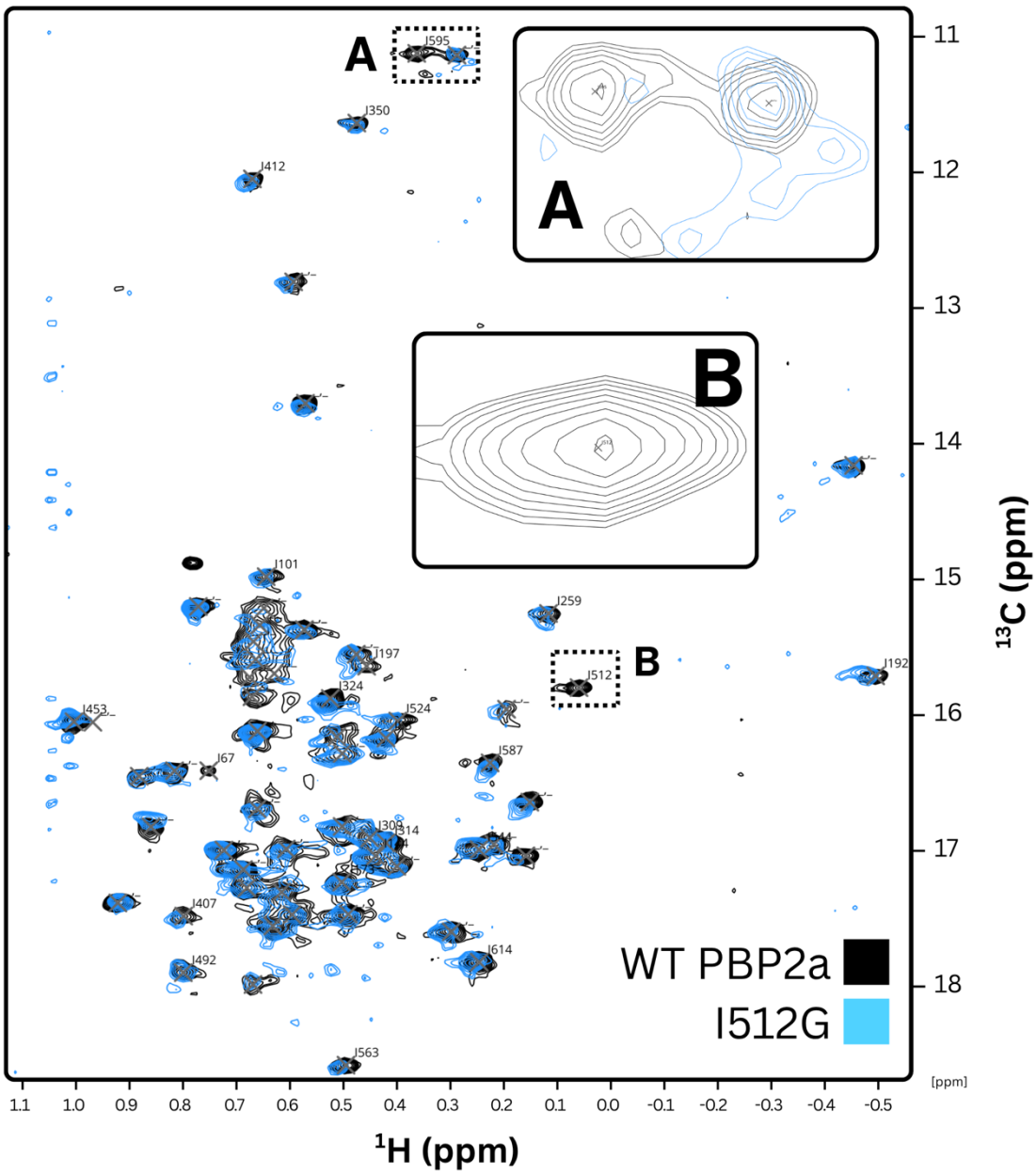

Figure 66: Assignment by selective mutagenesis (I512G) shows disappearance of a single Ile δ1 peak in SOFAST-HMQC

Overlay of wild-type (black) and I512G mutant (blue) 2D ^{1}H-^{13}C SOFAST-HMQC spectra. Peaks with confident assignments are annotated with single letter code. Insets display A, the WT peak at δ^{1}H = 0.42 ppm, δ^{13}C = 16.11 ppm (circled) disappears in I512G, giving a clear assignment.

While the I512G mutant indicates peaks with the same CSPs as the I595G spectra, however in the I512G spectrum, the peak assigned to I595 (Figure 66A) is likely to have moved near the neighbouring unassigned peak. No other peaks with CSPs are evident in either spectrum, nor are they in close proximity in the PBP2a structure (32 Å apart). As such, an ambiguous assignments are made for residues I512 and I595. I563 provides another unambiguous assignment (Figure 67):

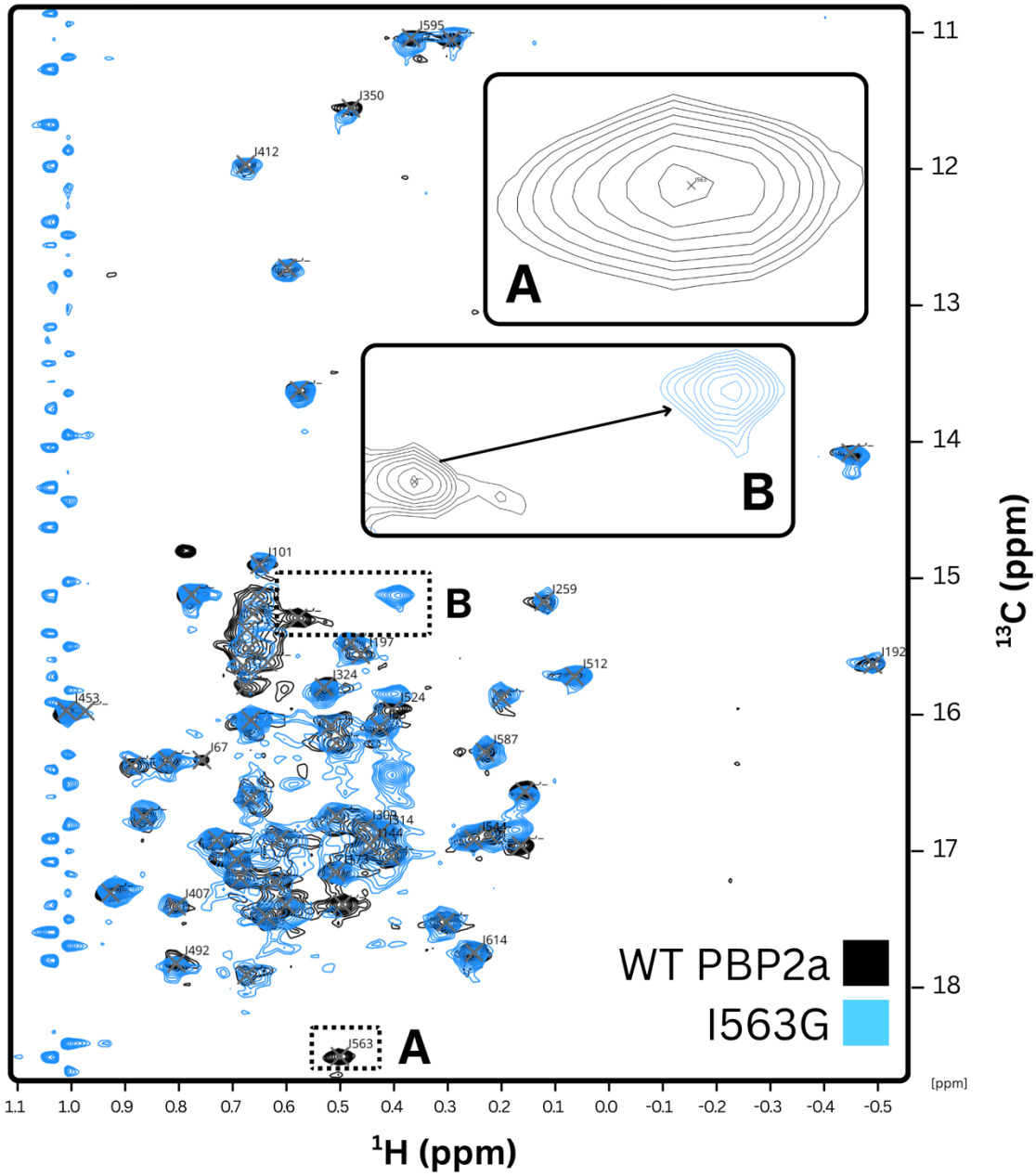

Figure 67: Assignment by selective mutagenesis (I563G) shows disappearance of a single Ile δ1 peak in SOFAST-HMQC

Overlay of wild-type (black) and I563G mutant (blue) 2D ^{1}H-^{13}C SOFAST-HMQC spectra. Peaks with confident assignments are annotated with single letter code. Insets display A, the WT peak at δ^{1}H = 0.42 ppm, δ^{13}C = 16.11 ppm (circled) disappears in I563G, giving a clear assignment.

One peak at δ^{1}H = 0.498 ppm, δ^{13}C = 18.474 ppm (Figure 67 – inset A) disappears with no other peaks disappearing in Figure 67. As such, an unambiguous assignment for I563 is made. Another unassigned peak at δ^{1}H = 0.577 ppm, δ^{13}C = 15.326 ppm (Figure 67 – inset B) shifts δ^{1}H = -0.187 ppm, δ^{13}C = -0.164 ppm, suggesting a nearby isoleucine might correlate with a potential candidate (Figure 68):

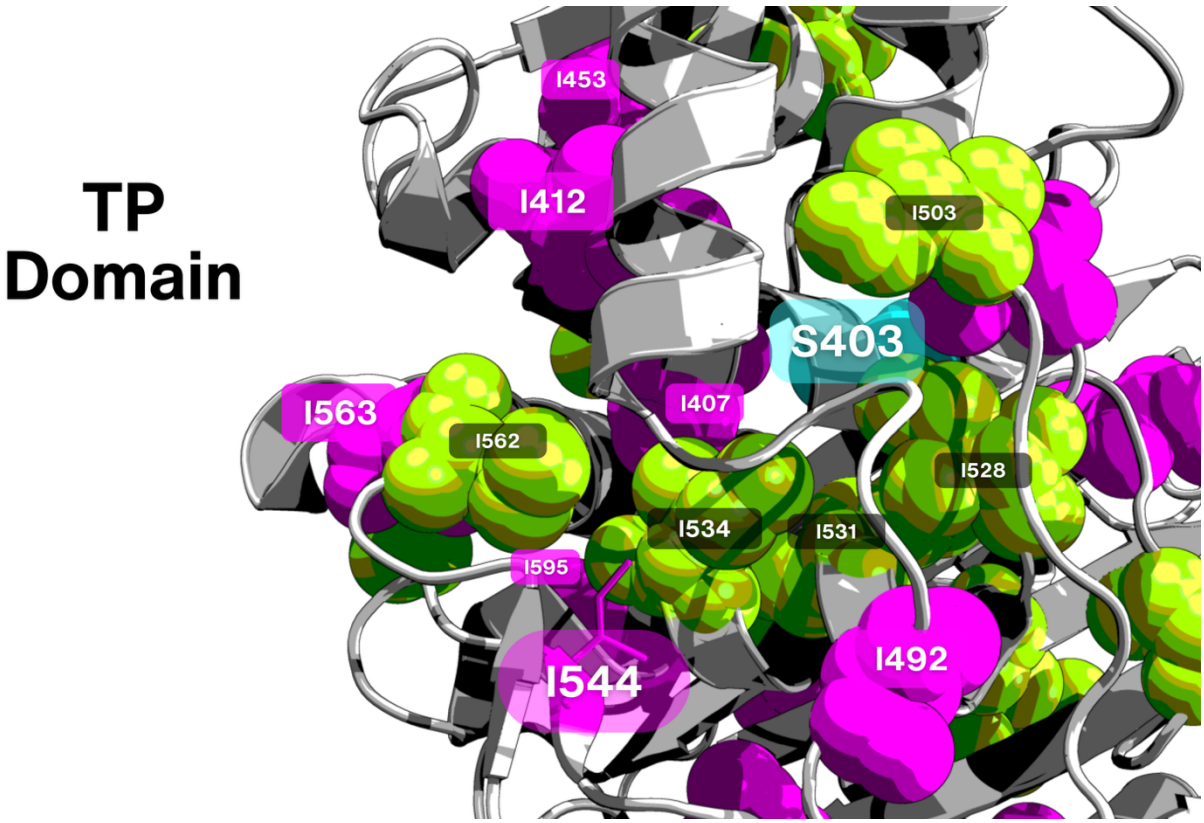

Figure 68: Structural mapping of potential assignment candidates for resonances with chemical shift perturbations nearby the I563G mutant of PBP2a (PDB ID: 1VQQ)[4].

I563 is highlighted in a magenta hue. Isoleucines <15 Å (Cα-Cα) of I563 are annotated as potential candidates for other peaks

Structural analysis reveals six neighbouring unassigned and assigned isoleucine residues <15 Å however, the most likely candidate corresponding to the CSP noted in Figure 67 inset B is I562, given that it is immediately cojoined to I563. This CSP is not seen in any other mutant tested in this study. I524 provided another unambiguous assignment (Figure 69):

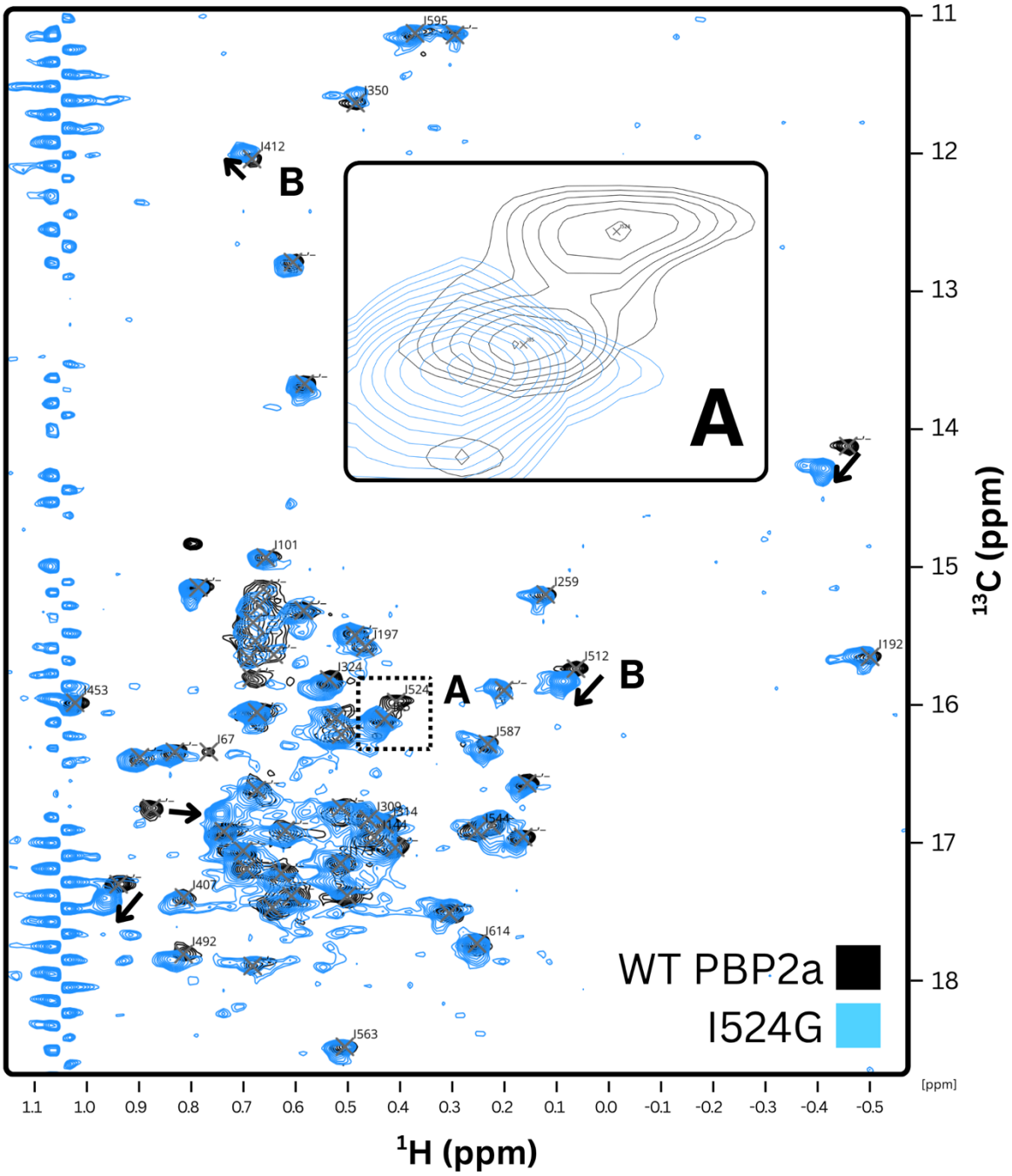

Figure 69: Assignment by selective mutagenesis (I524G) shows disappearance of a single Ile δ1 peak in SOFAST-HMQC

Overlay of wild-type (black) and I524G mutant (blue) 2D ^{1}H-^{13}C SOFAST-HMQC spectra. Peaks with confident assignments are annotated with single letter code. Insets display A, the WT peak at δ^{1}H = 0.401 ppm, δ^{13}C = 16.288 ppm (circled) disappears in I524G, giving a clear assignment.

One peak at δ^{1}H = 0.401 ppm, δ^{13}C = 16.288 ppm disappears with no other peaks disappearing in Figure 67. As such, an unambiguous assignment for I524 is made. Several other CSPs are noted in nearby assigned residues I492 (12.4. Å) and I512 (13.5 Å). Additionally, the residue above I192 suspected as I534 (8.7 Å) sees another notable CSP.

Finally, a large CSP is noted for the resonance ~δ^{1}H = 0.89 ppm, ~δ^{13}C = 16.65 ppm which likely corresponds with I503 (4.0 Å) or I526 (3.6 Å) (Figure 70):

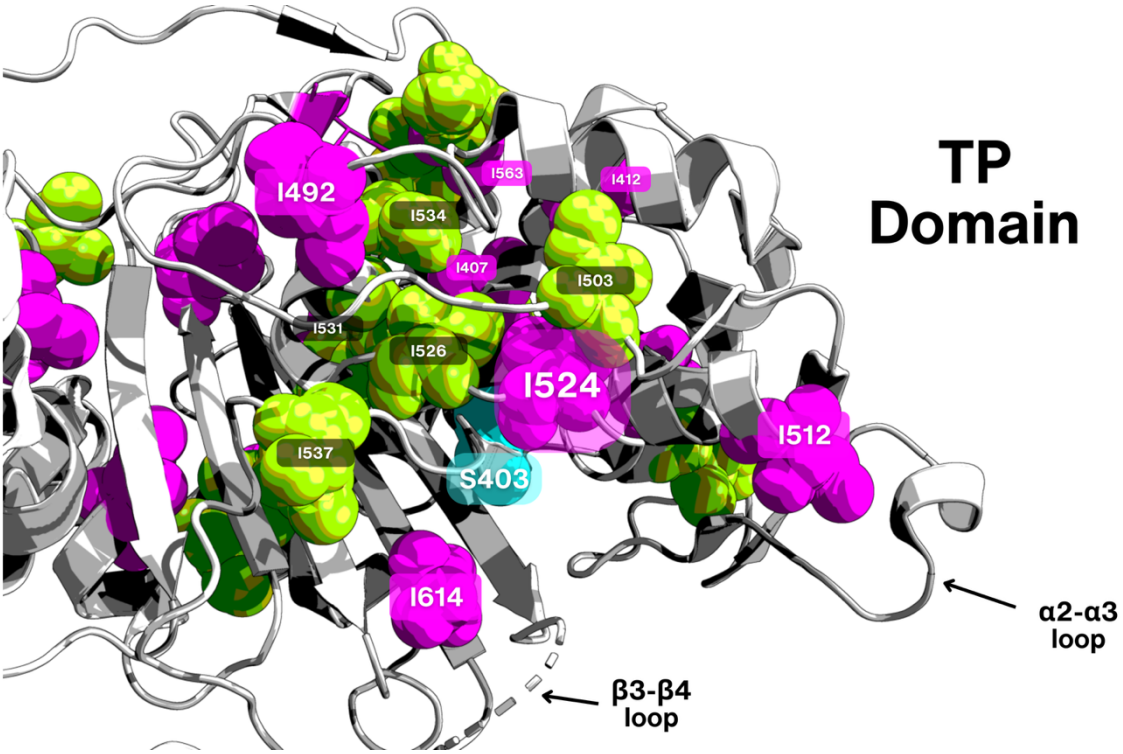

Figure 70: Structural mapping of potential assignment candidates for resonances with chemical shift perturbations nearby the I524G mutant of PBP2a (PDB ID: 1VQQ)[4].

I524 is highlighted in a magenta hue. Isoleucines <15 Å (Cα-Cα) of I101 are annotated as potential candidates for other peaks

Given that this CSP is noted in both I492G and I524G spectra and evidences a ~two-fold larger CSP, this suggests that I526 is the more likely candidate given that it is closer in proximity to both I524 and I492 (3.6 Å Vs 6.5 Å) versus I503 (4.0 Å Vs 12.9 Å). Further analyses are required to verify this putative assignment. From the above spectra, it was possible to confidently assign 23 isoleucine residues via selective mutagenesis, with sufficient distribution across key structural and functional interfaces within PBP2a to serve as probes for downstream analyses. Residues I69G, I80G, I132G, I144G, I154G, I171G, I186G, I278G, I314G, I324G, I328G, I336G and I465G were not assignable either due to unsuccessful recombinant protein expression or unfolding noted following experimentation; with spectra displaying a severe loss of chemical shift dispersion, with signals collapsing into a narrow cluster in the random-coil region of the spectrum (δ^{1}H =~0.4-0.8 ppm). As such, extensive peak overlap and loss of native structure prevented resonance assignment.

To identify more stabilising mutations to address the mutants that were previously unsuccessful, we performed *in silico* saturation mutagenesis using the Rosetta cartesian_ddg protocol[192] to predict amino acid substitutions that might be better tolerated without disrupting the structure of the protein. This approach predicts the energetic impact of every possible amino acid substitution at each target residue, expressed as the change in folding free energy (ΔΔG). In this context,

$$\Delta\Delta G = G_{mut} - G_{WT}$$

where G_{mut} represents the predicted folding free energy of the mutant structure and G_{WT} that of the wild-type reference. Negative ΔΔG values therefore indicate stabilising mutations (i.e. a lower predicted folding free energy relative to wild type), whereas positive ΔΔG values suggest destabilising substitutions that are less thermodynamically favourable. The Rosetta cartesian_ddg protocol employs a high resolution, all-atom energy function and optimises the structure in Cartesian coordinate space, allowing side chain and limited backbone flexibility to accommodate subtle conformational rearrangements introduced by mutation[192]. The change in folding free energy (ΔΔG) was calculated for substituting every isoleucine residue in PBP2a with the remaining 19 amino acids (Figure 71):

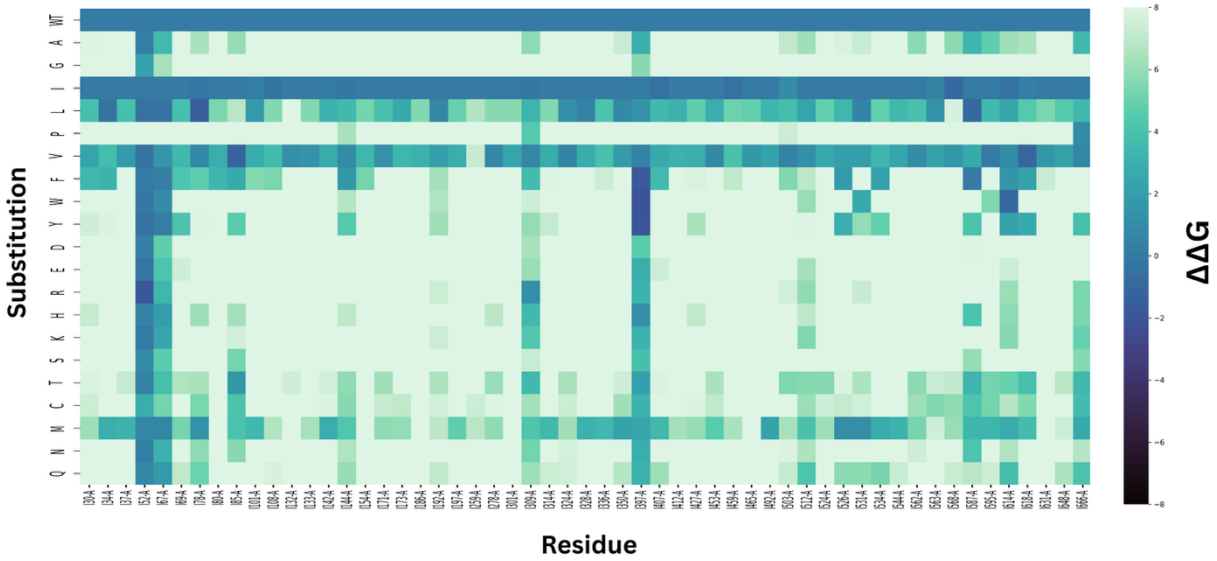

Figure 71: *in silico* saturation mutagenesis ΔΔG stability map for PBP2a from Staphylococcus aureus (PDB: 1VQQ) computed with the Rosetta cartesian_ddg protocol[192].

Columns correspond to the indicated residue positions (1VQQ numbering); rows list the twenty standard amino acids (top "WT" row shows the relaxed wild-type energy). Each cell reports the mean predicted change in folding free energy for the indicated single-site substitution: $\Delta\Delta G = G_{mut} - G_{WT}$. The colour scale bar (right) is centred at 0; darker blue shades indicate increasingly negative ΔΔG values (predicted stabilising relative to wild type), whereas lighter green to off-white shades indicates increasingly positive ΔΔG values (predicted destabilising).

The successful assignment of I67G, I80G, I101G, I173G, I192G, I197G, and I259G meant that I69G, I80G, I171G, I186G and I279G were not included in the revised selection strategy

as they were in areas of the protein where assigned resides were present and it was thought wider coverage where there were no available assignments would be better. Additionally, further mutations at positions I69, I80, and I132 were deprioritised, as they are located far from the allosteric domain - our primary region of interest. Efforts were refocused toward five new isoleucine to valine mutants. This set included two positions where glycine mutations previously failed, which were re-engineered as I314V and I324V. These were complemented by three entirely new target sites, I144V, I197V, and I259V, selected for their proximity to the allosteric domain and other regions of potential significance by previous computational analysis for which there were no existing assigned residues nearby[89]. I154 was deprioritised due to the extensive unfolding evident in its attempted HMQC where, given its buried position central to the purported allosteric communication pathway (Figure 54), there was greater faith in selecting alternative substitutions in residues I314, I324, and I144; selected with similar intent as the sparse Iles flanking the ceftaroline binding interface within the allosteric domain. Similarly, I328, I336 and I465 were deprioritised owing to the large number of probes successfully assigned in the TP domain. All re-engineered valine mutants expressed with greater yields and were successfully assigned with high quality spectra, indicating the *in silico* optimisation strategy was a success, that I>V was a less destabilising substitution versus I>G, and that substitutions with more negative ΔΔG estimations were effective at guiding more conservative mutagenesis choices.

Although full backbone assignment of PBP2a proved experimentally intractable, the work described in this chapter established a workable methyl-based NMR approach for this large and conformationally complex protein. Selective Ile δ1 labelling and targeted mutagenesis enabled the confident assignment of 23 isoleucine resonances spanning the major domains of PBP2a, creating a residue-specific probe set for downstream analysis. At the same time, the assignment process itself yielded useful insight into the behaviour of PBP2a, highlighting the extent to which backbone-based experiments are limited by relaxation, the restricted applicability of NOE-driven methyl assignment in this system, and the structural sensitivity of select residues, such as those positioned within interdomain regions. Together, these findings established both the practical experimental framework and the probe set required for the following chapter, in which ligand binding and conformational dynamics could be examined at residue-level resolution, as well as providing additional structural context for subsequent analyses.

Chapter 4 Characterisation of interactions with antibiotics and inhibition of PBP2a with de novo designed binders

4.1 Abstract

This chapter adds detail to the molecular underpinnings of methicillin-resistance in *Staphylococcus aureus* (MRSA), focusing on the allosteric regulation and inhibition of penicillin binding protein 2a (PBP2a). Using a combination of solution-state NMR spectroscopy and functional assays, this work explores the conformational landscape and ligand-binding dynamics of PBP2a. Chemical shift perturbation (CSP) analysis revealed that while the ineffective β-lactam oxacillin and the peptidoglycan component muramic acid show no detectable binding, the fifth-generation cephalosporin ceftobiprole (CFB) binds directly and with high affinity ($K_d \approx 0.3$ μM) to the transpeptidase (TP) domain of PBP2a, without engaging the allosteric site, distinguishing its mechanism from that of ceftaroline (CFT). Further characterisation of the PBP2a's dynamics using CPMG relaxation-dispersion experiments indicates that apo PBP2a exists in a poised state with significant intrinsic conformational flexibility, particularly in the transpeptidase (TP) domain, N-terminal extension (NTE) and Lobe 1 of the allosteric domain (AD). CFB binding was found to reduce conformational exchange overall while inducing a hybrid dynamic network, retaining apo-like mobility in the allosteric domain but reshaping dynamics around the TP active site to accommodate the inhibitor, distinct to that suggested for CFT by molecular dynamics (MD) simulations, reenforcing the suggestion that the antibiotics have distinct mechanisms of action.

Finally, this chapter explores the potential of *de novo* mini-protein design as a tool to combat antibiotic resistance determinants. Several mini-protein binders were designed, synthesised, and tested against PBP2a. One binder, P66, successfully restored oxacillin susceptibility in MRSA cultures in a dose-dependent manner, with near clinical efficacy. NMR titration experiments confirmed that P66 binds to PBP2a at multiple sites with micromolar affinity, primarily interacting with the allosteric domain's Lobe 1 and the TP domain, suggesting a mechanism that shifts the conformational equilibrium toward a state permissive for β-lactam binding. These findings collectively advance our understanding of PBP2a regulation and demonstrate the viability of computationally designed proteins as adjuvants to overcome antibiotic resistance.

4.2 Introduction

Earlier chapters showed that the remarkable resistance of MRSA to essentially all β-lactam antibiotics is mediated by the expression of PBP2a[4]. This enzyme functions as a bypass transpeptidase, maintaining peptidoglycan crosslinking even when native PBPs are acylated and inactivated by β-lactam antibiotics[4]. The molecular basis of this resistance lies in PBP2a's unusual structural organisation: its TP domain active site is occluded in the resting state, preventing β-lactam inhibition, and can only become catalytically accessible through long-range allosteric communication[4-7]. Binding of an effector molecule to an allosteric site ~60 Å from the catalytic serine (S403) triggers conformational rearrangements that open the active site and enable catalysis[4-7]. This mechanism is now recognised as the Achilles' heel exploited by next-generation anti-MRSA cephalosporins, such as CFT and CFB[7]. However, while this model provides a robust conceptual framework, many of the specific molecular interactions and conformational dynamics that underlie this regulation remain incompletely resolved – particularly in a solution-state context where intrinsic motions and coupling can be observed directly.

This chapter therefore seeks to address these gaps by combining NMR spectroscopy and computational modelling to characterise the conformational landscape and binding mechanisms of PBP2a in solution. Three interrelated questions guided the work: (1) What are the endogenous and antibiotic ligands that engage the allosteric site? (2) How does the binding of different effectors at the allosteric or transpeptidase domains reshape the dynamic network(s) within PBP2a? (3) Can novel synthetic or *de novo* designed effectors exploit this network to restore β-lactam susceptibility? To this end, three classes of ligands were investigated. First, natural peptidoglycan fragments, such as N-acetylmuramic acid (NAM), were tested to determine whether they serve as the physiological allosteric activators hypothesised from crystallographic and computational studies. Second, the clinically relevant cephalosporin CFB was examined to delineate its distinct binding modality and to clarify whether allosteric engagement is required for inhibition as in CFT[5]. Finally, to test whether PBP2a's allosteric communication can be externally manipulated, *de novo* designed mini-protein binders were created using *in silico* protein design tools (RFdiffusion, ProteinMPNN, and AlphaFold) and tested for binding *in vitro* and activity *in vivo*[21-23]. Given PBP2a's central role in conferring resistance to nearly all β-lactam antibiotics, strategies capable of inhibiting or modulating its activity represent a promising route to restore the efficacy of existing antibiotic classes or serve as potent adjuvants. The restoration of

antibiotic susceptibility to facilitate the repurposing of existing ineffective antibiotics is of financial and practical value[1]. Understanding the molecular mechanism of PBP2a function and inhibition at high resolution is therefore critical to overcoming current resistance mechanisms and informing the rational design of next-generation therapeutics. Collectively, these systems provided a platform to explore how ligand chemistry, binding site selection, and induced rigidity-mobility trade-offs govern PBP2a function. The overarching aim was to physically characterise the binding kinetics and conformational effects of these ligands, to map their interaction footprints, and to integrate the findings with previous computational dynamics models[6,89,97] and to establish whether *de novo* designed mini-proteins are a viable avenue for development of PBP2a inhibitors.

NMR spectroscopy is a versatile technique to study the dynamics of proteins in solution[108,113,117] which will allow determination of changes in conformational flexibility of PBP2a in different states. It also allows the detection of weaker interactions than many techniques [182,193]. With first-pass *de novo* designed mini-proteins likely to have low affinity, this makes NMR a good tool for studying binding. The large molecular weight of PBP2a (~75 kDa), however, presents major challenges to traditional NMR. To overcome this, a methyl-specific NMR strategy was employed, using a selectively labelled set of isoleucine δ1 methyl groups as probes. These resonances, distributed throughout the N-terminal extension (NTE), allosteric domain (AD), and transpeptidase (TP) domain, serve as site-specific reporters of both local and long-range conformational changes. By monitoring their CSPs during ligand titrations, it was possible to identify binding sites, quantify binding affinities (K_d) and to infer the propagation of structural signals across domains. Additionally, to move beyond static binding footprints and quantify conformational exchange, we complemented CSPs with methyl-CPMG relaxation-dispersion experiments. These measurements report μs-ms dynamics at specific probes and thereby capture the rigidity-mobility trade-offs that accompany (allosteric) ligand engagement[117], allowing a more comprehensive comparison of apo, antibiotic-bound, and binder-bound states within a unified kinetic-structural framework.

This targeted NMR framework thus provides a residue-level view of ligand binding, allosteric coupling, and dynamic redistribution within PBP2a, forming the foundation for the subsequent analyses. Together with functional MIC assays, these studies reveal how distinct

ligands differentially reshape the conformational energy landscape of PBP2a, and how these effects can be exploited to re-sensitise MRSA to β-lactam antibiotics.

4.3 Aims

The overarching aim of this chapter was to elucidate how distinct ligands – natural, antibiotic, and synthetic – bind to and influence the structural and dynamic landscape of PBP2a, and how these effects relate to enzymatic regulation and β-lactam susceptibility. Specifically, the work sought to:

Aim 1 – Characterise the molecular determinants of ligand binding across PBP2a using solution-state NMR spectroscopy.

(i) Map the binding footprints of diverse ligands – including N-acetylmuramic acid (NAM), oxacillin and ceftobiprole through CSP analysis of selectively $^{13}CH_3$-labelled isoleucine residues.
(ii) Determine whether *de novo* designed binders can be produced to bind to PBP2a, using CSP analysis and whether any successful binders have an *in vivo* effect on PBP2a function.
(iii) Quantify apparent dissociation constants (K_d) and assess the spatial distribution of binding interactions across the N-terminal extension, allosteric domain, and transpeptidase domain.

Aim 2 – Define the dynamic consequences of ligand engagement by probing μs-ms conformational exchange processes using methyl-CPMG relaxation-dispersion experiments.

(i) Compare relaxation dispersion profiles between the apo and ceftobiprole-bound states to determine how local conformational flexibility contributes to allosteric signalling and active-site accessibility.
(ii) Integrate these dynamics with previously reported MD simulations to identify regions that undergo coordinated mobility or stabilisation following effector binding.

Together, these aims sought to build an integrated mechanistic model describing how ligand-induced changes in mobility and inter-domain coupling govern the activity and inhibition of PBP2a, thereby revealing new opportunities for therapeutic re-sensitisation of MRSA to β-lactam antibiotics.

4.4 Results & Discussion

4.4.1 Analysis of PBP2a binding for effective and ineffective antibiotics

4.4.1.1 Non-productive ligands

Chemical shift perturbation (CSP) analysis is a well-established NMR technique for mapping solution-state ligand interactions in proteins[182,193]. Changes in chemical shifts directly reflect alterations in the local electronic environment and thus can sensitively report both direct binding events and propagated structural rearrangements. While CSPs do not directly reveal whether observed shifts arise from local binding or from conformational changes propagated from distal regions, they nonetheless provide a sensitive means of detecting ligand-induced perturbations in the local chemical environment[182,193]. To investigate the binding properties and allosteric regulation of PBP2a in the presence of various ligands, a series of NMR titration experiments were performed. The assigned ^{1}H-^{13}C methyl resonances of a selection of isoleucine residues strategically dispersed throughout the entire PBP2a structure served as sensitive probes to monitor ligand interactions. Three representative ligands were examined: the β-lactam antibiotic oxacillin, the peptidoglycan component muramic acid, and the anti-MRSA cephalosporin ceftobiprole (CFB). Previous studies have shown that ceftaroline (CFT), a cephalosporin related to CFB, exerts its inhibitory effect through a dual-binding mechanism – first engaging the distal allosteric domain (AD) to trigger opening of the transpeptidase (TP) active site, followed by covalent acylation of the catalytic serine[5,6,10]. Whether other antibiotics, such as CFB, share this same two-step allosteric activation mechanism or instead act directly at the TP domain, however, remains unresolved. For each ligand, a 2D ^{1}H-^{13}C SOFAST-HMQC spectrum of apo PBP2a was first acquired at 15^{o}C. Ligands were then titrated over concentration ranges to reflect a 0.5-7:1 molar excess relative to PBP2a to determine ligand-induced CSPs.

Oxacillin is a penicillin-class β-lactam that was specifically developed to be stable against the penicillinases commonly produced by *Staphylococcus aureus*[194]. For many years, it was a frontline therapy for susceptible staphylococcal infections. Resistance to oxacillin is often used in diagnostics to define methicillin resistance where a clinical isolate's resistance to oxacillin is indicative of an MRSA strain[195]. The biological function of PBP2a is to sustain persistent transpeptidase activity despite the presence of β-lactam antibiotics[4]. As oxacillin is not active against PBP2a, it is not expected to bind to the protein, therefore, oxacillin serves as an ideal negative control to establish a functional baseline for antibiotic interaction, where a complete lack of stable binding is the expected outcome. As such, PBP2a was first titrated with a 0.5-7:1 molar excess of oxacillin to PBP2a (Figure 72):

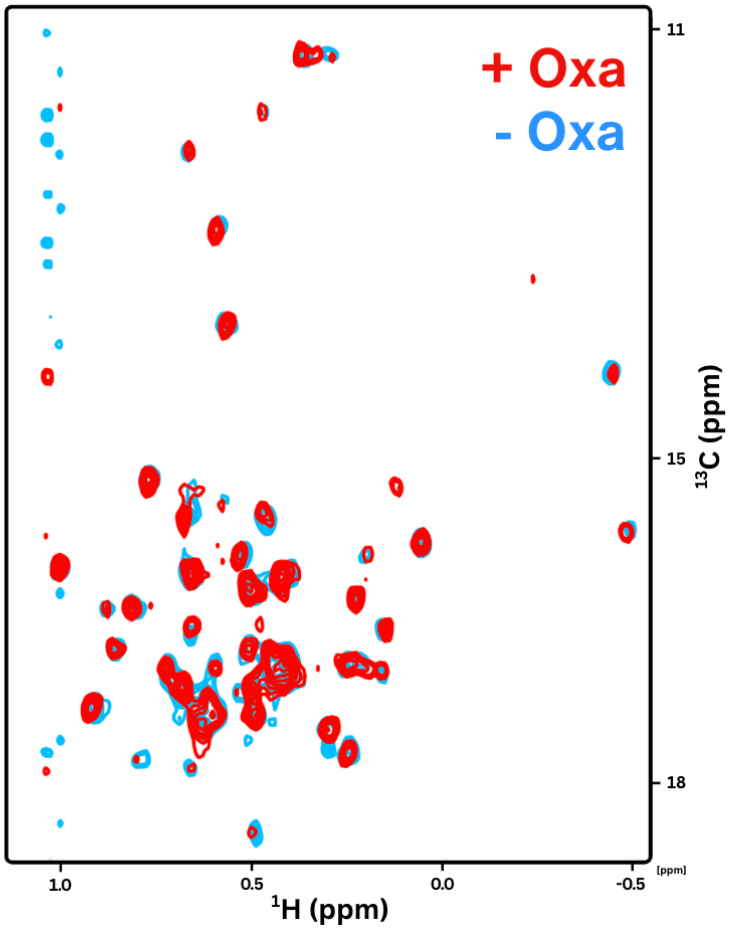

Figure 72: Oxacillin does not perturb PBP2a's isoleucine methyl resonances.

An overlay of the ^{1}H-^{13}C SOFAST-HMQC spectra of 100 µM PBP2a in the absence (blue) and presence of a high (7x) molar excess of oxacillin (red). No significant CSPs are observed.

Even at a 7-fold molar excess of oxacillin over PBP2a, no CSPs or line-shape changes were observed for any assigned or unassigned isoleucine resonances (Figure 72). Previous studies have reported weak (180 ± 25 µM) affinity for oxacillin binding within the allosteric domain in crystals of PBP2a soaked in oxacillin[6,89,196]. CSP-based HSQC/HMQC titrations routinely

detect weak binding in fast exchange with dissociation constants from high-nanomolar to low-millimolar, provided there is adequate signal-to-noise and coverage of the titration range where interactions with K_ds weaker than 10 mM are generally observable under standard conditions[197]. To gauge whether our oxacillin titration should have produced any CSPs, we estimated the fraction bound using the following quadratic[198]:

$$[P_b] = \frac{([P_t] + [L] + K_d) - \sqrt{([P_t] + [L] + K_d)^2 - 4[P_t][L]}}{2}$$

where P_b represents the concentration of bound PBP2a, P_t the total concentration of PBP2a used (μM), L the total concentration of CFB used, and K_d the dissociation constant. At a 7-fold molar excess, with the quoted K_d, ~77% of PBP2a would be expected to be bound with oxacillin, where readily measurable CSPs with peak movement toward the bound position across the series in a concentration-dependent fashion would be expected. The absence of any observable perturbation therefore indicates that oxacillin does not form a stable, solution-state complex with PBP2a that lies within the sensitivity limits of NMR. This is consistent with its functional classification as a non-susceptible β-lactam and reinforces that any apparent binding seen in previous crystallographic studies likely arose from non-physiological artifacts due to crystal soaking with high concentrations (5 mM)[89] of oxacillin in the previous author's results. Such binding events do not necessarily persist in free solution, explaining the absence of any CSPs in these titration data, confirming that oxacillin cannot effectively engage PBP2a under physiologically relevant conditions.

With the system validated, the next experiment sought to further detail the activation of the allosteric domain of PBP2a with a native substrate. Peptidoglycan (PG) reinforces the bacterial cell wall against intracellular turgor pressure through long glycan strands composed of alternating N-acetylglucosamine (NAG) and N-acetylmuramic acid (NAM) saccharides[42,43]. NAM is the unit to which the peptide stem is attached and is a cornerstone of peptidoglycan structure. Muramic acid is the core scaffold of the NAM sugar. The present allosteric regulation model hypothesis is that the binding of the glycan strand to the allosteric site triggers the conformational changes that increase the occupancy of the 60 Å distal transpeptidase (TP) domain (the active site) required for peptidoglycan transpeptidation or inhibition by β-lactam antibiotics[4,5,7,12]. Testing a fundamental building block like muramic acid is therefore a logical first step to further physically characterise the allosteric site. Previous structures of PBP2a crystals soaked in a synthetic disaccharide (complex 1 –

consisting of a single NAG-NAM disaccharide) provided early insights as to the allosteric domain binding interface of peptidoglycan[5] (Figure 73):

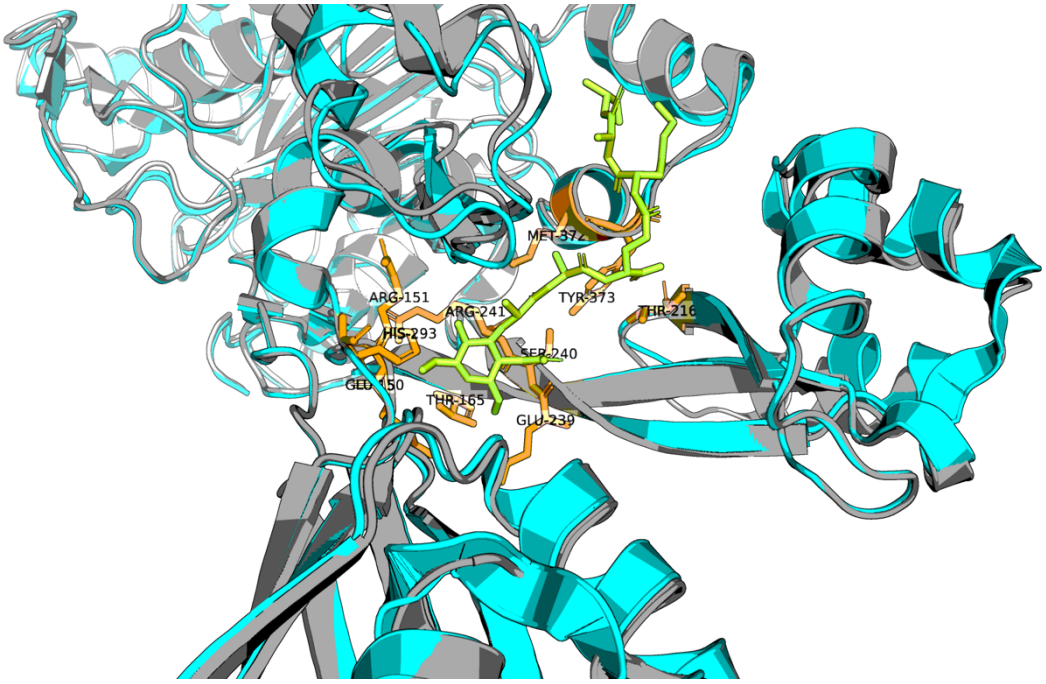

Figure 73: Binding of a synthetic peptidoglycan fragment within the allosteric domain of PBP2a.

Crystal structure of *S. aureus* PBP2a in complex with the synthetic peptidoglycan fragment complex 1 (green sticks; PDB 3ZG5[5]) illustrating its position within the allosteric domain and the coordinating residues (orange) that mediate recognition. For comparison, the apo PBP2a structure (1VQQ[4]) is shown in grey, overlaid with the 3ZG5 complex in cyan. The alignment highlights conformational differences between the apo and ligand-bound forms, particularly in the allosteric pocket, supporting the model in which peptidoglycan binding induces local rearrangements that facilitate distal activation of the transpeptidase domain.

Additional electron density observed in the allosteric domain believed to be due to carryover muramic acid monosaccharide from purification was modelled accordingly[5]. As such, a titration series with muramic acid was conducted to investigate how it might interact with the allosteric domain, specifically; to further detail the role of the D-Ala-D-Ala carrying monosaccharide in allosteric activation in isolation. Titrating PBP2a with muramic acid produced no significant CSPs for any isoleucine probes, even at 7:1 molar excess (Figure 74):

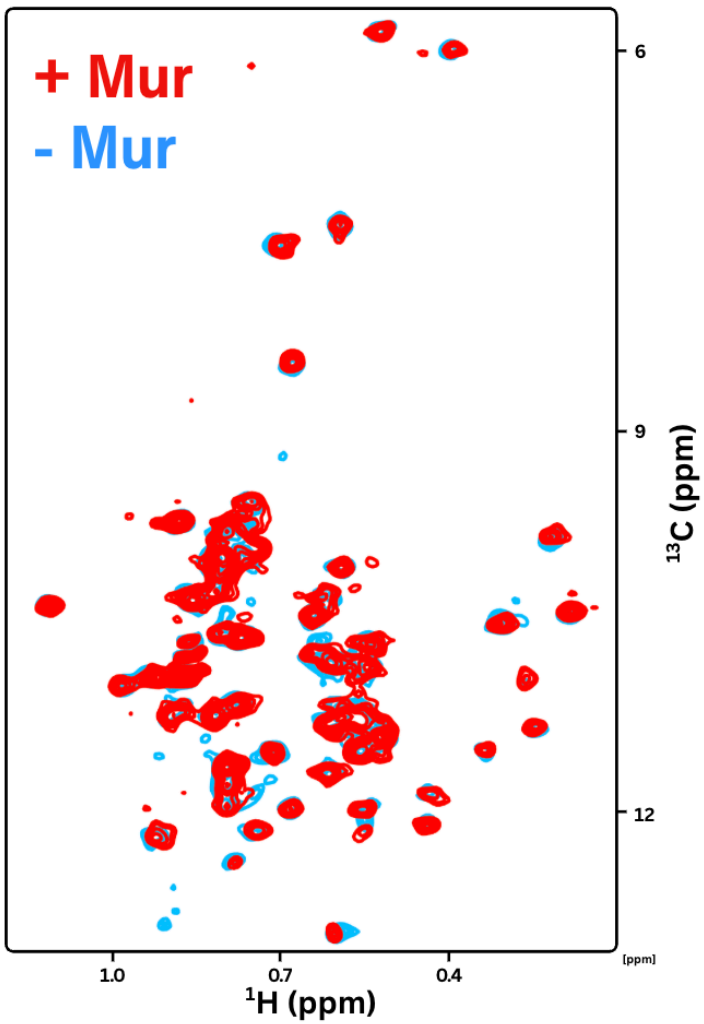

Figure 74: Muramic acid does not induce detectable binding to PBP2a.

An overlay of the ^{1}H-^{13}C SOFAST-HMQC spectra of 100 µM PBP2a in the absence (black) and presence of a 7x molar excess of muramic acid (blue), demonstrating a lack of CSPs for all assigned isoleucine probes.

This provides important context for the allosteric site recognition model established by Otero et al.[5], suggesting that the molecular requirements for binding may be more complex than initially apparent. These data provide direct evidence that muramic acid alone cannot form sufficient stable interactions within the allosteric site to trigger the increase in TP domain occupancy necessary for catalysis or inhibition. This suggests that the D-Ala-D-Ala pentapeptide stem is crucial for the activation of the allosteric domain, consistent with existing hypotheses[5-7,89,92], or indeed that PG molecular recognition depends on more extensive contacts than the single sugar unit can provide – requiring a complete disaccharide (NAG-NAM). Further, although clear structural rearrangements in the transpeptidase (TP) domain were evident in the 3ZG5 structure, a second synthetic fragment was not observed in the transpeptidase domain[5]. This contrasts to crystal structures of PBP2a in complex with ceftaroline (CFT) which clearly show one antibiotic non-covalently bound within the

allosteric domain, and another covalently bound to the catalytic serine (S403) within the transpeptidase domain (PDB ID 3ZG0)[5]. This could indicate that PBP2a's recognition of PG may be similar to PBP2x from *S. pneumoniae*, where additional PG strands may be necessary to act as guides, potentially positioning the allosteric domain as having multiple roles in substrate recognition and catalytic activation[96]. As such, despite PG and CFT showing similar dependency on the allosteric domain for their interaction with PBP2a, these may not be directly comparable with clear distinctions that remain to be characterised.

Previous work demonstrate that recognition of nascent PG occurs in PBP2x through complexation of pentapeptide stems at both allosteric and active sites within the same PG strand, with the allosteric site serving as a critical recognition motif that predisposes the substrate for productive binding at the active site (Figure 10)[72,96]. In this model, the allosteric domain would serve not merely as a passive binding site following rearrangement of the TP domain, but as an active participant in substrate selection and positioning. The inability of muramic acid alone to bind stably may suggest that PBP2a function is dependent on recognition of an entire NAG-NAM disaccharide or indeed multiple units of PG to provide the necessary binding surface and geometric constraints for productive enzyme-substrate interactions. This recognition mechanism would provide several functional advantages: enhanced substrate specificity for nascent over mature PG, to discriminate between PG and β-lactam agents, for proper substrate orientation for catalysis, and/or potentially cooperative binding effects that increase the local effective concentration of substrate at the active site. The requirement for extended peptidoglycan fragments may also explain the resistance mechanisms observed with certain β-lactam antibiotics, where disruption of this cooperative recognition process could modulate antibiotic effectiveness.

4.4.1.2 Susceptible antibiotics

Having established the insufficiency of muramic acid to induce measurable perturbations within PBP2a alone, the next titration series focused on characterising ligand interactions with clinically relevant β-lactams. CFB was selected as a representative fifth-generation cephalosporin with potent anti-MRSA activity and high efficacy against PBP2a[12,106,199]. Previous structural and kinetic studies of PBP2a have concentrated predominantly on CFT, which is known to exploit the allosteric mechanism by binding first to the AD before engaging the 60 Å distal TP domain wherein the active site is located[5]. As a similar

cephalosporin, it is reasonable to expect CFB to engage in similar interactions with PBP2a. However, despite this structural similarity (Figure 12) to CFT and comparable clinical effectiveness, only a single X-ray structure exists for PBP2a in complex with CFB (PDB ID: 4DKI[12]), showing covalent occupancy of the active site but no electron density in the allosteric domain. Consequently, there remains no direct experimental evidence that CFB binds to the AD or signals through the canonical allosteric pathway in solution. Clinical and experimental resistance patterns show clear divergence between CFB and CFT in how they map onto PBP2a. Across surveillance and laboratory-selection studies, CFB resistance (MIC ≥ 4 mg/L; typical susceptible MICs ~0.03–2 mg/L[20,200]) is driven almost exclusively by substitutions within the TP domain. The best-characterised single change is E447K[16,19], which sits adjacent to Y446 on the α2-α3 loop that gates TP domain accessibility. introducing a positive charge here can form a new electrostatic contact (e.g. with E460), distort the loop that frames the R2 channel[4,43], diminishing β-lactam accommodation. Transforming E447K alone into a naïve background confers high-level CFB resistance (MIC ~64 mg/L) but only low-level CFT resistance (MIC ~4 mg/L)[16].

Additional TP domain substitutions conferring CFB resistance cluster into two mechanistic sets (i) changes that introduce polarity near the catalytic core – V470E, F467Y, I563T – likely raising the energetic penalty for S403 acylation, and (ii) changes that alter direct ligand contacts – Y446L/N, E447K, S643N, S649A – which re-shape the R2 channel or remove key H-bonding at the M641 helix[19]. *in vitro* passage frequently yields these TP domain clusters, sometimes in combination with N146K (NTE) but notably, this substitution typically only results in low level resistance to CFB (MIC ≥ 4 mg/L) in isolation[20]. Consistent with this, an Italian MRSA survey reported a 12% rate of CFB resistance (MIC ≥ 4 mg/L) in MRSA isolates – higher than several European datasets (1.7–3.5%)[201,202] – mirrored only in a surveillance study (~15% CFB resistance) in an African cohort[18]. Where genotypes were available, TP domain changes predominated and were often accompanied by mutations in other PBPs[18,201,202]. By contrast, CFT resistance spreads across both the TP domain and the AD. TP-site alterations such as Y446N and E447K are again implicated in high-level CFT resistance (MIC > 32 mg/L) when present – alone or alongside additional TP alterations – by directly impairing binding access at the α2-α3 loop[14]. However, CFT non-susceptibility also tracks strongly with AD/NTE substitutions, notably N146K and E150K[5,6,13,17,18], and with deeper surface changes such as E239K[5,14,17]. In clinical and laboratory isolates, N146K appears repeatedly. Alone it typically produces low-to-moderate

resistance (CFT MIC ~1-2 mg/L; CFB MIC ~2-4 mg/L), but combinatorial AD mutants – e.g. N146K/E150K/G246E or N146K/N204K/G246E – are associated with high rates of CFT resistance and substantial CFB elevations[17,18]. Notably, E150K is a recurring CFT signal, alone, in the above combinations or as a double mutant with N146K[6] with additive effects on resistance, reinforcing the sensitivity of CFT to AD structure. However, in CFB-resistant backgrounds it rarely, if ever, occurs in isolation and instead appears only as part of multi-mutant TP-centric sets (with Y446L, E447K, F467Y, R589K, S649A, etc.), again emphasising the dominant TP contribution to CFB escape. Collectively, resistance mapping supports a TP-dominant paradigm for CFB and a dual-domain paradigm for CFT.

However, role of the AD in CFB resistance remains poorly characterised. To further detail on the resistance mechanisms of CFB, CSP experiments were performed to characterise the binding effects of CFB on PBP2a. These experiments aimed to determine whether CFB engages the AD similarly to CFT or indeed exerts its inhibitory action through direct, active-site binding alone. Titration of PBP2a with CFB produced significant, concentration-dependent CSPs exclusively for isoleucine probes within or adjacent to the transpeptidase domain. Substantial perturbations (exceeding one standard deviation; 0.024 ppm, Figure 75) were observed for residues I85, I197, I512, I524, I563, and I595. Notably, the largest perturbation observed (exceeding two standard deviations; 0.048 ppm) occurred at I407, positioned merely four residues from the catalytic S403. Critically, no significant perturbations were detected for any residues mapping to the core allosteric site. Indeed, some of the lowest CSPs observed in this titration series were those of assigned resonances deliberately selected for their proximity to CFT's binding interface in the allosteric domain (I309, I314), showing no evidence of binding in this region. Mapping the residues showing significant CSPs onto the PBP2a structure revealed a binding footprint clearly localised to the catalytic TP domain (Figure 75). These data therefore support the 4DKI structure that shows no evidence of binding of CFB in the allosteric site[12] and suggest that the mechanism of CFB inhibition of PBP2a is not the same as that of CFT. This correlates well with the different resistance profiles that have been identified for CFT and CFB which also suggest the AD is not required for CFB inhibition of PBP2a.

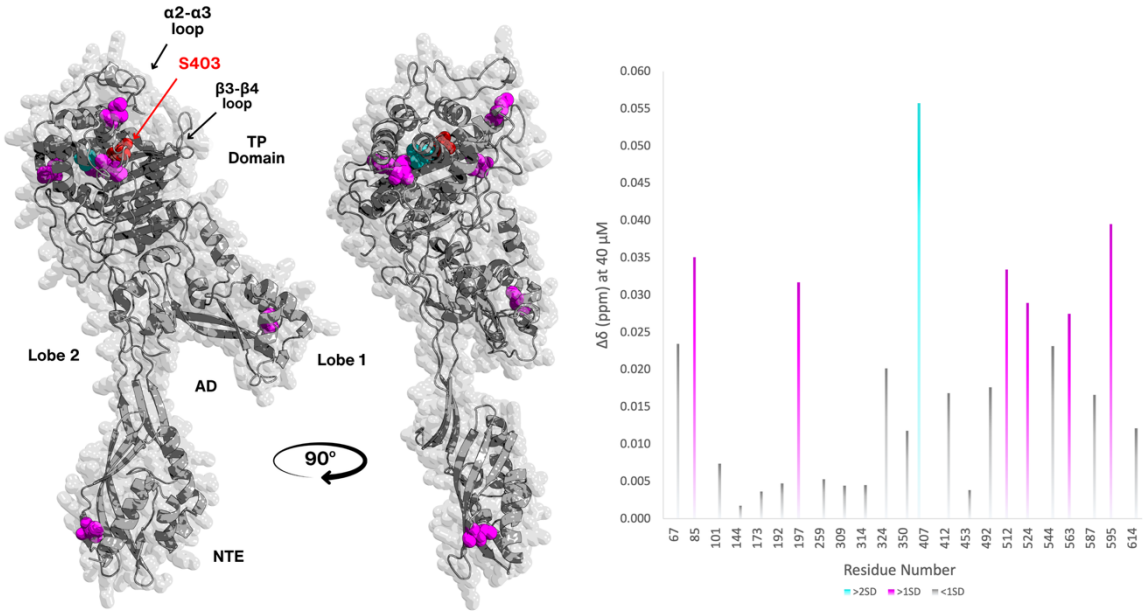

Figure 75: Solution-State NMR Confirms Ceftobiprole Binds Directly to the PBP2a Transpeptidase Domain

Left: PBP2a in complex with ceftobiprole (PDB: 4DKI[12]), with PBP2a shown in grey cartoon representation. PBP2a is also displayed with semi-transparent surface representation for clarity. The assigned isoleucine residues of PBP2a that experienced significant chemical shift perturbations (CSPs) upon CFB titration are shown as spheres. Probes with CSPs exceeding one standard deviation above the mean (>0.024 ppm) are coloured magenta, while those with stronger perturbations (>2 SD, >0.048 ppm) are coloured cyan. The catalytic serine (S403) is shown as red spheres for reference. Key structures are annotated. These data reveal a concentrated cluster of perturbations within the transpeptidase (TP) domain consistent with the expected binding modality of CFB but no comparable cluster in the allosteric site, showing no evidence of CFB binding in this region.

Quantitative analysis of the binding CSPs provided a direct measure of the interaction's high affinity. Fitting the concentration dependent CSPs for the most perturbed probe, I407, to a single site binding model yielded a dissociation constant (K_d) of 0.199 μM, while a combined fit for all significantly perturbed residues (>1 SD) reveals a K_d of 0.329 μM (

Figure 76). These sub-micromolar affinity values are indicative of a potent drug-target interaction and the first K_d reported for CFB, significantly stronger than previously reported inhibition constants for clinically effective anti-MRSA cephalosporin CFT (20 ± 4) μM[89].

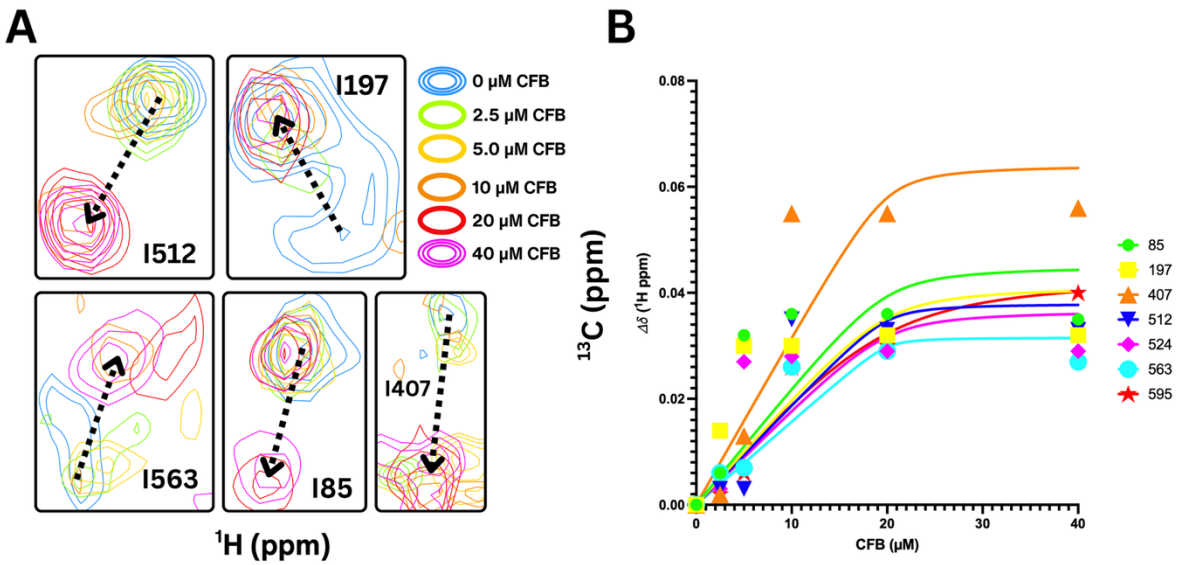

Figure 76: Representative CFB titration and fitted binding curves for PBP2a.

(A) Example ^{1}H-^{13}C SOFAST-HMQC spectra displaying representative significant (>1SD) CSPs upon titration of PBP2a with ^{13}C Ile δ1 selective-labelling with CFB. (B) Fitted binding curves for all residues with CSPs >1SD (>0.024 pm), derived from global and per-residue nonlinear least-squares fitting in CCPN Analysis 3.3.2.1[151].

This high-affinity interaction stands in stark contrast to that of ineffective β-lactams like oxacillin, whose affinity for PBP2a was estimated to be 180 ± 25 µM – but for which, NMR data earlier described show no evidence of binding and suggest any binding would be weaker than 1 mM affinity. These data provide a quantitative basis for ceftobiprole's efficacy, demonstrating that it achieves potent, sub-micromolar binding to PBP2a by engaging the transpeptidase domain directly. This solution-state pattern aligns precisely with previous crystallographic data, confirming that the primary interaction site is the TP domain[12]. The absence of detectable allosteric binding suggests that CFB can access and inhibit the TP domain directly, without requiring stable allosteric engagement, distinct from the closely related cephalosporin CFT[5,6]. Clinical resistance data support this interpretation. The single *mecA* mutation E447K – located in the TP domain – conferred high-level CFB resistance while producing only modest CFT resistance[16], indicating distinct interaction mechanisms. Additionally, high-level resistance to both compounds frequently involves mutations beyond *mecA* (e.g., in *pbp2*, *pbp4*, *gdpP*), suggesting a more complex interplay between PBP2a and other cellular factors[16]. Based on the convergence of solution-state NMR data, crystallographic evidence, and clinical resistance patterns, it is likely that TP domain regulation is not exclusively dependent on discrete allosteric effector binding. While the AD modulates active-site conformation, CFB appears to exploit pre-existing structural plasticity or an alternative conformational pathway to achieve direct inhibition, representing a mechanistically distinct subclass within anti-MRSA cephalosporins.

4.4.2 Probing intramolecular dynamics within PBP2a via CPMG relaxation dispersion

To examine whether conformational flexibility in PBP2a may play a role in the allosteric mechanism of PBP2a and whether ceftobiprole (CFB) binding affects the conformational flexibility of PBP2a, methyl multi-quantum CPMG relaxation-dispersion experiments were recorded for isoleucine residues in the apo state and compared with those of PBP2a in complex with CFB at saturating concentrations (Figure 77). Due to issues with long term sample stability and limits on workable concentrations, the relaxation dispersion data is noisy and could only be acquired at 950 MHz. However, it allows a qualitative analysis of which regions of the protein show µs-ms dynamics in different conditions. Previous crystal structures of PBP2a co-crystallised or soaked with CFB only found CFB bound covalently within the TP domain[12], in contrast with CFT structures wherein one CFT molecule is found non-covalently bound in the AD with another in the TP domain following allosteric domain activation and the subsequent increase in TP domain volume[5]. If CFB dependent inhibition of PBP2a was dependent on allosteric activation, a decrease in µs-ms exchange near the allosteric domain would be expected however, the opposite is evident.

4.4.2.1 Relaxation dispersion experiments in apo PBP2a suggest conformational flexibility that could aid the mechanism of activation:

In the absence of ligand, our CPMG dispersion data evidence 19 Ile residues with µs-ms motion and 6 residues with no dispersion. Generally, the distribution of the dispersion profiles indicates that PBP2a samples a heterogeneous conformational landscape with µs-ms exchange distributed across both the allosteric module and the TP domain (Figure 77):

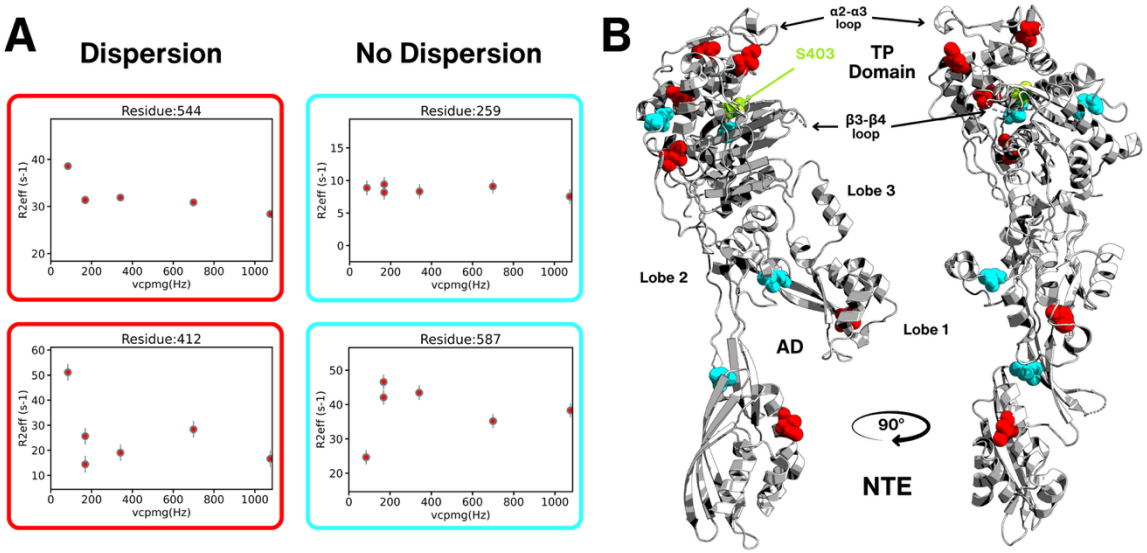

Figure 77: CPMG dispersion profiles of isoleucine residues in PBP2a in the apo state

A) Examples of dispersion profiles in Ile residues showing dispersion (red) and no dispersion (cyan) in PBP2a in the apo state. B) Mapping of Ile residues showing dispersion (red) and no dispersion (cyan) onto the PBP2a structure (PDB ID 1VQQ[4]) in spheres, with the catalytic serine (S403) highlighted in green and domains and key features annotated for clarity. A broad dispersion profile is evident

Dispersion at I67 (NTE) and I173 (Lobe 1 of the AD) points to intrinsic flexibility at the NTE-AD hinge and the Lobe-1 platform that frames the allosteric groove. Complementary exchange in the TP domain at I453 and I512 (near the α2-α3 gatekeeper loop) and I412 and I544 (behind the active site catalytic pocket containing S403) are likely to support local breathing motions required for ligand entrance to the catalytic pocket. Twelve additional, unassigned Ile methyl probes also exhibited dispersion. In contrast, only six probes among the assigned set, I259 (Lobe 2), I314 (AD), and I563/I587 (TP domain, behind the catalytic pocket) showed no dynamics on the μs-ms timescale, consistent with more stable microenvironments. This pattern of exchange in the NTE and Lobe 1 together with a corridor of TP domain-proximal exchange that includes positions adjacent to the α2-α3 loop (I512 and I453) and catalytic pocket (I412, I544) – matches the picture of an apo enzyme that samples wider conformational space, with interdomain breathing and mobile active-site loops. Functionally, this pattern of distributed exchange suggests that apo PBP2a exists in a poised, catalytically competent state characterised by interdomain breathing between the NTE/AD and TP domain, and by the mobile gatekeeper α2-α3 and β3-β4 loops that transiently modulate access to S403. Such coordinated flexibility is likely essential for substrate accommodation during PG biosynthesis, as supported by previous data[4-7,12,89,97]. Concerted motions at the NTE-AD hinge region may act as a mechanical coupler that synchronises distal conformational changes with local opening of the TP domain catalytic

pocket, while the α2-α3 and β3-β4 loop breathing facilitates recognition, positioning, and acylation of the D-Ala-D-Ala stem of lipid II-linked nascent PG precursors for transpeptidation[5-7,89,97]. This is supported by recent MD simulations which have demonstrated that even in the absence of allosteric effectors, apo PBP2a samples a wider distribution of active pocket volumes[97], with a dominant volume of 1450 $Å^3$ than previously anticipated, wherein an increase from 500 $Å^3$ to 1300 $Å^3$ has been believed be an event exclusive to AD activation[5,6]. The coexistence of stable scaffold regions with flexible hinge and loop segments reflects a carefully coordinated balance between stability required for catalysis and the adaptability needed to process a structurally heterogeneous substrate (mature versus nascent PG), whilst remaining selectively extrusive to β-lactam inhibitors.

By contrast, CFT engagement at the AD (CFT1) narrows the free-energy landscape, dampening mobility in the allosteric module while biasing the catalytic gatekeeper loops (α2-α3 and β3-β4) toward opening, wherein the Y446-M641 distance (located on α2-α3 and β3-β4 loops respectively) increases from ~13.5 Å to ~16.5 Å relative to the apo state[97], consistent with foundational work by Otero and colleagues[5]. Subsequent covalent occupation of the TP domain catalytic pocket by CFT2 re-stabilises these loops to levels comparable to the apo state, illustrating a concerted redistribution – not abolition – of motion across the fold[97]. Recent investigations reported that in the apo state, PBP2a occupies a broader free-energy surface than the CFT-bound state[97]. Principle component analysis (PCA) and 2D potential of mean force (PMF) profiles were calculated together with the interdomain angle in MD trajectories which revealed that – relative to the CFT-bound state – the apo state displayed larger interdomain angle fluctuations and consistently higher flexibility in the NTE and Lobe 1[97]. These data were supported by concordant residue-by-residue root-mean-squared fluctuation (RMSF) mapping which showed greater flexibility in the NTE, Lobe 1 and α2-α3 loops in the apo state relative to the CFT-bound state[97]. Our CPMG data mirrors these findings., where collectively, this apo-state behaviour is consistent with PBP2a being a protein with substantial interdomain breathing and loop mobility when unliganded, where the α2-α3 and β3-β4 gatekeepers sample conformations that modulate access to S403 without committing to an open, stabilised pocket. Additionally, network analysis shows a more fragmented coupling pattern (more communities) in apo PBP2a relative to CFT-bound states[97], consistent with weaker residue-residue communication across domains in the absence of ligands.

4.4.2.2 *CFB-bound PBP2a shows an overall reduction in the conformational flexibility compared with apo:*

To distinguish whether dispersion data in the CFB-bound state are reflective of transition between the CFB bound and unbound states or likely reflect dynamics within the protein in the CFB-bound state, experimental concentrations and the earlier (see 4.4.1.2) derived K_d (0.329 µM) were fit to the following equation:

$$[P_b] = \frac{([P_t] + [L] + K_d) - \sqrt{([P_t] + [L] + K_d)^2 - 4[P_t][L]}}{2}$$

where P_b represents the concentration of bound PBP2a, P_t the total concentration of PBP2a used (µM), L the total concentration of CFB used, and K_d the dissociation constant. Given that a 7:1 molar excess of CFB:PBP2a was used with the apparent K_d of 0.329 µM (determined in 4.4.1.2), PBP2a is expected to be 99.73% saturated. Dispersion data are therefore unlikely to reflect a binding-unbinding transition, and these results are hence interpreted in the context of PBP2a fully saturated with CFB. The number of dynamic residues decreased from 19 in the apo state to 14 in the CFB-bound state, while the number of residues displaying no dispersion correspondingly increased from 6 to 16. Many of the residues showing a loss of dispersion upon CFB binding are located in the TP domain (Figure 78).

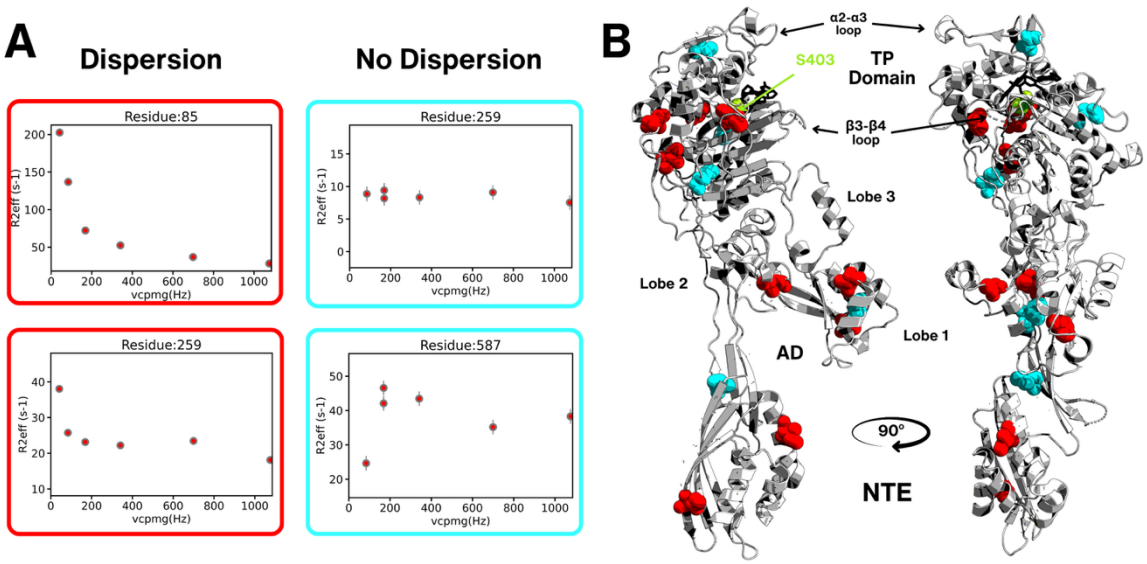

Figure 78: CPMG dispersion profiles of isoleucine residues in PBP2a following CFB binding

A) Examples of dispersion profiles in Ile residues showing dispersion (red) and no dispersion (cyan) in PBP2a in the CFB-bound state. B) Mapping of Ile residues showing dispersion (red) and no dispersion (cyan) onto the PBP2a structure (PDB ID 1VQQ[4]) in spheres, with the catalytic serine (S403) highlighted in green spheres

with CFB covalently bound as black sticks (modelled from 4DKI[12]) and domains and key features annotated for clarity. A broad dispersion profile is evident

This significant net reduction in global conformational exchange and increase in residues that do not show dispersion suggests that CFB binding reduces global conformational flexibility within PBP2a and dampens large-scale domain motions. This is particularly true in the TP domain. However, both the TP domain and AD show enhanced dispersion effects in the presence of CFB, suggesting CFB binding selectively modulates conformational flexibility in both regions, rather than abolishing or selecting for dynamics in either region. The residue-by-residue classification of dispersion behaviour in apo and ceftobiprole-saturated PBP2a is summarised in Table 10:

Table 10: Classification of Ile resonance dispersion in Apo and ceftobiprole-saturated PBP2a from CPMG relaxation dispersion experiments

Resonance ID	Region	Apo	Apo + CFB
A	N/A		
B	N/A	Possible dispersion	
C	N/A		
Ile67	N-terminal extension	Possible dispersion	Possible dispersion
D	N/A	Possible dispersion	Possible dispersion
Ile85	N-terminal extension		Dispersion
E	N/A	Possible dispersion	
Ile101	N-terminal extension		
F	N/A		
G	N/A		
Ile144	Allosteric domain		
H	N/A		Possible dispersion
I	N/A		
J	N/A		
Ile173	Lobe 1	Possible dispersion	Possible dispersion
K	N/A	Possible no dispersion	Possible no dispersion
Ile192	Lobe 1		Possible dispersion
Ile197	Lobe 1		Possible no dispersion
L	N/A		
M	N/A	Possible dispersion	
N	N/A		
Ile259	Lobe 2	No dispersion	Dispersion
O	N/A		Possible no dispersion

Resonance ID	Region	Apo	Apo + CFB
P	N/A	Possible dispersion	
Q	N/A		Possible no dispersion
R	N/A		
Ile309	Allosteric domain		
Ile314	Allosteric domain	Possible no dispersion	
S	N/A		Possible no dispersion
Ile324	Allosteric domain	Possible dispersion	
T	Allosteric domain		Possible no dispersion
U	Allosteric domain		
V	Allosteric domain		Possible no dispersion
W	Allosteric domain		
Ile350	Transpeptidase domain		
X		Possible dispersion	
Ile407	Transpeptidase domain		Dispersion
Ile412	Transpeptidase domain	Dispersion	
Ile453	Transpeptidase domain	Possible dispersion	
Y		Possible dispersion	
Z			Dispersion
A1			Possible dispersion
Ile492	Transpeptidase domain		Possible no dispersion
B1		Possible dispersion	Possible dispersion
Ile512	Transpeptidase domain	Possible dispersion	
C1		Possible dispersion	
Ile524	Transpeptidase domain		Possible dispersion
D1		Dispersion	
Ile544	Transpeptidase domain	Dispersion	Possible dispersion
E1			
Ile563	Transpeptidase domain	Possible no dispersion	Possible dispersion
F1		Dispersion	
Ile587	Transpeptidase domain	Possible no dispersion	Possible no dispersion
G1		Possible no dispersion	
Ile595	Transpeptidase domain		
Ile614	Transpeptidase domain		
H1		Dispersion	
I1			
J1			

Numbered entries indicate confidently assigned Ile residues. Lettered entries indicate unassigned Ile resonances given arbitrary identifiers for analysis and tracking purposes. Classifications were based on inspection of CPMG relaxation dispersion behaviour and are shown as dispersion, possible dispersion, no dispersion, or possible no dispersion. This apo-like behaviour is consistent with recent findings where molecular dynamics simulations of apo and CFT bound PBP2a revealed a marked reduction in root-mean-square fluctuation (RMSF) in the AD following CFT1 binding with concurrently enhanced dynamics within the TP domain to facilitate CFT2 access[97], supported by existing models[5-7,89]. Conversely, the greater stabilisation – in TP domain localised residues – is similar to that observed in the PBP2a_dual system also modelled in by Jiao and colleagues[97], where one CFT molecule bound in the allosteric domain (CFT1) and another CFT molecule covalently bound in the TP domain (CFT2) evidenced the lowest RMSF values in the TP domain and the fewest communities (n = 9) in dynamic network analysis[97], reflecting a reduction in flexibility of the TP domain. Plainly, CFT1 reduced flexibility in the allosteric region while increasing loop dynamics in the catalytic domain to facilitate CFT2 access, following which, CFT dual occupancy (PBP2a_dual) then re-stabilised the active-site loops. An analysis of the regional dynamics and network comparison across the three major domains (transpeptidase domain, allosteric domain and N-terminal extension) as seen in this study, reveals that the CFB-bound state adopts a hybrid dynamic network; one that reduces global conformational flexibility and rearranges stability/dynamics in residues within the TP domain but fails to establish the same dynamic signature of the AD trigger following CFT binding. This reinforces findings that CFB is not dependent on AD activation for PBP2a inhibition – as in CFT – but instead, maintains a more apo-like character.

In the TP domain, which houses the catalytic serine (S403) and the gatekeeper loops (α2-α3 and β3-β4 loops), CFB is expected to stabilise this region as a β-lactam inhibitor following covalent binding with S403 similar to the action of CFT2 in the PBP2a_dual system[97]. Notably, a subset of TP-proximal residues that retain or gain dispersion in the CFB complex – including I407, I524, I544, I563 – relative to the apo state likely reports the flexibility needed for the α2-α3 and β3-β4 gatekeeper loops to settle around the bulky, covalently attached CFB acyl-enzyme (Figure 79). The concordant loss in dispersion in I412, I453 and I512 (located near the catalytic core and α2-α3 loop) seen in the unbound state are consistent with expected counter rearrangements required to accommodate the shift in dynamics seen in these (and other) residues required to increase the occupancy of the catalytic pocket[7,89,97], perhaps supporting CFB binding locking the active site in place.

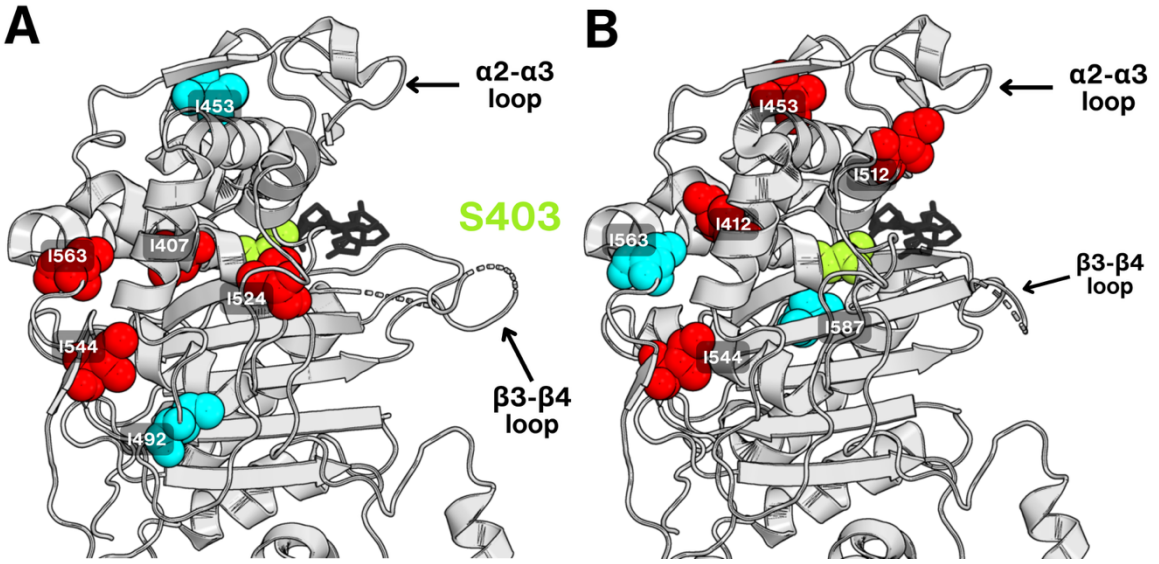

Figure 79: Comparison of dispersion profiles of CFB-bound and apo state PBP2a within the TP domain

Comparison of µs-ms dispersion profiles of residues showing dynamics (red spheres) and no dynamics (cyan) in assigned Ile residues between the CFB-bound (4DKI[12] - A) and apo (B) states within the PBP2a (1VQQ[4]) TP domain. These data reveal a coordinated rearrangement in dynamics that likely facilitates stabilisation of the α2-α3 and β3-β4 loops and open conformation of the catalytic pocket to enable CFB (black sticks) access to the catalytic S403 (green spheres).

Based on the remaining unassigned isoleucine positions within PBP2a and the CFB-induced rigidity-mobility pattern evidenced in this study and previous work[97], many of the unassigned non-dispersing residues (n = 11) in the CFB-bound data will likely map around isoleucines buried in/around the TP-domain catalytic core, necessary to maintain the dynamic equilibrium following covalent inhibition. By contrast, the unassigned, dispersing set (n = 5) may either be drawn from peripheral TP-entrance positions flanking the α2-α3/β3-β4 gatekeeper loops and/or hinge-proximal NTE/AD contacts, as per the CFB-bound state reflecting a more apo-like AD but a more CFT2-like TP domain. However, further

assignment is needed to confirm this. This highly coordinated alteration of the dynamic network in the TP domain likely underpins the shift in the conformational landscape necessary to accommodate CFB accessing of S403. Residues in both the AD and TP domain show persistence of µs-ms dynamics but with a different signature of residues displaying dispersion – or lack thereof – noted between the CFB-bound and apo states. This suggests that, like the apo state, covalent inhibition by CFB does not eliminate all conformational exchange motions within the TP domain functional regions, dynamically distinct from the PBP2a_dual state, where secondary CFT (CFT2) binding re-stabilises the TP domain[97]. Taken together, this shift in dynamics suggests that a local breathing rather than long-range allosteric opening underlies CFB binding within the TP domain, consistent with local accommodation of the inhibitor independent of prior allosteric activation.

Numerous assigned residues near the NTE and AD (67-324) are likely crucial for allosteric regulation. The dynamic pattern observed upon CFB binding contrasts significantly with the CFT1 allosteric trigger suggested by MD simulations[97], aligning more closely with the apo state. The PBP2a_closed_CFT1 allosteric mechanism relies on CFT1 selectively reducing the flexibility of the NTE and in Lobe 1 of the AD, where this decrease in dynamics relative to the apo state is hypothesised as a key trigger a propagation of structural rearrangements which opens the active site[97]. By contrast, CFB binding induces or retains conformational exchange in this region where I85, I192 and I259 show dispersion in the CFB-bound state but not in the apo state, while residues I67 and I173 retain similar dispersion profiles in both apo and CFB-bound states. This suggests an increase in dynamics within the AD as a consequence of CFB binding within the TP domain and its subsequent stabilisation independent of allosteric activation such as in CFT1 binding, where a reduction in flexibility would be expected[97]. This shift in dynamics in the CFB-bound AD qualitatively mirrors the MD simulations which revealed high intrinsic mobility of the apo protein with wider free energy surfaces and large interdomain motions, indicating high conformational dynamics in the AD in the unbound state[97], also mirrored by our apo state data. This in opposition to the dynamic requirements of the present understanding of the CFT1 allosteric mechanism, providing further support that CFB does not engage or activate the canonical CFT1 signalling pathway engaged by its allosteric trigger.

These data demonstrate that inhibition via CFB-binding occurs through a selective reorganisation of µs-ms dynamics across distinct structural regions, producing a coordinated

pattern of local stabilisation and compensatory flexibility. These changes collectively describe a mechanism in which the covalent acylation of the TP domain by CFB leads to a constrained but not static conformation – one that preserves the local breathing motions required for accommodation of the inhibitor within the catalytic pocket while retaining/enhancing apo state dynamics in the AD and NTE. Following CFB binding, within the NTE and connecting lobes (1-2) of the AD (residues I67, I85, I101, I173, I192, I197, I314, and I324), dynamic exchange was largely retained or modestly increased relative to the apo state. This behaviour is consistent with the expectation that these regions remain conformationally mobile even when the TP domain is stabilised following CFT/CFB binding in the absence of an allosteric effector[97]. The persistence of µs-ms motion in this region in the CFB-bound state relative to the apo state implies that the NTE-to-Lobe-1 hinge remains uncoupled from the structural stabilisation observed in the TP domain, wherein CFB-TP domain access is independent of allosteric activation. Relative to the apo state, residue I173 retained dispersion while I192 gained dispersion in the CFB-bound state, consistent with the expected dynamic trade-off to maintain the energetic balance of the protein's dynamic network.

Some residues in the NTE – I67 and I85 – likewise displayed µs-ms exchange following CFB binding, while I314 was persistently undynamic, confirming that this region maintains an apo-like character. The continued flexibility of the NTE and its connecting hinge in the CFB-bound state suggests that, despite covalent inhibition, the domain interface remains mobile and does not undergo the stabilisation associated with allosteric activation that would be expected as per the PBP2a_closed_CFT1 simulation[97]. The overall mirroring of the NTE in CFB-bound and apo states (Figure 77 and Figure 78) too supports that CFB binding does not trigger the conformational cascade characteristic of CFT binding but rather stabilises a state in which distal flexibility is maintained without propagating a structural signal toward the catalytic pocket. Previous data have observed a 3 Å shortening in the distance between Lobes 1 and 2[7,12,89] as well as a decrease in RMSF following AD activation following CFT binding[89,97]. A reduction in dynamics would be expected in Lobe 1 residues following allosteric effector binding where instead, a retention of dynamics is evident. I324 displayed a loss of dispersion in the CFB-bound state relative to the apo conformation with two possible interpretations: (i) the apo state dispersion reflects this region is dynamic between open and closed states, but following CFB binding and selection for the open state, these dynamics are lost, or (ii) given its proximity to the source residue of the CFT allosteric

communication network R297[97], although CFB binding does not depend on AD activation, it may engage similar structures in the C-terminal portion of the same network. Overall, the persistence of mobility across the NTE and Lobe 1 indicates that these regions act as dynamic buffers, absorbing the redistribution of conformational energy caused by TP domain rearrangement and stabilisation following CFB binding, maintaining structural equilibrium within PBP2a.

In contrast, a distinctly different pattern of behaviour was evidenced in the assigned residues within the TP domain (residues I407, I412, I453, I492, I512, I524, I544, I563, I587) between apo and CFB-bound states (Figure 79). Here, dispersion profiles indicated that CFB binding results in both the loss and gain of local dynamics, delineating a corridor of adaptive flexibility centred around the α2-α3 and β3-β4 gatekeeper loops that control access to the catalytic pocket and its surrounding residues. Several residues (I407, I524, and I563) gained μs-ms exchange, whereas others (I412, I453 and I512) lost dispersion, and I544 and I587 retained their dispersion/lack of dispersion between both apo and CFB-bound states. Given their proximity to the α2-α3 loop, the loss of dispersion in I453 and I512 in the CFB-bound state and the evidenced reduction in RMSF in the PBP2a_dual[97] (with CFT covalently bound in the TP domain) state following simulations relative to the apo states is consistent with some expected reduction in dynamics following TP domain binding. Conversely, the persistence in dynamics in I563 & I544 and gain in I524 – clustered near the outer face of the binding pocket – & I407, along with the loss in dispersion in I412 (both on the same helix as I403) and I492 in the CFB-bound relative to the apo state suggest peripheral fluctuations linked to structural rearrangements needed to maintain dynamic equilibrium following CFB binding (

Figure 79 79).

Collectively, the relaxation-dispersion data reveal that CFB binding retains apo-like dynamics near the AD, whilst reshaping dynamics around the TP domain. The TP domain of PBP2a transitions into a conformationally restrained but not rigid state, where local flexibility in the TP domain coexists with distal mobility in the allosteric region. This hybrid dynamic network defines a non-allosteric mode of inhibition: one in which CFB achieves covalent locking of the catalytic site through direct engagement, while the residual flexibility reflects adaptive accommodation rather than the propagation of an allosteric opening signal. Such a mechanism highlights how CFB exploits the intrinsic flexibility of PBP2a to achieve

inhibition independently of the canonical allosteric activation pathway, providing new insight into the conformational logic underlying β-lactam resistance and its circumvention.

4.5 Design of *de novo* protein binders against PBP2a

As well as the development of novel antibacterial agents, given the current threat from AMR and the lack of novel drugs in the pipeline, inhibiting existing resistance mechanisms is a potential alternative to rejuvinate the usefulness of current antibiotics. *De novo* designed mini-protein binders show promise in development of binders to proteins for which ligands are not available. In the case of PBP2a, these could provide inhibitiors of this protein, particularly as there is no need to gain entry into the cell and could therefore inhibit this resistance mechanism. To the best of our knowledge, to date, only one example of *de novo* designed binders with demonstrable affinity against antibiotic resistance determinants exists[203]. Further, such mini-proteins have not previously been used to target and effect antibiotic resistance mechanisms within MRSA *in vivo*. To determine if this was a viable strategy, mini-protein binders to PBP2a were designed by collaborator Dr Bob Schiffrin to both the mid-region of the transpeptidase domain and the allosteric domain either to constrain the TP domain into an accessible conformation or to activate the AD, to subsequently facilitate the restoration of susceptibility to previously ineffective antibiotics . An AlphaFold 3 model of PBP2a, created using https://alphafoldserver.com, was used as the target structure, with the N-terminal domain removed to reduce the size of the system. Binder backbones were created with RFdiffusion[204], stochastically sampling binder lengths between

```
python ~/RFdiffusion/scripts/run_inference.py \

"inference.output_prefix=output_files/Pbp2a/bind" \

inference.input_pdb=filt_20_AF_pbp2a.pdb \

'contigmap.contigs=[A147-149/A151-152/A163-163/A166-166/A168-
169/A191-191/A216-223/A238-241/A243-243/A246-297/A315-316/A318-
322/A340-340/A342-347/A360-406/A408-410/A412-413/A416-416/A418-
418/A426-446/A463-465/A467-531/A533-533/A546-547/A549-549/A558-
558/A599-616/A632-641/0 50-110]' \

'ppi.hotspot_res=[A438,A439,A440,A512,A506,A513,A515,A516,A522,A523
,A524,A525,A601,A602,A603,A604,A605,A606,A614]' \

inference.num_designs=50
```

50 and 110 residues. Residues in each region were provided as hotspot residues. An example RFdiffusion script is given below:

A total of ~3,000 protein backbones were designed to each region. Binder sequences were designed with ProteinMPNN and FastRelax[22,23], using one relax cycle, and one sequence per backbone. Structures of the PBP2a/binder complexes were then predicted with AlphaFold 2 using the af2_initial_guess protocol[21,23], which provides the designed structure as a template to the model. Filtering and selection of binders was performed by considering interface PAE (<10) and mean binder pLDDT (>80) scores, as well as visual inspection. Dr Schiffrin selected 6 designed mini-proteins, that were targeted at the AD binding interfaces of PG or CFT, regions scaffolding Lobes 1-3 with the TP domain, and regions near the α2-α3 and β3-β4 loops. All selected designs were all-helical. Models of each binder are illustrated in Figure 80:

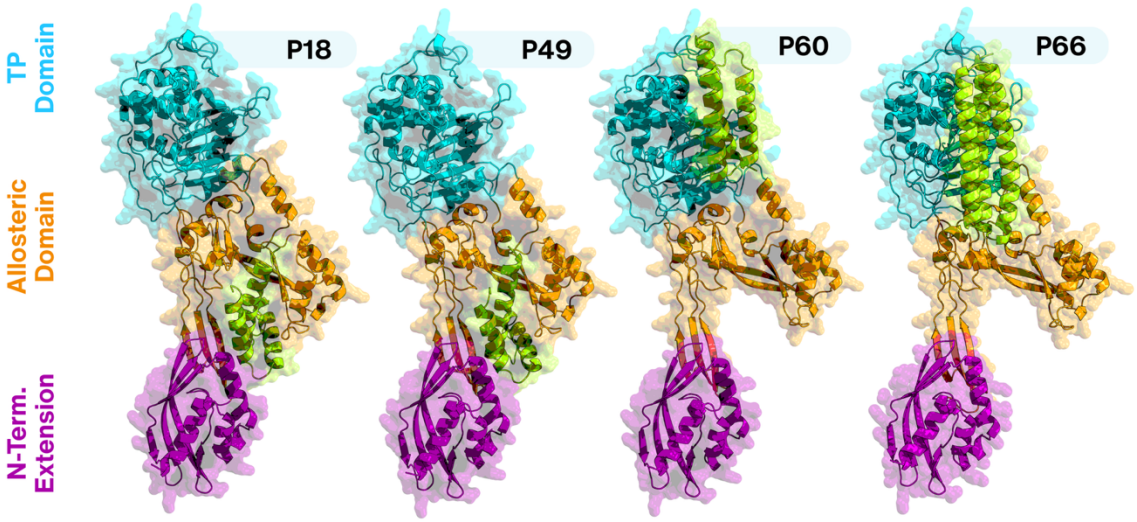

Figure 80: AlphaFold models of *de novo* designed protein binders P18, P49, P60, and P66 in complex with PBP2a.

AlphaFold models showing the predicted binding interfaces for four computationally designed protein binders (P18, P49, P60, and p66) positioned where they are predicted to bind to PBP2a (1VQQ[4]). PBP2a is shown with domains coloured according to the key (N-terminal extension in purple, allosteric domain in orange, and transpeptidase domain in cyan). Each binder (shown in limon cartoon representation) was designed to engage different surface features across the allosteric and transpeptidase domains to probe diverse regions of PBP2a.

4.5.1 Overexpression and structural validation of *de novo* designed protein binders

Expression of mini-protein binders in *E. coli* BL21 Gold in LB medium at 37°C (shaking at 220 rpm) for 6 hours resulted in high levels of expression of each recombinant protein binder, with a typical yield of 10 mL of 3 mM binder per 1 L of culture following purification via

Ni-NTA chromatography. Binders were validated for purity, molecular weight and folding as follows (Figure 81):

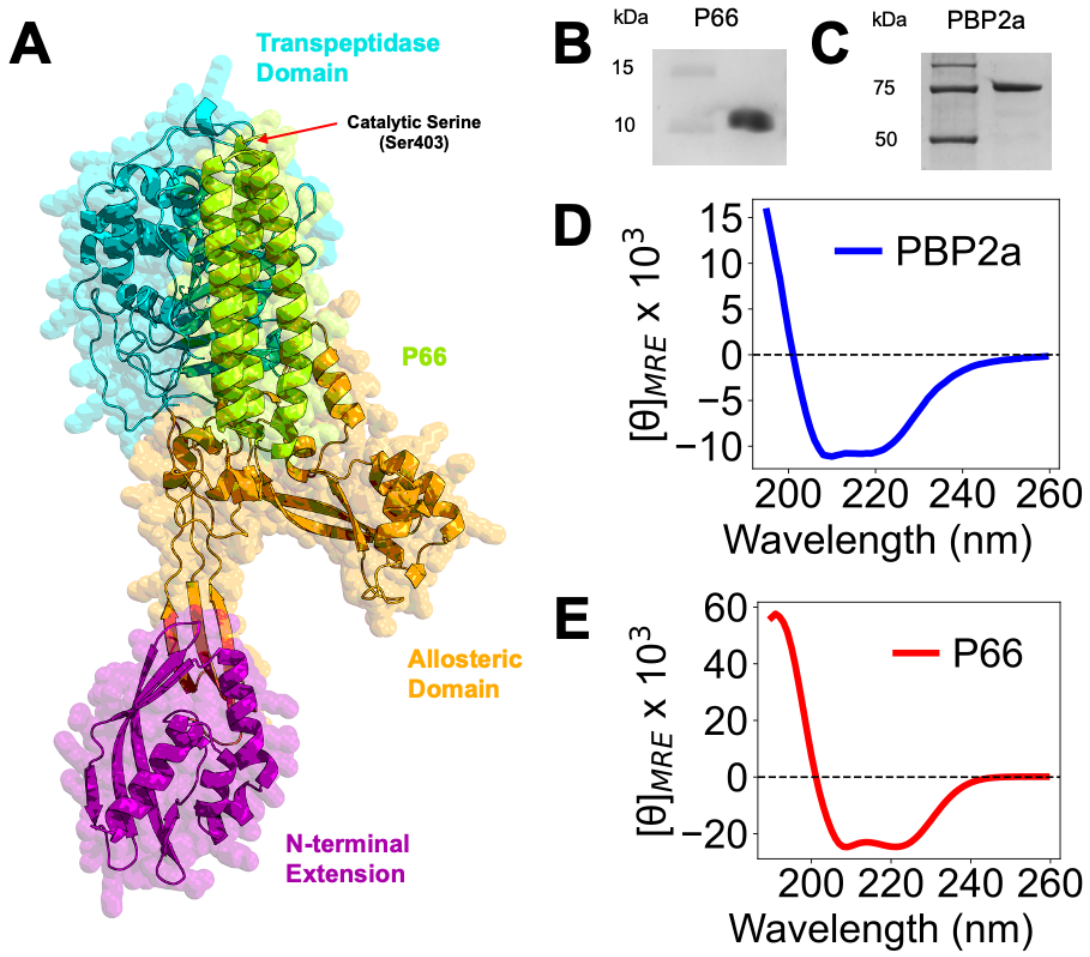

Figure 81: Experimental validation of P66, a *de novo* protein binder targeting *S. aureus* PBP2a designed with AlphaFold

A: Overview of P66:PBP2a predicted binding interface. P66 is shown as a green coloured cartoon with semi-transparent surface representation modelled onto PBP2a coloured by domain with the position of the catalytic serine (Se403) indicated with an arrow. P66 was designed such that it spans most of the transpeptidase (TP) domain, scaffolding across to the edge of the allosteric domain at the intersection of lobes 1-3. SDS-PAGE confirms the expected molecular weights of the Ni-NTA-purified components. B: P66 at ~11 kDa and C: PBP2a at ~76.5 kDa. Circular dichroism (CD) spectroscopy confirms both proteins are correctly folded. E: The spectrum for PBP2a shows features of a mixed α/β protein. F: the spectrum for P66 shows strong negative minima at ~208 and ~222 nm, indicative of a predominantly α-helical structure, consistent with its design.

SDS-PAGE confirmed the expected approximate molecular weights (Table 9) of each *de novo* designed binder and that the proteins were of sufficient purity. Circular dichroism spectra confirmed each binder and PBP2a was correctly folded prior to experimentation, with PBP2a displaying a mixed α/β profile and binders exhibiting their expected all-helical characteristics as designed.

4.5.2 Binder MICs

To assess whether *de novo*-designed binders could restore susceptibility to β-lactam antibiotics, USA300 (*S. aureus*) cultures were grown in 96-well plates with oxacillin (8 μg/mL) and serial dilutions of each binder. While 8 μg/mL is subinhibitory to MRSA, it is sufficient to inhibit the growth of methicillin-susceptible *S. aureus*. OD_{600} was measured after 20 hours at 38 °C. The effect of the all binders on the oxacillin resistance phenotype of *S. aureus* USA300 was assessed using a broth microdilution assay in Mueller-Hinton Broth (MHB) (Figure 82). Bacterial growth (measured as optical density at 600 nm, OD_{600}) was monitored across a range of binder concentrations, with control experiments conducted in the absence of oxacillin. In the absence of oxacillin, none of the binders show any significant inhibitory effect on cell viability at the concentrations tested, as shown in the example of P66 in Figure 82 (blue line), showing none of the binders are capable of antibiotic activity alone. In the parallel experiment, cells were grown in the presence of a sub-inhibitory concentration of oxacillin (8 μg/mL) while being treated with increasing concentrations of binder to determine whether the binders could inhibit PBP2a and therefore resensitise MRSA to oxacillin. For P18, P25, P49, P60 and P74 no growth inhibition by oxacillin was observed so these proteins had no inhibitory effects on PBP2a. However, a clear dose-dependent inhibition of growth was observed for P66 (red line in Figure 82), with a sharp decrease in OD_{600} occurring at approximately 9 μM of P66. This demonstrates that P66 acts synergistically with oxacillin, re-sensitising the otherwise resistant USA300 to a previously ineffective β-lactam antibiotic, indicating a phenotypic effect consistent with enhanced antibiotic susceptibility. Among all tested constructs, P66 was the only binder to show a consistent decrease in OD_{600} at sub-micromolar concentrations. However, this demonstrates that the use of *de novo* designed mini-proteins can be a successful strategy to rejuvenate the effectiveness of β-lactam antibiotics against strains harbouring PBP2a.

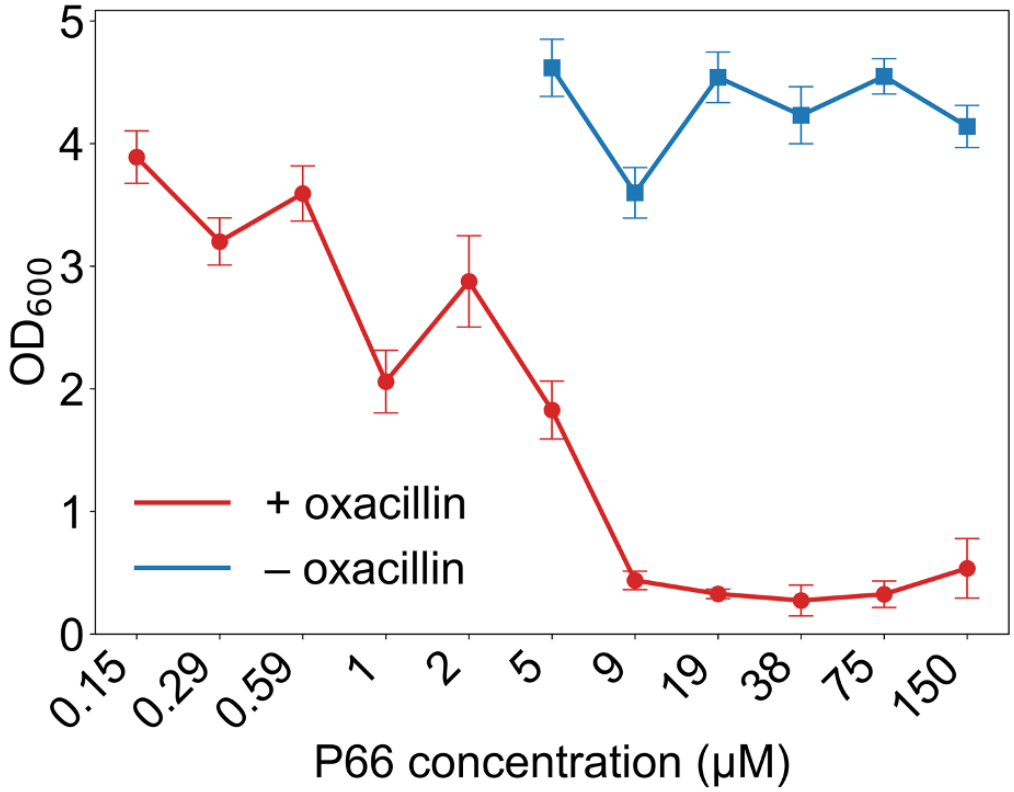

Figure 82: *de novo* designed binder p66 restores oxacillin susceptibility in *S. aureus* USA300

A broth microdilution assay of binder p66 on the growth (OD_{600}) of *S. aureus* USA300 in the presence and absence of oxacillin. The control experiment (blue line – p66 binder and USA300 only) shows that p66 alone has no inhibitory effect on cell viability in the absence of oxacillin. In the presence of a sub-inhibitory concentration of oxacillin (8 µg/mL, red line), p66 results in a dose-dependent inhibition of growth, demonstrating successful re-sensitisation of MRSA to oxacillin. Data points represent the mean of three biological replicates ± standard deviation.

4.5.3 Chemical shift perturbations following binder titration

To further characterise any binding interactions between each of the binders and wild-type PBP2a, a titration series using 2D ^{1}H-^{13}C SOFAST-HMQC spectra of increasing stoichiometric ratios of binder:PBP2a (from 0.5-5.0:1.0) was conducted. Consistent with their lack of functional activity *in vivo*, *de novo*-designed binders P18, P25, P49, P60 and P74 did not produce detectable CSPs following NMR titrations with wild-type PBP2a up to a molar excess of 7:1 binder:PBP2a, showing that these mini-proteins do not bind to PBP2a (Figure 83):

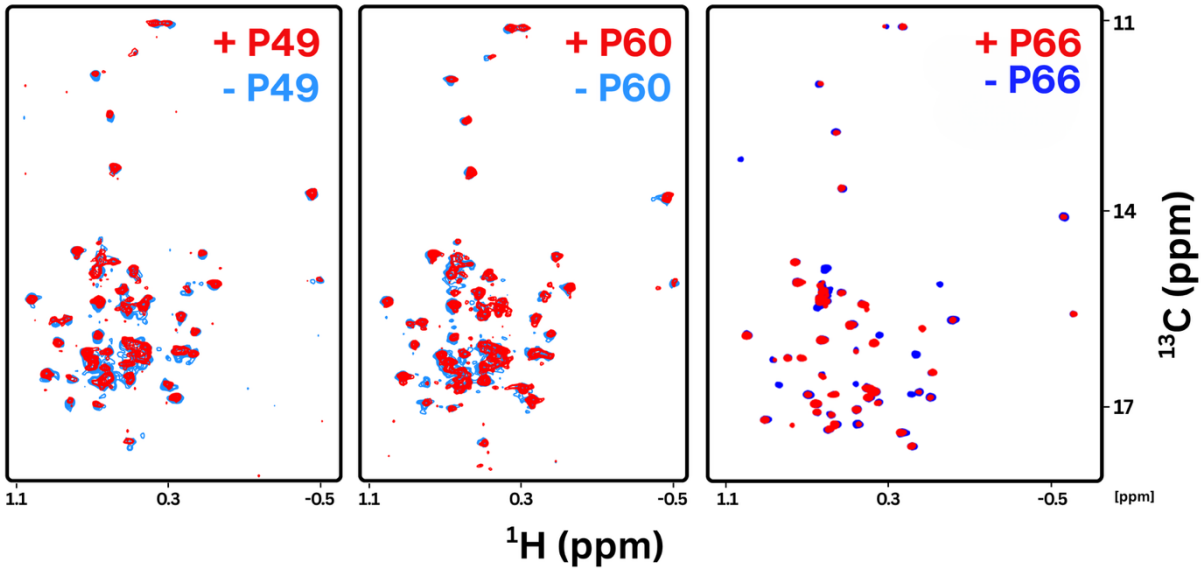

Figure 83: *de novo* designed binders P60 and P49 Show No Detectable Interaction with PBP2a.

Overlaid 2D ^{1}H-^{13}C SOFAST-HMQC spectra recorded for 20 μM PBP2a with ^{13}C Ile δ1 selective-labelling in the absence (blue) and presence (red) of a five-fold molar excess of each binder. The spectral overlays for both the P49 titration (left panel) and the P60 titration (middle panel) and P66 (right panel) show no significant chemical shift perturbations for any of the isoleucine methyl probes for P49 or P60, indicating that neither form a detectable complex with PBP2a. By contrast, several significant chemical shift perturbations are shown in P66, demonstrating a direct interaction between P66 and PBP2a.

In contrast, P66 exhibited clear CSPs across multiple residues, suggesting binding to the target protein (Figure 83), consistent with P66 showing an effect on oxacillin MIC. P66 was designed to scaffold between both the allosteric and transpeptidase domains of PBP2a, spanning Lobes 1-3, with the intention of constraining the TP domain in an open conformation, accessible to β-lactam antibiotics. Titration of PBP2a with ^{13}C Ile δ1 selective-labelling with unlabelled P66 (from 0.5-5.0:1.0 concentrations of P66:PBP2a) produced significant, concentration-dependent CSPs across multiple isoleucine probes, confirming direct protein-protein interaction. The binding footprint was systematically mapped by identifying residues exhibiting chemical shift perturbations exceeding one and two standard deviations (Figure 84).

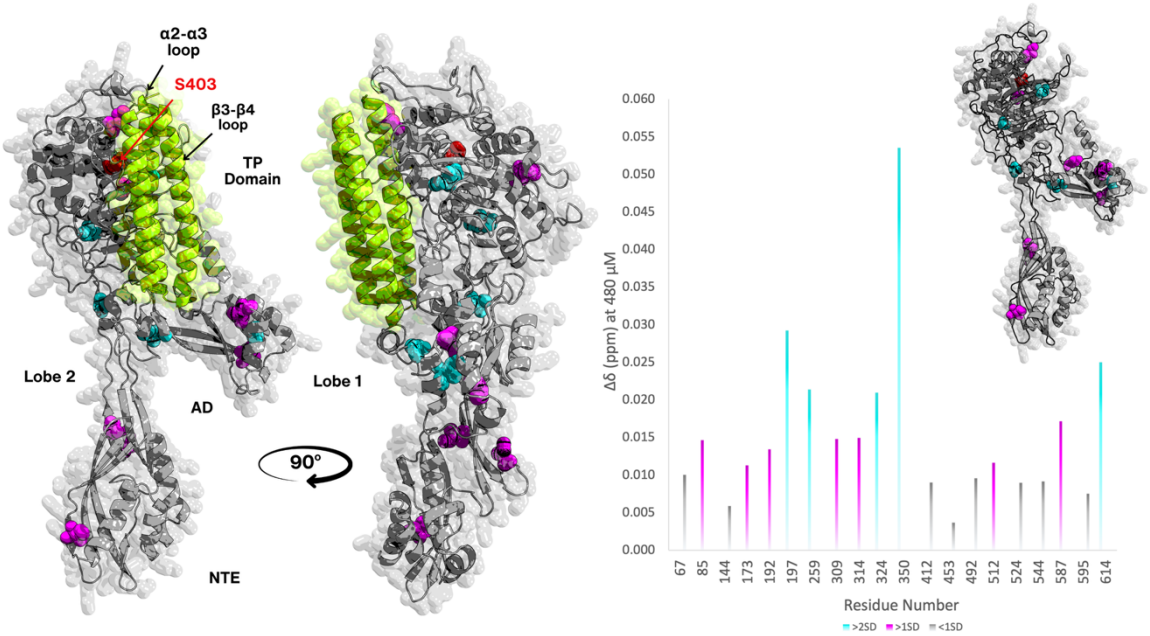

Figure 84: Experimental mapping of the PBP2a-P66 binding interface

Computational model of P66 in complex with PBP2a (PDB: 1VQQ[4]) in the position in which P66 was designed to bind, with PBP2a shown in grey cartoon representation and the P66 binder in limon cartoon representation. Both P66 and PBP2a have semi-transparent surface representations included for clarity. The assigned isoleucine residues of PBP2a that experienced significant CSPs upon P66 titration are shown as spheres. Probes with CSPs >1 SD are coloured magenta, while probes with stronger perturbations (>2 SD) are coloured cyan. The catalytic serine (Ser403) is shown in red spheres for reference. The experimental data confirm a broad interaction footprint with a clear high affinity "hotspot" near the allosteric domain. Data reproduced with P66 omitted top right for further clarity.

The most substantially perturbed residues (greater than two standard deviations, cyan, Figure 84) included I197, I259, I324, I350, and I614, distributed across both the allosteric and transpeptidase domains. Structural mapping of these perturbed isoleucine probes onto the PBP2a crystal structure (PDB: 1VQQ[4]) demonstrated that while several residues cluster near the computationally predicted P66 interface bridging the Lobe 1 and TP face, additional sites of perturbation were detected across the distal allosteric surface (Figure 84). This pattern suggests that P66 may interact with multiple regions of PBP2a, or that its binding induces broader conformational adjustments extending beyond the immediate docking interface. The observed chemical shift changes within the allosteric region could therefore reflect either secondary contacts formed by the binder or allosterically propagated effects of engagement at the TP-Lobe 1 junction. Importantly, these data indicate that P66 binding does not fully occlude the catalytic pocket, consistent with its demonstrated capacity to restore oxacillin susceptibility *in vivo*. Together, these findings support a model in which P66 associates with a distributed interface spanning both the allosteric and catalytic domains, while preserving conformational accessibility of the active site required for β-lactam acylation.

Quantitative analysis of binding affinities was performed through systematic fitting of titration data using CCPN Analysis 3.3.2.1 (Figure 85). A global fit incorporating all isoleucine resonances yielded an apparent dissociation constant (K_d) of 60.89 µM. However, this global value masks significant regional variations in affinity, suggesting a non-uniform, multi-modal binding event. When probes were grouped by structural region, a clear hierarchy of affinities was evident. The tightest binding was observed for probes located in Lobe 1 of the allosteric domain (I173, I192, I197) and the adjacent N-terminal extension (I85, I309, I314), which yielded highly similar local K_d values of 12.9 µM and 18.7 µM, respectively. Moderate affinity was noted for the residues (I512, I524, I544, I614) clustered in the TP domain (K_d = 69.6 µM) and was weakest for those (I259, I324) in Lobe 2 of the allosteric domain (K_d = 335 µM). These results suggest the existence of multiple interaction surfaces rather than a single discrete binding site for P66 on PBP2a.

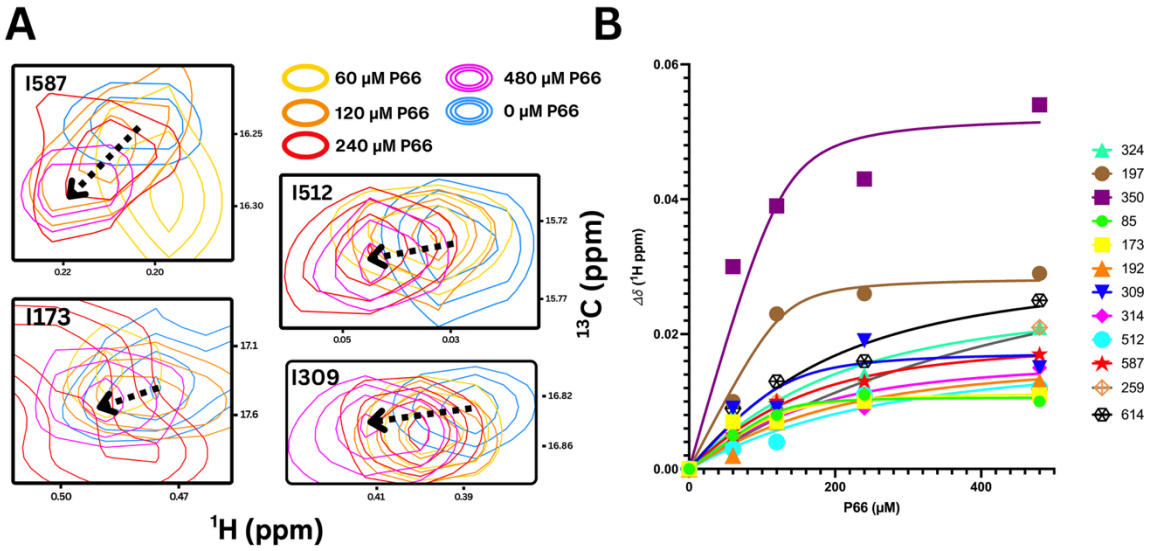

Figure 85: Representative chemical shift perturbations and binding isotherms for assigned PBP2a residues following P66 titration

(A) Example ^{1}H-^{13}C SOFAST-HMQC spectra displaying representative significant (>1SD) chemical shift perturbations (CSPs) upon titration of P66 into PBP2a with ^{13}C Ile δ1 selective-labelling. (B) Fitted binding curves for all residues with CSPs >1SD, derived from global and per-residue nonlinear least-squares fitting in CCPN Analysis 3.3.2.1.

The strong affinities observed in Lobe 1 (~13 µM) are consistent with P66 partially anchoring near the allosteric platform, in line with its design, and comparable in magnitude to CFT's reported non-covalent binding within the same domain (~20 µM)[6]. In the model proposed by Jiao et al.[97], stabilisation of Lobe 1 following CFT binding reduces competing motions in the allosteric scaffold and biases the interdomain hinge to permit the α2-α3/β3-β4 gatekeeper loop movement required for TP domain opening. Moderate affinity contacts on the TP face (I512-I614; ~70 µM) likely play a stabilising rather than driving role—

supporting the partially opened conformation while preserving loop breathing for substrate or antibiotic accommodation. This Lobe 1-TP domain coupling may provide one structural rationale for the observed MIC phenotype, in which P66 shifts the conformational equilibrium toward states permissive of oxacillin acylation without β-lactam mimicry.

However, the pattern of affected residues extends beyond the original design footprint. Numerous signals (I173, I192, and I197) appear within the distal allosteric region of Lobe 1, suggesting that P66 may not bind exclusively at one site. Instead, it may engage several low-affinity patches spanning the Lobe 1-TP interface or sample both regions flexibly within a broad binding envelope. Such partial promiscuity could preserve conformational communication between the allosteric and catalytic domains, supporting functional activation even if binding occurs outside a single canonical pocket; similar to CFT. This behaviour may explain the extensive perturbations observed experimentally and P66's ability to preserve TP-site accessibility. Whether these distributed interactions represent a mechanistically meaningful dual-site mode or stem from reduced site fidelity during design remains unresolved; this could be clarified by a second-generation redesign to improve geometric complementarity, followed by MIC evaluation of refined variants.

The interaction pattern in the NTE provides further insight into how P66 engagement influences PBP2a structure. Although residues in this region (I85, I309, and I314) show tight apparent affinities (~19 μM), comparable to those in Lobe 1, however these values may not reflect direct contact. To further test whether P66 could bind directly to the NTE, docking of each of its helices was performed in HADDOCK using only the experimentally affected residues (I85, I309, I314) as ambiguous interaction restraints. None of the resulting top-ranked clusters yielded geometrically or energetically plausible complexes. The best-scoring cluster exhibited an average HADDOCK score of approximately -55 ± 12 with interface RMSDs > 4 Å, indicating low structural convergence. Per-term energy decomposition further supported the absence of a meaningful interface: van der Waals (≈ -35 ± 10) and electrostatic energies (≈ -60 ± 25) were weak, the desolvation term was positive (+15 ± 8), and the buried surface area did not exceed 600 $Å^3$, consistent with transient or non-specific surface contact rather than stable complex formation. Instead, these affinities could arise from conformational coupling between the NTE and Lobe 1 through the interdomain hinge (residues 234-314). In molecular-dynamics studies[7,89], this hinge exhibits high RMSF in the apo state, reflecting its role as a dynamic coupler that accommodates breathing between the

NTE and the rest of the allosteric module. Effector or ligand engagement at Lobe 1 reduces this hinge mobility – effectively narrowing the interdomain angle and stabilising the orientation of the NTE relative to the allosteric core[6,89,97]. When P66 binds to Lobe 1, motion within this adjoining hinge may be restricted, altering the orientation of the flexibly linked NTE and changing its local magnetic environment. This indirect structural rearrangement produces measurable chemical-shift changes and apparently low K_d values, even in the absence of direct interaction. Nevertheless, an alternative explanation cannot be excluded. The spatial distribution of affected probes across both Lobe 1 and the NTE leaves open the possibility that P66 may span both regions as part of an extended binding interface. In this scenario, P66 would bridge the hinge between domains – binding with lower specificity but maintaining functional communication across the allosteric network. Although such behaviour differs from the intended single-site design, it could still achieve the desired outcome: partial activation of the allosteric system, facilitating oxacillin access to the TP domain. Current data do not discriminate between these possibilities – (i) indirect hinge-mediated coupling versus (ii) distributed, extended binding – but both remain plausible. The first aligns with molecular-dynamics simulations showing the NTE hinge exhibits high root-mean-square fluctuation (RMSF) in the apo state, acting as a dynamic coupler that transmits breathing motions between domains. The second is supported by the physical proximity of affected residues and by CSP-based binding footprints consistent with an elongated interaction surface. Docking using HADDOCK with these experimentally derived constraints could resolve whether P66 feasibly spans both regions, while subsequent redesigns could refine its specificity to test whether such an extended binding mode is mechanistically relevant or merely a by-product of partial specificity loss during initial design.

These data, therefore, show that *de novo* designed mini-proteins can be a viable antibiotic adjuvant to increase the susceptibility of MRSA to β-lactam antibiotics to which it is resistant. This could allow for the development of novel therapeutics that can rejuvenate the usefulness of these β-lactam antibiotics.

4.5.3.1 *Comparison of cryoEM reconstruction with NMR data supports the model in which apo PBP2a can access the open state.*

Consistent with the NMR data presented in this work, cryo-electron microscopy (cryo-EM) reconstructions of the apo PBP2a, produced by Dr B. Schiffrin, revealed density features that more closely resemble the PBP2a open confirmation (Figure 86):

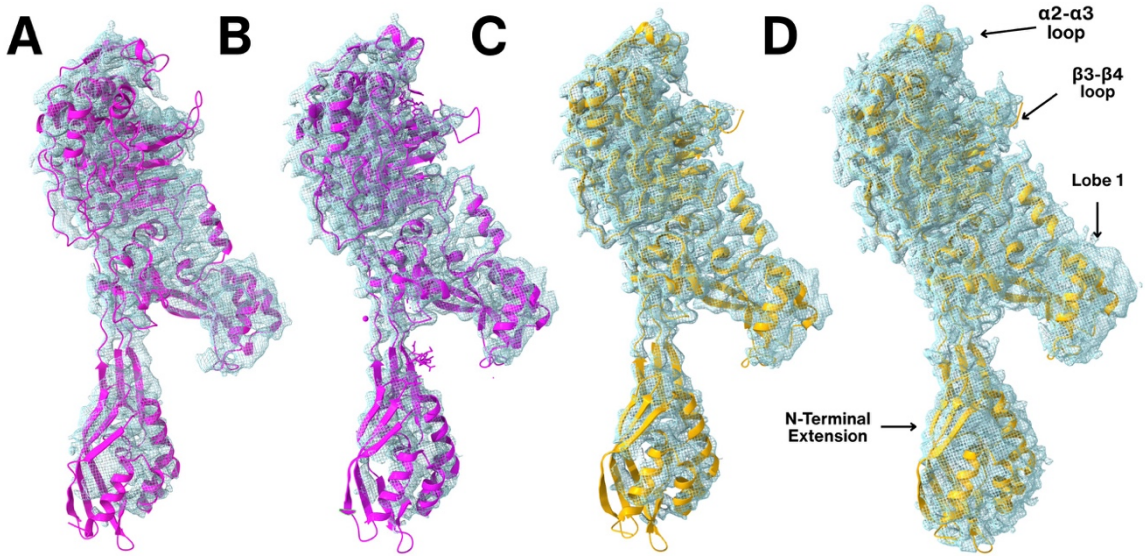

Figure 86: Cryo-EM reconstruction (0.74 Å) of apo PBP2a reveals a conformation consistent with ligand-induced activation states

Experimental cryo-EM maps of PBP2a overlaid with reference PBP2a structures (A) apo PBP2a (1VQQ[4]), (B) CFT-bound (3ZG0[5]), and (C/D) CFB-bound (4DKI[12]). DThe α2-α3 and β3-β4 gatekeeper loop densities align more closely with the ligand-bound (CFT/CFB) conformations than with the closed apo state. This configuration indicates that PBP2a shows partial ordering of the TP-domain entrance, compatible with greater β-lactam accessibility to the catalytic pocket than seen in the crystal structure. This is consistent with dynamics identified in the apo protein which suggest a conformational exchange in this area in solution. In contrast, the reduced electron density within the N-terminal extension (NTE) across panels A-C relative to the remainder of the structure suggests increased mobility and conformational heterogeneity in this region, consistent with its flexible coupling to the allosteric domain.

When the experimental map was overlaid with reference structures (A: 1VQQ[4], B: 3ZG0[5], C/D: 4DKI[12]), the α2-α3 and β3-β4 gatekeeper loop electron density more closely aligns with the CFT-/CFB-bound conformations rather than the closed apo configuration. This conformational alignment further supports the other findings of this study and the recent work by Jiao and colleagues[97] which evidence that apo state PBP2a has the conformational flexibility to breathe in and out of more open conformations. Such plasticity is consistent with existing data in this and previous work[12] wherein CFB is able to access the catalytic core without engagement of the AD. Additionally, in the models at lower contours (Figure 86A-C), less electron density is noted around the NTE relative to the rest of the structure, adding further support to the inherent dynamics in the apo state in this region. This is supported by increased RMSF values noted in previous studies[89,97]. Collectively, these

features align with the data presented in this study wherein the broad distribution of μs-ms timescale dynamics in the absence of allosteric effector binding retains sufficient structural flexibility to sample between multiple a range of conformations in both the AD and TP domain.

Chapter 5 Summary and Concluding Remarks

Antibiotic resistance remains one of the most pressing threats to global health, and methicillin-resistant *Staphylococcus aureus* (MRSA) continues to represent one of its most formidable challenges[1,4]. The resilience of MRSA lies largely in its expression of penicillin binding protein 2a (PBP2a), a unique enzyme that sustains bacterial cell-wall synthesis even in the presence of β-lactam antibiotics[4]. PBP2a achieves this through an atypical molecular architecture and dynamic regulation that collectively render it refractory to inhibition by most β-lactams[4-7]. Understanding how this protein resists antibiotic inactivation – and conversely, how it can be selectively targeted or re-sensitised – remains a central goal in the development of new antimicrobial strategies.

This work set out to explore the molecular mechanisms that underpin PBP2a's resistance and its inhibition by modern anti-MRSA cephalosporins. The study also aimed to evaluate whether these same properties could be exploited through the rational design of novel synthetic protein inhibitors to restore β-lactam susceptibility. Addressing these questions required the use of high-resolution biophysical approaches capable of probing molecular motion and ligand binding with residue-level precision – an inherently challenging task for a large, multidomain protein such as PBP2a.

To make such investigations feasible, a targeted nuclear magnetic resonance (NMR) strategy was developed. Given PBP2a's high molecular weight (~76 kDa), anisotropic shape, and intrinsic flexibility, conventional amide-based backbone assignment was not tractable under standard solution-state conditions. Multiple triple-resonance and TROSY-based experiments were performed but relaxation losses and sample instability ultimately constrained progress. To overcome this, a selective methyl-labelling approach was utilised, focusing on the ^{1}H-^{13}C δ1 methyl groups of isoleucine residues dispersed across the protein, with assignment by mutation. This provided a practical and informative partial assignment that effectively converted the methyl groups into conformational probes, allowing local and long-range structural responses to be monitored during ligand binding.

The resulting methyl-specific NMR platform enabled a solution state residue-level interrogation of PBP2a's behaviour in both its apo form and in complex with ligands of clinical and experimental relevance. Contrary to the mechanisms of structurally-related

cephalosporin ceftaroline (CFT) – which binds sequentially to both the AD and TP domain[5-7] – CSP analysis showed that ceftobiprole (CFB) interacts directly and exclusively with the TP domain, in line with previous research[12]. Methyl titration experiments demonstrated sub-micromolar affinity ($K_d \approx 0.33$ μM) with a binding footprint localised to the TP domain, with no detectable perturbations in residues associated with the canonical allosteric site.

CPMG relaxation dispersion experiments were subsequently used to qualitatively investigate how binding events alter the protein's conformational landscape. In its unbound (apo) state, PBP2a exhibited extensive μs–ms conformational exchange across both the allosteric (AD) and transpeptidase (TP) domains, consistent with a dynamic equilibrium between open and closed conformations. The presence of motion at the N-terminal extension (NTE) and within Lobe 1 of the allosteric domain indicated that these regions act as a flexible hinge system, likely modulating communication with the catalytic TP domain. Corresponding dynamics in residues flanking the α2-α3 and β3-β4 "gatekeeper" loops of the TP domain suggest local breathing motions that transiently expose the catalytic pocket containing Ser403. This picture aligns closely with previous molecular dynamics simulations[89,97], which depict the apo enzyme as a conformationally plastic system in which long-range allosteric coupling and loop mobility enable substrate access and product release. Collectively, these data provide experimental evidence for a dynamic, allosteric-ready architecture – one that balances stability with the mobility required for efficient peptidoglycan cross-linking, yet selectivity for β-lactam extrusion. Upon binding the fifth-generation cephalosporin CFB, the conformational network of PBP2a was reorganised.

Relaxation dispersion data revealed that CFB binding selectively dampened global dynamics while retaining or enhancing motions within the α2-α3 and β3-β4 gatekeeper loops. The overall number of residues exhibiting conformational exchange decreased, but a subset within the TP domain – particularly I407, I524, and I563 – displayed increased flexibility, consistent with residual breathing required to accommodate the bulky, covalently attached β-lactam. In contrast, residues behind the catalytic pocket (I412, I453, I512) lost exchange, reflecting local stabilisation of the acyl-enzyme complex. The persistence of motion in the AD and NTE, coupled with stabilisation of the TP domain, defines a hybrid dynamic state upon CFB binding – globally constrained yet locally adaptive. These observations support a model in which CFB acts as a direct, non-allosteric inhibitor, exploiting the intrinsic flexibility of the TP domain to achieve binding and covalent acylation without the allosteric

activation required by CFT. This mechanistic distinction aligns with structural and microbiological evidence: CFB-resistant MRSA mutants almost exclusively harbour substitutions within the TP domain (e.g. E447K, Y446L, S649A)[16,18-20,105,202], whereas CFT resistance involves mutations in both the AD and TP domains[13-18], often disrupting interdomain communication or cooperative interactions with other PBPs. The present data therefore reinforce the concept that CFB inhibition bypasses the need for AD engagement, operating instead through direct stabilisation and local restructuring of the catalytic site.

Building on these insights, a series of synthetic mini-protein binders were designed using *in silico* deep-learning tools (RFdiffusion, ProteinMPNN, and AlphaFold 2)[21-23] to target distinct surfaces of PBP2a. Among these, the binder designated P66 demonstrated clear experimental binding in solution, producing well-defined CSPs across both the AD and TP domains in line with computational design predictions. Notably, P66 exhibited its highest apparent affinities in Lobe 1 of the AD and at the adjacent TP domain face – suggesting that it stabilises an interdomain configuration conducive to active-site accessibility, similar to the conformational change normally induced by allosteric activation. In bacterial assays, P66 restored susceptibility of MRSA strain USA300 to oxacillin at concentrations of 8 μg/mL – an antibiotic otherwise ineffective against MRSA. This represents the first experimental demonstration of a *de novo* designed protein capable of modulating PBP2a activity in living bacteria and demonstrates that *de novo* designed mini-proteins are a viable route towards resensitising MRSA to β-lactam antibiotics.

In addition to these findings, several immediate experimental priorities emerge that would deepen the mechanistic understanding developed in Chapters 3 and 4, more precisely define the mechanistic basis of the P66 binding footprint and strengthen the translational potential of both the inhibitor and adjuvant strategies. Hydrogen-deuterium exchange mass spectrometry (HDX-MS) measures the rate at which backbone amide hydrogens exchange with deuterium from solvent, thereby reporting on regional solvent accessibility and conformational dynamics[205]. HDX-MS has several attractive properties that make it an ideal complement to the NMR techniques used in this study. It requires only picomoles of native protein, provides complete sequence coverage without the need for isotopic labelling – which is both expensive and can impose expression and folding stress – and does so at peptide-level resolution over far shorter timescales than multidimensional NMR[205-207]. Although HDX-MS cannot provide single-residue resolution or directly probe μs-ms

conformational exchange in the way that CPMG relaxation dispersion can, it would offer a rapid and comprehensive means of screening the broader PBP2a interactome in the presence of different ligands. In this context, HDX-MS could help determine whether the CSPs observed following P66 titration arise from direct off-target binding or instead reflect indirect hinge-mediated propagation. It could also confirm across the complete sequence that CFB perturbs only TP-domain regions, with no detectable AD protection changes, including in assignment blind spots such as the interdomain hinge where I154 mutagenesis failed due to structural sensitivity and ILVA coverage remains limited. Beyond this, HDX-MS may also be useful for pre-screening existing and future mini-protein binder candidates and for probing regions of PBP2a that remain experimentally inaccessible by NMR. Given that backbone amide-based assignment proved intractable for this system, and that several structurally informative regions remain unassigned even following selective mutagenesis, HDX-MS offers an orthogonal route to interrogate candidate sites such as I154 and the surrounding hinge region, as well as nearby hydrophobic residues including L147, L155, V160, L162 and A163 should they too prove intractable to mutagenesis in future experiments. To this end, the interdomain hinge is of particular interest, as both this study and previous work suggest that it may play a functionally important role in mediating long-range conformational communication within PBP2a[97]. It may also prove informative for other regions of mechanistic interest, such as the α2/α3 and β3/β4 loops, which may contribute to the CFB interaction landscape. Taken together, an effective future strategy would be to use HDX-MS for rapid global ligand footprinting, followed by targeted NMR experiments for residue-specific dynamics, thereby combining the breadth of HDX-MS with the mechanistic resolution of solution-state NMR.

However, because HDX-MS cannot directly report on µs-ms exchange, a second magnetic field remains essential for extending the dynamic analysis presented here. While the current single-field CPMG data provided a qualitative description of ligand-induced exchange behaviour, acquisition at a second field strength would permit quantitative fitting of exchange parameters including k_{ex}, the minor-state population, and the chemical shift difference between exchanging states[208]. These parameters are degenerate at a single field because Δω scales with field strength whereas k_{ex} and population do not, such that a second field breaks this degeneracy[117,208]. Mapping these values onto the PBP2a structure would distinguish fast and slow exchange regimes across the AD and TP domains and determine whether the TP-domain reorganisation observed upon CFB binding reflects altered exchange

kinetics, population redistribution, or both. Repeated acquisitions at 750 MHz were unsuccessful due to insufficient sample sensitivity, and at the time of writing, local higher – >950 MHz – instruments (e.g. the Bruker 1.2 GHz instrument at the University of Birmingham) were not operational. Access to either of these additional fields in future would therefore add significant mechanistic granularity beyond the qualitative picture presently available.

A second major priority is further detailing the P66 binding footprint. Although P66 restored oxacillin susceptibility, perturbations at NTE-proximal probes including I85, I309 and I314 remain difficult to interpret, as they may reflect either direct off-target binding – perhaps due to excluding the NTE from the RFdiffusion input or limited sequences – or indirect conformational propagation through the interdomain hinge. Distinguishing between these possibilities would more clearly define P66's mechanism of action and better guide second-generation design. Paramagnetic relaxation enhancement (PRE) offers a direct and distance-dependent means of distinguishing between these scenarios. Introduction of a paramagnetic spin label such as MTSL via an engineered cysteine on P66 would allow comparison of spectra in the paramagnetic and diamagnetic states, such that residues within approximately 15-25 Å of the label would be expected to show substantial broadening or disappearance[209]. If the observed CSPs arise from direct P66-NTE contact, these probes should display strong PRE effects; if instead they reflect indirect hinge-mediated coupling, little or no PRE-induced broadening would be expected[209,210]. As PRE is inherently sensitive to transient proximity, it would provide a stronger spatial constraint on the P66-NTE interaction than CSPs alone and would be particularly well suited to this question. This ambiguity could then be addressed more directly at the design stage through second-generation binder optimisation. Because the NTE was excluded from the original RFdiffusion input to reduce system size, it was never penalised for off-target complementarity. Repeating the same design pipeline with explicit negative design constraints against NTE engagement during ProteinMPNN sequence optimisation, followed by AlphaFold 2 filtering for designs that retain high interface confidence at the intended Lobe 1-TP domain interface while avoiding NTE contacts, would improve binding specificity and facilitate cleaner interpretation of subsequent binding footprints. In parallel, the original conservative design strategy of one sequence per backbone with one FastRelax cycle could be expanded to 4-5 cycles and to generate 8-16 sequences per backbone, improving the retrieval of well-folded candidates

with stronger specificity and potentially enhancing MIC restoration through more targeted conformational modulation[21,204].

Finally, the same *de novo* design framework could be repurposed to address one of the major technical limitations encountered throughout this study: PBP2a sample instability at NMR-relevant concentrations. SAP analysis identified discrete hydrophobic patches around the active-site cleft, Ω-loop edge and C-terminal helical face that likely drove the intermolecular self-association that limited sample longevity. Cryo-EM experiments independently supported this interpretation by revealing dimeric and trimeric subclasses (data not shown) consistent with self-association of folded molecules rather than non-specific aggregation of denatured species. Rational design of small mini-protein binders targeting these computed hotspots could therefore quench exposed hydrophobic surfaces without occluding the allosteric or TP-domain interfaces relevant to ligand-binding studies. By suppressing the concentration-dependent self-association that represented the principal barrier to multi-day acquisitions, such binders could improve PBP2a monodispersity at the concentrations required for NMR, thereby aiding follow-up CPMG datasets at a second field and improving/rescuing spectral quality even under existing conditions. In this sense, *de novo* designed binders could serve not only as functional modulators of PBP2a, but also as experimental chaperones for extending the tractable size and stability range of challenging protein targets in solution-state NMR. These future directions would sharpen and extend the present work by more precisely defining how CFB reorganises the TP domain and further detailing the mechanistic underpinnings of P66-mediated restoration of β-lactam susceptibility.

Collectively, the work presented in this thesis connects PBP2a's conformational dynamics, antibiotic inhibition, and potential for rational re-sensitisation. The establishment of a partial, methyl-based assignment overcame the technical barriers that have could limit solution-state NMR investigations of this enzyme and allowed for further solution NMR based studies into the function and dynamics of PBP2a. Through integration of residue-specific dynamics, and binding interactions this study demonstrates that PBP2a's resistance mechanism is not solely defined by steric exclusion of β-lactams, but by a finely tuned dynamic equilibrium between flexible and stabilised states that govern access to its catalytic core.

By elucidating how CFB inhibits PBP2a through a direct, non-allosteric route – and contrasting this with CFT's allosterically dependent mechanism – these findings reconcile structural, dynamic, and clinical observations of resistance. Furthermore, the successful design and validation of P66 adds another frontier in antimicrobial strategy: targeting allosteric regulation with *de novo* designed mini-protein scaffolds in order to restore susceptibility to previously effective agents. In doing so, this work demonstrates that the resistance conferred by PBP2a can be functionally reversed, even without traditional small-molecule antibiotics, through designed molecular scaffolds that rewire its dynamic network.

This research therefore further details the mechanism of CFB inhibition of PBP2a and provides additional details contributing towards the development of the next generation of rational antibiotic adjuvants – agents capable of re-sensitising MRSA to long-established β-lactams. In the face of mounting antibiotic resistance, such approaches are a welcome step towards extending the lifespan of existing antimicrobial therapies and overcoming "one of the most urgent global health threats we face today", as defined by the WHO[211].

Reference list / Bibliography

1 O'Neill, J. Tackling drug-resistant infections globally: final report and recommendations. (2016).

2 Bai, A. D. *et al.* Staphylococcus aureus bacteraemia mortality: a systematic review and meta-analysis. *Clin Microbiol Infect* **28**, 1076-1084 (2022). https://doi.org/10.1016/j.cmi.2022.03.015

3 Naghavi, M. *et al.* Global burden of bacterial antimicrobial resistance 1990–2021: a systematic analysis with forecasts to 2050. *The Lancet* **404**, 1199-1226 (2024). https://doi.org/10.1016/S0140-6736(24)01867-1

4 Lim, D. & Strynadka, N. C. Structural basis for the beta lactam resistance of PBP2a from methicillin-resistant Staphylococcus aureus. *Nat Struct Biol* **9**, 870-876 (2002). https://doi.org/10.1038/nsb858

5 Otero, L. H. *et al.* How allosteric control of Staphylococcus aureus penicillin binding protein 2a enables methicillin resistance and physiological function. *Proceedings of the National Academy of Sciences* **110**, 16808-16813 (2013). https://doi.org/doi:10.1073/pnas.1300118110

6 Fishovitz, J. *et al.* Disruption of allosteric response as an unprecedented mechanism of resistance to antibiotics. *J Am Chem Soc* **136**, 9814-9817 (2014). https://doi.org/10.1021/ja5030657

7 Acebrón, I., Chang, M., Mobashery, S. & Hermoso, J. A. The Allosteric Site for the Nascent Cell Wall in Penicillin-Binding Protein 2a: An Achilles' Heel of Methicillin-Resistant Staphylococcus aureus. *Curr Med Chem* **22**, 1678-1686 (2015). https://doi.org/10.2174/0929867322666150311150215

8 Villegas-Estrada, A., Lee, M., Hesek, D., Vakulenko, S. B. & Mobashery, S. Co-opting the cell wall in fighting methicillin-resistant Staphylococcus aureus: potent inhibition of PBP 2a by two anti-MRSA beta-lactam antibiotics. *J Am Chem Soc* **130**, 9212-9213 (2008). https://doi.org/10.1021/ja8029448

9 Laudano, J. B. Ceftaroline fosamil: a new broad-spectrum cephalosporin. *J Antimicrob Chemother* **66 Suppl 3**, iii11-18 (2011). https://doi.org/10.1093/jac/dkr095

10 Duplessis, C. & Crum-Cianflone, N. F. Ceftaroline: A New Cephalosporin with Activity against Methicillin-Resistant Staphylococcus aureus (MRSA). *Clin Med Rev Ther* **3** (2011). https://doi.org/10.4137/cmrt.S1637

11 Bogdanovich, T., Ednie, L. M., Shapiro, S. & Appelbaum, P. C. Antistaphylococcal activity of ceftobiprole, a new broad-spectrum cephalosporin. *Antimicrobial agents and chemotherapy* **49**, 4210-4219 (2005).

12 Lovering, A. L. *et al.* Structural insights into the anti-methicillin-resistant Staphylococcus aureus (MRSA) activity of ceftobiprole. *J Biol Chem* **287**, 32096-32102 (2012). https://doi.org/10.1074/jbc.M112.355644

13 Mendes, R. E. *et al.* Characterization of methicillin-resistant Staphylococcus aureus displaying increased MICs of ceftaroline. *J Antimicrob Chemother* **67**, 1321-1324 (2012). https://doi.org/10.1093/jac/dks069

14 Long, S. W. *et al.* PBP2a mutations causing high-level Ceftaroline resistance in clinical methicillin-resistant Staphylococcus aureus isolates. *Antimicrob Agents Chemother* **58**, 6668-6674 (2014). https://doi.org/10.1128/aac.03622-14

15 Alm, R. A. *et al.* Analysis of Staphylococcus aureus clinical isolates with reduced susceptibility to ceftaroline: an epidemiological and structural perspective. *Journal of Antimicrobial Chemotherapy* **69**, 2065-2075 (2014). https://doi.org/10.1093/jac/dku114

16 Chan, L. C. *et al.* Ceftobiprole- and ceftaroline-resistant methicillin-resistant Staphylococcus aureus. *Antimicrob Agents Chemother* **59**, 2960-2963 (2015). https://doi.org/10.1128/aac.05004-14

17 Kelley, W. L., Jousselin, A., Barras, C., Lelong, E. & Renzoni, A. Missense Mutations in PBP2A Affecting Ceftaroline Susceptibility Detected in Epidemic Hospital-Acquired Methicillin-Resistant Staphylococcus aureus Clonotypes ST228 and ST247 in Western Switzerland Archived since 1998. *Antimicrobial Agents and Chemotherapy* **59**, 1922-1930 (2015). https://doi.org/doi:10.1128/aac.04068-14

18 Schaumburg, F., Peters, G., Alabi, A., Becker, K. & Idelevich, E. A. Missense mutations of PBP2a are associated with reduced susceptibility to ceftaroline and ceftobiprole in African MRSA. *J Antimicrob Chemother* **71**, 41-44 (2016). https://doi.org/10.1093/jac/dkv325

19 Banerjee, R., Gretes, M., Basuino, L., Strynadka, N. & Chambers, H. F. In vitro selection and characterization of ceftobiprole-resistant methicillin-resistant Staphylococcus aureus. *Antimicrob Agents Chemother* **52**, 2089-2096 (2008). https://doi.org/10.1128/aac.01403-07

20 Morroni, G. *et al.* High Rate of Ceftobiprole Resistance among Clinical Methicillin-Resistant Staphylococcus aureus Isolates from a Hospital in Central Italy. *Antimicrobial Agents and Chemotherapy* **62**, 10.1128/aac.01663-01618 (2018). https://doi.org/10.1128/aac.01663-18

21 Jumper, J. *et al.* Highly accurate protein structure prediction with AlphaFold. *Nature* **596**, 583-589 (2021). https://doi.org/10.1038/s41586-021-03819-2

22 Dauparas, J. *et al.* Robust deep learning–based protein sequence design using ProteinMPNN. *Science* **378**, 49-56 (2022). https://doi.org/doi:10.1126/science.add2187

23 Bennett, N. R. *et al.* Improving de novo protein binder design with deep learning. *Nature Communications* **14**, 2625 (2023). https://doi.org/10.1038/s41467-023-38328-5

24 Poudel, A. N. *et al.* The economic burden of antibiotic resistance: A systematic review and meta-analysis. *PLoS One* **18**, e0285170 (2023). https://doi.org/10.1371/journal.pone.0285170

25 Graham, M. E., Wilson, B. A., Ramkumar, D., Rosencranz, H. & Ramkumar, J. Unseen Drivers of Antimicrobial Resistance: The Role of Industrial Agriculture and Climate Change in This Global Health Crisis. *Challenges* **16**, 22 (2025).

26 Durso, L. M., Shamimuzzaman, M., Dillard, B. & Nickerson, K. W. Novel antibiotic resistance profiles in bacteria isolated from oil fly larvae Helaeomyia petrolei living in the La Brea Tar Pits. *Antonie Van Leeuwenhoek* **118**, 42 (2024). https://doi.org/10.1007/s10482-024-02050-z

27 Stanley, D., Batacan, R., Jr. & Bajagai, Y. S. Rapid growth of antimicrobial resistance: the role of agriculture in the problem and the solutions. *Appl Microbiol Biotechnol* **106**, 6953-6962 (2022). https://doi.org/10.1007/s00253-022-12193-6

28 Blair, J. M., Webber, M. A., Baylay, A. J., Ogbolu, D. O. & Piddock, L. J. Molecular mechanisms of antibiotic resistance. *Nat Rev Microbiol* **13**, 42-51 (2015). https://doi.org/10.1038/nrmicro3380

29 Seung, K. J., Keshavjee, S. & Rich, M. L. Multidrug-Resistant Tuberculosis and Extensively Drug-Resistant Tuberculosis. *Cold Spring Harb Perspect Med* **5**, a017863 (2015). https://doi.org/10.1101/cshperspect.a017863

30 Almeida Da Silva, P. E. & Palomino, J. C. Molecular basis and mechanisms of drug resistance in Mycobacterium tuberculosis: classical and new drugs. *J Antimicrob Chemother* **66**, 1417-1430 (2011). https://doi.org/10.1093/jac/dkr173

31 Bush, K. & Bradford, P. A. β-Lactams and β-Lactamase Inhibitors: An Overview. *Cold Spring Harb Perspect Med* **6** (2016). https://doi.org/10.1101/cshperspect.a025247
32 Castanheira, M., Simner, P. J. & Bradford, P. A. Extended-spectrum β-lactamases: an update on their characteristics, epidemiology and detection. *JAC Antimicrob Resist* **3**, dlab092 (2021). https://doi.org/10.1093/jacamr/dlab092
33 Bonomo, R. A. *et al.* Carbapenemase-Producing Organisms: A Global Scourge. *Clin Infect Dis* **66**, 1290-1297 (2018). https://doi.org/10.1093/cid/cix893
34 Munita, J. M. & Arias, C. A. Mechanisms of Antibiotic Resistance. *Microbiol Spectr* **4** (2016). https://doi.org/10.1128/microbiolspec.VMBF-0016-2015
35 Ramirez, M. S. & Tolmasky, M. E. Aminoglycoside modifying enzymes. *Drug Resist Updat* **13**, 151-171 (2010). https://doi.org/10.1016/j.drup.2010.08.003
36 Nishino, K., Yamasaki, S., Nakashima, R., Zwama, M. & Hayashi-Nishino, M. Function and Inhibitory Mechanisms of Multidrug Efflux Pumps. *Frontiers in Microbiology* **Volume 12 - 2021** (2021). https://doi.org/10.3389/fmicb.2021.737288
37 Li, X. Z. & Nikaido, H. Efflux-mediated drug resistance in bacteria: an update. *Drugs* **69**, 1555-1623 (2009). https://doi.org/10.2165/11317030-000000000-00000
38 Li, X. Z., Plésiat, P. & Nikaido, H. The challenge of efflux-mediated antibiotic resistance in Gram-negative bacteria. *Clin Microbiol Rev* **28**, 337-418 (2015). https://doi.org/10.1128/cmr.00117-14
39 Hooper, D. C. & Jacoby, G. A. Topoisomerase Inhibitors: Fluoroquinolone Mechanisms of Action and Resistance. *Cold Spring Harb Perspect Med* **6** (2016). https://doi.org/10.1101/cshperspect.a025320
40 Ju, M. *et al.* Predictors of mortality in adult patients with methicillin-resistant Staphylococcus aureus bloodstream infection: a meta-analysis and systematic review. *Ann Palliat Med* **10**, 8617-8627 (2021). https://doi.org/10.21037/apm-21-932
41 Rohde, M. The Gram-Positive Bacterial Cell Wall. *Microbiol Spectr* **7** (2019). https://doi.org/10.1128/microbiolspec.GPP3-0044-2018
42 Silhavy, T. J., Kahne, D. & Walker, S. The bacterial cell envelope. *Cold Spring Harb Perspect Biol* **2**, a000414 (2010). https://doi.org/10.1101/cshperspect.a000414
43 Lovering, A. L., Safadi, S. S. & Strynadka, N. C. Structural perspective of peptidoglycan biosynthesis and assembly. *Annu Rev Biochem* **81**, 451-478 (2012). https://doi.org/10.1146/annurev-biochem-061809-112742
44 Wang, M., Buist, G. & van Dijl, J. M. Staphylococcus aureus cell wall maintenance - the multifaceted roles of peptidoglycan hydrolases in bacterial growth, fitness, and virulence. *FEMS Microbiol Rev* **46** (2022). https://doi.org/10.1093/femsre/fuac025
45 Vollmer, W., Blanot, D. & De Pedro, M. A. Peptidoglycan structure and architecture. *FEMS Microbiology Reviews* **32**, 149-167 (2008). https://doi.org/https://doi.org/10.1111/j.1574-6976.2007.00094.x
46 Wheeler, R. *et al.* Bacterial Cell Enlargement Requires Control of Cell Wall Stiffness Mediated by Peptidoglycan Hydrolases. *mBio* **6**, e00660 (2015). https://doi.org/10.1128/mBio.00660-15
47 Chan, Y. G., Frankel, M. B., Missiakas, D. & Schneewind, O. SagB Glucosaminidase Is a Determinant of Staphylococcus aureus Glycan Chain Length, Antibiotic Susceptibility, and Protein Secretion. *J Bacteriol* **198**, 1123-1136 (2016). https://doi.org/10.1128/jb.00983-15

48 Schaefer, K. *et al.* Structure and reconstitution of a hydrolase complex that may release peptidoglycan from the membrane after polymerization. *Nat Microbiol* **6**, 34-43 (2021). https://doi.org/10.1038/s41564-020-00808-5

49 Costa, K. *et al.* The morphological transition of Helicobacter pylori cells from spiral to coccoid is preceded by a substantial modification of the cell wall. *J Bacteriol* **181**, 3710-3715 (1999). https://doi.org/10.1128/jb.181.12.3710-3715.1999

50 Chaput, C., Labigne, A. & Boneca, I. G. Characterization of Helicobacter pylori lytic transglycosylases Slt and MltD. *J Bacteriol* **189**, 422-429 (2007). https://doi.org/10.1128/jb.01270-06

51 Ghuysen, J. M., Frère, J. M., Leyh-Bouille, M., Nguyen-Distèche, M. & Coyette, J. Active-site-serine D-alanyl-D-alanine-cleaving-peptidase-catalysed acyl-transfer reactions. Procedures for studying the penicillin-binding proteins of bacterial plasma membranes. *Biochem J* **235**, 159-165 (1986). https://doi.org/10.1042/bj2350159

52 Barreteau, H. *et al.* Cytoplasmic steps of peptidoglycan biosynthesis. *FEMS Microbiol Rev* **32**, 168-207 (2008). https://doi.org/10.1111/j.1574-6976.2008.00104.x

53 Bouhss, A., Trunkfield, A. E., Bugg, T. D. & Mengin-Lecreulx, D. The biosynthesis of peptidoglycan lipid-linked intermediates. *FEMS Microbiol Rev* **32**, 208-233 (2008). https://doi.org/10.1111/j.1574-6976.2007.00089.x

54 Sauvage, E., Kerff, F., Terrak, M., Ayala, J. A. & Charlier, P. The penicillin-binding proteins: structure and role in peptidoglycan biosynthesis. *FEMS Microbiol Rev* **32**, 234-258 (2008). https://doi.org/10.1111/j.1574-6976.2008.00105.x

55 Taguchi, A. *et al.* FtsW is a peptidoglycan polymerase that is functional only in complex with its cognate penicillin-binding protein. *Nat Microbiol* **4**, 587-594 (2019). https://doi.org/10.1038/s41564-018-0345-x

56 Lovering, A. L., de Castro, L. H., Lim, D. & Strynadka, N. C. Structural insight into the transglycosylation step of bacterial cell-wall biosynthesis. *Science* **315**, 1402-1405 (2007). https://doi.org/10.1126/science.1136611

57 Meroueh, S. O. *et al.* Three-dimensional structure of the bacterial cell wall peptidoglycan. *Proc Natl Acad Sci U S A* **103**, 4404-4409 (2006). https://doi.org/10.1073/pnas.0510182103

58 Kamiryo, T. & Matsuhashi, M. The Biosynthesis of the Cross-linking Peptides in the Cell Wall Peptidoglycan of Staphylococcus aureus. *Journal of Biological Chemistry* **247**, 6306-6311 (1972). https://doi.org/10.1016/S0021-9258(19)44798-4

59 Schneider, T. *et al.* In vitro assembly of a complete, pentaglycine interpeptide bridge containing cell wall precursor (lipid II-Gly5) of Staphylococcus aureus. *Mol Microbiol* **53**, 675-685 (2004). https://doi.org/10.1111/j.1365-2958.2004.04149.x

60 Münch, D. & Sahl, H.-G. Structural variations of the cell wall precursor lipid II in Gram-positive bacteria — Impact on binding and efficacy of antimicrobial peptides. *Biochimica et Biophysica Acta (BBA) - Biomembranes* **1848**, 3062-3071 (2015). https://doi.org/https://doi.org/10.1016/j.bbamem.2015.04.014

61 Nöldeke, E. R. *et al.* Structural basis of cell wall peptidoglycan amidation by the GatD/MurT complex of Staphylococcus aureus. *Scientific Reports* **8**, 12953 (2018). https://doi.org/10.1038/s41598-018-31098-x

62 Münch, D. *et al.* Identification and in vitro analysis of the GatD/MurT enzyme-complex catalyzing lipid II amidation in Staphylococcus aureus. *PLoS Pathog* **8**, e1002509 (2012). https://doi.org/10.1371/journal.ppat.1002509

63 Monteiro, J. M. *et al.* The pentaglycine bridges of Staphylococcus aureus peptidoglycan are essential for cell integrity. *Scientific Reports* **9**, 5010 (2019). https://doi.org/10.1038/s41598-019-41461-1
64 Jarick, M. *et al.* The serine/threonine kinase Stk and the phosphatase Stp regulate cell wall synthesis in Staphylococcus aureus. *Scientific Reports* **8**, 13693 (2018). https://doi.org/10.1038/s41598-018-32109-7
65 Tipper, D. J. & Strominger, J. L. Mechanism of action of penicillins: a proposal based on their structural similarity to acyl-D-alanyl-D-alanine. *Proc Natl Acad Sci U S A* **54**, 1133-1141 (1965). https://doi.org/10.1073/pnas.54.4.1133
66 Goffin, C. & Ghuysen, J.-M. Multimodular penicillin-binding proteins: an enigmatic family of orthologs and paralogs. *Microbiology and molecular biology reviews* **62**, 1079-1093 (1998).
67 Heaslet, H., Shaw, B., Mistry, A. & Miller, A. A. Characterization of the active site of S. aureus monofunctional glycosyltransferase (Mtg) by site-directed mutation and structural analysis of the protein complexed with moenomycin. *Journal of Structural Biology* **167**, 129-135 (2009). https://doi.org/https://doi.org/10.1016/j.jsb.2009.04.010
68 Sung, M.-T. *et al.* Crystal structure of the membrane-bound bifunctional transglycosylase PBP1b from Escherichia coli. *Proceedings of the National Academy of Sciences* **106**, 8824-8829 (2009). https://doi.org/doi:10.1073/pnas.0904030106
69 Yuan, Y. *et al.* Crystal structure of a peptidoglycan glycosyltransferase suggests a model for processive glycan chain synthesis. *Proceedings of the National Academy of Sciences* **104**, 5348-5353 (2007). https://doi.org/doi:10.1073/pnas.0701160104
70 Contreras-Martel, C. *et al.* Crystal Structure of Penicillin-binding Protein 1a (PBP1a) Reveals a Mutational Hotspot Implicated in β-Lactam Resistance in Streptococcus pneumoniae. *Journal of Molecular Biology* **355**, 684-696 (2006). https://doi.org/https://doi.org/10.1016/j.jmb.2005.10.030
71 Macheboeuf, P. *et al.* Active site restructuring regulates ligand recognition in class A penicillin-binding proteins. *Proceedings of the National Academy of Sciences* **102**, 577-582 (2005). https://doi.org/doi:10.1073/pnas.0407186102
72 Gordon, E., Mouz, N., Duée, E. & Dideberg, O. The crystal structure of the penicillin-binding protein 2x from Streptococcus pneumoniae and its acyl-enzyme form: implication in drug resistance11Edited by R. Huber. *Journal of Molecular Biology* **299**, 477-485 (2000). https://doi.org/https://doi.org/10.1006/jmbi.2000.3740
73 Goffin, C. & Ghuysen, J. M. Biochemistry and comparative genomics of SxxK superfamily acyltransferases offer a clue to the mycobacterial paradox: presence of penicillin-susceptible target proteins versus lack of efficiency of penicillin as therapeutic agent. *Microbiol Mol Biol Rev* **66**, 702-738, table of contents (2002). https://doi.org/10.1128/mmbr.66.4.702-738.2002
74 Ghosh, A. S., Chowdhury, C. & Nelson, D. E. Physiological functions of D-alanine carboxypeptidases in Escherichia coli. *Trends in microbiology* **16**, 309-317 (2008).
75 Pazos, M. & Vollmer, W. Regulation and function of class A Penicillin-binding proteins. *Current Opinion in Microbiology* **60**, 80-87 (2021). https://doi.org/https://doi.org/10.1016/j.mib.2021.01.008
76 Wilke, M. S., Lovering, A. L. & Strynadka, N. C. β-Lactam antibiotic resistance: a current structural perspective. *Current opinion in microbiology* **8**, 525-533 (2005).
77 Bouley, R. *et al.* Discovery of antibiotic (E)-3-(3-carboxyphenyl)-2-(4-cyanostyryl)quinazolin-4(3H)-one. *J Am Chem Soc* **137**, 1738-1741 (2015). https://doi.org/10.1021/jacs.5b00056

78 Sjuts, H. *et al.* Molecular basis for inhibition of AcrB multidrug efflux pump by novel and powerful pyranopyridine derivatives. *Proceedings of the National Academy of Sciences* **113**, 3509-3514 (2016). https://doi.org/doi:10.1073/pnas.1602472113
79 Pereira, S. F., Henriques, A. O., Pinho, M. G., de Lencastre, H. & Tomasz, A. Role of PBP1 in cell division of Staphylococcus aureus. *J Bacteriol* **189**, 3525-3531 (2007). https://doi.org/10.1128/jb.00044-07
80 Pinho, M. G., Filipe, S. R., de Lencastre, H. & Tomasz, A. Complementation of the essential peptidoglycan transpeptidase function of penicillin-binding protein 2 (PBP2) by the drug resistance protein PBP2A in Staphylococcus aureus. *J Bacteriol* **183**, 6525-6531 (2001). https://doi.org/10.1128/jb.183.22.6525-6531.2001
81 Monteiro, J. M. *et al.* Cell shape dynamics during the staphylococcal cell cycle. *Nat Commun* **6**, 8055 (2015). https://doi.org/10.1038/ncomms9055
82 Reichmann, N. T. *et al.* SEDS-bPBP pairs direct lateral and septal peptidoglycan synthesis in Staphylococcus aureus. *Nat Microbiol* **4**, 1368-1377 (2019). https://doi.org/10.1038/s41564-019-0437-2
83 Pinho, M. G., de Lencastre, H. & Tomasz, A. An acquired and a native penicillin-binding protein cooperate in building the cell wall of drug-resistant staphylococci. *Proc Natl Acad Sci U S A* **98**, 10886-10891 (2001). https://doi.org/10.1073/pnas.191260798
84 Sieradzki, K. & Tomasz, A. Gradual alterations in cell wall structure and metabolism in vancomycin-resistant mutants of Staphylococcus aureus. *J Bacteriol* **181**, 7566-7570 (1999). https://doi.org/10.1128/jb.181.24.7566-7570.1999
85 Severin, A. *et al.* High level oxacillin and vancomycin resistance and altered cell wall composition in Staphylococcus aureus carrying the staphylococcal mecA and the enterococcal vanA gene complex. *J Biol Chem* **279**, 3398-3407 (2004). https://doi.org/10.1074/jbc.M309593200
86 Tinajero-Trejo, M. *et al.* Control of morphogenesis during the Staphylococcus aureus cell cycle. *Science Advances* **11**, eadr5011 (2025). https://doi.org/doi:10.1126/sciadv.adr5011
87 Ito, T. *et al.* Staphylococcal Cassette Chromosome mec (SCCmec) analysis of MRSA. *Methods Mol Biol* **1085**, 131-148 (2014). https://doi.org/10.1007/978-1-62703-664-1_8
88 Lakhundi, S. & Zhang, K. Methicillin-Resistant Staphylococcus aureus: Molecular Characterization, Evolution, and Epidemiology. *Clin Microbiol Rev* **31** (2018). https://doi.org/10.1128/cmr.00020-18
89 Mahasenan, K. V. *et al.* Conformational Dynamics in Penicillin-Binding Protein 2a of Methicillin-Resistant Staphylococcus aureus, Allosteric Communication Network and Enablement of Catalysis. *J Am Chem Soc* **139**, 2102-2110 (2017). https://doi.org/10.1021/jacs.6b12565
90 Wu, C. Y. *et al.* Site-directed mutagenesis of the mecA gene from a methicillin-resistant strain of Staphylococcus aureus. *J Bacteriol* **176**, 443-449 (1994). https://doi.org/10.1128/jb.176.2.443-449.1994
91 Lu, W. P. *et al.* Penicillin-binding protein 2a from methicillin-resistant Staphylococcus aureus: kinetic characterization of its interactions with beta-lactams using electrospray mass spectrometry. *Biochemistry* **38**, 6537-6546 (1999). https://doi.org/10.1021/bi990025e
92 Fuda, C. *et al.* Activation for catalysis of penicillin-binding protein 2a from methicillin-resistant Staphylococcus aureus by bacterial cell wall. *J Am Chem Soc* **127**, 2056-2057 (2005). https://doi.org/10.1021/ja0434376

93 Mouz, N. *et al.* Identification of a structural determinant for resistance to beta-lactam antibiotics in Gram-positive bacteria. *Proc Natl Acad Sci U S A* **95**, 13403-13406 (1998). https://doi.org/10.1073/pnas.95.23.13403

94 Dessen, A., Mouz, N., Gordon, E., Hopkins, J. & Dideberg, O. Crystal Structure of PBP2x from a Highly Penicillin-resistant Streptococcus pneumoniae Clinical Isolate: A MOSAIC FRAMEWORK CONTAINING 83 MUTATIONS *. *Journal of Biological Chemistry* **276**, 45106-45112 (2001). https://doi.org/10.1074/jbc.M107608200

95 Changeux, J. P. Allostery and the Monod-Wyman-Changeux model after 50 years. *Annu Rev Biophys* **41**, 103-133 (2012). https://doi.org/10.1146/annurev-biophys-050511-102222

96 Bernardo-García, N. *et al.* Allostery, Recognition of Nascent Peptidoglycan, and Cross-linking of the Cell Wall by the Essential Penicillin-Binding Protein 2x of Streptococcus pneumoniae. *ACS Chemical Biology* **13**, 694-702 (2018). https://doi.org/10.1021/acschembio.7b00817

97 Jiao, F. *et al.* Unraveling the mechanism of ceftaroline-induced allosteric regulation in penicillin-binding protein 2a: insights for novel antibiotic development against methicillin-resistant Staphylococcus aureus. *Antimicrob Agents Chemother* **67**, e0089523 (2023). https://doi.org/10.1128/aac.00895-23

98 Hernandez, P. O., Lema, S., Tyring, S. K. & Mendoza, N. Ceftaroline in complicated skin and skin-structure infections. *Infect Drug Resist* **5**, 23-35 (2012). https://doi.org/10.2147/idr.S17432

99 Clarke, D. *et al.* Identifying Allosteric Hotspots with Dynamics: Application to Inter- and Intra-species Conservation. *Structure* **24**, 826-837 (2016). https://doi.org/10.1016/j.str.2016.03.008

100 Kumar, V. *et al.* Structural Insights into Ceftobiprole Inhibition of Pseudomonas aeruginosa Penicillin-Binding Protein 3. *Antimicrobial Agents and Chemotherapy* **64**, 10.1128/aac.00106-00120 (2020). https://doi.org/doi:10.1128/aac.00106-20

101 Sacco, M. D. *et al.* A unique class of Zn2+-binding serine-based PBPs underlies cephalosporin resistance and sporogenesis in Clostridioides difficile. *Nature Communications* **13**, 4370 (2022). https://doi.org/10.1038/s41467-022-32086-6

102 Alexander, J. A. N. *et al.* Structural and kinetic analyses of penicillin-binding protein 4 (PBP4)-mediated antibiotic resistance in Staphylococcus aureus. *Journal of Biological Chemistry* **293**, 19854-19865 (2018). https://doi.org/10.1074/jbc.RA118.004952

103 Sauvage, E. 6G88 – PBP2a complexed with ceftobiprole. *RCSB Protein Data Bank* (2018).

104 Alahmadi, T. *et al.* The Prevalence and Clinical Characteristics of Multidrug-resistant Hospital-acquired Staphylococcus aureus in Medina, Saudi Arabia. *Journal of Pure and Applied Microbiology* **17** (2023). https://doi.org/10.22207/JPAM.17.1.44

105 Antonelli, A. *et al.* Staphylococcus aureus from hospital-acquired pneumonia from an Italian nationwide survey: activity of ceftobiprole and other anti-staphylococcal agents, and molecular epidemiology of methicillin-resistant isolates. *Journal of Antimicrobial Chemotherapy* **74**, 3453-3461 (2019). https://doi.org/10.1093/jac/dkz371

106 Borbone, S., Campanile, F., Bongiorno, D. & Stefani, S. In vitro bactericidal activity of ceftobiprole against hospital- and community-associated methicillin-resistant Staphylococcus aureus. *Journal of Antimicrobial Chemotherapy* **65**, 591-594 (2010). https://doi.org/10.1093/jac/dkp483

107 Karplus, M. & Kuriyan, J. Molecular dynamics and protein function. *Proc Natl Acad Sci U S A* **102**, 6679-6685 (2005). https://doi.org/10.1073/pnas.0408930102
108 Sekhar, A. & Kay, L. E. NMR paves the way for atomic level descriptions of sparsely populated, transiently formed biomolecular conformers. *Proc Natl Acad Sci U S A* **110**, 12867-12874 (2013). https://doi.org/10.1073/pnas.1305688110
109 Wider, G. & Wüthrich, K. NMR spectroscopy of large molecules and multimolecular assemblies in solution. *Curr Opin Struct Biol* **9**, 594-601 (1999). https://doi.org/10.1016/s0959-440x(99)00011-1
110 Pervushin, K., Riek, R., Wider, G. & Wüthrich, K. Attenuated T2 relaxation by mutual cancellation of dipole-dipole coupling and chemical shift anisotropy indicates an avenue to NMR structures of very large biological macromolecules in solution. *Proc Natl Acad Sci U S A* **94**, 12366-12371 (1997). https://doi.org/10.1073/pnas.94.23.12366
111 Tugarinov, V., Hwang, P. M., Ollerenshaw, J. E. & Kay, L. E. Cross-correlated relaxation enhanced 1H[bond]13C NMR spectroscopy of methyl groups in very high molecular weight proteins and protein complexes. *J Am Chem Soc* **125**, 10420-10428 (2003). https://doi.org/10.1021/ja030153x
112 Lundström, P., Vallurupalli, P., Hansen, D. F. & Kay, L. E. Isotope labeling methods for studies of excited protein states by relaxation dispersion NMR spectroscopy. *Nat Protoc* **4**, 1641-1648 (2009). https://doi.org/10.1038/nprot.2009.118
113 Sprangers, R. & Kay, L. E. Quantitative dynamics and binding studies of the 20S proteasome by NMR. *Nature* **445**, 618-622 (2007). https://doi.org/10.1038/nature05512
114 Grutsch, S., Brüschweiler, S. & Tollinger, M. NMR Methods to Study Dynamic Allostery. *PLoS Comput Biol* **12**, e1004620 (2016). https://doi.org/10.1371/journal.pcbi.1004620
115 Rosenzweig, R. & Kay, L. E. Bringing dynamic molecular machines into focus by methyl-TROSY NMR. *Annu Rev Biochem* **83**, 291-315 (2014). https://doi.org/10.1146/annurev-biochem-060713-035829
116 Tomlinson, J. H., Thompson, G. S., Kalverda, A. P., Zhuravleva, A. & O'Neill, A. J. A target-protection mechanism of antibiotic resistance at atomic resolution: insights into FusB-type fusidic acid resistance. *Sci Rep* **6**, 19524 (2016). https://doi.org/10.1038/srep19524
117 Korzhnev, D. M., Kloiber, K., Kanelis, V., Tugarinov, V. & Kay, L. E. Probing slow dynamics in high molecular weight proteins by methyl-TROSY NMR spectroscopy: application to a 723-residue enzyme. *J Am Chem Soc* **126**, 3964-3973 (2004). https://doi.org/10.1021/ja039587i
118 Baek, M. *et al.* Accurate prediction of protein structures and interactions using a three-track neural network. *Science* **373**, 871-876 (2021). https://doi.org/doi:10.1126/science.abj8754
119 Cao, L. *et al.* Design of protein-binding proteins from the target structure alone. *Nature* **605**, 551-560 (2022). https://doi.org/10.1038/s41586-022-04654-9
120 Plotnikov, A. N., Hubbard, S. R., Schlessinger, J. & Mohammadi, M. Crystal structures of two FGF-FGFR complexes reveal the determinants of ligand-receptor specificity. *Cell* **101**, 413-424 (2000). https://doi.org/10.1016/s0092-8674(00)80851-x
121 Croll, T. I. *et al.* Higher-Resolution Structure of the Human Insulin Receptor Ectodomain: Multi-Modal Inclusion of the Insert Domain. *Structure* **24**, 469-476 (2016). https://doi.org/10.1016/j.str.2015.12.014

122 Wiesmann, C., Ultsch, M. H., Bass, S. H. & de Vos, A. M. Crystal structure of nerve growth factor in complex with the ligand-binding domain of the TrkA receptor. *Nature* **401**, 184-188 (1999). https://doi.org/10.1038/43705
123 Garrett, T. P. *et al.* Crystal structure of a truncated epidermal growth factor receptor extracellular domain bound to transforming growth factor alpha. *Cell* **110**, 763-773 (2002). https://doi.org/10.1016/s0092-8674(02)00940-6
124 Shim, A. H. *et al.* Structures of a platelet-derived growth factor/propeptide complex and a platelet-derived growth factor/receptor complex. *Proc Natl Acad Sci U S A* **107**, 11307-11312 (2010). https://doi.org/10.1073/pnas.1000806107
125 Xu, Y. *et al.* How ligand binds to the type 1 insulin-like growth factor receptor. *Nat Commun* **9**, 821 (2018). https://doi.org/10.1038/s41467-018-03219-7
126 McElroy, C. A., Dohm, J. A. & Walsh, S. T. Structural and biophysical studies of the human IL-7/IL-7Ralpha complex. *Structure* **17**, 54-65 (2009). https://doi.org/10.1016/j.str.2008.10.019
127 Radaev, S. *et al.* Ternary complex of transforming growth factor-beta1 reveals isoform-specific ligand recognition and receptor recruitment in the superfamily. *J Biol Chem* **285**, 14806-14814 (2010). https://doi.org/10.1074/jbc.M109.079921
128 Barton, W. A. *et al.* Crystal structures of the Tie2 receptor ectodomain and the angiopoietin-2-Tie2 complex. *Nat Struct Mol Biol* **13**, 524-532 (2006). https://doi.org/10.1038/nsmb1101
129 Arnett, K. L., Harrison, S. C. & Wiley, D. C. Crystal structure of a human CD3-epsilon/delta dimer in complex with a UCHT1 single-chain antibody fragment. *Proc Natl Acad Sci U S A* **101**, 16268-16273 (2004). https://doi.org/10.1073/pnas.0407359101
130 Lemmon, M. A. & Schlessinger, J. Cell signaling by receptor tyrosine kinases. *Cell* **141**, 1117-1134 (2010). https://doi.org/10.1016/j.cell.2010.06.011
131 Marković, I. & Savvides, S. N. Modulation of Signaling Mediated by TSLP and IL-7 in Inflammation, Autoimmune Diseases, and Cancer. *Front Immunol* **11**, 1557 (2020). https://doi.org/10.3389/fimmu.2020.01557
132 Gillespie, J. J. *et al.* Structural Insight into How Bacteria Prevent Interference between Multiple Divergent Type IV Secretion Systems. *mBio* **6**, e01867-01815 (2015). https://doi.org/10.1128/mBio.01867-15
133 Huang, Y., Yang, C., Xu, X.-f., Xu, W. & Liu, S.-w. Structural and functional properties of SARS-CoV-2 spike protein: potential antivirus drug development for COVID-19. *Acta Pharmacologica Sinica* **41**, 1141-1149 (2020). https://doi.org/10.1038/s41401-020-0485-4
134 Ekiert, D. C. *et al.* Cross-neutralization of influenza A viruses mediated by a single antibody loop. *Nature* **489**, 526-532 (2012). https://doi.org/10.1038/nature11414
135 Fleishman, S. J. *et al.* Computational design of proteins targeting the conserved stem region of influenza hemagglutinin. *Science* **332**, 816-821 (2011). https://doi.org/10.1126/science.1202617
136 Kadam, R. U. *et al.* Potent peptidic fusion inhibitors of influenza virus. *Science* **358**, 496-502 (2017). https://doi.org/10.1126/science.aan0516
137 van Dongen, M. J. P. *et al.* A small-molecule fusion inhibitor of influenza virus is orally active in mice. *Science* **363** (2019). https://doi.org/10.1126/science.aar6221
138 Cao, L. *et al.* De novo design of picomolar SARS-CoV-2 miniprotein inhibitors. *Science* **370**, 426-431 (2020). https://doi.org/10.1126/science.abd9909
139 Case, J. B. *et al.* Ultrapotent miniproteins targeting the SARS-CoV-2 receptor-binding domain protect against infection and disease. *Cell Host Microbe* **29**, 1151-1161.e1155 (2021). https://doi.org/10.1016/j.chom.2021.06.008

140 Gul, S. & Hadian, K. Protein–protein interaction modulator drug discovery: past efforts and future opportunities using a rich source of low- and high-throughput screening assays. *Expert Opinion on Drug Discovery* **9**, 1393-1404 (2014). https://doi.org/10.1517/17460441.2014.954544
141 Zhang, L. & Zhang, H. Recent advances of affibody molecules in biomedical applications. *Bioorg Med Chem* **113**, 117923 (2024). https://doi.org/10.1016/j.bmc.2024.117923
142 Ståhl, S., Lindberg, H., Hjelm, L. C., Löfblom, J. & Dahlsson Leitao, C. Engineering of Affibody Molecules. *Cold Spring Harbor Protocols* **2024**, pdb.top107760 (2024). https://doi.org/10.1101/pdb.top107760
143 Yang, W. *et al.* Design of high-affinity binders to immune modulating receptors for cancer immunotherapy. *Nature Communications* **16**, 2001 (2025). https://doi.org/10.1038/s41467-025-57192-z
144 Rocklin, G. J. *et al.* Global analysis of protein folding using massively parallel design, synthesis, and testing. *Science* **357**, 168-175 (2017). https://doi.org/10.1126/science.aan0693
145 SnapGene. *pET-28(+)*, <https://www.snapgene.com/plasmids/pet_and_duet_vectors_(novagen)/pET-28a(+)> (2025).
146 Paliy, O., Bloor, D., Brockwell, D., Gilbert, P. & Barber, J. Improved methods of cultivation and production of deuteriated proteins from E. coli strains grown on fully deuteriated minimal medium. *J Appl Microbiol* **94**, 580-586 (2003). https://doi.org/10.1046/j.1365-2672.2003.01866.x
147 Jorgensen, J. H. & National Committee for Clinical Laboratory Standards, i. b. *Methods for dilution antimicrobial susceptibility tests for bacteria that grow aerobically : approved standard*. Third edition. edn, (National Committee for Clinical Laboratory Standards, 1993).
148 Wiegand, I., Hilpert, K. & Hancock, R. E. W. Agar and broth dilution methods to determine the minimal inhibitory concentration (MIC) of antimicrobial substances. *Nature Protocols* **3**, 163-175 (2008). https://doi.org/10.1038/nprot.2007.521
149 O'Callaghan, C. H., Morris, A., Kirby, S. M. & Shingler, A. H. Novel method for detection of beta-lactamases by using a chromogenic cephalosporin substrate. *Antimicrob Agents Chemother* **1**, 283-288 (1972). https://doi.org/10.1128/aac.1.4.283
150 Delaglio, F. *et al.* NMRPipe: a multidimensional spectral processing system based on UNIX pipes. *J Biomol NMR* **6**, 277-293 (1995). https://doi.org/10.1007/bf00197809
151 Skinner, S. P. *et al.* CcpNmr AnalysisAssign: a flexible platform for integrated NMR analysis. *Journal of Biomolecular NMR* **66**, 111-124 (2016). https://doi.org/10.1007/s10858-016-0060-y
152 Maciejewski, M. W. *et al.* NMRbox: A Resource for Biomolecular NMR Computation. *Biophys J* **112**, 1529-1534 (2017). https://doi.org/10.1016/j.bpj.2017.03.011
153 Meissner, A. & SŁrensen, O. W. Three-dimensional protein NMR TROSY-type (15)N-resolved (1)H(N)-(1)H(N) NOESY spectra with diagonal peak suppression. *J Magn Reson* **142**, 195-198 (2000). https://doi.org/10.1006/jmre.1999.1961
154 Schanda, P. & Brutscher, B. Very fast two-dimensional NMR spectroscopy for real-time investigation of dynamic events in proteins on the time scale of seconds. *J Am Chem Soc* **127**, 8014-8015 (2005). https://doi.org/10.1021/ja051306e

155 Mureddu, L. & Vuister, G. W. Simple high-resolution NMR spectroscopy as a tool in molecular biology. *The FEBS Journal* **286**, 2035-2042 (2019). https://doi.org/https://doi.org/10.1111/febs.14771
156 Pritišanac, I. *et al.* Automatic Assignment of Methyl-NMR Spectra of Supramolecular Machines Using Graph Theory. *Journal of the American Chemical Society* **139**, 9523-9533 (2017). https://doi.org/10.1021/jacs.6b11358
157 Monneau, Y. R. *et al.* Automatic methyl assignment in large proteins by the MAGIC algorithm. *J Biomol NMR* **69**, 215-227 (2017). https://doi.org/10.1007/s10858-017-0149-y
158 Frueh, D., Goodrich, A., Mishra, S. & Nichols, S. NMR methods for structural studies of large monomeric and multimeric proteins. *Current opinion in structural biology* **23** (2013). https://doi.org/10.1016/j.sbi.2013.06.016
159 Kozak, S. *et al.* Optimization of protein samples for NMR using thermal shift assays. *J Biomol NMR* **64**, 281-289 (2016). https://doi.org/10.1007/s10858-016-0027-z
160 Kay, L. E. & Gardner, K. H. Solution NMR spectroscopy beyond 25 kDa. *Curr Opin Struct Biol* **7**, 722-731 (1997). https://doi.org/10.1016/s0959-440x(97)80084-x
161 Clore, G. M. & Gronenborn, A. M. NMR structure determination of proteins and protein complexes larger than 20 kDa. *Curr Opin Chem Biol* **2**, 564-570 (1998). https://doi.org/10.1016/s1367-5931(98)80084-7
162 Wagner, G. Prospects for NMR of large proteins. *J Biomol NMR* **3**, 375-385 (1993). https://doi.org/10.1007/bf00176005
163 Venters, R. A. *et al.* High-level 2H/13C/15N labeling of proteins for NMR studies. *J Biomol NMR* **5**, 339-344 (1995). https://doi.org/10.1007/bf00182275
164 Mann, L. R. & Moses, V. Properties of Escherichia coli grown in deuterated media. *Folia Microbiol (Praha)* **16**, 267-284 (1971). https://doi.org/10.1007/bf02872808
165 Xu, Y. & Matthews, S. MAP-XSII: an improved program for the automatic assignment of methyl resonances in large proteins. *J Biomol NMR* **55**, 179-187 (2013). https://doi.org/10.1007/s10858-012-9700-z
166 Wilkins, M. R. *et al.* Protein identification and analysis tools in the ExPASy server. *Methods Mol Biol* **112**, 531-552 (1999). https://doi.org/10.1385/1-59259-584-7:531
167 Liao, Y. D., Jeng, J. C., Wang, C. F., Wang, S. C. & Chang, S. T. Removal of N-terminal methionine from recombinant proteins by engineered E. coli methionine aminopeptidase. *Protein Sci* **13**, 1802-1810 (2004). https://doi.org/10.1110/ps.04679104
168 Li, Z., Yalcin, T. & Cassady, C. J. C-terminal amino acid residue loss for deprotonated peptide ions containing glutamic acid, aspartic acid, or serine residues at the C-terminus. *J Mass Spectrom* **41**, 939-949 (2006). https://doi.org/10.1002/jms.1053
169 Studier, F. W. & Moffatt, B. A. Use of bacteriophage T7 RNA polymerase to direct selective high-level expression of cloned genes. *J Mol Biol* **189**, 113-130 (1986). https://doi.org/10.1016/0022-2836(86)90385-2
170 Davanloo, P., Rosenberg, A. H., Dunn, J. J. & Studier, F. W. Cloning and expression of the gene for bacteriophage T7 RNA polymerase. *Proc Natl Acad Sci U S A* **81**, 2035-2039 (1984). https://doi.org/10.1073/pnas.81.7.2035
171 Cai, M., Huang, Y., Yang, R., Craigie, R. & Clore, G. M. A simple and robust protocol for high-yield expression of perdeuterated proteins in Escherichia coli grown in shaker flasks. *J Biomol NMR* **66**, 85-91 (2016). https://doi.org/10.1007/s10858-016-0052-y

172 Litvinenko, L. A. *et al.* [Effect of heavy water on the growth, glucose assimilation and stability of Escherichia coli to freezing-thawing]. *Mikrobiologiia* **61**, 1030-1037 (1992).
173 Opitz, C., Ahrné, E., Goldie, K. N., Schmidt, A. & Grzesiek, S. Deuterium induces a distinctive Escherichia coli proteome that correlates with the reduction in growth rate. *J Biol Chem* **294**, 2279-2292 (2019). https://doi.org/10.1074/jbc.RA118.006914
174 Aggarwal, R. K. & Narang, A. Inducer exclusion, by itself, cannot account for the glucose-mediated lac repression of Escherichia coli. *Biophys J* **121**, 820-829 (2022). https://doi.org/10.1016/j.bpj.2022.01.016
175 Aggarwal, R. K. & Narang, A. Positive feedback exists and drives the glucose-mediated repression in Escherichia coli. *Biophys J* **121**, 808-819 (2022). https://doi.org/10.1016/j.bpj.2022.01.017
176 Tugarinov, V., Choy, W.-Y., Orekhov, V. Y. & Kay, L. E. Solution NMR-derived global fold of a monomeric 82-kDa enzyme. *Proceedings of the National Academy of Sciences* **102**, 622-627 (2005). https://doi.org/doi:10.1073/pnas.0407792102
177 Kay, L. E. New Views of Functionally Dynamic Proteins by Solution NMR Spectroscopy. *Journal of Molecular Biology* **428**, 323-331 (2016). https://doi.org/https://doi.org/10.1016/j.jmb.2015.11.028
178 Park, S. J., Kostic, M. & Dyson, H. J. Dynamic Interaction of Hsp90 with Its Client Protein p53. *J Mol Biol* **411**, 158-173 (2011). https://doi.org/10.1016/j.jmb.2011.05.030
179 Gelis, I. *et al.* Structural basis for signal-sequence recognition by the translocase motor SecA as determined by NMR. *Cell* **131**, 756-769 (2007). https://doi.org/10.1016/j.cell.2007.09.039
180 Kreishman-Deitrick, M. *et al.* NMR analyses of the activation of the Arp2/3 complex by neuronal Wiskott-Aldrich syndrome protein. *Biochemistry* **44**, 15247-15256 (2005). https://doi.org/10.1021/bi051065n
181 Kelly, A. E., Ou, H. D., Withers, R. & Dötsch, V. Low-Conductivity Buffers for High-Sensitivity NMR Measurements. *Journal of the American Chemical Society* **124**, 12013-12019 (2002). https://doi.org/10.1021/ja026121b
182 Purslow, J. A., Khatiwada, B., Bayro, M. J. & Venditti, V. NMR Methods for Structural Characterization of Protein-Protein Complexes. *Front Mol Biosci* **7**, 9 (2020). https://doi.org/10.3389/fmolb.2020.00009
183 Reinhard, L., Mayerhofer, H., Geerlof, A., Mueller-Dieckmann, J. & Weiss, M. S. Optimization of protein buffer cocktails using Thermofluor. *Acta Crystallogr Sect F Struct Biol Cryst Commun* **69**, 209-214 (2013). https://doi.org/10.1107/s1744309112051858
184 Bell, D. *et al.* Sedimentation of large, soluble proteins up to 140 kDa for (1)H-detected MAS NMR and (13)C DNP NMR - practical aspects. *Res Sq* (2024). https://doi.org/10.21203/rs.3.rs-3972885/v1
185 Golovanov, A. P., Hautbergue, G. M., Wilson, S. A. & Lian, L.-Y. A Simple Method for Improving Protein Solubility and Long-Term Stability. *Journal of the American Chemical Society* **126**, 8933-8939 (2004). https://doi.org/10.1021/ja049297h
186 Vagenende, V., Yap, M. G. & Trout, B. L. Mechanisms of protein stabilization and prevention of protein aggregation by glycerol. *Biochemistry* **48**, 11084-11096 (2009). https://doi.org/10.1021/bi900649t
187 Voinov, M. *et al.* Cysteine-Specific Labeling of Proteins with a Nitroxide Biradical for Dynamic Nuclear Polarization NMR. *The journal of physical chemistry. B* **119 32**, 10180-10190 (2015). https://doi.org/10.1021/acs.jpcb.5b05230

188 Saio, T., Guan, X., Rossi, P., Economou, A. & Kalodimos, C. G. Structural basis for protein antiaggregation activity of the trigger factor chaperone. *Science* **344**, 1250494 (2014). https://doi.org/10.1126/science.1250494
189 Tugarinov, V., Sprangers, R. & Kay, L. E. Probing Side-Chain Dynamics in the Proteasome by Relaxation Violated Coherence Transfer NMR Spectroscopy. *Journal of the American Chemical Society* **129**, 1743-1750 (2007). https://doi.org/10.1021/ja067827z
190 Amero, C. *et al.* A systematic mutagenesis-driven strategy for site-resolved NMR studies of supramolecular assemblies. *Journal of Biomolecular NMR* **50**, 229-236 (2011). https://doi.org/10.1007/s10858-011-9513-5
191 Poulsen, F. M., Hoch, J. C. & Dobson, C. M. Structural study of the hydrophobic box region of lysozyme in solution using nuclear Overhauser effects. *Biochemistry* **19**, 2597-2607 (1980). https://doi.org/10.1021/bi00553a011
192 Sora, V. *et al.* RosettaDDGPrediction for high-throughput mutational scans: From stability to binding. *Protein Sci* **32**, e4527 (2023). https://doi.org/10.1002/pro.4527
193 Becker, W., Bhattiprolu, K. C., Gubensäk, N. & Zangger, K. Investigating Protein-Ligand Interactions by Solution Nuclear Magnetic Resonance Spectroscopy. *Chemphyschem* **19**, 895-906 (2018). https://doi.org/10.1002/cphc.201701253
194 Kirby, W. M., Rosenfeld, L. S. & Brodie, J. Oxacillin: laboratory and clinical evaluation. *JAMA* **181**, 739-744 (1962). https://doi.org/10.1001/jama.1962.03050350001001
195 Yu, M. *et al.* Simple and Rapid Discrimination of Methicillin-Resistant Staphylococcus aureus Based on Gram Staining and Machine Vision. *Microbiol Spectr* **11**, e0528222 (2023). https://doi.org/10.1128/spectrum.05282-22
196 Fuda, C., Suvorov, M., Vakulenko, S. B. & Mobashery, S. The Basis for Resistance to β-Lactam Antibiotics by Penicillin-binding Protein 2a of Methicillin-resistant Staphylococcus aureus*. *Journal of Biological Chemistry* **279**, 40802-40806 (2004). https://doi.org/10.1074/jbc.M403589200
197 Williamson, M. P. Using chemical shift perturbation to characterise ligand binding. *Prog Nucl Magn Reson Spectrosc* **73**, 1-16 (2013). https://doi.org/10.1016/j.pnmrs.2013.02.001
198 Jarmoskaite, I., AlSadhan, I., Vaidyanathan, P. P. & Herschlag, D. How to measure and evaluate binding affinities. *Elife* **9** (2020). https://doi.org/10.7554/eLife.57264
199 Davies, T. A. *et al.* Binding of ceftobiprole and comparators to the penicillin-binding proteins of Escherichia coli, Pseudomonas aeruginosa, Staphylococcus aureus, and Streptococcus pneumoniae. *Antimicrob Agents Chemother* **51**, 2621-2624 (2007). https://doi.org/10.1128/aac.00029-07
200 Testing, E. C. o. A. S. (version, 2020).
201 Pfaller, M. *et al.* Antimicrobial activity of ceftobiprole and comparator agents when tested against contemporary Gram-positive and-negative organisms collected from Europe (2015). *Diagnostic Microbiology and Infectious Disease* **91**, 77-84 (2018).
202 Farrell, D. J., Flamm, R. K., Sader, H. S. & Jones, R. N. Ceftobiprole activity against over 60,000 clinical bacterial pathogens isolated in Europe, Turkey, and Israel from 2005 to 2010. *Antimicrobial agents and chemotherapy* **58**, 3882-3888 (2014).
203 Haq, I., Anwar, F. & Tong, Y. De Novo Design of Highly Stable Binders Targeting Dihydrofolate Reductase in Klebsiella pneumoniae. *Proteins: Structure, Function, and Bioinformatics* **93**, 1675-1687 (2025). https://doi.org/https://doi.org/10.1002/prot.26835

204 Watson, J. L. *et al.* De novo design of protein structure and function with RFdiffusion. *Nature* **620**, 1089-1100 (2023). https://doi.org/10.1038/s41586-023-06415-8

205 Konermann, L., Pan, J. & Liu, Y.-H. Hydrogen exchange mass spectrometry for studying protein structure and dynamics. *Chemical Society Reviews* **40**, 1224-1234 (2011). https://doi.org/10.1039/C0CS00113A

206 Vinciauskaite, V. & Masson, G. R. Fundamentals of HDX-MS. *Essays Biochem* **67**, 301-314 (2023). https://doi.org/10.1042/ebc20220111

207 Masson, G. R. *et al.* Recommendations for performing, interpreting and reporting hydrogen deuterium exchange mass spectrometry (HDX-MS) experiments. *Nature Methods* **16**, 595-602 (2019). https://doi.org/10.1038/s41592-019-0459-y

208 Carver, J. P. & Richards, R. E. A general two-site solution for the chemical exchange produced dependence of T2 upon the carr-Purcell pulse separation. *Journal of Magnetic Resonance (1969)* **6**, 89-105 (1972). https://doi.org/https://doi.org/10.1016/0022-2364(72)90090-X

209 Clore, G. M. & Iwahara, J. Theory, Practice, and Applications of Paramagnetic Relaxation Enhancement for the Characterization of Transient Low-Population States of Biological Macromolecules and Their Complexes. *Chemical Reviews* **109**, 4108-4139 (2009). https://doi.org/10.1021/cr900033p

210 Clore, G. M. Practical Aspects of Paramagnetic Relaxation Enhancement in Biological Macromolecules. *Methods Enzymol* **564**, 485-497 (2015). https://doi.org/10.1016/bs.mie.2015.06.032

211 Organization, W. H. *Global report on infection prevention and control*. (World Health Organization, 2022).